Paolo Errante

LARGE EDDY SIMULATION ANALYSIS OF FLUID JETS IN CROSS FLOW

Tesi di Laurea Magistrale

Università di Pisa

Data: 06/10/2016

UNIVERSITÀ DI PISA
Scuola di Ingegneria

Corso di Laurea Magistrale in INGEGNERIA ENERGETICA

LARGE EDDY SIMULATION ANALYSIS OF JET IN CROSS FLOW

Tesi di:
Paolo Errante

Relatori:

Ulrich Bieder . . . .

Walter Ambrosini . . . .

Candidato:

Paolo Errante . . . .

V Appello 2016
Anno Accademico 2015/2016

Aknowledgments

This work has involved the contribution of many persons that I would to thank. They are not reported in any order of importance, because there is no cardinality in the way the helped me to improve the quality of this master thesis, and each one has done his part. I would like to express my gratitude to:

My advisor Prof. Walter Ambrosini, who gave me the opportunity to challenge my self with the multidisciplinary subjects involved in this work. For his patience in this recent period, for his kindness and for his precious support.

The CEA Laboratory Chief of LMSF, Anne Burbeau, who allowed me to join her group in Saclay for my stage. I would like to thank her for the way she welcomed me and get me involved into the laboratory activities.

My supervisor at CEA, the engineer Ulrich Bieder, for his availability and for the help that he gave me during the whole duration of my stage, which was both technical and motivational. If I have learned a lot from this experience, it is also thanks to him.

Maria Giovanna Rodio, researcher engineer of the LMSF group, who helped me with all the practical issues that I had to face before and after I have arrived in France. If I managed to achieve this goal it is also thank to her.

Céline Capitaine, the responsible in charge of the TRUST/TrioCFD support team. I would like to say thank to her for guiding me during the modelization process and for the precious hints about the use of the code and the cluster, which allowed me to carry on this work.

Pascal Omnès, researcher engineer of the LMSF group, for his kindness and for the helpful French lessons, and his sympathy.

Qingqing Feng and Sofiane Houbar, internship students of the LMFS, for sharing with me this experience.

The whole SALOME development team, for their kindness and availability.

the National Computing Center for Higher Education (CINES) for gaving me the access to the Occigen resources, without which the practical part of this work would not have been accomplished.

Thank you all!

Abstract

This work has been carried out at the "Laboratoire de Modélisation et Simulation en mécanique des Fluides" of CEA during a stage of 6 months.
The main subject of this work involves jets in cross flow, which are of fundamental industrial importance and play an important role in the validation of turbulence models. Two jet configurations are investigated with the TrioCFD code:

- a tee junction of circular tubes where a hot jet discharges into a cold main flow.
- a rectangular channel discharging a jet marked by a scalar into a main channel flow.

The *tee-junction* configuration is very important for the phenomena of thermal fatigue. The OECD/NEA benchmark on the Vattenfall tee junction flow is analyzed. This test case is selected because, beside the experimental results, various calculation results with several turbulence modelling approaches have been published. A Large Eddie Simulation (*LES*) modelling and calculation strategy is developed and validated on these data for jets in crossflow under thermal fatigue conditions.
The *rectangular* jet configuration is important for basic physical understanding and modelling and has been analyzed experimentally at CEA in previous studies. Such work was focused on the turbulent mixing between a rectangular channel flow with grid turbulence exiting a heated jet into a confined grid turbulent crossflow, with both kinematic and passive scalar high quality measurements in order to characterize its statistical properties (energy spectra, Reynolds stresses anisotropy and PdF). These experiments are analyzed for the first time with LES by applying the strategy developed for the first configuration. The turbulent inlet boundary conditions are well controlled in both experiment and calculation (grid turbulence). Structured and unstructured grids are used to predict the measured mean values and turbulent fluctuations (velocity and scalar) as well as the Reynolds stresses.
The activities aimed also to test the capabilities of the TrioCFD code results through the inspection of their agreement with the experimental datas obtained for T-junctions mixing ducts for a preliminary analysis of TrioCFD performances and to get a balanced compliance of the code's capabilities.

Contents

List of Figures

List of Tables

Chapter1

Introduction

In this section an overall view of the main subjects dealt with is provided. Starting from the main reasons which drive studies on thermal fatigue from jets in cross flow configuration, this chapter describes the main issues related to this subject, giving details from both a scientific and an industrial application point of view. At the end, some experimental facilities installed to arise technical and theoretical knowledge upon jets in cross flow are presented.

1.1 Motivations for the work

In the last decades, the nuclear industry aimed to better understand thermal fatigue phenomena in order to improve operative margins of reactors components and to increase their overall lifetime. Besides this main industrial request, experimental data have been produced to validate Computational Fluid Dynamics (CFD) codes and further model developments. The intrinsic advantages given by numerical approaches shows an interesting potential and their application can lead to an in-depth understanting of complex operating conditions and geometries which are difficult and/or expensive to be reproduced for experimental investigations. Moreover detailed validations of CFD codes are still needed to achieve a better understanting on their limits whenever they are used for studying such kind of phenomena.

With these objectives, the Direction de l'Energie Nucléaire (DEN) has planned to develop a new generation of simulation utilities for thermohydraulic problems, in which *TrioCFD* represent the main tool for Large Eddy Simulation (LES), in order to give an answer to the above mentioned problems.

1.2 Problems related to jets in cross flow

The interactions between two fluid streams into the Jets In Crossflow (JICF) represent an important challenge in different applications domains, even beside those treated in this work.

One can refer to the aeronautic field, by recalling the Vertical Short Take-Off Landing (V-STOL) that exploit this configuration.

Moreover, the cooling capabilities of JICF still raise interest in thermal applications of turbomachinery where it constitutes a crucial point for the lifetime of turbine components.

Nonetheless JICFs are actually investigated to achieve polluttant emissions reduction, as most of them are already involved in systems where chemical reagent are mixed (e.g. fuels in combustion chambers). All in all, the simple temperatures prediction given by the mixing process is still an important parameter to be known to achieve a good design and control of the hydraulic circuits. Regarding thermal fatigue, it can be equally important to observe the interaction between two transversal jets in order to predict thermal stress cycles on the boundary walls.

1.3 State of the art

This section will present a literature review of the main works developed so far about JICF configurations. After a general description of the flows and their transient, the result of different studies will be given.

1.3.1 Global JICF main characteristics

Speed ratio

In a simplified approach, JICF can be considered as the result of two momentum flows. Therefore, the main characteristic parameter it is given by the ratio between the two flows of momentum J defined as:

$$J = \frac{\rho_j U_j^2}{\rho_\infty U_\infty^2} \tag{1.1}$$

where the j index is adopted for jet quantity and ∞ are the same for the main stream. This ratio is often replaced with the following:

$$r = \sqrt{J} = \sqrt{\frac{\rho_j U_j^2}{\rho_\infty U_\infty^2}} \tag{1.2}$$

which becames a simple speed ratio whenever the mixing fluids are the same and keep negligible differences in terms of temperature.

General characteristics

In Fig. **??** (Chassaing et al. 1974 [**?**]) a simplified schematization of JICF is given in a symmetry plane, where the streams meet each other perpendicularly ($\delta_j = 90$). Other studies have been conducted for different injection angles ($\delta_j \neq 90$); they will not be treated in this work, which will be focused just on perpendicular flows.

The jet evolution is generally decomposed into three characterisc zones as described below (Fougairolle [**?**]):

- the potential zone, which is located right on the exit of the jet channel. In this part the flow characteristics keeps nearly the same of those realized in the injection duct: the injection velocity U_j and all the marking scalars (concentration or temperature) are at maximum levels with respect to the whole domain. The extent of this zone higly depends on r and on the injection channel shape.

- the maximal deflection zone, as its name suggests, is characterized by the maximum curvature that the jet stream is subjected to the effect of the main stream coming from the main channel. In this part the jet stream experiences the maximum bend and starts its deformation, as it will be shown in the next sections, the core starts to loose the original injection shape to achieve a "bean" shape.

- at the end, the turbulent zone (also called "far field") is developed and the jet stream acquires the same direction of the main flow. This zone is characterized by the presence of two counter-rotating vortices that proceeds along the center jet line.

Lines are used as well to describe the jet evolution:

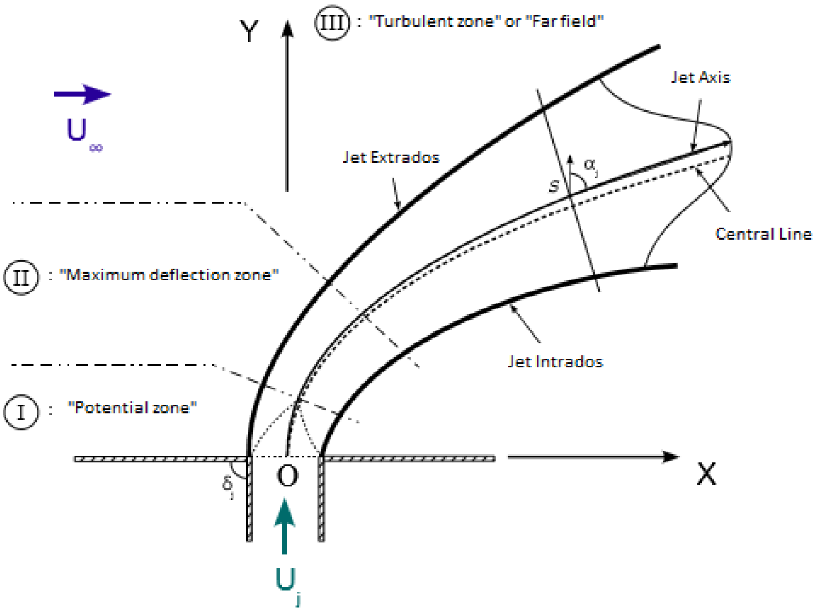

Figure 1.1: JICF configuration in a symmetry plane (Chassaing et. al [?])

- The inner and outer lines which bound the jet flow in the overall domain, they follow the jet section expansion law; the outer line is associated with the jet penetration lenght. Some authors (Patrick 1967 [?]) extend this lenght to the zone where the marking scalar reaches half of the injection value.
- The jet axis which defines the axis trajectory. It is generally assumed as the maximum speed locus. At a general location along the line, the deflection angle is defined by α_j, defined as the angle between the normal Y and the tangent to the jet axis.
- The central line is defined starting from the inner and outer lines, as a median between them.

Trajectory

Patrick [?] has been one of the first authors who provided experimental data on the jet trajectories for r between 6 and 50. These empirical results have been based on concentration measurements of nitrogen monoxide injected into an air jet stream.
It is possible to distinguish three lenght-scales which describes the jet behaviour. The first one is intuitively the jet hydraulic diameter d_j. One of most used equation for the description of the trajectory line is:

$$\frac{Y}{d_j} = A\left(\frac{1}{r}\right)^n \left(\frac{X}{d_j}\right)^m \tag{1.3}$$

where A, m, and n are experimental constants, X and Y are the coordinates aligned respectively with the main and jet channel axes.
Another attempt to describe the trajectory has been proposed by Pratte et Baines (1967) [?] by the following equation:

$$\frac{Y}{rd_j} = A\left(\frac{X}{rd_j}\right)^m \tag{1.4}$$

Using this formulation, the separation limit between the potential zone and the far field has been found at $X = 3.2rd_j$.The reference lenght rd_j gives the possibility to compare the trajectories, potential zone and far field of different configurations. Despite of this advantage, this scale is still not sufficient to regroup those trajectories with really high differences in terms of r (as already proved by Smith and Mungal [**?**]). Broadwell and Breidenthal (1984) [**?**] performed a theoretical study to model the JICF behaviour, this work led to the identification of the equation (**??**) with $m = \frac{1}{3}$.

Other authors have used the product $r^2 d_j$. It is the case of Keffer and Baines (1963) [**?**] who introduced this term into the potential field for r ratios from 2 to 10. The limits of this works lies in the consideration of a virtual orifice located into the jet exit section, that can be applied just in the overall potential field, but not elsewhere. This consideration partly explains the consinstancy of their results with experimental data.

Other different parameters can influence the jet penetration lenght into the main stream. One of these widely recognised to be the velocity profile. New et al. (2006) [**?**] have shown in particular, using Digital Particle Image Velocimetry (*DPIV*) and Laser-induced Fluorescence (*LIF*) (for a circular jet and r between 2.3 and 5.8), that a jet with a parabolic profile in velocity penetrates more deeply in the main stream than one with a flat profile. Su and Mungal [**?**] also found in this fact an explanation of the differences between their trajectory equation and the one obtained in the previous work made by Smith and Mungal [**?**]. The boundary layer thickness of the main flow, influences as well the jet trajectory; Cortelezzi and Karagozian (2001) [**?**] found through numerical simulation that the jet penetration lenght increases with the main stream boundary layer thickness. In conclusion Muppidi (2008) [**?**] took both these aspects to add into the trajectory expression a parameter which introduces the relative inertia of the two streams. As already mentioned, the scalar taken into account (speed, concentration, etc.) to define the jet trajectory has an influence as well. This is shown by Kamotani and Greber (1972) [**?**], in Fig. **??** showing measurements taken by hotwire anemometers and thermocouples for r values of 3.9 and 7.7. Local maximum velocity curves are close to those one reported by Margason (1968) [**?**].

The shape, dimensions and orientation of the jet channel also play an important role in defining the jet penetration lenght. McMahon and Mosher (1969) [**?**] observed, starting from pressure measurements, that a rectangular section with the major lenght parallel to the main stream direction achieves a greater penetration compared to the same shape with main dimension disposed perpendicularly or to a circular one. A detailed collection of JICF trajectory has been composed by Margason (1993) [**?**]. Table **??** summarises trajectory expressions obtained by some authors. Focusing on rectangular sections, some results of Barre (1998) [**?**] and Humber et al. (1993) [**?**] are reported as well.

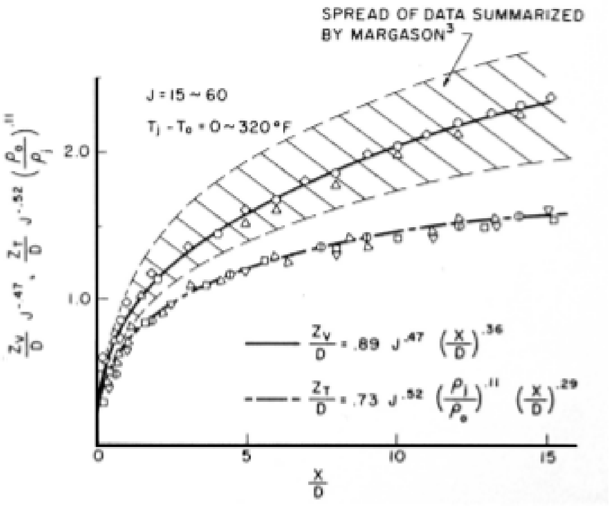

Figure 1.2: Experimental trajectories found by Kamotani and Greber (1972) [?]. Axis: abscissae (coordinate $\frac{X}{d_j}$) and ordinates (coordinate $\frac{Y}{d_j}$). Transported scalar: Lines (velocity), Dashed lines (temperature)

Author	**Ratio r**	**Trajectory equation**
Patrick (1967) [?]	$6 < r < 50$	$\frac{y}{d_j} = r^{0.85} \left(\frac{x}{d_j}\right)^{0.38}$
Kamotani and Greber (1967) [?]	$r = 3.9$ and 7.7	$\frac{y}{d_j} = 0.89 r^{0.94} \left(\frac{x}{d_j}\right)^{0.36}$
Chassaing et al. (1974) [?]	$2.37 < r < 6.35$	$\frac{2y}{d_j} = (1.53 + 0.9r) \left(\frac{2x}{d_j}\right)^{0.385}$
Patrick (1967) [?]	$6 < r < 50$	$\frac{y}{d_j} = r^0.85 \left(\frac{x}{rd_j}\right)^{0.38}$
Pratte and Baines (1967) [?]	$5 < r < 35$	$\frac{y}{rd_j} = 2.05 \left(\frac{x}{rd_j}\right)^{0.28}$
Kamotani and Greber (1972) [?]	$r = 3.9$ and 7.7	$\frac{y}{d_j} = 0.73 r^{1.04} \left(\frac{\rho_j}{\rho_\infty}\right)^{0.11} \left(\frac{x}{d_j}\right)^{0.29}$
Humber et al. (1993) [?]	$r = 2$ and 3.4	$\frac{y}{rd_j} = 1.91 \left(\frac{x}{rd_j}\right)^{0.342}$
Barre (1998) [?]	$r = 5$	$\frac{y}{d_j} = 0.72 r^{1.01} \left(\frac{x}{d_j}\right)^{0.36}$
Su and Mungal (2004) [?]	$r = 5.7$	$\frac{y}{rd_j} = 1.95 \left(\frac{x}{rd_j}\right)^{0.302}$

Table 1.1: Trajectory expressions from several authors. Based on maximum velocity locus (top part) and maximum transported scalar locus (bottom part)

Considering the above, it can be noted that there is a wide variety of configurations and that it seeims impossible to synthetise all the observations with few universal laws.

Scalar decay

Along the jet trajectory line, both diffusive and transport phenomena act on the scalars transported by the jet. This mixing effects cause the scalar reduction up to the zone where the two streams are fully mixed. Smith and Mungal (1998) [**?**] focus their interests on scalar decay upon the center line of a circular jet, with speed ratio r between 5 and 25. They adopted induced fluorescence by laser while marking the jet flow using acetone. The decay lines obtained by this method are presented in Fig. **??**. Beyond the potential region, where the concentration scalar stays at its maximum value, an intermediate zone can be noted which shows a $s^{-1.3}$ law (for $10 < r < 25$), which is steeper than the one of a free jet (s^{-1}) (Fougairolle [**?**]). Once the jet is aligned with the main stream, in the far field, it is possible to observe the presence of "re-connection points" (highlighted with an x in Fig. **??**) in which the scalar decay sharply changes its slope. Starting from these locations the concentration of the scalar (for $r = 5$) follows a $s^{-2/3}$ law, as predicted by the analytic work carried out by Hasselbrink and Mungal (1996) [**?**] as well by Broadwell and Breidenthal (1984) [**?**]. Despite this agreements, for all the other values of r different power laws apply, and in some cases, the "re-connection point" are not even observed for domain extension reasons.

Su and Mungal (2004) [**?**] detected (at $r = 5.7$) a decay law s^{-1} just after the near field and a remarkable decay zone once the "re-connection point" is passed. The main differences between these studies lies in the jet exit velocity profile adopted, in fact, Su and Mungal used a parabolic one.

Patrick (1967) [**?**] published an empirical formula based on the scalar concentration decay data. In Eq.**??** C_s stands for the scalar concentration at the curved abscissae s, while d_0 is the jet section diameter and r the already known speed ratio.

$$\frac{1}{C_s} = \left[\left(\frac{s}{d_j} \right) exp \left(\frac{7.8}{r} - 1.856 \right) \right]^{1.18} \tag{1.5}$$

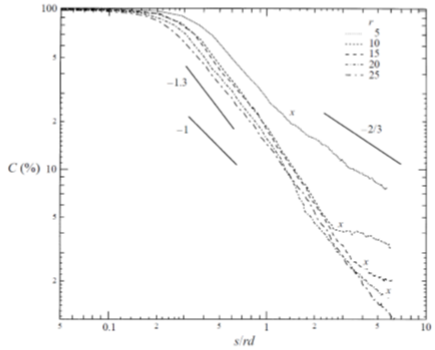

Figure 1.3: Concentration decay lines of Smith and Mungal (1998) [**?**]

1.3.2 Transient structures and their mechanics

The JICF configuration is extremely tridimensional; four structures types were identified by the past authors. In Fig. **??** it is possible to observe them globally: a "horseshoe" vortex, eddies belonging to the mixing layer, a tracking vortex and counter-rotating vortex pair (CVP).

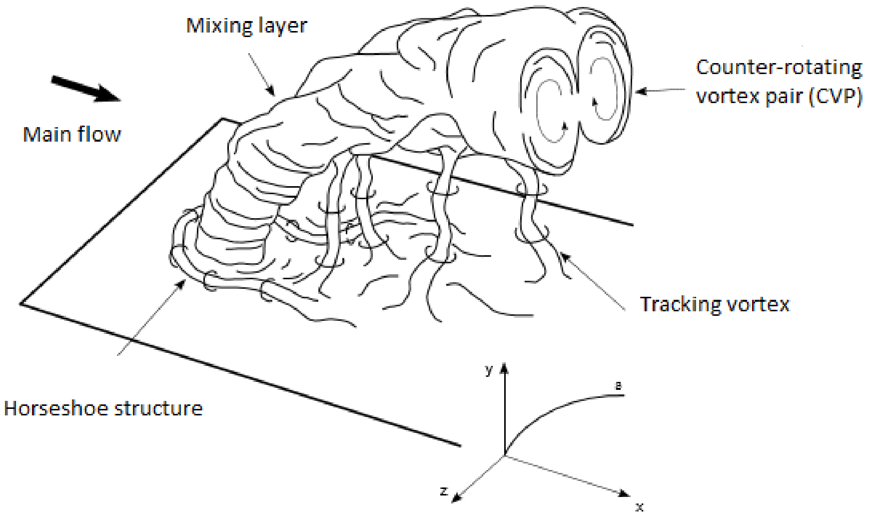

Figure 1.4: Schematization of the main eddies structure of Jet In Cross Flow (Fric and Roshko [?]

A brief description of these transient structures is reported below, starting from the interactions between the three structures located in the near field zone up to the CVP wich is dominant in the far field.

- ***Horseshoe vortex***
  The Horseshoe vortex is located downstream the jet exit section. This main shape is given by the interactions between the main flow boundary layer and the pressure gradient generated by the obstacle represented by the jet. After the appearence of a detachment, a vortex which bounds the jet column is formed. Kelso and Smiths (1995) [?], for a speed ratio $r = 4$ have observed the appearence of this structure and proposed a model which describes the streamlines behaviour (Fig. **??**).

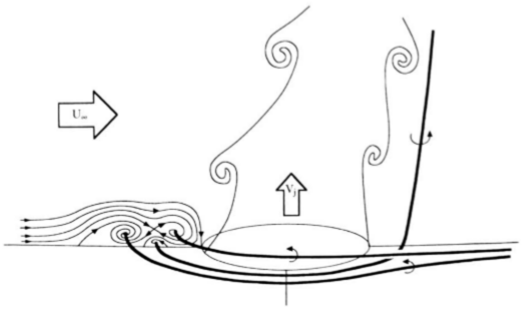

Figure 1.5: Streamlines of the Horseshoe vortex (Kelso and Smiths (1996) [?])

.

The nature of these structures is unstable, as confirmed by Krothapalli et al. (1989) [?] who found, from structures generated with a rectangular jet of aspect ratio 10, a Strouhal number of the same magnitude of flows around cylinder bodies. Fric and Roshko (1989) [?] also visualized this structure for r from 2 to 10 (circular jet of 3.75 cm diameter and $3800 < Re_\infty < 11400$) using smoke as tracing method, Fig. **??**.

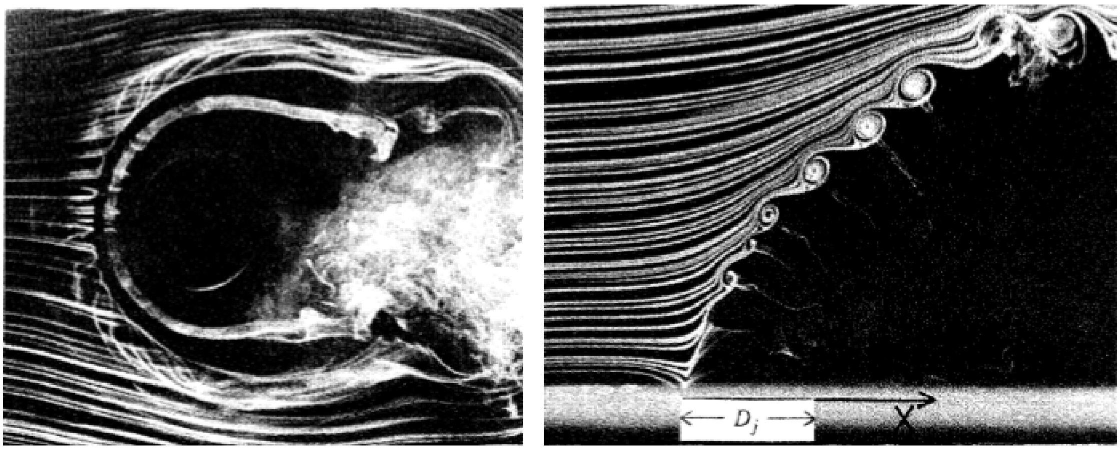

Figure 1.6: Vortex system shown by Fric and Roshko [?] $r = 2$ and $Re_\infty = 3800$. Horseshoe vortex structure (left) and mixing layer vortex (right).

- ***Mixing layer vortex***
  The jet mixing layer is formed by turbulent Kelvin-Helmholtz structures type. These structures are convected periodically with the jet and increase their main lenght during their lifetime. Fric and Roshko (1994) [?] identified the jet boundary layer as a vorticity source responsible for the generation of these structures in the near field, while Kelso et al. [?] also found the influence of this vortex on the CVP structures downstream, in the far field.

  Moreover, Kelso et al. [?] measured at a distance of three hydraulic diameters downstream the jet section (with $r = 2.2$) a characteristic winding frequency of this structure, stated at 7.1 Hz, with a Strouhal number based on the main stream of $St_\infty = \frac{f d_j}{U_\infty} = 0.65$ with f as winding frequency. Cortelezzi and Karagozian [?] proposed a modification for the mean velocity to be adopted in the Strouhal number formulation, by replacing the main stream mean velocity value with the sum of both the jet and main stream velocities (even noted the not perfect coherence of the hydraulic diameter definition)

  $$St_{mean} = \frac{2 f d_j}{U_\infty + U_j} \tag{1.6}$$

  Through a numerical investigation, for $r = 2.5$ and a boundary layer thickness of 0.5 d_∞ they founded a $St_{mean} = 1.14$ where the same formulation, in the case of Kelso et al. would give 0.4. Even though that this approximation lead to the right magnitude scale of the Strouhal number it does not take into account for variation in the upstream boundary layer thickness, which also affects rollup process.

- ***Tracking vortices***
  Tracking structures are generated behind the jet column connecting the main channel boundary layer with the jet main structure from the inner region of the exit section up to few hydraulic diameters downstream (Kuzo (1984) [?]). Fric and Roshko [?] observed these structures as well (Fig. **??**). It must be underlined that the origin of these structures is different compared to the analogous ones observable for flows around a cylindrical body. On contrary, Moussa et. al (1977) [?] considered a von Karman behaviour which consists in a repeating pattern of swirling vortices caused by the unsteady separation of the flow around blunt bodies According to Fric and Roshko [?], the main stream boundary layer starts to detach downstream the jet, caused by the adverse pressure gradient generated

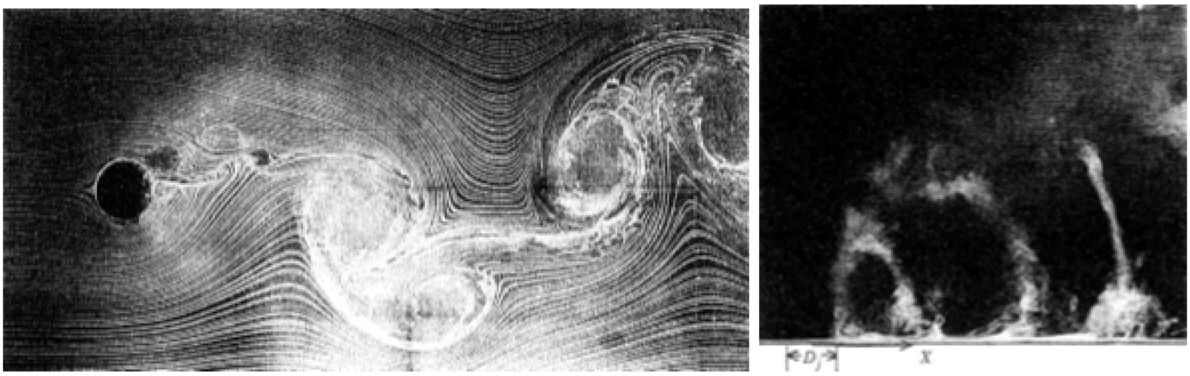

Figure 1.7: Tracking vortex shown by Fric and Roshko [?] $r = 4$. Left: Front view ($Re_\infty = 11400$). Right: lateral view ($Re_\infty = 3800$)

around the jet before it starts to wind itself in a vertical movement. Therefore, the vorticity of this boundary layer will be the origin of these tracking vortices structures. Kelso et al. [?] have found a shape dependency of these vortices on Re_j (Reynolds number calculated with the jet quantities) and r into the range $2 \leq r \leq 4$. Fric and Roshko [?] also found the characteristic Strouhal number of these structures to be one order of magnitude below those generated around a cylindrical body (for $Re_\infty = 11400$). In the case of a protruding pipe crossing into the main flow, Moussa et al. [?] observed that the Strouhal number does not show significant differences between the cylindrical body case ($St \simeq 0.2$). McMahon et al. (1971) [?] detected tracking vortex structures using hot-wire anemometers, obtaining a $St = 0.1$.

Hower, McMahon point out that the choice of a suitable lenght scale in the definition of this dimensionless number (e.g. the characteristic lenght of the jet core) would represents better the real deflection and lead to values close to those observed for a solid cylinder. In conclusion it is worth to mention the work by Eiff et al. (1995) [?] who studied the periodic behaviour of these structures as well.

- ***CVP***
  The Counter-rotative vortex pair develop their structure in the far field, where the jet trajectory starts to be aligned with the main channel flow direction. As already outlined, CVP are originated by the interaction between the main and the jet streams boundary layers (Moussa et al. [?], Fric and Roshko [?] or Andreopoulos and Rodi (1984) [?]). Lim et al. (2001) [?] proposed a CVP formation mechanism, starting from in-water visualizations at low Reynolds numbers ($Re = 1600$ and $r = 4.6$) represented in Fig. **??**.

  The jet boundaries are made rotating by the main stream action, in a way that can be compared with the wake flow behind a solid obstacle. According to some authors, the vortices belonging to the mixing layer are stretched and reoriented to form an "arm" shape. At the level of the jet penetration lenght, the formed structures, both coming from the inner and outer regions of the jet column, will gather to form the CVP structure.
  A similar mechanism is described by Kelso et al. [?] for an air jet operating at $r = 2.2$. Fig. **??** is used by the authors to explain some of their observations concerning the mean reorientation of the mixing layer vorticity, responsible of the CVP structure formation.

  The CVP origins were also confirmed by numerical studies by Cortelezzi and Karagozian [?] who calculated a 3D velocity field without using preventive informations on the vorticity field. The phenomenological study made by Muppidi [?], based on a 2D model also ex-

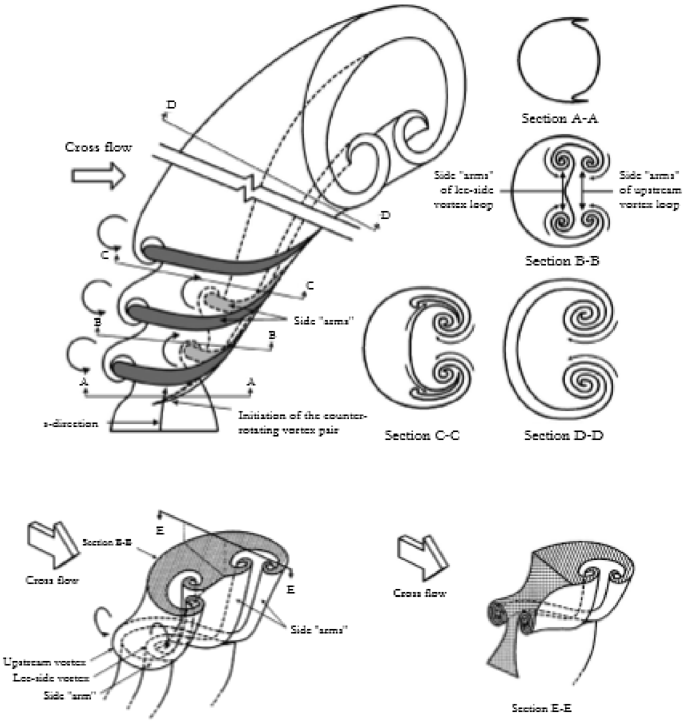

Figure 1.8: Formation mechanism of CVP. Lim et al. [?]

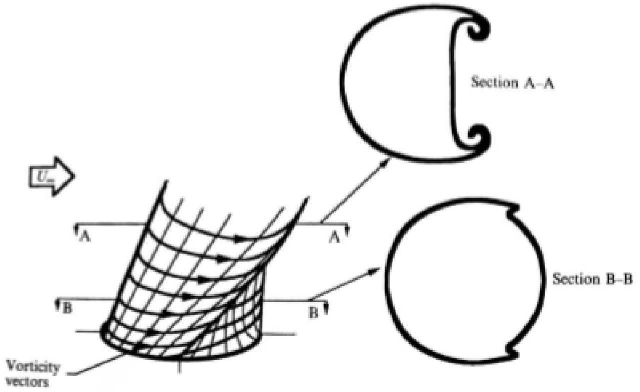

Figure 1.9: Reorientation of vorticity lines into the CVP formation mechanism. Kelso et al. [?]

plained the winding process and the jet deformation using acceleration and pressure fields.

Moreover, Smith and Mungal [?] observed that the CVP formation is retarded the more the speed ratio r is increased. These vortices are afterwards seen as a mechanism which can be linked with the mixing properties of JICF compared to free jets.

The global rotation of these structures are caused by pressure effects and are observed by all the authors in the far field, and some of them recognized that initial conditions can affect the structure of the far field, as well as the orifice shape. Fraticelli et al. (2004) [?

] remarked this aspect using a square jet section and taking velocity measurements with PIV in water.

In summary, through there is agreement among the authors about the exisentece of these four turbulent structures, their origin, development and dynamic roles, nowadays this subject represents still open questions to be better analysed.

1.3.3 Some complementary bibliographic aspects on JICF numerical simulations

In the previous sections the global and transient JICF characteristics have been examined basing on experimental observations. In this section, details on numerical approaches are instead provided. Most of publications related to these aspects are quite recent. Yuan et al. (1999) [**?**] conducted a LES analysis for cases at $r = 2$ and 3.3 ($Re = 1050$ and 2100), based on the jet diameter and the main stream bulk velocity. Some of the profiles obtained concern mean velocity and kinetic energy fields, togheter with 3D streamlines and vorticity lines for each jet structures, mostly in the near field. Ma et al. (2007) [**?**] performed LES analyses of a temperature marked jet. In their case, the jet free surface was almost perpendicular to the main stream axis ($\delta_j = 85°$), and the speed ratio was $r = 11.5$. The results provided by these studies were velocity field, trajectories that would be comparable to those obtained by a $k - \varepsilon$ analysis, made during the same work. With such high speed ratio the interaction with the frontal wall of the main channel also play a role on the full development of the jet, but no reference is given by the authors about this aspect.

A complete LES study was performed as part of the Ph.D. thesis by Prièrè (2005) [**?**]. The author simulated configurations with speed ratios suggested by Andreopoulos and Rodi [**?**] and Smith and Mungal [**?**] works The velocity profiles, vorticity cartography and the injected mass fraction decay obtained via experiments are compared with the results given by numerical simulations. The author performed several simulations using no-slip conditions on the wall, and some others using a wall law. In the first cases the results are quite distant from the experimental data (especially in the case of Andreopoulos and Rodi [**?**]), while the agreement between the data is satisfactory whereas a law of the wall is used.These observations lead Prièrè to draw attention to the importance of boundary conditions to use and their impact on the simulation results . When the jet is produced by a long pipe, using a laws of the wall is recommended. The exit profiles of the jet speed has strong influence on the jet behavior and penetration lenght. Particular attention must be paid to the mesh and to the model used for the representation of the physical reality at this point.

Finally, a comprehensive study by direct numerical simulation (DNS) of passive scalar transport in JICF was recently conducted by Muppidi and Mahesh (2008) [**?**], and a detailed description of this study is reported in the Muppidi Ph.D. thesis (2006) [**?**] The aspects studied are many, both on the kinematic field and the scalar field. Different parameters such as the profile of the jet exit speed are considered to evaluate its penetration and mixing capability. Good agreement is found between simulations and experimental data of Su and Mungal [**?**]. This study notably contains interesting information about the effect of scalar gradients and its transport or the pressure gradients and the acceleration of the jet on its deformation and the driving effects on the fluid from the main flow.

1.4 Thermal fatigue in nuclear reactors

Thermal fatigue is defined as a progressive damage of a component material exposed to thermal stress cycles. The presence of alternate phases of cooling and heating under conditions of partial or complete thermal expansions hindrance, can lead to the wreckage of the addressed part. When temperatures reach values in the order of a quarter of the material melting temperature, the material strenght is considerably lowered and its dependence on frequencies and amplitudes of the above-mentioned cycles, plays an important role for the components integrity.
The material strenght drop with temperature is explained with an increase of structural dislocations in the crystal lattice directly caused by thermal agitation of particles; the outcome of this process is a transition from the transcrystalline to the intracrystalline propagation of cracks (Fig. **??**).

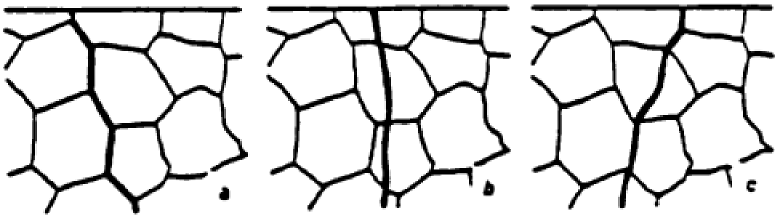

Figure 1.10: Scheme of different cracks propagations within the crystalline lattice: *a) Transcrystalline regime ; b) Intracrystalline regime ; c) Mixed behaviour.* Merola and Biggio (1988) [**?**]

An interesting parameter, given from a general solution of the unsteady Fourier equation with time-dependent boundary conditions, is the penetration lenght δ of a thermal wave in a solid medium, which can be expressed as:

$$\delta \propto \sqrt{\frac{\lambda}{\rho \omega c_p}} \tag{1.7}$$

This formula suggests how the frequency ω of the thermal fluctuations on the boundaries affects the temperature field inside a medium with thermal conductivity λ and specific heat at constant pressure c_p, in addition it gives the lenght scale where thermal fatigue plays a predominant role on nucleation of cracks. Once this phenomena occurs, while the low frequencies fluctuations continue, the exposure of materials to a potentially chemically aggressive environment is prolonged in time and extended in space. According to analytical results, experimental data show a decrease the life time of materials within lower frequency cycles (Fig. **??**).

This malicious damage has recalled an increasing attention in the nuclear field after several integrity components failures occurred due to unexpected propagations of cracks caused by thermal cycles. Thermal striping and fatigue problems where initially studied in the Liquid-Metal Fast Breeder Reactors (LMFBR) context, where the high thermal conductivity of the liquid-metal put in evidence such phenomena. The issue has been observed as well in Light Water Reactors (LWR) in tee junctions belonging to the Residual Heat Removal System (RHRS), both in Pressurized Water Reactors (PWR) and Boiling Water Reactors (BWR). A better understanding of the mechanism of thermal fatigue can lead to an improvement of the design process of several nuclear plant components exposed to such thermal fluctuations and allows to make suitable prediction upon the life expectancy in those components which are already operative. Some of the most significative cases in which thermal fatigue plays an important role:

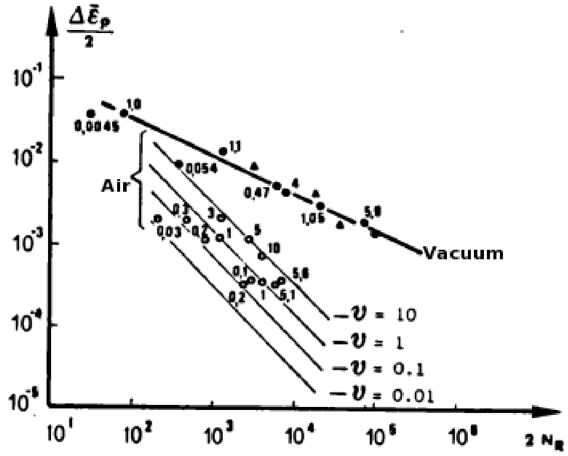

Figure 1.11: Manson and Coffin curves (relationship between plastic deformation and break cycles) for AISI A-286 stainless steel; ν indicates number or cycle per minute in ordinates the plastic deformation

1. Safety injection Line: leaking valves may introduce cold water in the safety injection branch line, which, under operating conditions, contains hot primary water. A lack of mixing leads to thermal stratification and then induces high local thermal stresses. These stresses, in turn, may initiate cracking if other aggravating features are present (geometrical singularities or residual stresses i.e.). This problem occurred in Farley (USA), Tihange (Belgium) and Dampierre (France) with cracks going through the wall and inducing a primary leak.

2. Steam Generator Feedwater Nozzle: when operating with a low flowrate of cold feed water, hot fluid may return from the steam generator in the pipe. As in the previous case, stratification induces thermal stresses which may be concentrated in geometrical singularities around the pipe-to-nozzle weld. Crack initiates and may, in worst cases, propagate through the wall. Such a degradation was found in many units in US NPP. In France, only shallow defects were found when examining replaced steam generators (less than 1 mm in depth).

3. Surge Line Nozzle and Pipe: It is the basis of a PWR unit design to have pressurized temperature and to have more or less important water flowrate between pressurizer and main piping, depending on operating conditions. Important temperature differences have been detected between these close points. Structural mechanics analysis and integrity assessment showed the presence of risks of fatigue damage before the plant end-of-life.

4. Balance-of-plant: in very few cases thermal fatigue has been experienced on the balance-of-plant. One of these cases deals with venting pipes inside reheaters on some 1.3 GW plants in which several tubes had to be replaced, also other cracking phenomena were found in turbine bypass components directly connected to the condenser.

5. Upper core structure and plenum region above the core: these areas are considered critical due to the mixing phenomena between hot and cold streams at the exit of the fuel and control rod channels.

6. Secondary circuits: In LMFBR, during normal operation, sodium at low temperature flows into the main pipe of the secondary circuit. A small pipe, connected to the main one, discharges sodium at higher temperature. Initial cracks were found in Phenix on a tee junction.

7. Residual Heat Removal Systems: often these systems are designed to provide their service in short time, due to the needs required in nuclear reactor safety. In order to give a fast response to the system, the use of mixing flows achieves this objective, though on the other hand, it exposes the interested parts to thermal stress cycles. One of the well known cases of this issues has been experienced in Civaux 1.

The impact of thermal fatigue on safety is argued to be strong since it may induce through-wall cracking on safety-related equipments. However experience shows that in most cases, operating conditions and material behaviour are detectable in a way that, when a leakage occurs, it is possible to maintain adequate functions of the plant and keep the accident under control. In France, only safety injection line issues led to an INES severity scale level 2 incident.
Thermal fatigue can involve the availability of the plants: under operating conditions, a relevant leakage implies a shut-down of the plant and a forced outage. In the safety injection line issues, pipe replacements in the last few years induced 80 days of outage extension.
Furthermore in the nuclear island, all activities on primary loop or branch lines are very costly with respect to radiation exposure. Doses associated with in-service inspection are almost 300mSv/year for 900 MW units: a pipe replacement represents about 40 mSv and the inspection of one surge line represents between 2 and 15 mSv depending on the unit. The availability of skilled personnel still below the allowable dose limits can be a real problem.
Finally costs must be considered. To give an idea of expenses related to thermal fatigue, some figures, declared by EDF, may be given:

- For the safety injection line issue, in-service inspection costs are almost 0.63 M€/year for an overall production of 34.9 GW. The costs of pipe replacement are more than 0.15 M€ and the additional costs related to the studies and investigations performed to understand the phenomena represent more than 8.6 M€ (80 % of those are spent for instrumentation);
- inspection of the surge line costs about 0.23 M€/unit every 3 years. Repair is estimated to cost between 4 and 8 M€.;
- for the feedwater issue, in-service inspection costs about 1 M€ every year.;
- in cases of balance-of-plant, the total cost experienced was about 0.8 M€;

It is not difficult to see how safety, radiation-exposure and cost-effectiveness issues make thermal fatigue a serious and challenging subject for plant owners.
Besides these preliminary explanations, this document proposes a closer view to tee junctions pipes where two fluid at different temperatures are mixed together creating potential conditions under which cracking by thermal fatigue may occur due to temperature fluctuations and stratification. Several issues related to this kind of geometry singularities have been reported through years; in the following sections some of the already known cases are summarised.

1.4.1 Nuclear reactor accidents

To highlight the differences in the nature of thermal loads and their consequences on the integrity of power-plants components as well the related duty assigned by the designer, some examples of accidents occurred in the past decades are here reported.

1. In December 1971 a small leakage has been detected in the area of the control rod penetration in the first pilot BWR built in Germany. In the next two days, the leakage increased and the reactor was shut down to cold depressurized conditions. The investigations shown a through wall crack penetrated the outside diameter on a circumferential weld of the control rod penetration, covering 35% of the circumference for a depth of 3%. Non penetrating cracks where found in similar locations in other control rod penetrations.

The fracture was identified as transgranular stress corrosion. Thermal cycles may have played a role in this accident.

2. In 1984, during the system pressure test, a leakage occurred at a nozzle of the pressurizer of a VVER 440/230 unit located in Greifswald. A developed crack has reached the outer circumference of the base metal, nearby a welded region. Probably a sharp edge was introduced from mechanical drilling during the weld preparation.

3. In 1987, 1988 and 1992, water leakages occurred on non-isolable safety injection lines of the primary circuit on Westinghouse 900 MWe NPP of Farley 2, Tihange 1 and Dampierre 2. In these NPP, the high pressure and low temperature volumetric control circuit can leak into the safety injection system connected to the primary circuit. This leakage creates a mixing area where the non-isolable part of the lines meets the turbulent flows coming from the main primary circuit, hence it generates a source of high thermal loads, leading to cracks. In 1996 at Dampierre 1 cracks were found on the straight part of the pipe, as well as three other plants. After the pipe replacement, the problem occurred again in 1997: during 8 months another extended fissure (up to one third of the pipe thickness) appeared.

4. On June 6, 1988, fatigue failure occurred on the Genkai (Japan) 559 MW PWR Unit 1 . An inspection revealed a leakage through-wall crack in the weld of the horizontal pipe upstream of the residual heat removal system inlet isolation valve.

These reported cases are just few compared to the totality of the thermal fatigue accidents occurred in the nuclear field. To better understand the typical operating conditions that generate such kind of impairments in the further section, an in-sight upon the Civaux and Phenix accidents will be given.

1.4.1.1 Phenix

An inspection campaign executed in May 1993 brought to light several defects in different areas of the 250 MWe LMFBR demonstration plant, located in the Marcoule site, Phenix. In the sodium discharge area, the fluid comes from the hot leg of the loop (550 °C) and flows into the expansion tanks (Fig. **??** operating at cold temperature (350 °C). The deepest fissure were localised on the tank welds (AISI-304), passing through its overall thickness. Other more superficial cracks were detected on the base material. Further investigations showed the damaged zone to be situated in a recirculation zone of the tank, where there was a detour of the hot fluid near the tank wall. Since the adjacent zones were at cold temperature, this phenomena induced a hot spot on the wall surface, creating a steep thermal gradient (170 °C) and the consequent fissure.

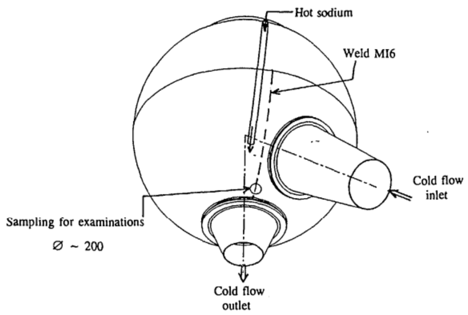

Figure 1.12: Expansion Tank of the Phenix LMFR

Moreover, through cracks (transgranular) of about 100 mm lenght have been detected on the secondary circuit, in a circumferential weld located 160 mm downstream the small branch axis of a mixing tee (Fig. **??**). In this configuration, the hot sodium coming from the branch pipe has a mass-flow rate was 7 $kg \cdot s^{-1}$ at temperatures of 430 °C, while the cold sodium flows with a mass flow rate of 800 $kg \cdot s^{-1}$ at temperature of 340 °C.

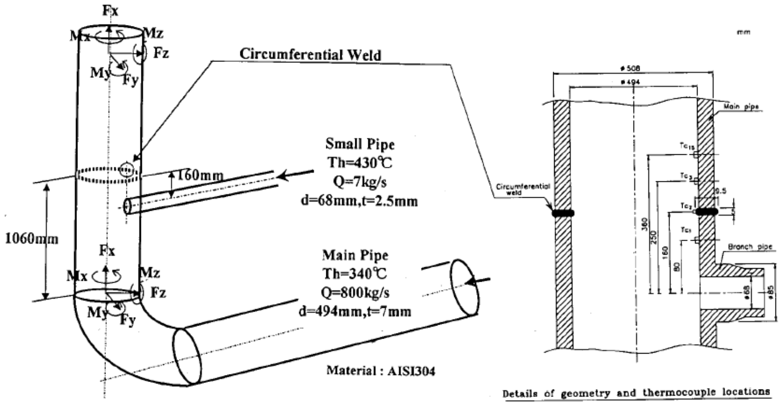

Figure 1.13: Geometrical characteristics of the Phenix secondary piping system

Hot and cold fluids had respectively mean bulk velocities of 4.77 and 2.26 $m \cdot s^{-1}$. The Reynolds number ranged from $5 \cdot 10^5$ to $6.4 \cdot 10^6$, while the Richardson number in these conditions it is in the range of $4.9 \cdot 10^{-3}$ so that advection dominates buoyancy effects. In order to evaluate the characteristic lenghts of the turbulence in the region of interest it is useful to evaluate the shear velocity w_τ exploiting the identity given by the correlation between total shearing stress (given by the laminar and turbulent contributions) and friction losses as stated by Chapuliot et al. (2005) [**?**].

$$\rho w_\tau^2 = \frac{1}{8} \Lambda \rho w^2; \qquad \Lambda = 0.316 Re^{-\frac{1}{4}} \tag{1.8}$$

where the dimensionless coefficient of resistance Λ is given by the empirical correlation by Blasius (1913) [**?**], applicable to fully turbulent flows in smooth pipes with circular cross-section. Once the relation between the bulk velocity and the shear stress is given, it is possible to find the time scale known as *turnover time* which represents the longest life time of a turbulent structure.

$$t_\tau = \frac{L}{w_\tau} \tag{1.9}$$

where L represent the characteristic size of the turbulent structure considered. In the thermal fatigue context, particular attention has to be paid to lower frequencies phenomena, which are often associated to larger lenght scales due to inertial effects, this justifies the choice to focus on the largest turbulent structures and then use the pipe diameter as characteric size for the evaluation of t_τ.

Even though this time scale can give preliminary information on the the frequencies associated to the presence of swirling structures, inertial phenomena plays also a role on thermal cycles and cannot be underestimated, therefore, it is mandatory to take them into account in order to evaluate which one of these effects is predominant.

One can argue the characteristic time scale associated to inertial phenomena, t_L given, in analogy to t_τ, by:

$$t_L = \frac{L}{w} \tag{1.10}$$

where w is the bulk velocity of the stream. It is quite easy to see that this time scale just represents the time needed to the flow to cover a distance L. If we speculate on a vortex structure to behave as a rigid body, then is quite evident that the time t_L, known as *transit time*, represents as well the time needed for the frozen vortex structure to cover the distance L.

By making a comparison between these two time scales it is possible to evaluate which phenomena is the main responsible source of thermal fluctuations at certain frequencies, between the generation-dissipation of swirling structures and the advective effects.

The order of magnitude for both the time scales given by the flow conditions are respectively $t_\mathcal{T} = 3.66\ s$ and $t_L = 10^{-1}\ s$. Given the fact that advection dominates diffusion, scalar fluctuations are mostly driven by the first phenomena which is stricly bounded to the vortices characteristic life times. If we imagine to measure the temperature at a certain point of the domain, it is possible to argue that our fluctuations can be caused by two advection mechanism. If the center of hot vortices do not moves along the pipe, they just rotate and dissipate their thermal energy, decreasing their diameter over and over until they disappear. In this case, the temperature fluctuation frequency is stricly linked with the turnover time scale. On the other hand, if vortices conserve their thermal energy, and just moves along the pipe lenght, we experience a temperature variation which lasts the time that the vortex takes to pass through our measurement region. Considering the starting assumption, in which we said that scalar fluctuations are caused by vortices, the minimum and maximum frequencies are given by these two behaviours. It must be underlined that, in the real cases, vortices both spin and moves through the domain, producing fluctuations which have frequencies that lies into these extreme cases. In the Phenix scenario the turbulent structures conserve their shape for a time which is longer than the one needed to cross their overall lenght. Therefore the higher fluctuation frequencies corresponds to the inverse of the transit time (9.75 Hz) while the inverse of the turnover time (0.27 Hz) gives us the lower fluctuation frequency.

1.4.1.2 Civeaux

In May 1998, a leak of 8.3 $kg \cdot s^{-1}$ occurred inside the RHRS of the PWR Civaux 1 plant (1.45 GWe). Inspections showed the presence of a through wall crack upon the outer surface of a pipe elbow, for a total lenght of 180 mm. The bend was located nearby a mixing zone area, metallurgical expertises higlighted thermal fatigue as the origin of this degradation, driven by temperature fluctuations on the mixing tee. The transition from cracks initiation to fully developed fissure of significant depth happened in a relatively short time (1500 h). The section of interest is shown in Fig **??** it starts from the Valve 101 VP on the hot leg and the cold leg Valve 071 VP and terminates with to the downstream zone of the tee. The system pressure is 36 bar, with a total mass flow rate of 152.8 $kg \cdot s^{-1}$, 122.2 of them are introduced from the hot leg at a temperature of 180 C, the remaining is given by the cold leg at a temperature of 20 C.

Metallurgical examinations revealed also the presence of cracks network in the proximity of welds where no fabrication defects were present. On the right part of Fig **??** is possible to see the mainly damaged locations:

(a) outside the bend downstream of the mixing tee ;

(b) on the mixing tee ;

(c) at the bottoms of weld beadds and the circumferential weld roots ;

(d) in the straight sections of piping ;

Hot and cold fluids had respectively mean bulk velocities of 2.97 and 0.59 $m \cdot s^{-1}$. The Reynolds number ranged from $1.5 \cdot 10^5$ to $3.9 \cdot 10^6$, hence the flows were turbulent and the Richardson number on these conditions it is in the scale of $2.6 \cdot 10^{-2}$ so that advection dominates

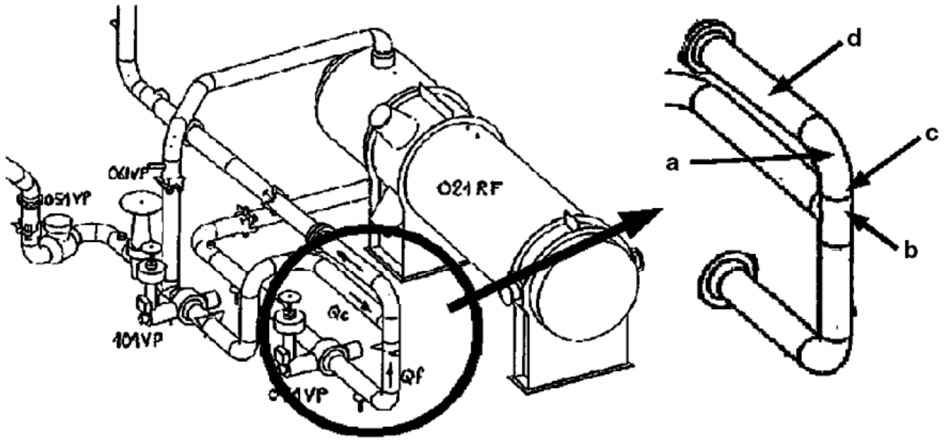

Figure 1.14: View of the Civaux RHRS

buoyancy effects. In this configuration the *transit time* t_L and the *turnover time* t_T evaluated are respectively 0.68 and $1.8 \cdot 10^{-2}$ s, therefore the main temperature fluctuations lies in the range between 1.49 and 53.89 Hz.

1.4.2 Experiments related to thermal fatigue

1.4.2.1 Common parameters adopted

The problem of thermal fatigue is rather complex since it involves different scientific disciplines:

1. Solid Mechanics, which gives an analisys of mechanical loads under operative conditions and the response that could be given from the system.

2. Science of material, which analyzes the related physical materials properties that plays an important role on the overall behaviour of the components.

3. Heat transfer, needed to a deep understanding of the thermal field affecting the system, since temperature and heatflow directly represent the source of the stresses induced in materials, hence needed informations for the solid mechanics analisys.

4. Fluid mechanics, involved through the request of the above disciplines to examine the original mechanics which are responsible of thermal fluctuations. In turbulent flows, vortices transport the temperature scalar, therefore the advection contributes play a significant role in this sense. The analisys of the flow field supplies precious information for the heat transfer problems.

Owing to this multidisciplinary context, pure analytical models that include all the interactions between the above mentioned phenomena shows their limits, hence experimental programs to obtain basic data are needed. Focusing on the turbulent mixing of jets, the main parameters of interests are often reported in dimensionless form. Since the main phenomena are driven by temperature and velocity gradients, the absolute values are not intimately representive, thus, all the information can be condensed in non-dimensional form in order to easily evaluate when the mixing phenomena are pronounced and, moreover, they allow potential comparisons between different operating conditions.

Hereafter are listed the definitions of the common parameters observed to characterize thermal loads and their relationship with the velocity field:

- Time Average, root mean square and Fourier transform of the general non-dimensional scalar ϕ:

$$\overline{\phi} = \frac{1}{\Delta t}\int_{t}^{t+\Delta t} \phi(t)dt \tag{1.11}$$

$$\sigma_{\phi} = \sqrt{\frac{1}{\Delta t}\int_{t}^{t+\Delta t} (\phi(t) - \overline{\phi})^2 dt}; \tag{1.12}$$

$$\tilde{\phi}(\omega) = \int_{-\infty}^{\infty} \phi(t)e^{-2\pi i t\omega}dt; \tag{1.13}$$

- The dimensionless temperature

$$T^* = \frac{T - T_{cold}}{T_{hot} - T_{cold}} \tag{1.14}$$

- The dimensionless amplitude of the fluid temperature fluctuations.

$$\sigma_T^* = \frac{\sigma_T}{T_{hot} - T_{cold}}; \tag{1.15}$$

- The dimensionless velocity i-component:

$$u_i^* = \frac{u_i}{U_{bulk}} \tag{1.16}$$

- The dimensionless amplitude of the velocity i-component fluctuations:

$$\sigma_{u_i}^* = \frac{\sigma_{u_i}}{U_{bulk}} \tag{1.17}$$

All of these quantities are already well known and often used in the turbulence context.

1.4.2.2 Reactor scale experiments: FATHER

Experimental studies close to the scale of the industrial mixing configurations have carried out in CEA CADARACHE in order to realistically reproduce the circumstances under which thermal fatigue occurs. A large experimental facility named FATHER (Fig. ??) has been built (2001) with the main objective to investigate how the temperature fluctuations are generated, where their maximum values are located and to visualize the critical thermo-hydraulic parameters in thermal loads. Moreover, the experiments were aimed to reproduce the structural crack and stripping damages, due to complete further investigations on the crack propagation behaviour. An 8 MW oil fired boiler serves the facility as thermal source to the hot leg water flow connected to the cold leg with a tee junction, where thermocouples are placed along the whole test section.

The overall equipment allows the whole system to operate in steady conditions for several hundred hours, with maximum temperatures above 160 °C and flow velocities of 4 $m \cdot s^{-1}$. Even if the general purpose is to get closer to industrial conditions, the facility has been scaled (0.6) comparing to the Civaux Plant 1 keeping in range the dimensionless numbers regarding the turbulence and the heat transfer ($Re = 3.8 \cdot 10^6$ and $Nu = 4.02 \cdot 10^3$ in FATHER, $Re = 3.9 \cdot 10^6$ and $Nu = 7.25 \cdot 10^3$ in Civaux). Thereby the convective heat transfers coefficient between fluid and solid walls obtained is approximately $1.6 \cdot 10^4$ $W \cdot m^{-2} \cdot K^{-1}$ which is argued to mantain the same characteristic conditions of the large industrial plants.

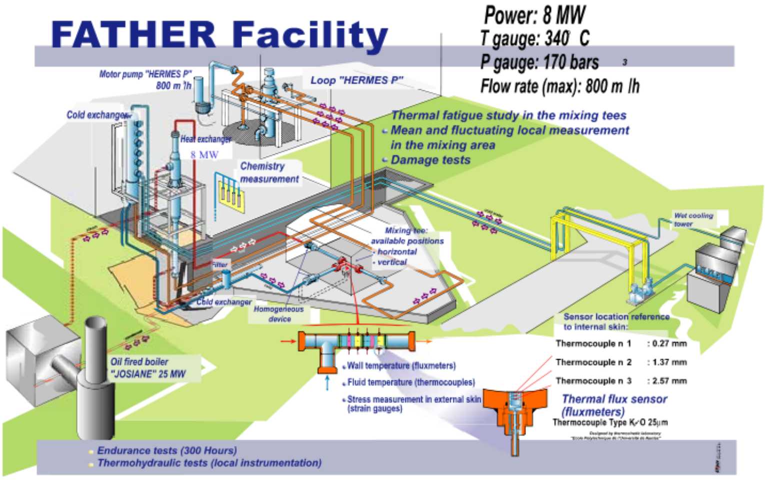

Figure 1.15: Overview of the Father Facility

1.4.2.3 Reduced scale tests: Vattenfall and TRANSAT

Experimental data have been also produced to validate Computational Fluid Dynamics (CFD) codes and further models developments. In fact, to correctly predict and avoid thermal striping problems, CFD tools shows an interesting potential and their application can lead to an in-depth understanding of complex operating conditions and geometries which are difficult and/or expensive to be reproduced for experimental investigations. Small experimental test sections have been exploited to give reference data to pursue this objective and then allow the scientific community to compare the results provided by different numerical approaches. In this work, particular attention is given to two reduced scale tests experiments:

- T-junction mixing tests carried out at the Alvkarleby Laboratory of Vattenfall Research and Development in Sweden during November 2008 (Brain Smith et al. (2009) [**?**]) . The experimental section consists of two manufactured Plexiglas tubes connected by a hollow cube to form a T-shape, the fluid transported is water. Such kind of configuration is investigated, as it is possible to notice on the previous sections, because of its large use on the industrial context.

- TRANSAT closed-loop wind tunnel of the CEA center located in Grenoble (Fougairolle (2009) [**?**]). In this case, the geometry of the experimental test section channels is rectangular, while the fluid is air. Several experiences have been performed to study the thermal-fluid-dynamics properties of jet in cross-flow, on varying the ratios between the jet and the main stream velocity (r) to give a valid reference for rectangular section ducts and a closer view to the interactions between the jet flow and the opposite wall for higher values of r. Such kind of configuration is often used whenever the penetration lenght of the jet is required to reach high values. The physical phenomena involved in the experiments are characterized by transient and 3D vortex structures, which provides a formidable challenge from a numerical point of view.

Data originated by these two experimental campaigns have been taken into account for the validation of the *TrioCFD* code, which was the main objectives of CEA.

Chapter2

Description of small scale experiments

In this section further details on the small scale experiments treated in this work are given, for both the OECD Vattenfall Tee-junction benchmark and the TRANSAT Closed-Loop wind tunnel.

2.1 The OECD Vattenfall benchmark

The model of the tee junction is composed by two manufactured Plexiglas tubes. The first pipe, horizontally positioned, has an inner diameter (D_2) of 140 mm and transports a 9 $l \cdot s^{-1}$ (Q_2) water flow at the temperature of 292 K, while the branch pipe has a diameter D_1 of 100 mm and transports a water flow (Q_1) of 6 $l \cdot s^{-1}$ at the temperature of 309 K. The junction between the tubes is realized by a hollow Plexiglass cube where the two pipes are inserted, the intersection is slighlty smoothed, with a small curve radius (not measured); the experimenters declared a value below 0.2 mm. The test rig is shown in Fig **??**.

The cold water is supplied from a reservoir with the necessary holdup to provide the required flow-rate during the experiments. An horizontal weir is used to uncouple the mass-flow rate with the water level. The mass-flow rate is measured by an electro-magnetic flow meter (the square in the left part of Fig **??**). Downstream the reservoir a stagnation chamber with a diameter of 400 mm is mounted. In order to disrupt large scale turbulent structures, three perforated plates connected by a tube bundle form the chamber. Each of these tubes has an inner diameter of 10 mm for a lenght of 150 mm. On the terminal part of the chamber

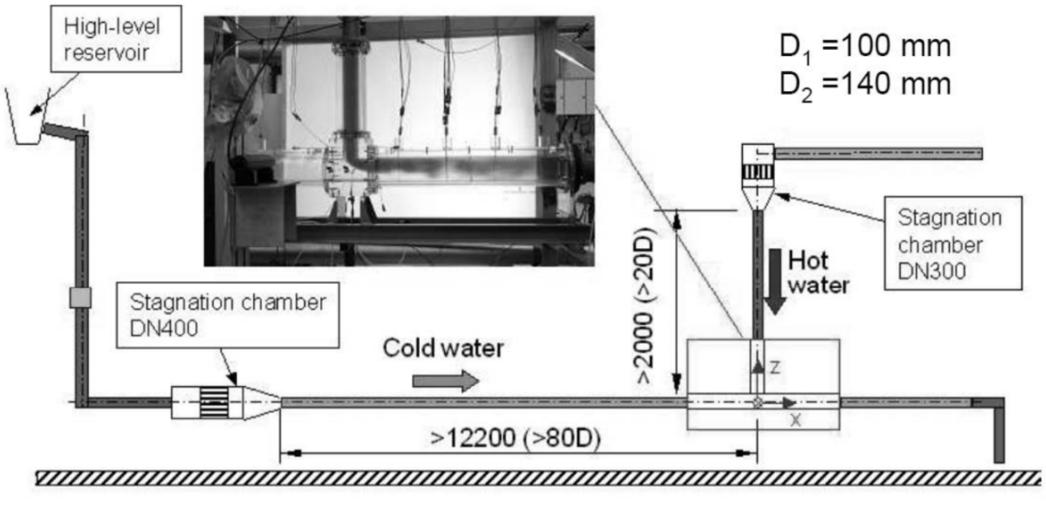

Figure 2.1: Side view of the Vattenfall test rig. Brian et al. [**?**]

a convergent channel with an area ratio of 8.2 has been placed. Following the stagnation chamber, an Acrylonitrile butadiene styrene (ABS) pipe (inner diameter D_2) of 10 m connects the reservoir to the Plexiglass test section, which extends 1260 mm upstream the junction. The overall lenght of the ABS and Plexiglass pipes ensures fully developed flow conditions at the entrance of the Junction for all the flowrates tested during the experimental campaign. On the hot branch, the water is fed by a 80 m^3 reservoir. A pump transports the hot water to the junction while it keeps a constant flowrate. As in the cold branch, a stagnation chamber with a diameter of 300 mm is placed. Downstream a convergent duct with an area ratio of 9 is placed; the hot water flows on a steel pipe (inner diameter D_1) for the next 20 hydraulic-dyameters. At the end of this section, the plexiglass tee junction connects the hot branch to the cold one. In this case, experimenters declared the flow to be not fully developed but still lacking of large scale turbulence.

2.1.1 CAD information

Since velocity measurements are available at 3 and 3.1 hydraulic diameters respectively from the main and the branch pipe, the overall computational domain has been shortened to these sections upstream the junction. Downstream the t-junction, the branch pipe is prolonged to 22 hydraulic diameters in order to observe the complete evolution of the mixed flow.
The geometrical domain has been modelled using the Geometry Tool of SALOME 7.7.1, subshapes have been created to specify the local lenght of the mesh elements. The origin of the coordinate system coincides with the intersection between the two cylinder axes, which form an angle of 90°. The axes form a right-handed set, with the x and z versors aligned with the cylinders axis (Fig. **??**).

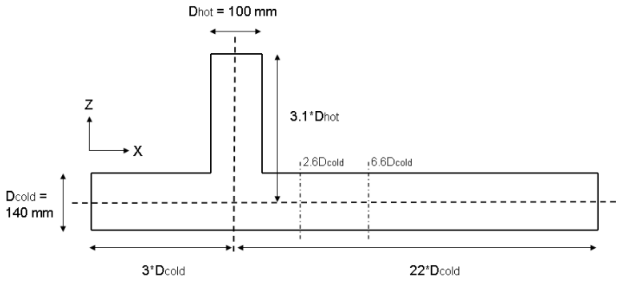

Figure 2.2: Schematization of the Vattenfall tee Junction computational domain

2.1.2 Boundary conditions of the test

The operating conditions described in subsection 3.1 are briefly summarised in table **??**.

	U_{bulk} $\left[\frac{m}{s}\right]$	D_h $[m]$	T $[K]$	ρ $\left[\frac{kg}{m^3}\right]$	μ $[Pa \cdot s]$	β $\left[\frac{1}{K}\right]$	k $\left[\frac{W}{m \cdot K}\right]$
Cold Inlet	0.58	0.14	292	998.49	$1.06 \cdot 10^{-3}$	$2.07 \cdot 10^{-4}$	0.60
Hot Inlet	0.76	0.10	309	993.73	$7.67 \cdot 10^{-4}$	$3.40 \cdot 10^{-4}$	0.62

Table 2.1: Vattenfall test operating conditions

The inlet velocities data collected during the experimental campaign shown in this section have been measured upstream the t-junction using a two-component Laser Doppler Velocimeter (LDV). This device provided the axial component of velocity in the main flow direction and the transverse one. The coordinate systems adopted in the measuring planes are described in Fig. **??**.

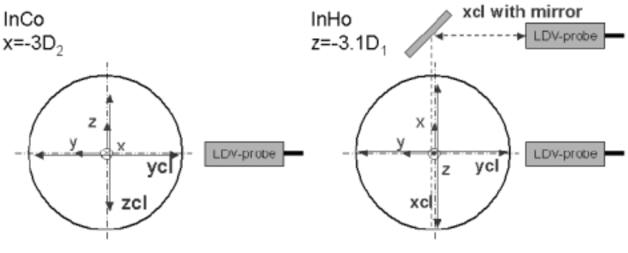

Figure 2.3: Outline of the coordinates system adopted. Brian et al. [**?**]

Velocity distributions and the corresponding turbulence statistical values measured shown in Fig. **??** and **??**

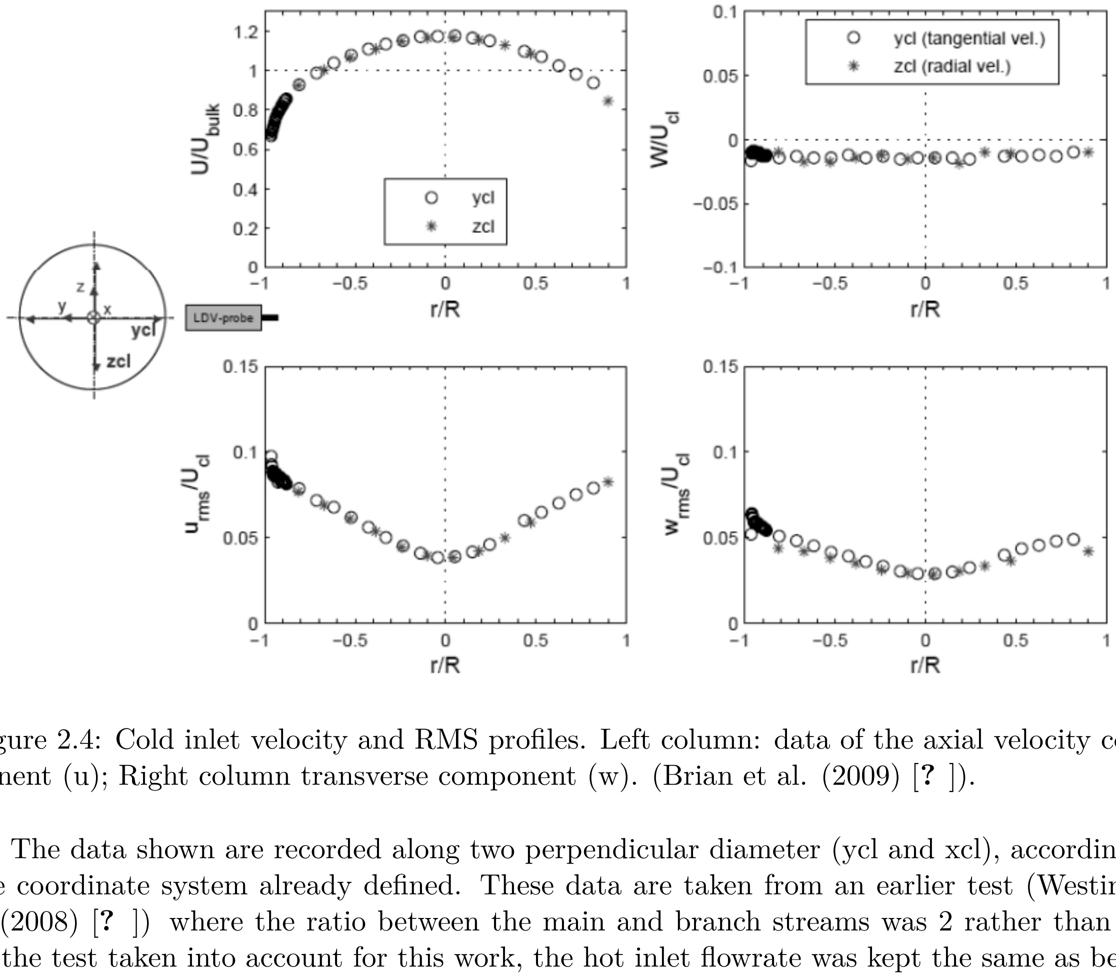

Figure 2.4: Cold inlet velocity and RMS profiles. Left column: data of the axial velocity component (u); Right column transverse component (w). (Brian et al. (2009) [**?**]).

The data shown are recorded along two perpendicular diameter (ycl and xcl), according to the coordinate system already defined. These data are taken from an earlier test (Westin et. al (2008) [**?**]) where the ratio between the main and branch streams was 2 rather than 1.5. In the test taken into account for this work, the hot inlet flowrate was kept the same as before (6.0 l/s), while the cold stream was 9 l/s instead of 12.0 l/s. Since the velocity profile in the cold inlet is fully developed, the inlet measurements here presented will be scaled in order to fit the correct flowrate. Experimenters preferred to perform measurements under isothermal conditions as well. This check has been carried out to observe if the changes in the refractive index of the water due to temperature differences would cause a distortion of the laser beams in the mixing region. Both sets of data show good correspondence. Velocity data have been

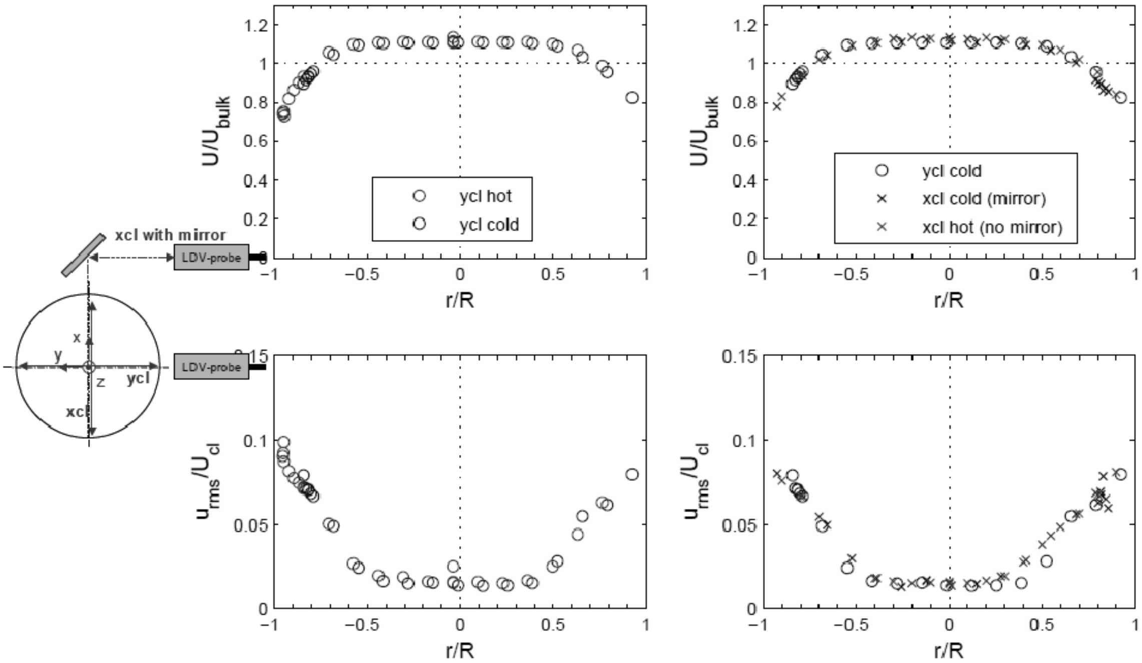

Figure 2.5: Hot inlet axial velocity and RMS profiles. Left column: *ycl* with hot and cold (isothermal case) water. Right column: *ycl* with cold water, xcl with hot and cold water. (Brian et al. (2009) [**?**]).

collected by a Laser Doppler Velocimetry (LDV) During the isothermal measurements, the receiver has not been disposed in the same direction of the emitter, therefore, the optical signal has been deflected towards first by a mirror.

The root mean square values obtained from the measurements are scaled with the centerline velocity (U_{cl}). This quantity is calculated as $U_{cl} = 1.17\ U_{bulk}$ for the cold inlet and $U_{cl} = 1.11\ U_{bulk}$ for the hot inlet. It is possible to observe that the inlet velocity data reported are reasonably symmetrical with respect to the channels axes. These information will justify further the use of axisymmetrical profiles to reproduce the velocity inlet boundaries with a good approximation. The evaluation of the characteristics time scales made with these boundary conditions presents a t_τ of 3.19 s and a t_L of 0.14 s.

2.1.3 Available measurements and accuracy

Data collected through LDV have been taken in cross sections located between 2.6 and 6.6 diameters downstream the t-junction (Fig. **??**). Additional tests have been carried out during 2008 on the same experimental rig. Particle Imaging Velocimetry (PIV) measurement were added to record velocities in sections located at 1.6, 2.6, 3.6 and 4.6 hydraulic diameters downstream the junction. This system uses tracer particles with a spherical diameters distribution ranging from 2 to 30 μm and a density of $1.2 \cdot 10^{-3} kg \cdot m^{-3}$. The uncertainty given by the LDV and PIV systems are of random and systematic nature. For the streamwise components measured with LDV, the uncertainty on the mean values were 2 and 3 %, while the statistical uncertainty in the root mean square lies between 3 and 4 % (these values are normalized with U_{bulk}). PIV measurements shows instantaneous errors to be less than 1% for both these quantities. The systematic errors derive from the positioning of the measurement systems (uncertainities of about 0.5 mm). The global uncertainty is estimated to lie in a range between 6 and 8 % for both the systems. These errors have been propagated to the root mean square measurements. An overall discrepancy of 5% has been observed between the flowrate calculated on the basis of

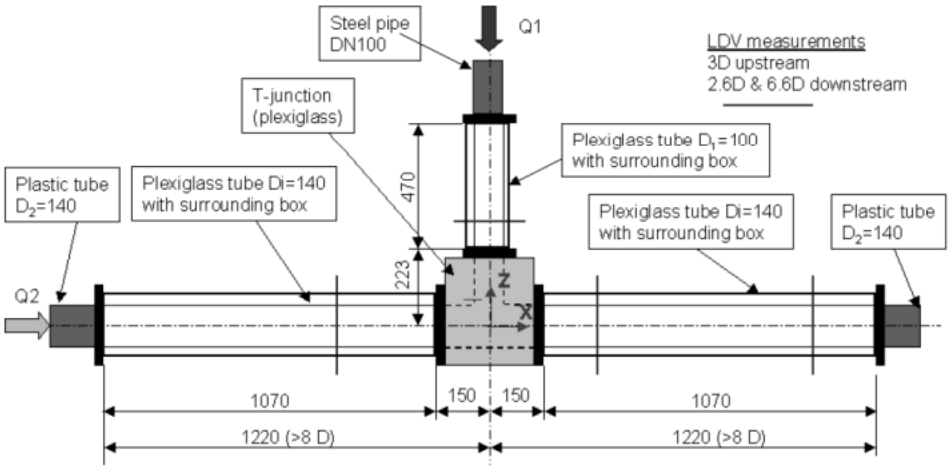

Figure 2.6: LDV measurements stations. ([**?**])

the LDV measurements and the one directly given from the flowmeters located upstream the junction. It should be underlined that refraction effects caused by the curved surfaces led to a slight distortion in measurements, with a consequent lower accuracy on measurements in the near-wall locations.

The experimenters provided also the Reynolds shear stresses using the correlation between the streamwise and the tangential velocity component (this has been made in order to confirm the hypothesis of axisymmetric flow) and the correlation between the streamwise and radial velocity component. From this information they were able to derive the friction velocity with a linear fit, which resulted to be 0.026 m/s. Using this value they were able to declare a spatial resolution given from the LDV measurement in the order of $\Delta y^+ = 30$.

Temperature histories were recorded using thermocouples positioned 1 mm far from the wall, along the downstream section of the main pipe, at seven different locations (Fig. **??**). The response time measured for each thermocouple was of 13 ms, while the uncertainty associated to these instruments is estimated to be in the scale of 0.5 °C, which gives a constant uncertainty of 3% in terms of normalised values. The statistical uncertainties in the root mean square values are in the order of 5%. Therefore the overall uncertainty is estimated to be 8%

2.1.4 Experimental results

Experimental data available in this document, have been taken from literature (Brian et al. [**?**]) by converting plot data in numerical form. The software Gnuplot has been used to report the profiles taken. The following figures use the standard notation of U, V and W for the x, y and z components of velocity. The dimensionless coordinates reported on the horizontal axis indicate the direction along which the measurements have been taken (along the diameter lines).

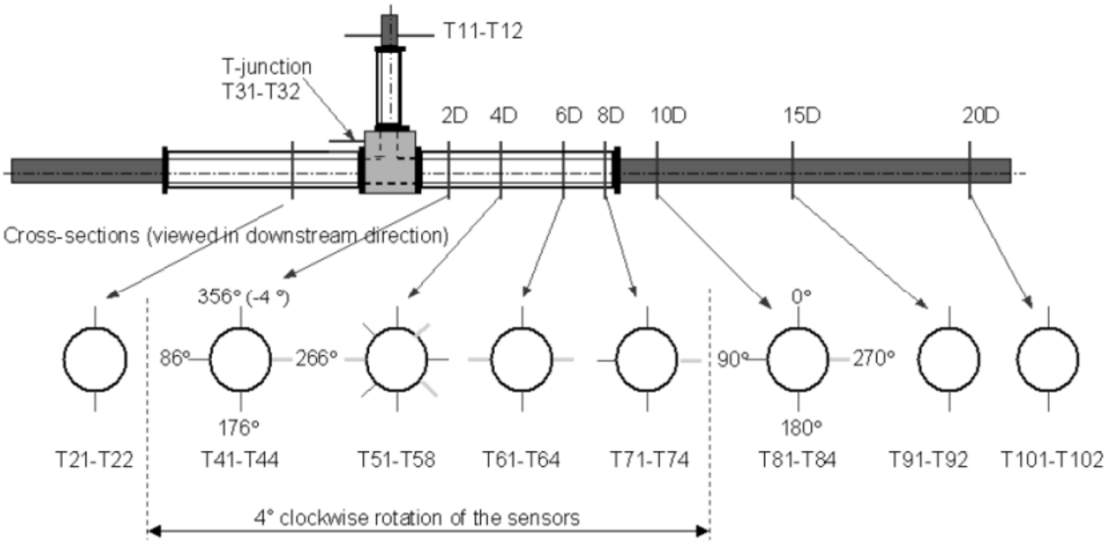

Figure 2.7: Thermocouples positions. Brian et al. [**?**]

On the section located 1.6 hydraulic diameters downstream the jet the streamwise component of the flow in the horizontal direction (Fig. ?? (a)) presents a depression in the central part. This is caused by the jet stream which slows down the the fluid in the main channel in the axial direction. In the vertical direction (Fig. ?? (b)) this behaviour is shown as well.

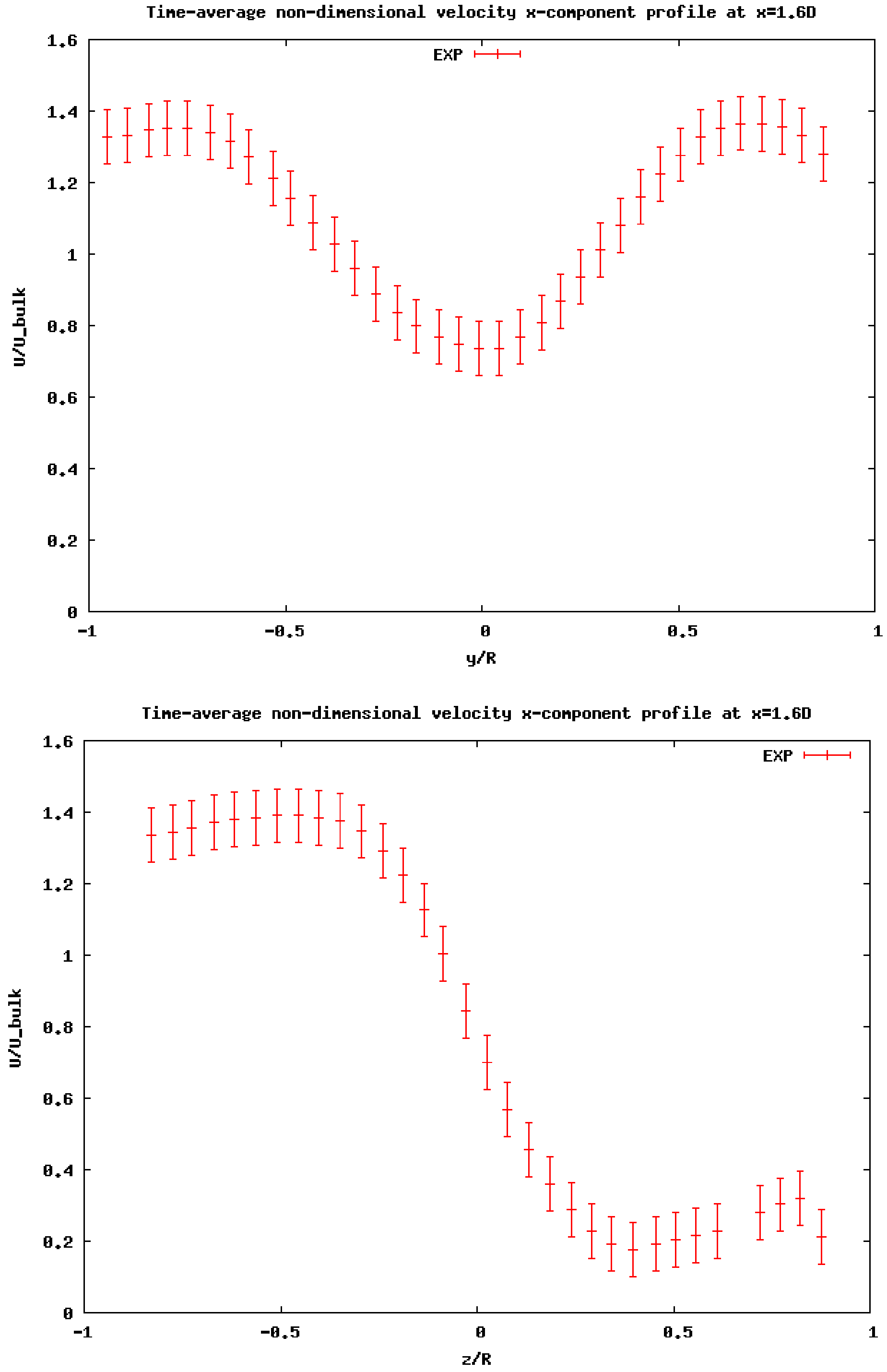

Figure 2.8: Available data on the section located 1.6 hydraulic diameters downstream the junction. Streamwise velocity component. Along the y axis (a) and z axis (b)

At 2.6 hydraulic diameters downstream the jet exit region, the velocity z-component is investigated. As the flat profile shown in Fig. **??** (a) the transversal component along the horizontal diameter is negligible compared to the bulk velocity. On the other hand Fig. **??** (b) shows the presence of some fluctuations which grow from the wall to the central part of the jet.

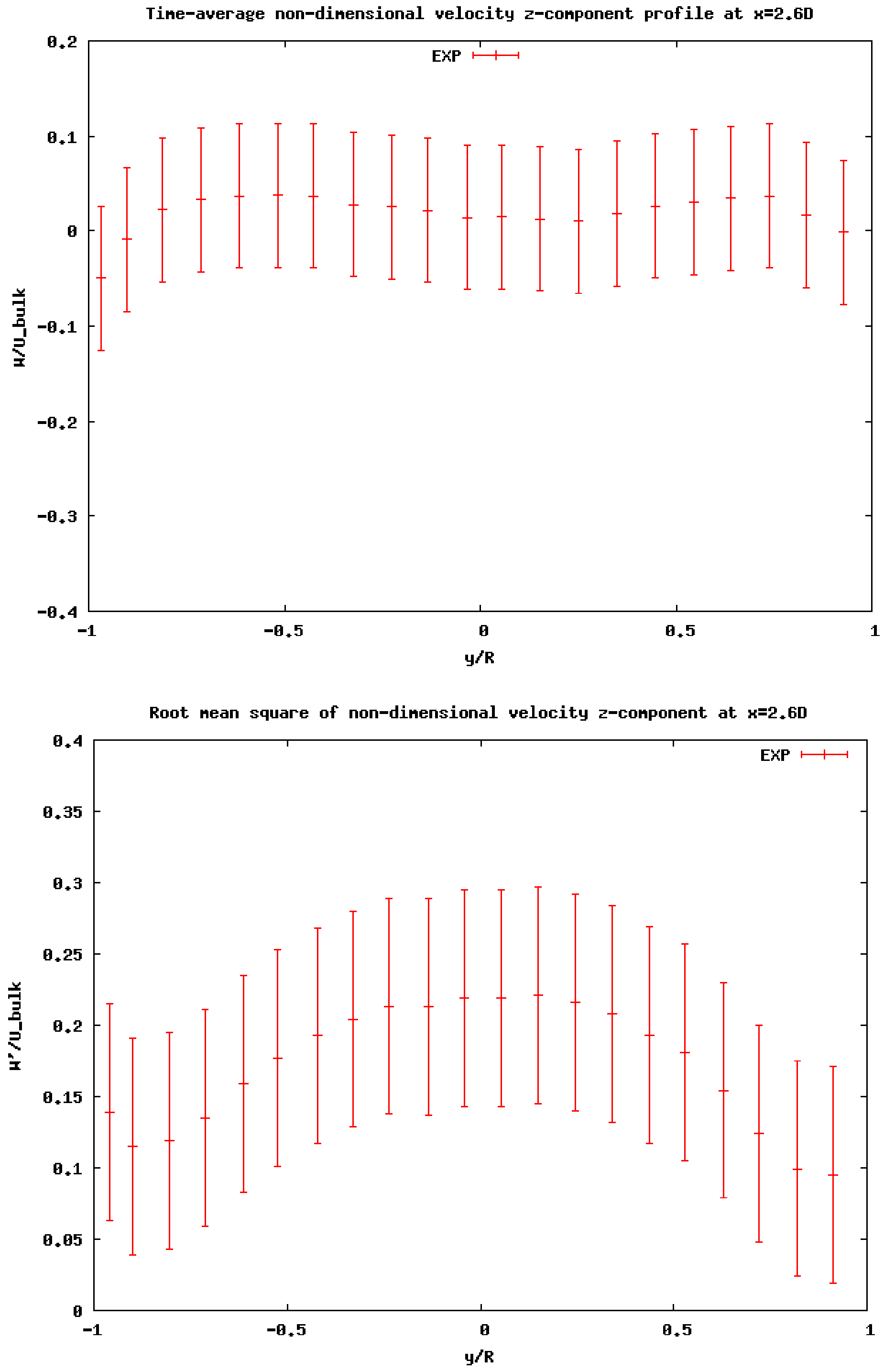

Figure 2.9: Available data on the section located 2.6 hydraulic diameters downstream the junction. Vertical velocity component along the y axis. Mean value (a) RMS (b)

At the same location, along the vertical direction (Fig. **??** (a)), the mean value of the velocity z component mantains the flat distribution, even if there is a slight asymmetry. The fluctuations reported by Fig. **??** (b) reveal an higher turbulence on the top part of the channel, which is caused by the tracking vortices structures.

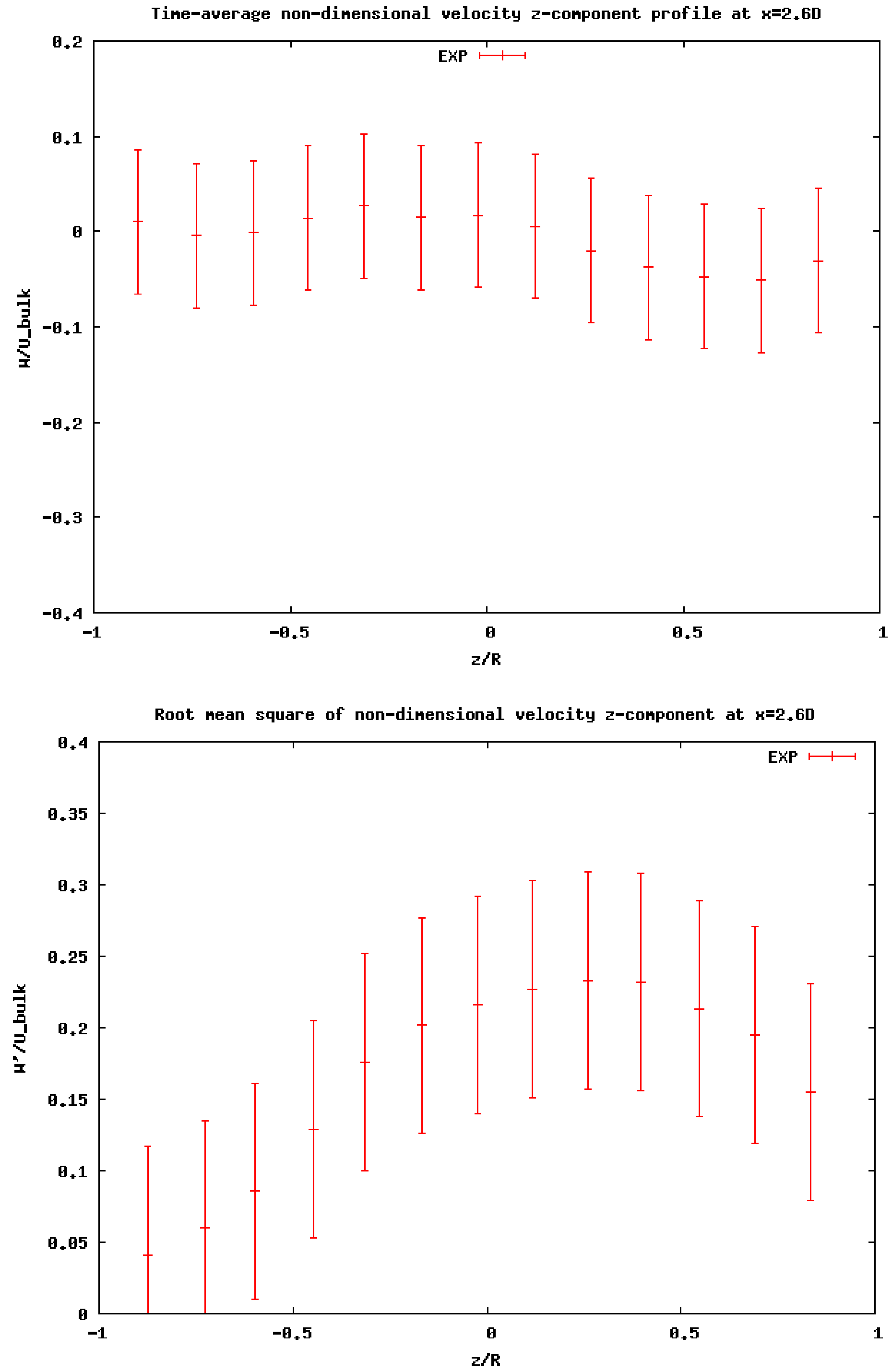

Figure 2.10: Available data on the section located 2.6 hydraulic diameters downstream the junction. Vertical velocity component along the z axis. Mean value (a) RMS (b)

Passing to the next measurement station the axial velocity component shows that at this point the flow is almost full developed. This is confirmed by the flat profile in Fig. **??** (a). Fig. **??** (b) shows that the initial depression caused by the jet impingement is nearly lost, and the flows starts to assume again an axisymmetric profile.

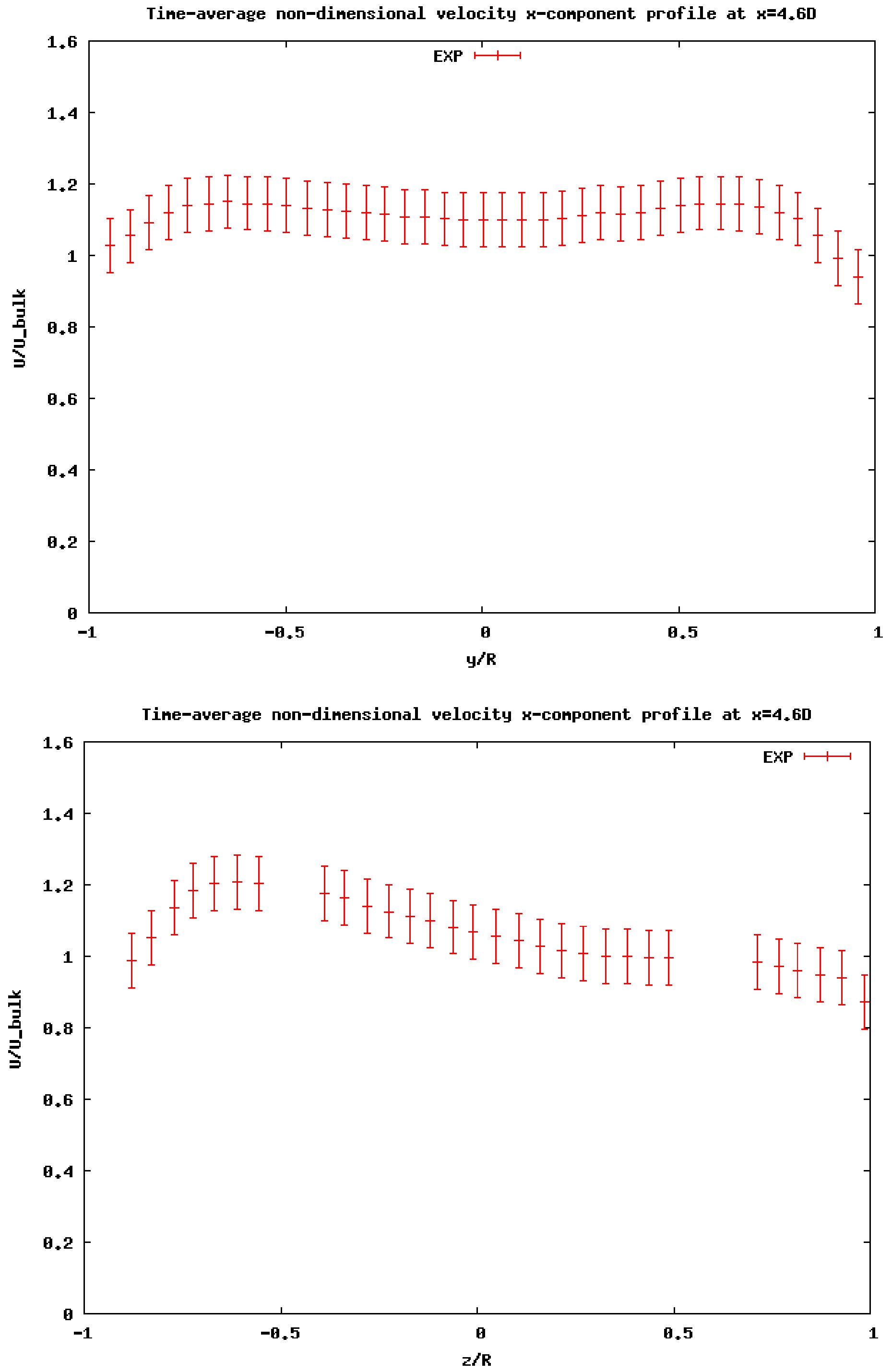

Figure 2.11: Available data on the section located 4.6 hydraulic diameters downstream the junction. Streamwise velocity component. Along y axis (a) Along z axis (b)

Temperatures measurements along the axial line located on the top part of of the main pipe (Fig. **??** (a)), shows that the temperature drops rapidly once the jet potential zone is passed and it keeps almost the same value through the whole lenght, with a slight decrease. In Fig. **??** (b) the fluctuations point out that the turbulent behaviour is characterized by structures that grow smaller along the fluid path.

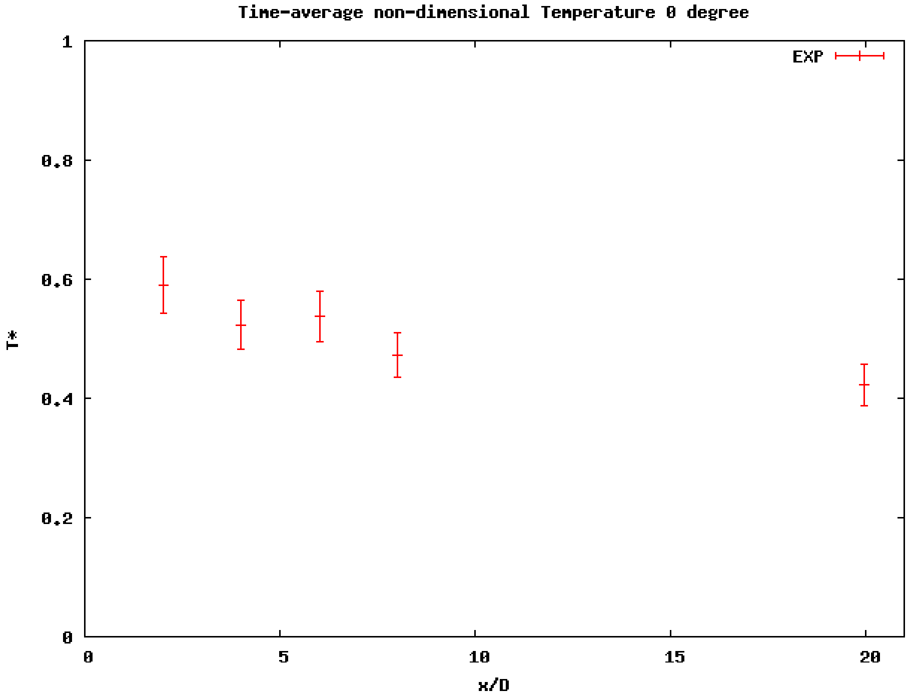

(a) $\overline{T^*}$

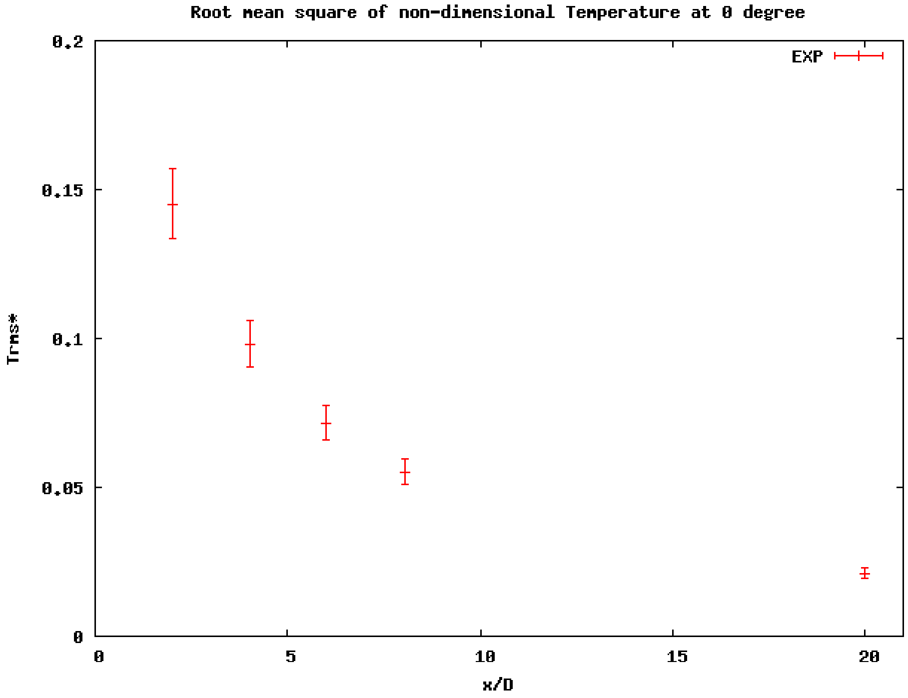

(b) σ_T^*

Figure 2.12: Dimensionless temperature available experimental data from the Vattenfall Tee Junction (0°) Time average (a) Root mean square (b)

In both the right and left axial lines of the pipe, the experimental values show some degree of symmetry. In fact, the two profiles are almost the same and both show that fluid coming from the main pipe is involved in mixing phenomena once the jet contours are enlarged by the action of the mixing layer vortices. In both parts, once the two streams are fully mixed, the temperature value is kept constant (Fig. **??** and **??**).

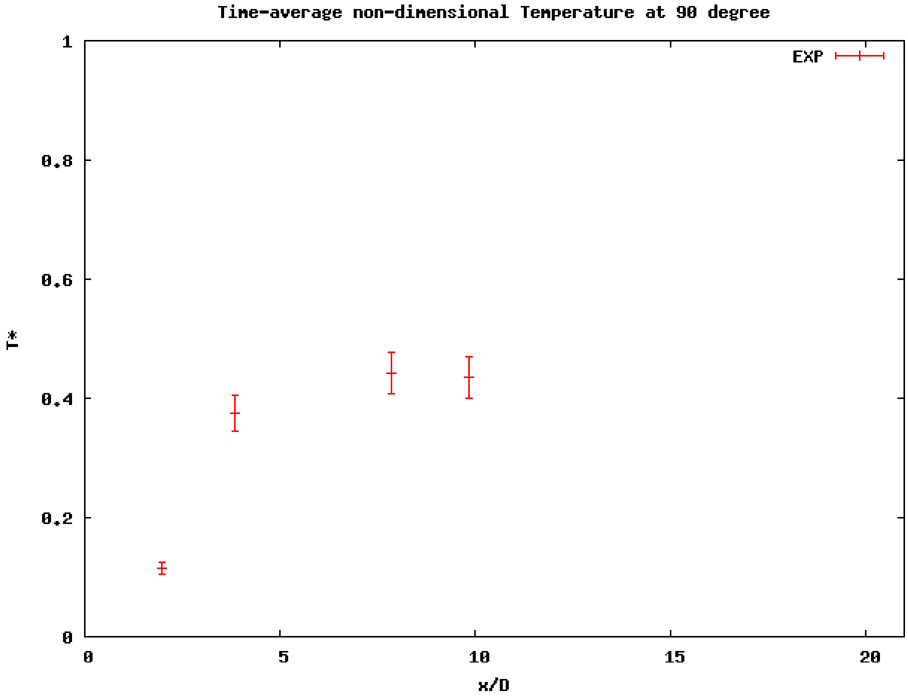

(a) $\overline{T^*}$

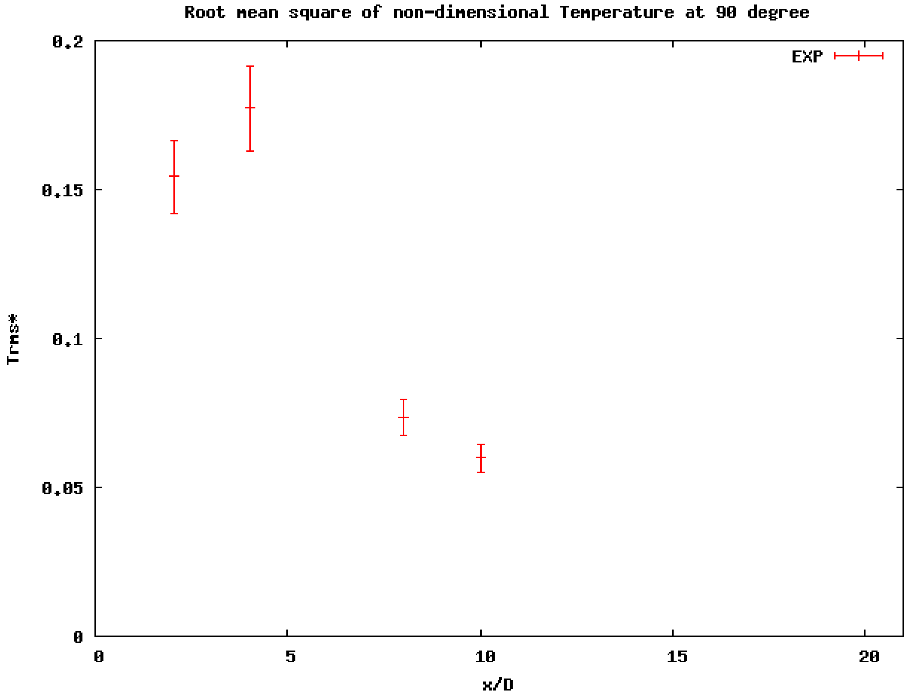

(b) σ_T^*

Figure 2.13: Dimensionless temperature available experimental data from the Vattenfall Tee Junction (90°). Time average (a) Root mean square (b)

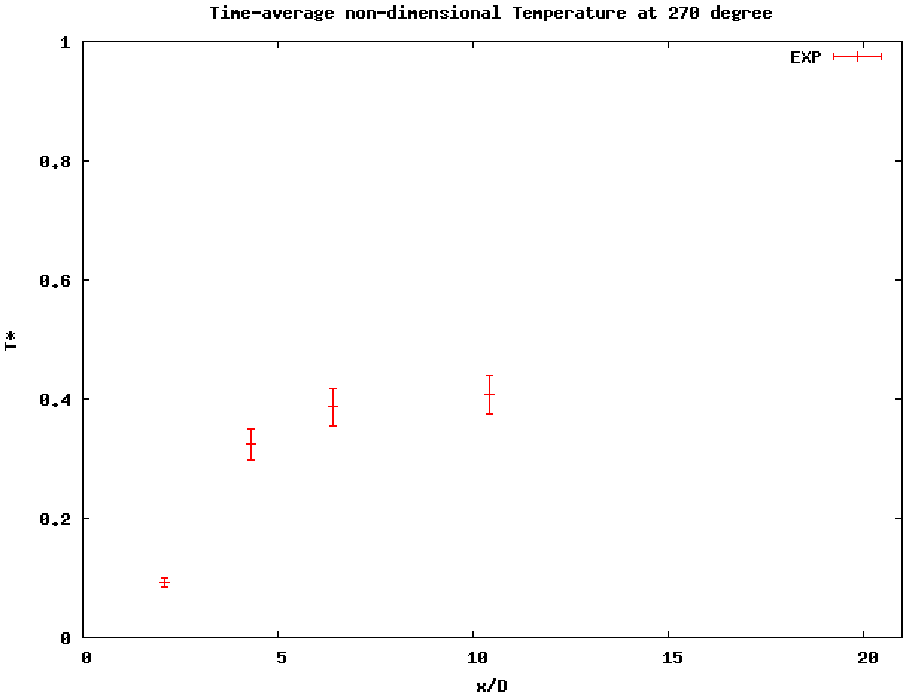

(a) $\overline{T^*}$

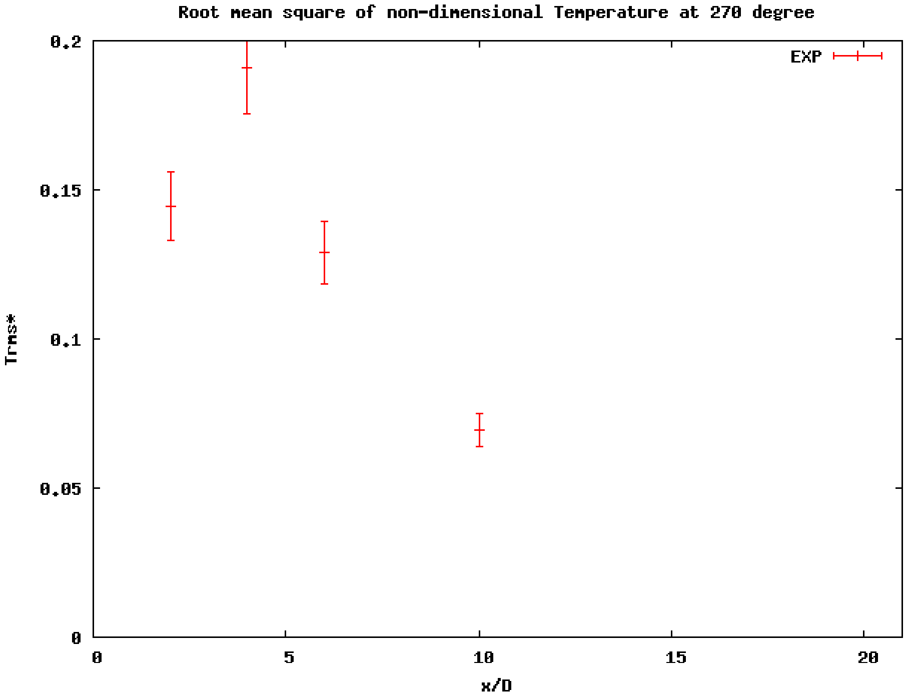

(b) σ_T^*

Figure 2.14: Dimensionless Temperature available experimental data from the Vattenfall Tee Junction (270°). Time average (a) Root mean square (b)

Along the bottom axial line the temperature measurements (Fig. **??** (a)) show that this part of the main pipe is in colder conditions. However mixing phenomena start to involve this part before 5 hydraulic diameters. The turbulent fluctuations arise rapidly with a marked shift before this lenght (Fig. **??**), in agreement with the other profiles, the turbulence involves vortices that decrease their dimension the more they get far from the jet section.

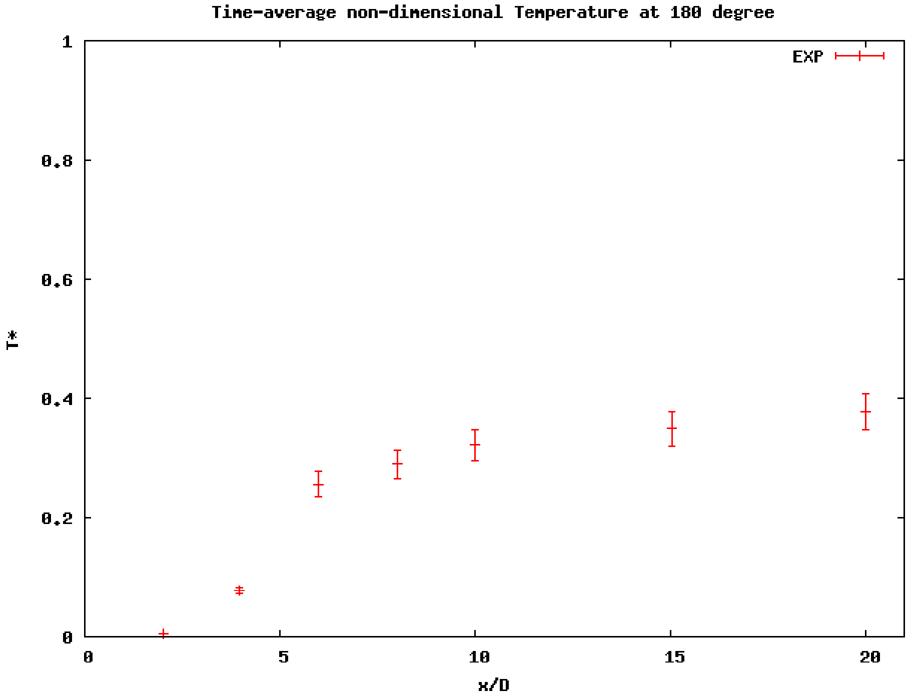

(a) $\overline{T^*}$

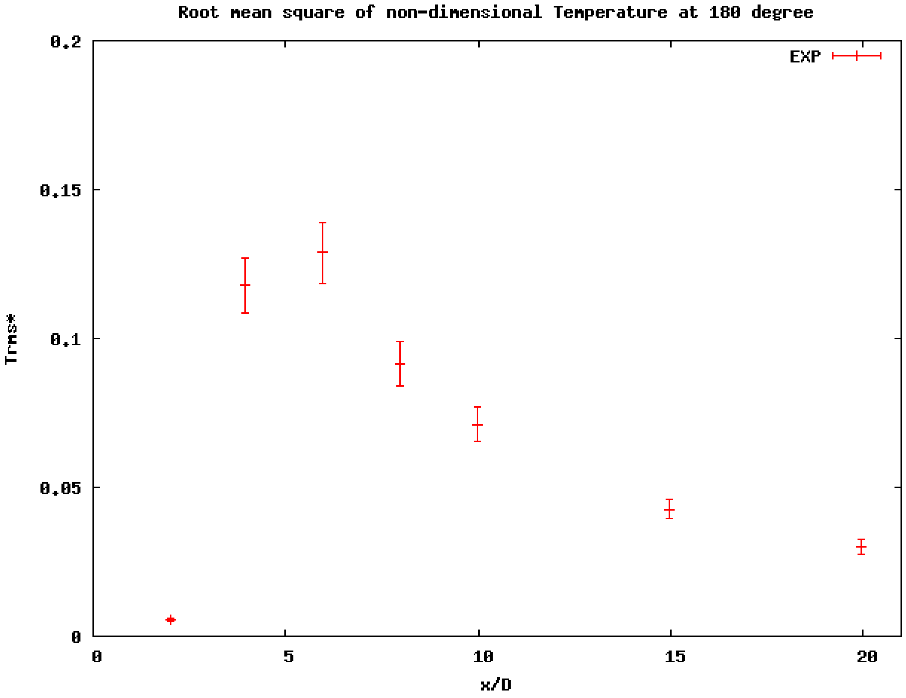

(b) σ_T^*

Figure 2.15: Dimensionless temperature available experimental data from the Vattenfall Tee Junction (180°). Time average (a) Root mean square (b)

Thermal spectra measured in the left part of the channel (Fig. **??** (a)), 2 hydraulic diameters downstream the jet section, shows that higher fluctuations amplitudes happens at lower frequencies up to 3 Hz, afterwards the inertial subrange starts and the distribution follows the -5/3 Kolmogorov law. A peak is presented at frequencies around 2 and 4 Hz, these frequencies corresponds to a lenght scale which is approximatively equal to the main pipe diameter.

1.6 hydraulic diameters downstream the jet section, the axial velocity spectra have been obtained as well (Fig. **??** (b)). No significant peaks can be underlined in this plot, however, the global distribution of the amplitude fluctuations lies in range of frequencies that matches with the temperature spectra, this fact confirms that the advection phenomena determine most of the thermal fluctuations in the fluid.

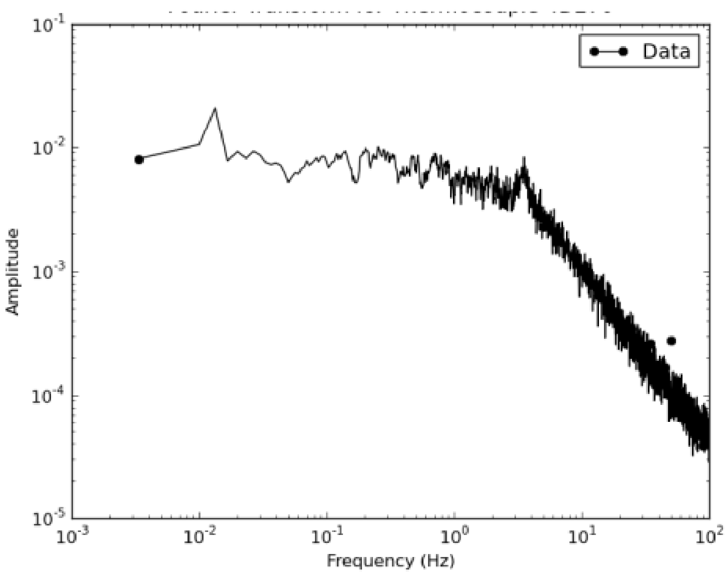

(a) $\tilde{T}$ $(x = 2D_{cold} \quad ; \quad angle = 270°)$

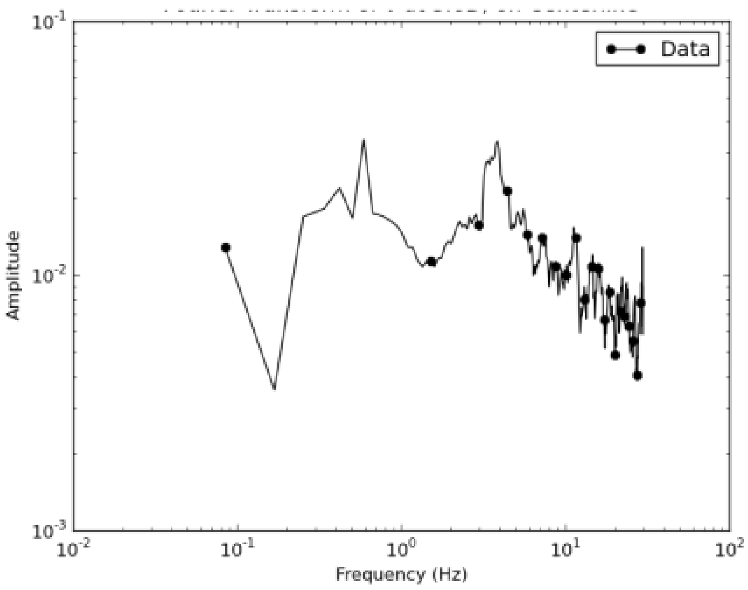

(b) $\tilde{U}$ $(x = 1.6D_{cold} \quad ; \quad y = -35mm \quad ; \quad z = 0mm)$

Figure 2.16: Temperature (a) and velocity (b) spectra available from the experimental campaigns (Brian et al. [**?**]

2.2 Description of TRANSAT

The TRANSAT facility located at the CEA center of Grenoble is a closed loop wind-tunnel. A simplified scheme of the overall structure of the tunnel is shown in Fig. **??**

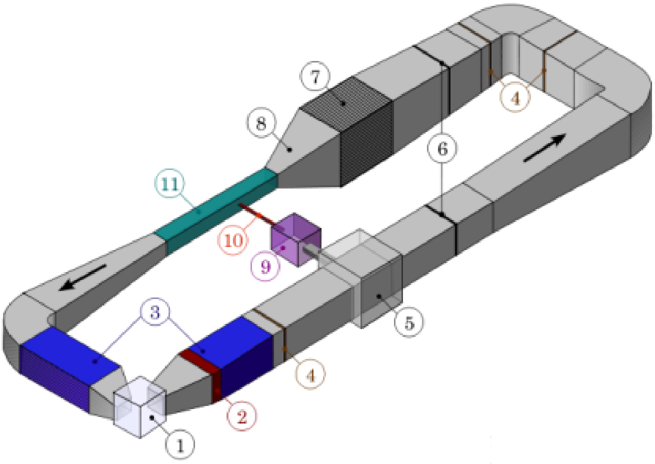

Figure 2.17: Schematization of the Transat facility

Following the index numbers in Fig. **??** the main components of the facility are described below:

1. Centrifugal fan which can provide a maximum flowrate of 4.5 $m^3 \cdot s^{-1}$ using an electrical synchronous 8 kW engine controlled by an inverter.
2. Air-liquid heat exchanger with a capability of 30 kW, used to remove both compression and thermal energy given respectively by the fan and the heater.
3. Silencers installed; with the purpose of collecting pressure fluctuations at the walls, to secure a sound intensity of 60 dB within the channel.
4. Glass fiber filters with an efficiency 99.997% for particles larger than 0.3 μm
5. Jet collector, where a part of the main channel air flow is collected to feed the jet.
6. Large mesh grid with a free-surface coefficient $\frac{A_{free}}{A_tot} = 0.4$ (where A_{free} stands for the free surface of the gridm and A is the total surface) essential to eliminate larger vortices formed through the duct.
7. Calm chamber, composed by a sequence of honeycomb structures which gradually provides a good homogenization of the air flow.
8. Convergent duct, disposed to eliminate residual vortices at the outlet of the calm chamber. It also reduce the turbulence intensity in order to achieve an uniform velocity profile at the inlet of the test section.
9. Adjustable heater providing from 0 to 5 thermal kW to the jet flow.
10. Jet channel containing the analogous sequences of silencer, calm chamber and convergent ducts as well. It has a total lenght of 3 m and an outlet rectangular section 50 mm high (H_j) and 80 mm width (L_j)

11. The test section located at the outlet of the convergent duct, has a rectangular section 0.6 m width (L_c) and 0.5 m height (H_c) for a lenght of 5 m. The jet channel outlet is located at middle heigth, 2.1 m far from the bottom of the main channel inlet section (Fig. **??**)

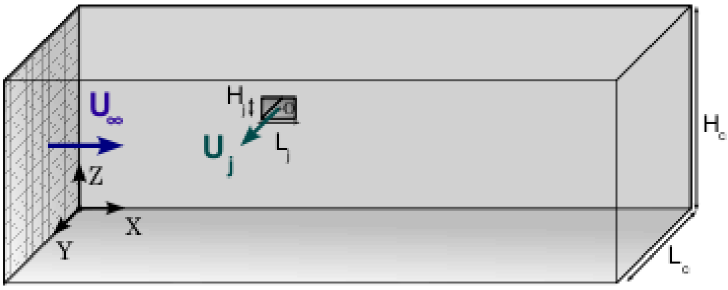

Figure 2.18: Schematization of the Transat test section. Fougairolle [**?**].

The whole lenght of the wind tunnel is coated to keep the main air flow temperature between 286 and 288 K and to decrease environment effects. The jet heater is calibrated to give a ΔT of 10 K. In order to find an optimal basic setup, the CFD calculation is focused on experimental conditions where interactions between the jet and the wall can be assumed negligible. This configuration is characterized by an r ratio of 3.3 where the jet bulk speed (U_j) is 7 $m \cdot s^{-1}$ while the main channel bulk speed (U_∞) is 2.1 $m \cdot s^{-1}$.

2.2.1 CAD information

As outlined previously, the test section of the Transat facility is composed by two channels with rectangulars section connected perpendicularly. The spatial discretization required, considering the turbulent regime of the operating conditions coupled with the extension of the domain, would represent an hard challenge in terms of computational on obtained results costs. In order to reduce the CPU time required, a study on the impact of the domain size has been performed. Two $k-\varepsilon$ calculations have been carried out using both the original and a reduced domain size passing from a total lenght of 5 m to 2 m (Fig. **??**). The elements density is kept constant in both cases so that the original domain mesh had 12411780 elements while the reduced one 4964712 elements. The schemes adopted to obtain the solutions shown in Fig. **??** are reported in table **??**

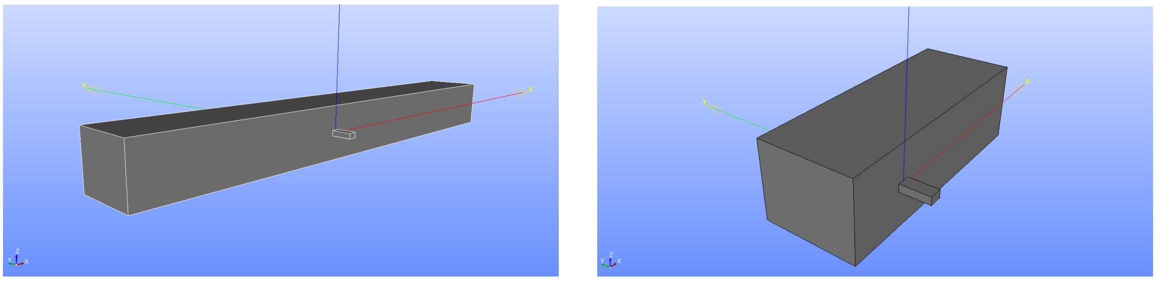

(a) Original Domain

(b) Reduced Domain

Figure 2.19: View of the two Geometrical models adopted for the Transat Test Section

The outcome of this process (Fig. **??**) show no relevant differences between the original and the reduced domain; hence the following CFD applications related to the TRANSAT in this document, have been performed adopting the smaller geometry, as a convenient compromise between results veracity and computational time and resources required.

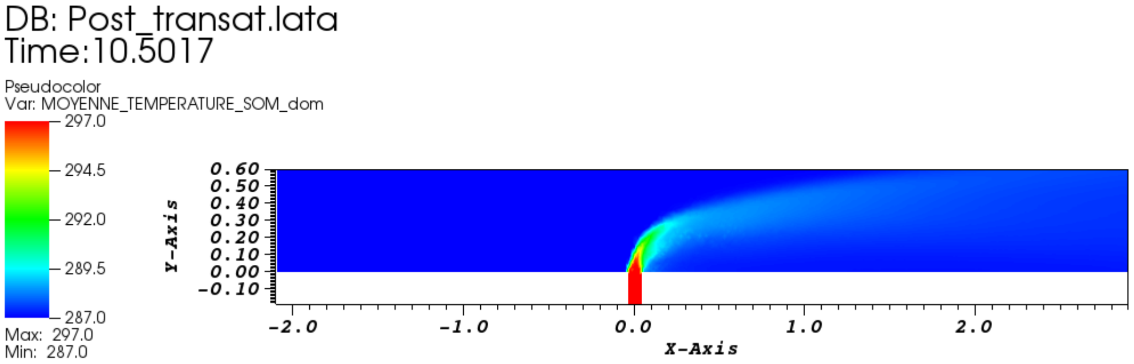

(a) Original Domain

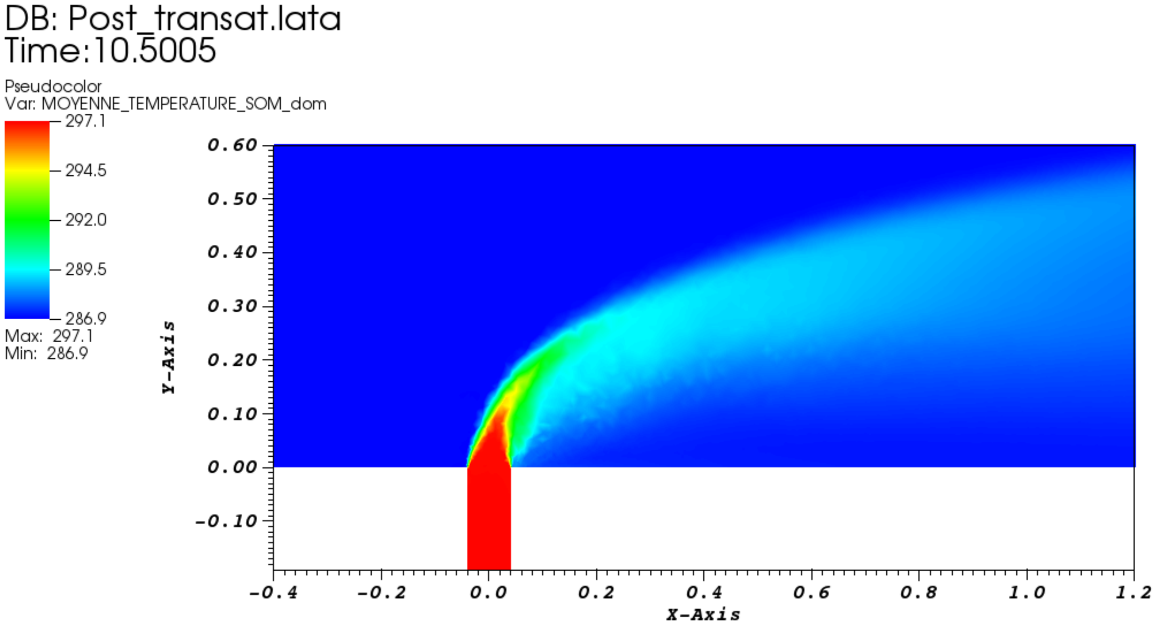

(b) Reduced Domain

Figure 2.20: Comparison between time-Average Temperature fields for the two domain size investigated. Both calculations have been performed with RANS $k-\varepsilon$ model

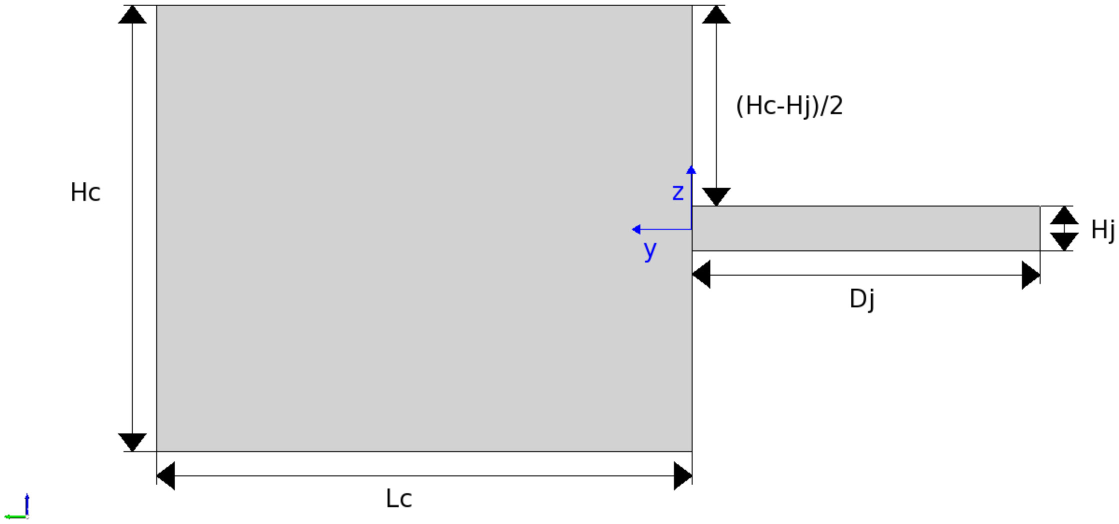

(a) Front view of the Transat test section

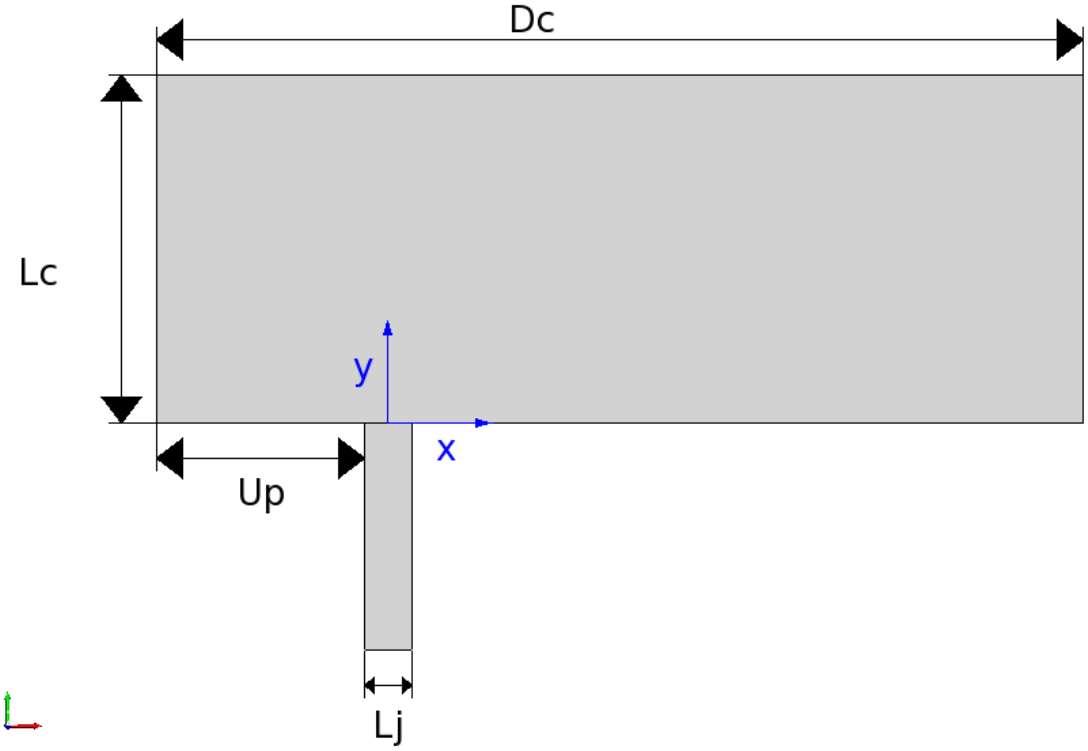

(b) Top view of the Transat test section

Figure 2.21: Schematization of the computational domain adopted for the Transat test section

In Fig. **??** top and front view are shown within the related dimensions and nomenclature. Sizes used for both the reduced and the extended domain are reported in table **??**

	Hc [mm]	Lc [mm]	Dc [mm]	Hj [mm]	Lj [mm]	Dj [mm]	Up [mm]
Original domain	500	600	5000	50	80	3000	2460
Reduced domain	500	600	1600	50	80	390	360

Table 2.2: Dimensions of the large and the small domain

The origin of the reference frame adopted corresponds to the geometrical center of the jet outlet section, with the x and y axis respectively parallel to the streamwise direction of the two streams as outlined in Fig. **??**.

2.2.2 Boundary conditions of the test

The operating conditions taken into account are those related to $r = 3.3$ where the hot air flux coming from the jet channel with a bulk speed (U_j) of $7\ m \cdot s^{-1}$ crosses the main channel without having kinetic interactions with the opposite wall. Flow conditions on the inlet sections are briefly summarised in Tab. **??**.

	$U_{bulk}\ \left[\frac{m}{s}\right]$	$D_h\ [m]$	$T\ [K]$	$\rho\ \left[\frac{kg}{m^3}\right]$	$\mu\ [Pa \cdot s]$	$\beta\ \left[\frac{1}{K}\right]$	$k\ \left[\frac{W}{m \cdot K}\right]$
Tunnel Inlet	2.1	0.54	287	1.24	$1.78 \cdot 10^{-5}$	$3.48 \cdot 10^{-3}$	$2.51 \cdot 10^{-2}$
Jet Inlet	7	0.06	297	1.14	$1.86 \cdot 10^{-5}$	$3.30 \cdot 10^{-3}$	$2.58 \cdot 10^{-2}$

Table 2.3: Transat operating conditions

During the experimental campaign inlet velocity profiles were not directly measured in both the channels inlet sections due to practical issues. However measurements taken in other sections are given to provide a qualitative description of the flow behavior. Downstream the large mesh grid it is possible to observe rather homogeneous flow conditions in the main channel inlet through the flat velocity profiles and low turbulence intensity (1.5%) shown in Fig. **??**

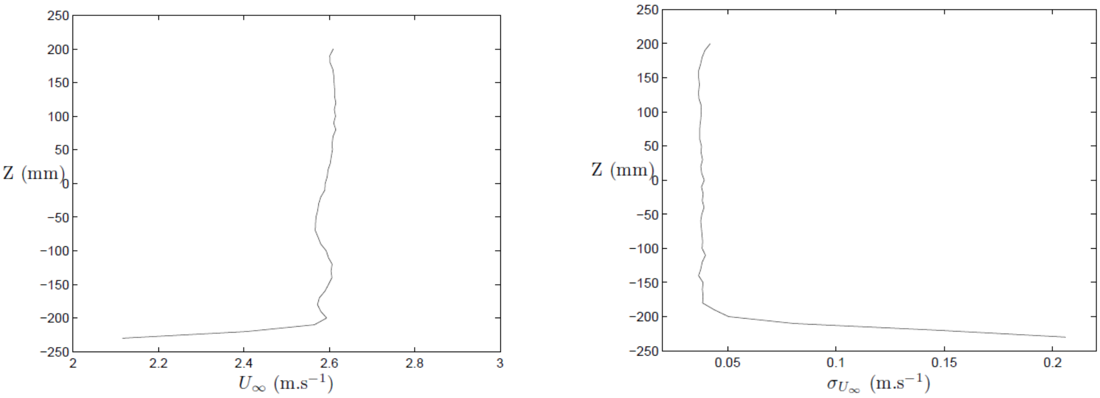

(a) U_∞

(b) σ_{U_∞}

Figure 2.22: Main channel vertical velocity characteristics. (Fougairolle [**?**])

In the jet channel, a slight asymmetry of the velocity profile has been observed in the outlet section, mostly caused by boundary effects (Fig. **??**. Close to the wall, the turbulence intensity varies in a range between 5 and 15 %. In Fig. **??** velocity and its fluctuations plots are shown to give a qualitative description of this behaviour. These measurements have been taken with different operating conditions with respect to those described in the previous Tab. **??**, so that the jet bulk velocity in this case is 6.5 m/s.

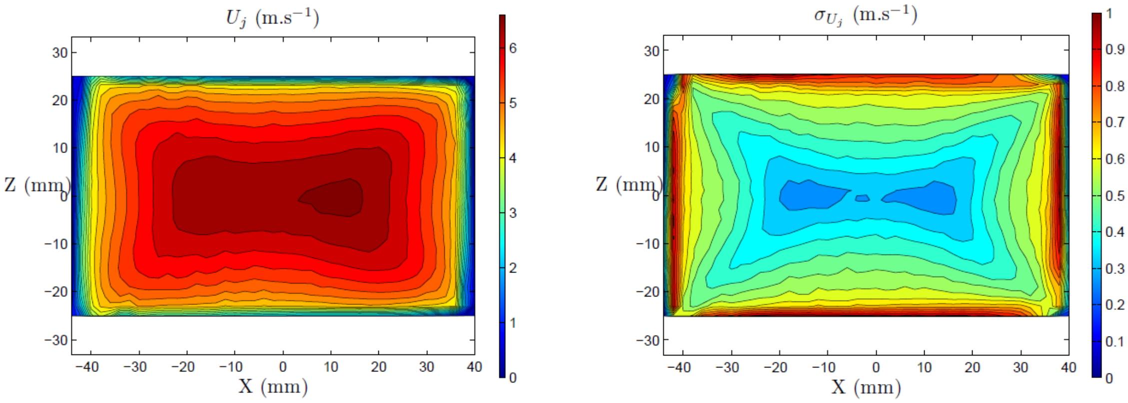

(a) U_j

(b) σ_{U_j}

Figure 2.23: Velocity characteristics on the jet outlet section. Fougairolle [**?**]

Hereafter horizontal velocity profile measurements are shown at $Y/L_j = 0.06$ for the tests considered for our studies (Fig. **??**). It is possible to notice that the same slight asymmetry is observed for these conditions. In order to ensure negligible effects of temperature stratification, thermal conditions throughout the working hours are measured as well; experimental data show negligible vertical thermal gradients (less than 2 °C/m). Measurements of thermal profiles have been taken on the main channel test section, the differences between the laboratory environment temperature (taken as reference) are below 0.8 °C for most of the hours of the day (Fig. **??**).

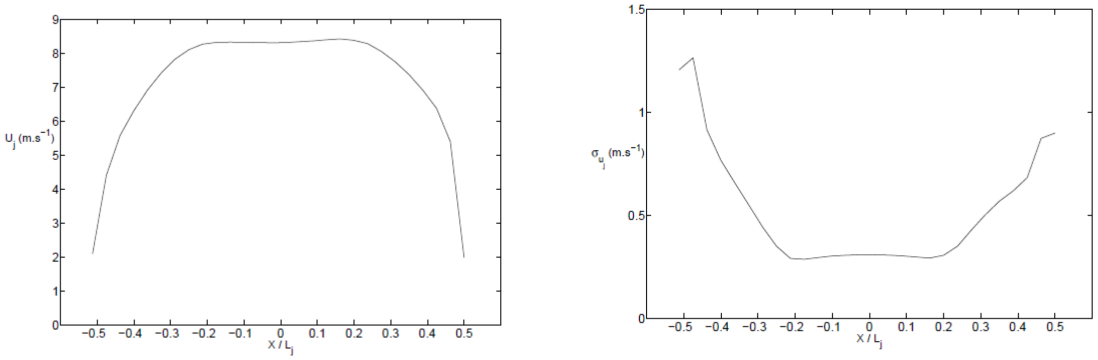

(a) U_j (b) σ_{U_j}

Figure 2.24: Horizontal velocity profiles on the jet outlet section. Fougairolle [**?**]

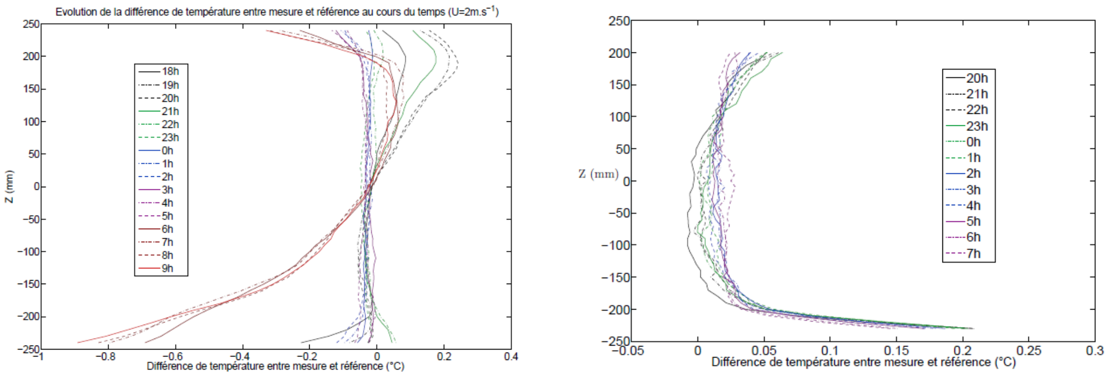

(a) $T - T_{ref}$ (b) $\sigma_{T-T_{ref}}$

Figure 2.25: Horizontal temperature profiles on test main channel. Fougairolle [**?**]

The calm chamber located upstream the jet channel ensures flat thermal profiles with fluctuations below 0.2 °C on the central part of the jet (Fig. **??**).

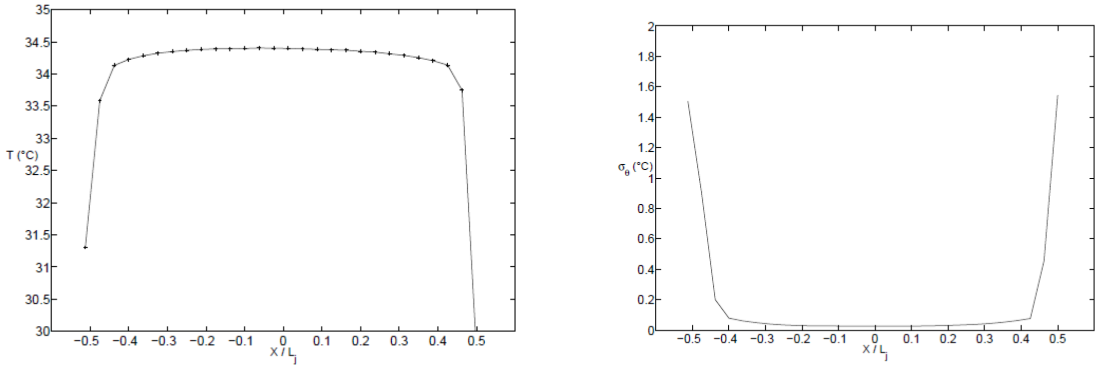

(a) T (b) σ_T

Figure 2.26: Horizontal temperature profiles of jet channel. Fougairolle [**?**]

In conclusion, temperature measurement along the larger dimension of the jet exit section are shown in Fig. ??. The characteristic turbulence time scale analysis are outlined. The turnover and transit time scales are respectively 5.18 and 0.24 s. It is interesting to notice that the ratio between these two times is nearly the same as the one given by the Vattenfall experimental conditions.

2.2.2.1 Available measurements and accuracy

Measurement of velocity components ($\sqrt{u^2+v^2}$ and $\sqrt{u^2+w^2}$) were taken using hot wire anemometers with a sampling frequency of 21 kHz. The instruments are located on planes parallel to the main channel section (plane yz in Fig. ??), at 240 and 480 mm downstream the jet outlet section. The errors in velocity measurements depend mostly on the orientation of the hotwire with respect to the flow, the highest normalized value reported is 2.5 % Temperatures have been measured using Pt 100 Resistance Temperature Detectors (RTD) with frequencies up to 50 kHz on the same planes mentioned before. More measurements are taken on plane xy at the origin of the coordinate system and several planes parallel to the jet outlet section (plane xz). Uncertainities related to temperature measurements are not directly declared, however, the general errors regarding Pt 100 RTD are in the order of 0.5 °C, which means less than 0.1 % in terms of normalized values. The measurement planes are briefly identified in table **??**. Spectra of velocity and temperature have been taken during the experiment, but in different conditions with respect to those assumed in this study. In the following section these are shown to give an idea of their meaningful trends.

Application point coordinates [mm]	Plane	Dimensionless temperature	Velocity [m/s]
(0 ; 0 ; 0)	xy	✓	✗
(0 ; 2 ; 0)	xz	✓	✗
(0 ; 20 ; 0)	xz	✓	✗
(0 ; 40 ; 0)	xz	✓	✗
(0 ; 60 ; 0)	xz	✓	✗
(240 ; 0 ; 0)	yz	✓	✓
(480 ; 0 ; 0)	yz	✓	✓

Table 2.4: Measurements summary. The symbols ✓and ✗ represents respectively the availability or not availability of the measurements on the specified plane located at the correspondant application point.

2.2.3 Experimental results

Experimental measurements have been performed through the test section in different planes (table **??**) within the measurements available. The contour plots shown below are built from data matrices in which the measurements were reported with a spatial step of 2 mm in average, obtained by moving the sondes through out the measurement planes.
On the horizontal xy plane (Fig. **??**) Fig. **??** (a) shows a moderate penetration lenght of the jet; its core part extends up to 2 Y/L_j where the temperature is still at the 95% of the maximum value. Fig. **??** (b), shows the Root mean square of the temperature values at the same location. Zones with higher temperature fluctuations are in evidence as they represent the spacial extent of the mixing zone, which is located right along the deflection zone. Tracking vortices are visible as well, downstream the jet exit on the inner part.

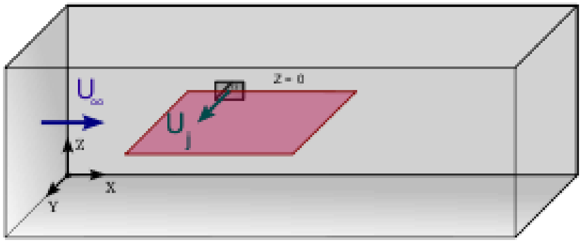

Figure 2.27: Overview of the horizontal XY plane position Fougairolle [**?**]

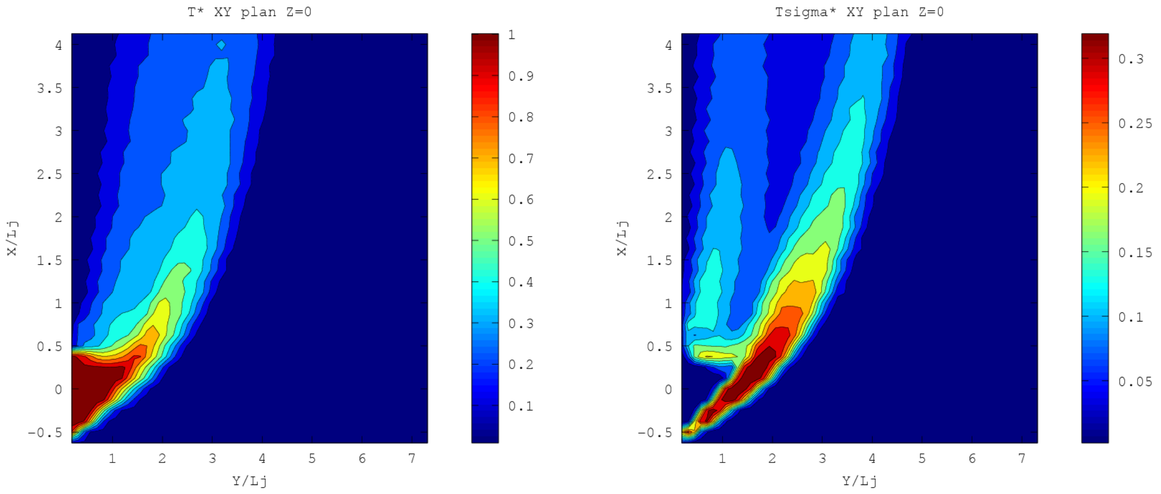

(a) $\overline{T^*}$

(b) σ_T^*

Figure 2.28: Dimensionless Temperature plots taken on the horizontal cut plane. Fougairolle [**?**]

At the jet exit (Fig. **??**) Fig. **??** (a) shows in correspondance of $Z/L_j \approx \pm 0.4$ with $Y/L_j \approx -0.4$ the presence of mixing vortices structures which start to arise on the outer trailing edge. The temperature fluctuations (Fig. **??** (b)) are concentrated on the outer region of the jet and a mixing layer is already formed at this point, even though its thickness is still contained with respect to the main dimension of the jet.

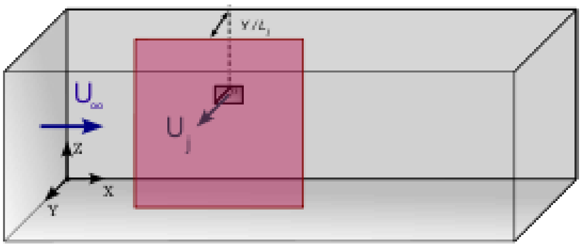

Figure 2.29: Overview of the vertical XZ cutplane. Fougairolle [**?**].

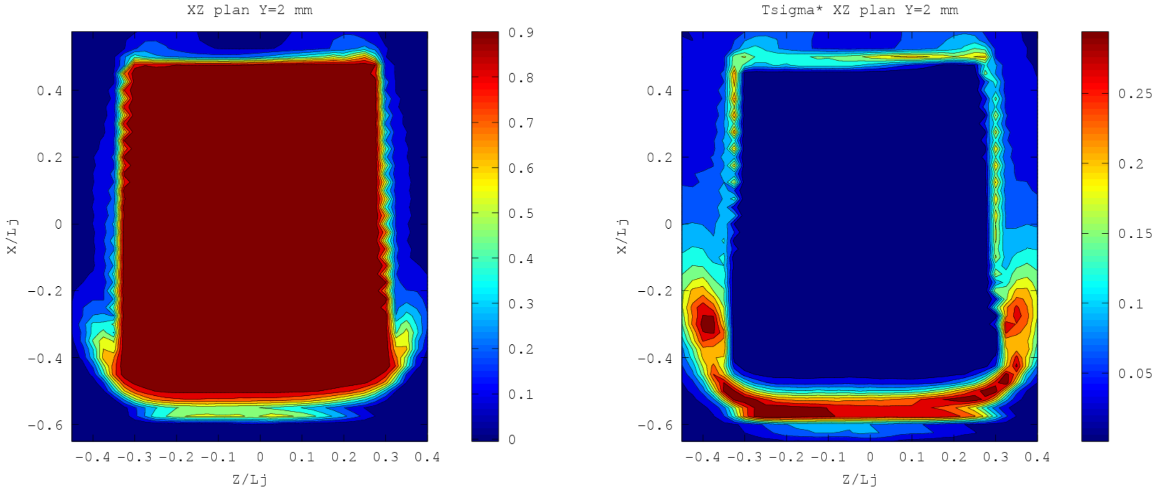

(a) $\overline{T^*}$

(b) σ_T^*

Figure 2.30: Dimensionless Temperature plots taken at the exit of the jet (XZ plane at y=2 mm) . Fougairolle [**?**]. Time average (a) and Root Mean Square (b)

On a parallel plane, at a distance of 20 mm, it is possible to see the evolution of the jet potential field (Fig. **??**). The time average value of the temperature field show the development of the mixing layer vortices which starts to propagate their effects on the outer contours of the jet up to the downstream zone. It is also possible to observe a slight deformation on the inner region, sign that the tracking structures arise as well. Globally the fluctuations are concentrated on the contour lines of the jet and a recirculation zone is visible approximatively on locations where the trailing edge vortices were noticed in the exit section plane. Almost the same consideration can be done for the temperature field detected by the experimenters in a parallel plane 40 mm from the jet exit section (Fig **??**)

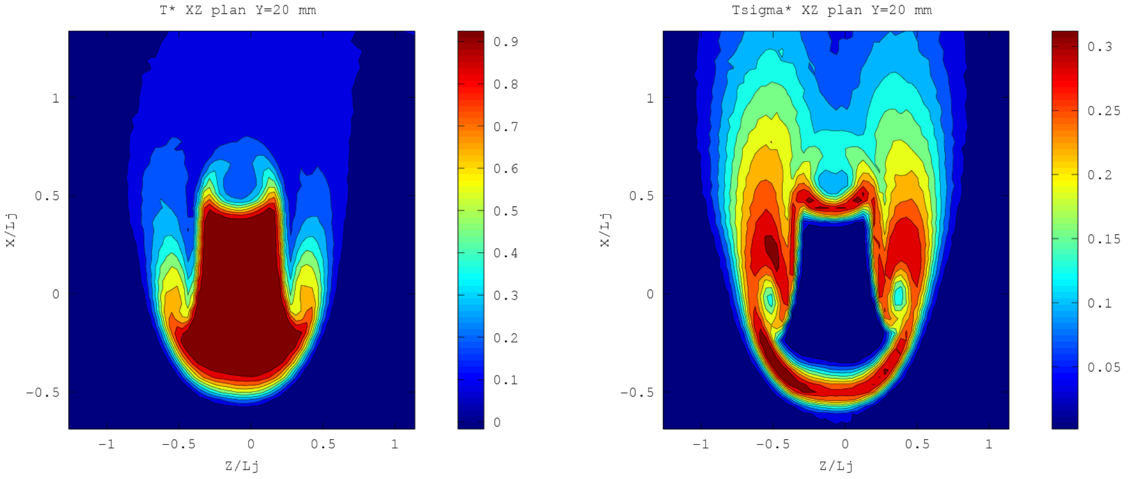

(a) $\overline{T^*}$ (b) σ_T^*

Figure 2.31: Dimensionless Temperature plots taken at the exit of the jet (XZ plane at y=20 mm) Fougairolle [**?**]. Time average (a) and Root Mean Square (b). Time average (a) and Root Mean Square (b)

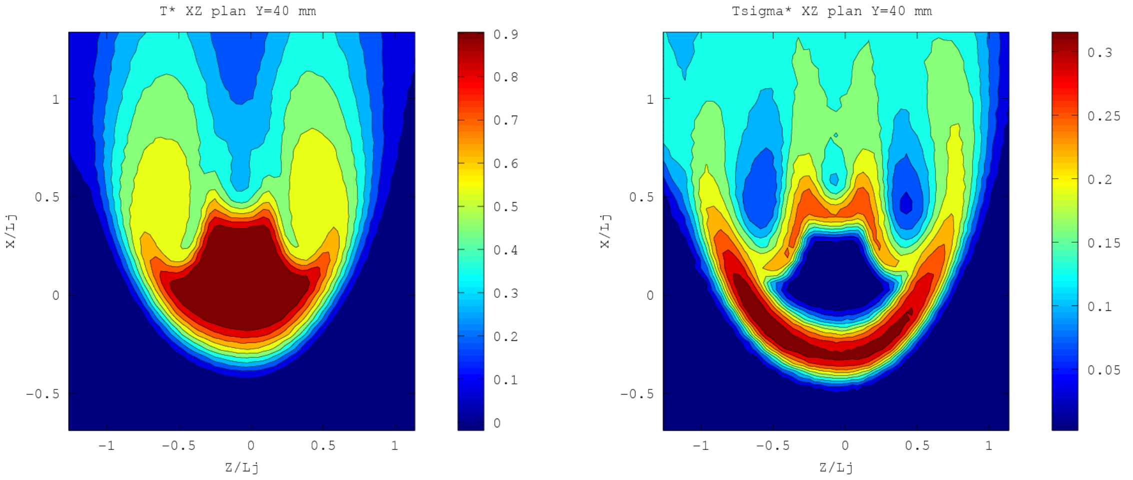

(a) $\overline{T^*}$ (b) σ_T^*

Figure 2.32: Dimensionless Temperature plots taken on the penetration zone of the jet (XZ plane at y=40 mm). Fougairolle [**?**]. Time average (a) and Root Mean Square (b)

The more the measurement plane is shifted in the Y direction, the more the mixing layer and tracking vortices became larger and approach to develop the horseshoe structure. As it can be notice by Fig **??** the jet does not conserve anymore the original rectangular shape of the jet channel section. Moreover the trailing edge vortices are disrupted and shift on the inner part of the jet. At this point of the penetration lenght the mxing layer thickness is enlarged and occupy a good portion of the outer region.

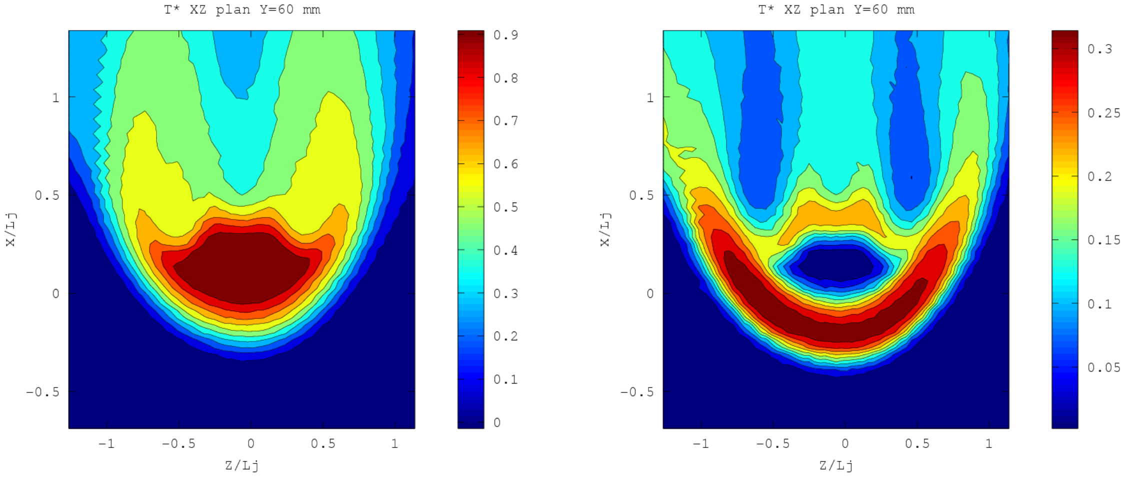

(a) $\overline{T^*}$ (b) σ_T^*

Figure 2.33: Dimensionless Temperature plots taken on the penetration zone of the jet (XZ plane at y=60 mm). Fougairolle [**?**]. Time average (a) and Root Mean Square (b)

Once the turbulent field is reached, measurements proceed to the YZ planes (Fig. **??**). The kinematics of the flow is investigated in a section located 240 mm downstream the jet. Velocity fields such as those one reported in Fig. **??** and **??** shows that the jet structure is globally symmetrical with respect to the centerline plane. However, it can be noticed from the core contours that the jet trajectory does not rotate on a XZ plane (Fig. **??** (a)) while the bean shape assumed by the mean $\sqrt{u^2+v^2}$ profile (Fig. **??**) suggests the presence of a slight rotation on the XY plane. In the mixing layer, the root mean square plots show that the prevailing direction in which the velocity field fluctuates is the streamwise one, on the other hand the core zone presents stronger fluctuations on the Y direction with respect to the Z one.

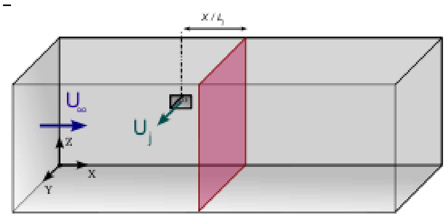

Figure 2.34: Overview of the YZ cutplane

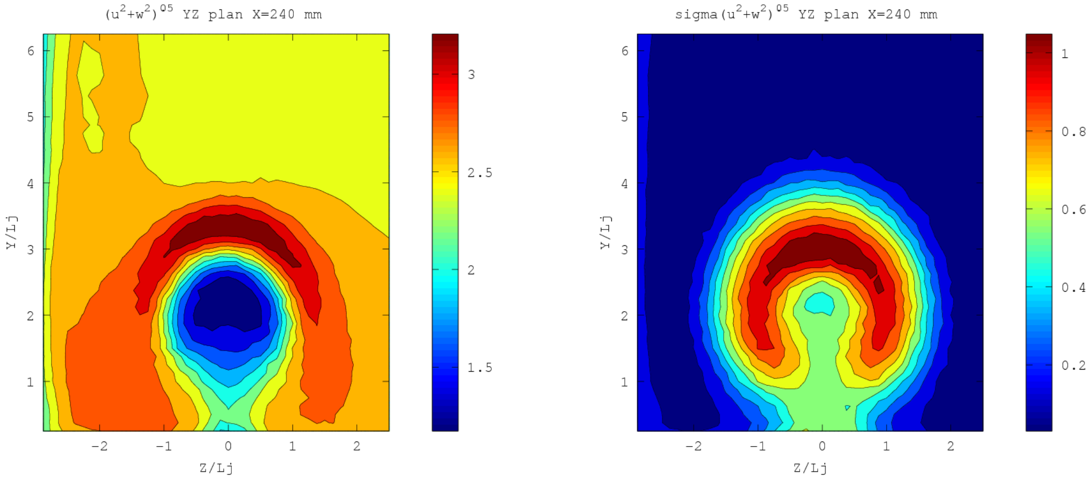

(a) $\overline{\sqrt{u^2+w^2}}$

(b) $\sigma_{\sqrt{u^2+w^2}}$

Figure 2.35: Turbulent zone (YZ plane at x=240 mm) time-average velocity $\sqrt{u^2+w^2}$ (colorbar in [m/s]). Fougairolle [**?**]. Time average (a) and Root Mean Square (b)

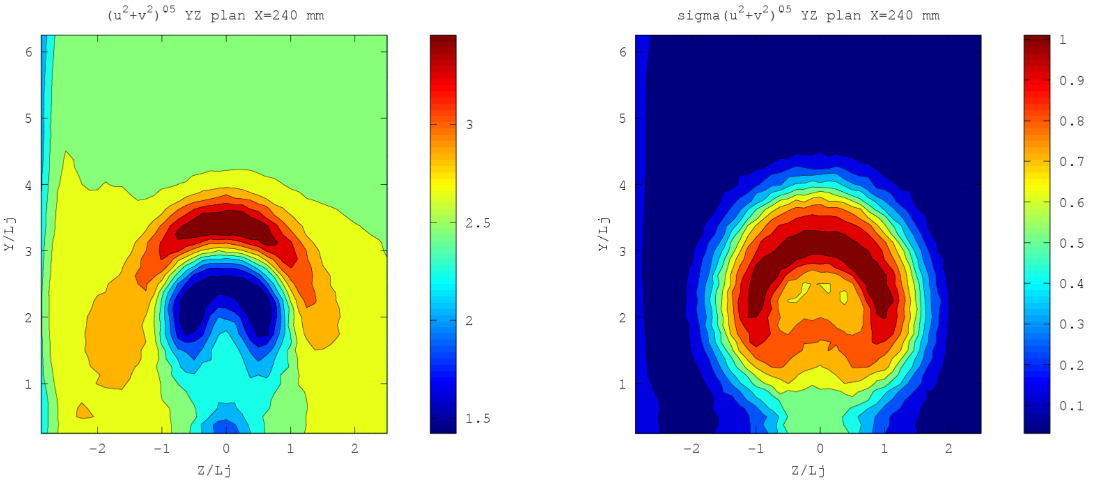

(a) $\sqrt{u^2+v^2}$ (b) $\sigma_{\sqrt{u^2+v^2}}$

Figure 2.36: Turbulent zone (YZ plane at x=240 mm) time-average velocity $\sqrt{u^2+v^2}$ (colorbar in [m/s]) Fougairolle [**?**]. Time average (a) and Root Mean Square (b)

Two different temperature measurement have been carried out on the same plane shown in Fig. **??** and **??**. The profiles agree with each other for both the time average and the fluctuations. In the core of the horseshoe structure, the dimensionless temperature reaches a maximum value which is approximatively 1/4 of the starting value. The root mean square contours shows that the CVP structure is developed in this region.

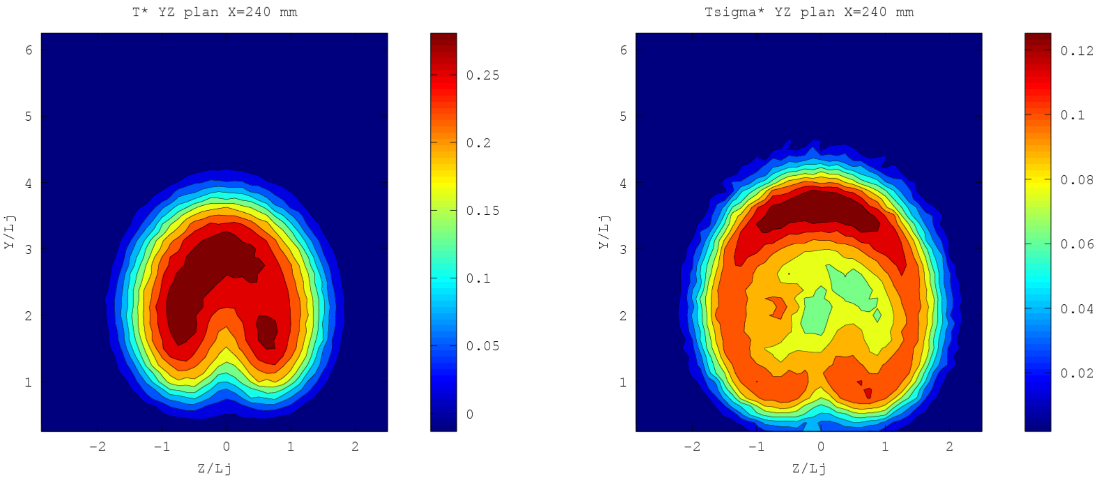

(a) $\overline{T^*}$ (b) σ_T^*

Figure 2.37: Dimensionless Temperature plots taken on the development zone of the jet (YZ at x=240 mm). Fougairolle [**?**]

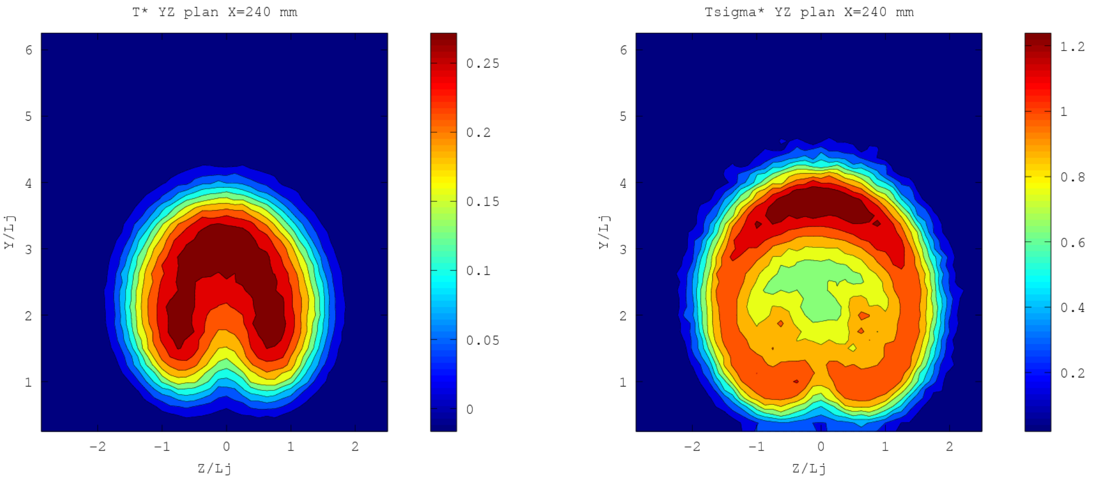

(a) $\overline{T^*}$ (b) σ_T^*

Figure 2.38: Dimensionless Temperature plots taken on the development zone of the jet (YZ at x=240 mm). Fougairolle [**?**]. Time average (a) and Root Mean Square (b)

Through the far field the measurement of velocity (Fig. **??** (a)) shows that the maximum velocity is still in the mixing zone. The field keeps its symmetry with respect the XY plane. However the fluctuations are reduced both in temperature (Fig. **??** (b)) and velocity (Fig. **??** (b)) as the gradients are less steep.

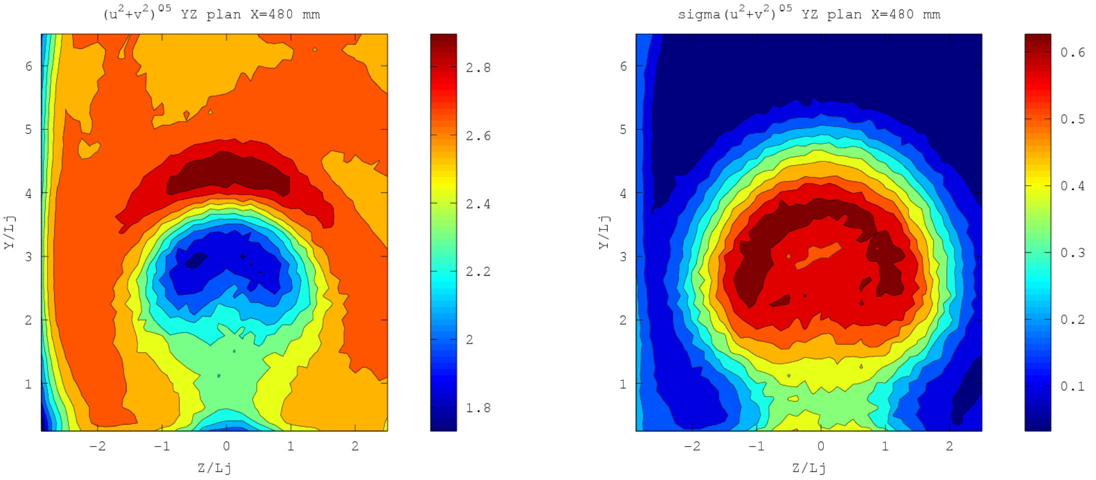

(a) $\overline{\sqrt{u^2+v^2}}$ (b) $\sigma_{\sqrt{u^2+v^2}}$

Figure 2.39: Developing zone (YZ plane at x=480 mm) time-average velocity $\sqrt{u^2+v^2}$ (colorbar in [m/s]) Fougairolle [**?**]. Time average (a) and Root Mean Square (b)

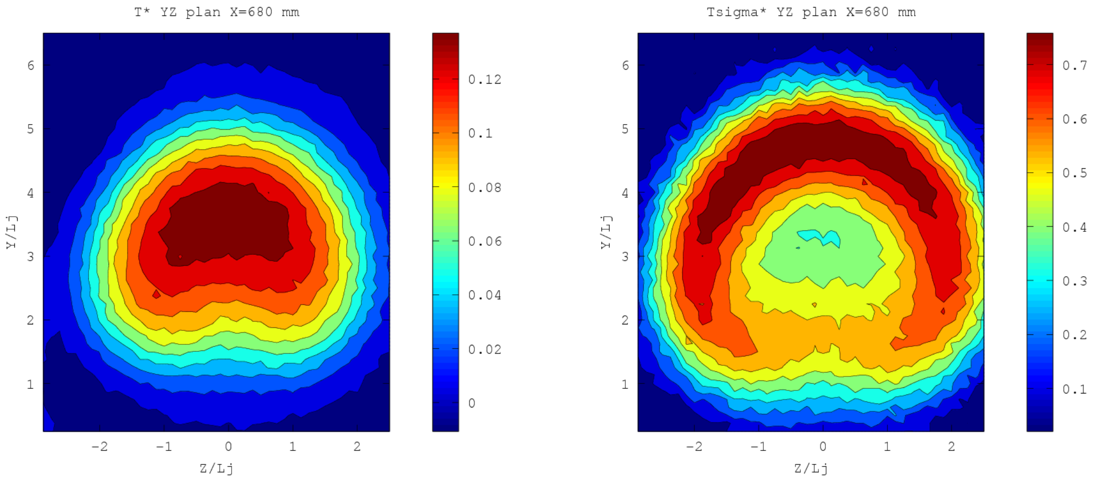

(a) $\overline{T^*}$ (b) σ_T^*

Figure 2.40: Dimensionless Temperature plots taken on the far field (YZ plane at x=480 mm) of the jet. Fougairolle [**?**]. Time average (a) and Root Mean Square (b)

Finally velocity and temperature spectra are presented. In Fig. **??** the location of these points is shown; each measurement point has been chosen in order to capture the characteristic frequency distribution of each turbulent structure. The A point is located upstream the jet, on the outer region; it has been chosen to study the starting mixing layer structures, while the C point has the same objective but for the enlarged and developed structures of the mixing layer. Finally, the point B has been chosen to observe the characteristic frequencies on the jet core. The coordinate details of these points are reported in table **??**.

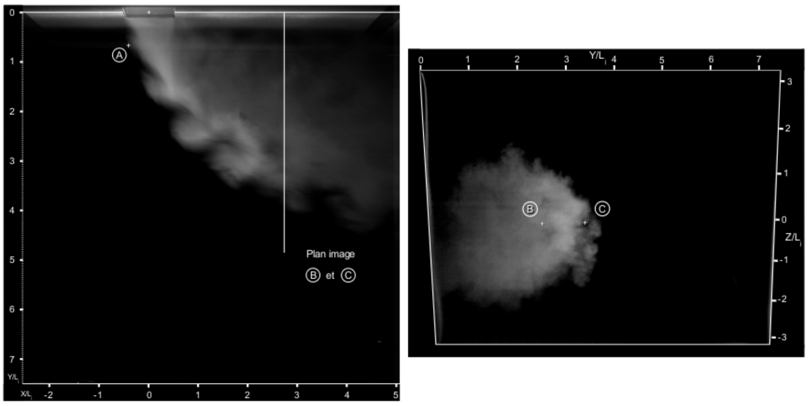

Figure 2.41: View of the spectra measurement point. Fougairolle [**?**]

Point Name	Coordinates [mm]
A	(-40,250,0)
B	(220,200,0)
C	(220,270,0)

Table 2.5: Spectra measurements locations

Looking at the results it is possible to distinguish a clear amplitude peak of the velocity spectra in point A (Fig. **??** (a)). This peak is located in a range of frequencies around 70 Hz and can be associated to those structures generated by the impact between the two boundary layers which generates the mixing layer vortices on the outer part of the jet. Spectra of point

B and C cannot easily be distinguished, since the lenght scale of the vortices of the core zone are nearly the same of those of the CVP structures.

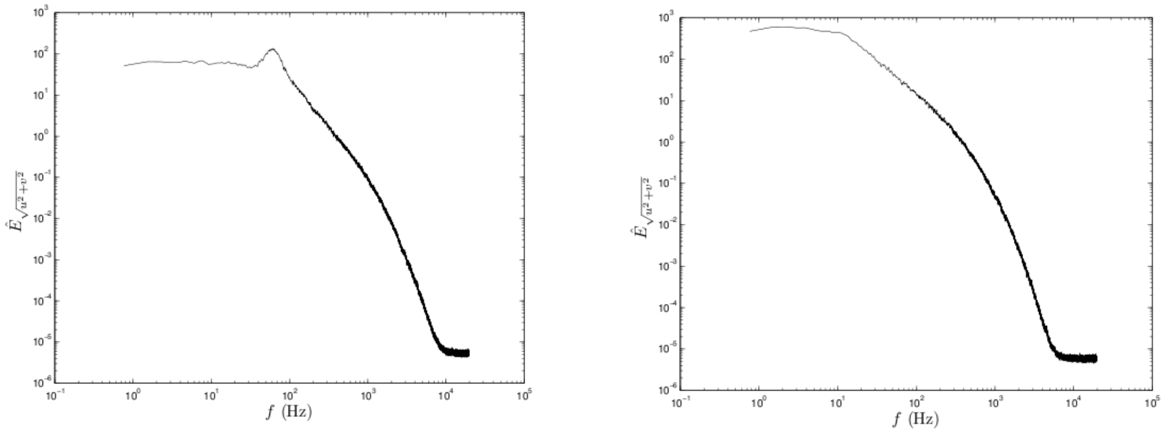

(a) Point A

(b) Point B

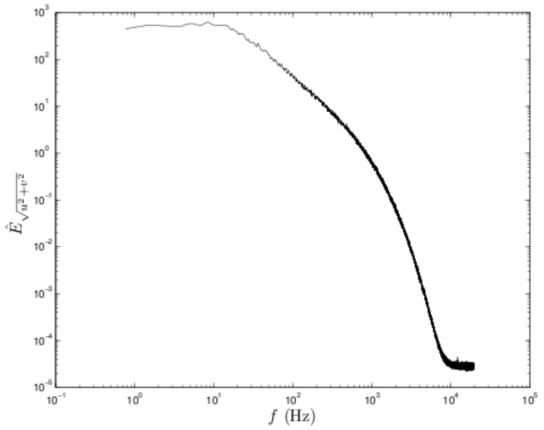

(c) Point C

Figure 2.42: Velocity $\sqrt{u^2+v^2}$ spectra. Fougairolle [**?**]

The temperature spectra (Fig. **??**) do not shows particular peaks for all the three point distributions, so that it is not possible to distinguish a particular amplitude of the fluctuations that can be associated to a certain frequency range or lenght scale. However, it is possible to see that there is still an agreement about the frequency that signs the passage to the inertial subrange between point C and point B. The point A temperature spectra shows that this passage happens to higher frequencies, in agreement with the fact that the starting turbulent structures of the mixing layer are smaller with respect to the jet core dimensions.

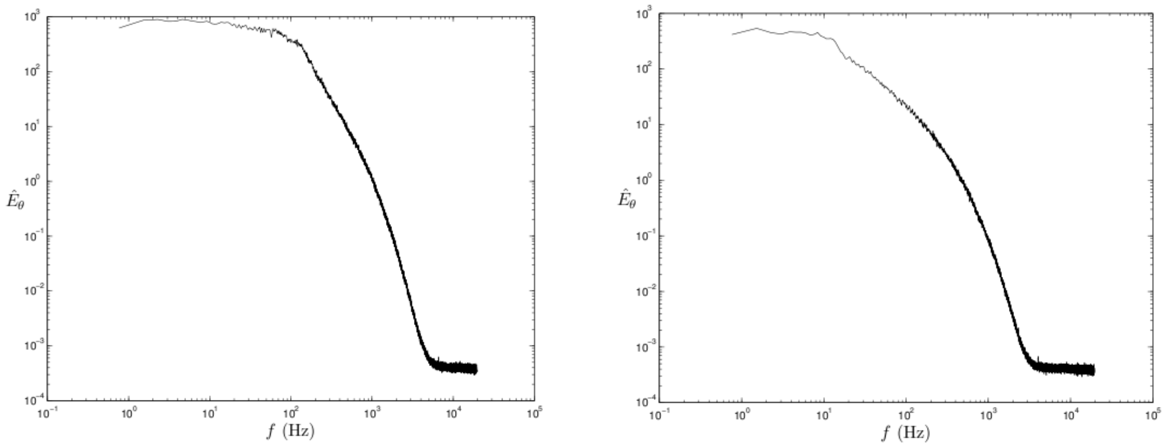

(a) Point A
(b) Point B

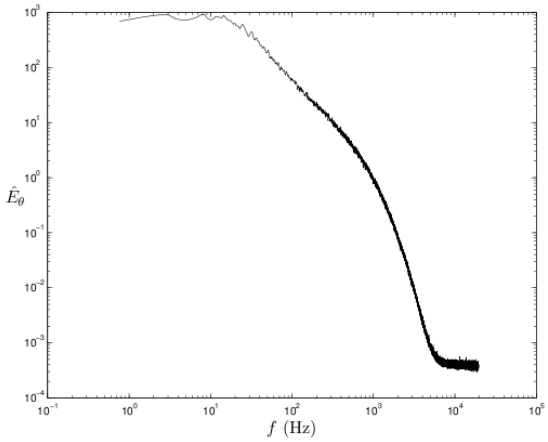

(c) Point C

Figure 2.43: Temperature spectra. Fougairolle [**?**]

Chapter3

Numerical approach to analyze thermal fatigue

In a large part of cases, turbulent flows can be described with good accuracy and small computational costs by using two-equations models for solving Reynolds Averaged Navier-Stokes Equations (RANS), whenever the user aims to obtain consistant time-averaged fields. On the other hand, to achieve detailed turbulence data, Large Eddy Simulation (LES) shows higher capabilities. Thermal fatigue involves small lenght and time scale phenomena, hence LES is a mandatory approach to obtain such detailed solutions. Besides, validations of CFD tools are still needed to achieve a better understanding on their limitations, whenever they are used for studying such kind of phenomena. In the present work, the experimental campaigns described previously are taken into account to evaluate the TrioCFD code performances while adopting the settings explained in detail in the following subsection.

In the thermal fatigue context the frequencies that are assumed to be dangerous for the material integrity, with respect to what has been observed during the experimental campaigns, lie in ranges between 0.1 and 10 Hz. In the described cases the temperature fluctuations are driven predominantly by advective effects, which highly depend on vorticity structures that are generated at different scales in the domain. According to momentum conservation, turbulence space and time scales are strictly interrelated; due to this fact vorticity increases passing from large to small turbulent structures, and each frequency can be associated to a certain spatial extension of eddies. In order to capture this phenomena it is necessary to correctly resolve vortices scales which correspond to the frequencies of interest; this can be made by applying the appropriate discretizations for both time and space. In both the cases treated in this work, to adopt a time (and consequently in space) discretization finer than the transit time scale would be an approach that apparently gives more information than those required. One can argue that all the informations related to phenomena that occurs under a defined Δt smaller than the one linked to the higher frequencies fluctuations involved in thermal fatigue are not significant to its analysis, but, on the other hand, to directly resolve the required scales with LES, the effects given by sub-grid-stress modelization must be controlled. The turbulent viscosity definition have not a pure. Therefore, the required time and spatial discretization must be finer than that one estimated from a simple dimensional analysis.

At high Reynolds numbers, a wide range of vortices length scales can be found in the domain. These scales higly depend on the configurations studied, therefore it is not surprising that in literature is not possible to find clear length scale criteria that can be directly exploited to distinguish the small scale turbulence and the large scale motions.

The simplest statistics containing information on the spatial structure of any random field, is the two-point, one-time autocovariance often better known as the two-point correlation, here given for two general scalars s_1 and s_2.

$$R_{i,j}(\vec{r},t) = \overline{s_1(\vec{x},t)s_2(\vec{x}+\vec{r},t)} \tag{3.1}$$

In turbulence theory context, this quantity can be used to estimate the relation between neighbouring velocity fluctuations, which is reasonably assumed to be the characteristic lenght of the vortices.

For a vector field it is possible to define the correlation tensor, in particular detail, for the velocity field, under homogeneous and isotropic turbulence hypothesis this tensor is diagonal and each terms is independent of $\vec{x}$. Moreover, assuming a direct proportionality between the correlation of fluctuations and the correlation of instantaneous values, it is possible to determine each component using:

$$R_{ii}(r,t) = \frac{u_i'^2}{u_i^2}\overline{u_i(\vec{x},t)u_i(\vec{x}+\vec{i}r,t)} \tag{3.2}$$

better known as the longitudinal autocorrelation function. On the basis of this function, it is possible to define other lenghscale, one of these is the Taylor microscale defined as [**?**]:

$$\lambda_{ii} = \sqrt{\frac{2u'^2}{\overline{\frac{\partial u_i^2}{\partial x_i^2}}}} \tag{3.3}$$

which, under the hypothesis of isotropic and homogeneous turbulence can be written [**?**]:

$$\lambda_{ii} = \sqrt{15\nu\frac{\overline{u_i' u_i'}}{\varepsilon}} \tag{3.4}$$

For high Reynolds number flows for which reliable DNS or fine LES results are not available, it is imperative to use RANS results to predict the turbulence lengthscales. Therefore the derived form of the taylor lenght scale can be exploited:

$$\lambda = \sqrt{10\nu\frac{k}{\varepsilon}} \tag{3.5}$$

As it is possible to observe from the latter form of the Taylor lenght scale, its magnitude is larger whenever the turbulent kinetic energy prevails on its dissipation, and the contrary occurs in the opposite case. This happens following the turbulent energy cascade, where the energy dissipation ratio progressevely increases with the smaller scales, following the Kolmogorov law from the inertial to the viscous subrange.

The use of the Taylor microscale has already shown interesting outcomes on describing the turbulence characteristics in plane channels at Re_T below 1000, and really close agreement between DNS and LES have been achieved (Gaitonde [**?**] Fig.**??**)

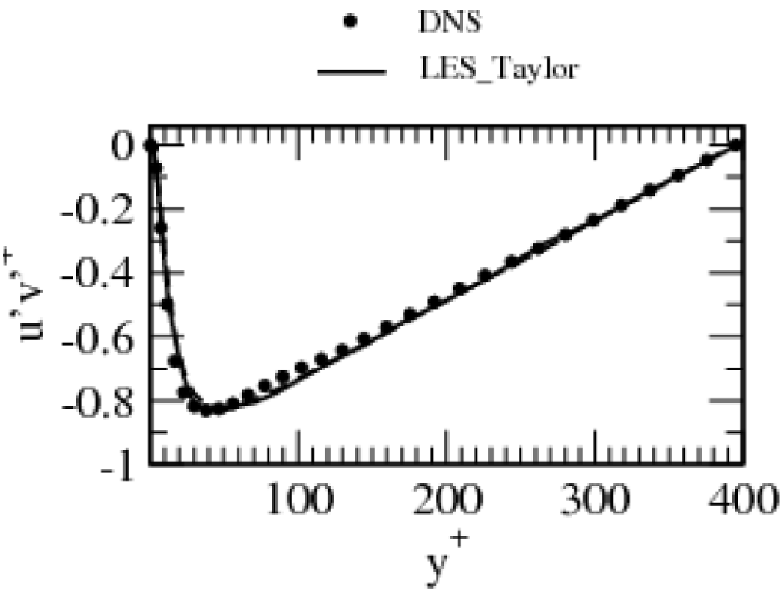

Figure 3.1: Correlation of velocity fluctuations obtained with LES using grid that adopt the Taylor lenght scale scales. Results are compared with a DNS calculation [**?**]

Following these arguments, preliminary simulations have been carried out using unsteady RANS equations with a $k-\varepsilon$ model, in order to achieve a better understanding on the grid refinement and the accuracy on both boundary and initial conditions. This information has been used to correctly set up the LES models and to evaluate whereas it was a reasonable choice to reduce the domain size, allowing lower costs in terms of memory and CPU time spent. This had given the possibility to tests a higher number of differents setups in a short-time. In order to avoid steep gradient on the mesh size, and then contain numeric influences, the generated mesh size does not follow locally the Taylor microscale described by k and ε values; hence it has been calculated from the distributions obtained in the most meaningful zones of the flow field, which belong to the mixing layers created from the impact between the main and the jet flow. This scale has been then applied to the whole domain, keeping a limited stretch factors for those zones where the turbulence description is not required to be detailed.

The Taylor scales adopted using this method, ensure reasonable values of y^+ on the cells close to the walls, whenever a wall-law is applied.

The use of a wall-law has been pursued for all the calculations performed due to the advantage given by the less wall refinement requirements that it gives.

3.1 Navier-Stokes equations

Whenever thermal fluid dynamics problems have to be faced, it is generally convenient to approach the overall phenomena from a macroscopic point of view. Assuming the fluid as a deformable continuum, occupying a portion of space Ω bounded by its surface Σ_Ω. The overall mass at the instant t can be written in conservative form as:

$$M_\Omega(t) = \int_{\Omega(t)} \varrho d\omega \tag{3.6}$$

Where ϱ is the fluid density, and $d\omega$ the infinitesimal volume portion of Ω. Assuming the absence of sources and sink terms the mass conservation is given by:

$$\frac{d}{dt}\int_{\Omega(t)} \varrho d\omega = 0 \tag{3.7}$$

Then, applying the Reynolds theorem:

$$\frac{d}{dt}\int_{\Omega(t)} \varrho d\omega = \int_{\Omega(t)} \left[\frac{\partial \varrho}{\partial t} + \nabla \cdot (\varrho \vec{u})\right] d\omega = 0 \tag{3.8}$$

where $\vec{u}$ is the fluid velocity. On arguing about the arbitrary on the choice of the volume Ω it finally possible to write the differential form of the mass balance:

$$\frac{\partial \varrho}{\partial t} + \nabla \cdot (\varrho \vec{u}) = \frac{\partial \varrho}{\partial t} + \nabla \rho \cdot \vec{u} + \rho \nabla \cdot \vec{u} = 0 \tag{3.9}$$

by applying the momentum balance to the volume taken in account we have:

$$\frac{d}{dt}\int_{\Omega(t)} \varrho \vec{u} d\omega = \int_{\Omega(t)} \rho \vec{f} d\omega + \int_{\Sigma\Omega(t)} \vec{\vec{T}} \cdot \vec{n} d\sigma \tag{3.10}$$

where $\vec{f}$ represents the volume forces and $\vec{\vec{T}}$ the internal forces tensor applied to the portion of surface $d\sigma$ with normal $\vec{n}$. Manipulating this integral formulation using the same speculations for the mass balance, the differential form of the momentum balance is given:

$$\frac{\partial \varrho \vec{u}}{\partial t} + \nabla \cdot (\varrho \vec{u} \cdot \vec{u} - \vec{\vec{T}}) = \rho \vec{f} \tag{3.11}$$

Moreover the energy conservation law equation is:

$$\frac{d}{dt}\int_{\Omega(t)} \varrho E d\omega + \int_{\Sigma\Omega(t)} \vec{q} \cdot \vec{n} d\sigma = \int_{\Sigma\Omega(t)} (\vec{\vec{T}} \cdot \vec{n}) \cdot \vec{u} d\sigma + \int_{\Omega(t)} \rho \vec{f} \cdot \vec{u} d\omega + \int_{\Omega(t)} \rho r d\omega \tag{3.12}$$

where E indicates the specific total energy, composed by the internal and kinetic energy contribution

$$E = e + \frac{1}{2}|\vec{u}|^2 \tag{3.13}$$

$\vec{q}$ is the heat flux flowing through the boundary surfaces of the control volume and r the thermal power source. The energy balance equation assumes its differential form

$$\frac{\partial \rho E}{\partial t} + \nabla \cdot (\rho E \vec{u} - \vec{u} \cdot \vec{\vec{T}} - \vec{q}) = \rho(\vec{f} \cdot \vec{u} + r) \tag{3.14}$$

The set composed by equations **??**, **??** and **??**, often reported as Navier-Stokes equations must be solved to obtain the fluid motion and temperature field.

3.1.1 Basic Hypotheses

The great description accuracy provided by Navier Stokes equations is payed in terms of calculus difficulties. The presence of non-linearities makes this set analytically unresolvable in most of cases. Therefore a numerical approach is nowadays the only method within which approximate solutions can be given. Nevertheless, the form given in the previous section, still presents some complexities that must be faced by using hypotheses which can simplify the problem.

For the case treated during this study, for both water and air temperature or pressure variations in time do not lead to considerable changes on the density field, spatial gradients are as well negligible, therefore equation **??** is therefore modified:

$$\frac{\partial \cancel{\rho}}{\cancel{\partial} t} + \cancel{\nabla \rho \cdot \vec{u}} + \rho \nabla \cdot \vec{u} = 0 \tag{3.15}$$

This assumption therefore equivalent to assume incompressible fluids. Attention must be paid to this statement considering that compressibility can be referred both to fluids and flows.

In the first case it a measure of the relative volume change in response to a pressure change. It is defined regardless of whether or not this fluid is flowing since it is a thermodynamic characteristic of that fluid. On the other hand, the compressibility of a flow is directly related to the value of the Mach number in the flow. One can show that second order taylor decomposition of the momentum equation leads to a term for fluctuating pressure that scales as Ma^2. As a consequence, one can consider that the flow is incompressible as long as the Mach number is lower than 0.3 regardless of the specific fluid in consideration. In the case $Ma = 0.3$, the "acoustic" fluctuating pressure (as it often called this second order term in pressure) corresponds to 10 % of the convective (or aerodynamic) pressure term. In conclusion in our cases incompressible hypothesis is made on the fluid, because the Mach number will not exceed the limit value.

Another assumption that can lead to further simplifications is the viscous and non-polar fluid hypothesis. This assumption implies the symmetry of the tensor $\vec{\vec{T}}$ which can be decomposed by subtracting the hydrostatic part:

$$\vec{\vec{T}} = -p\vec{\vec{I}} + \vec{\vec{\tau}} \tag{3.16}$$

where I is the identical matrix, and $\vec{\vec{\tau}}$ is better known as the viscous forces tensor. Considering water and air as Newtonian fluids, $\vec{\vec{\tau}}$ is linear and isotropic on the deformation velocity tensor $\vec{\vec{S}}$:

$$\vec{\vec{\tau}} = 2\mu\vec{\vec{S}} + \lambda\cancelto{}{\nabla \cdot \vec{u}}\vec{\vec{I}} \tag{3.17}$$

Where:

$$\vec{\vec{S}} = \frac{1}{2}(\nabla\vec{u} + \nabla^T\vec{u}) \tag{3.18}$$

indicating as μ and λ respectively the dynamic viscosity coefficient and the second viscosity coefficient; due to the incompressible fluid hypothesis its related term disappear. Moreover, due to the absence of external electromagnetic fields interacting with the fluid, gravitational forces are kept ignoring density gradients. In fact, the Richardson number does not exceed a scale of 10^{-2} for the flow conditions of interest; hence convective effects overtake buoyancy and its associated term $\beta(\vartheta - \vartheta_0)$ known as Boussinesq fluid assumption is neglected. Therefore it is:

$$\frac{\partial \rho\vec{u}}{\partial t} + \nabla \cdot (\rho\vec{u} \cdot \vec{u} + p\vec{\vec{I}} - 2\mu\vec{\vec{S}}) = \rho\vec{g} \tag{3.19}$$

The experimental temperature conditions are far from those where Maxwell-Cattaneo hypothesis shows considerable effects on the thermal field, therefore the Fourier law is still acceptable. The thermal conductivity χ of the fluid is assumed isotropic in our cases

$$\nabla \cdot \vec{q} = -\chi\Delta\vartheta \tag{3.20}$$

where ϑ is the temperature. Furthermore the absence of thermal sources is assumed in our cases. By introducing the total specific entalpy as:

$$h = E + \frac{p}{\rho} \tag{3.21}$$

The energy balance equation can be rewritten as:

$$\frac{\partial \rho E}{\partial t} + \nabla \cdot (\rho h\vec{u} - \vec{u} \cdot \vec{\vec{\tau}} - \chi\nabla\vartheta) = \rho(\vec{g} \cdot \vec{u}) \tag{3.22}$$

Even with the assumed simplifications, the energy balance would introduce high non-linearity when the kinetic contribution is taken in account. On the other hand the mechanical terms in the overall balance would not give a relevant contribution to the flow field since, from a macroscopic point of view, thermal and kinetic energy are interfaced mainly on the viscous dissipation scales. Experience has well shown that in most cases, the temperature field would not be changed by ignoring the internal exchanges between thermal and mechanical energy. It is then possible to eliminate the last contributions, and then substitute the total energy balance with the conservation of the internal energy by considering $e = c_p\vartheta$.

$$\rho c_p \left[\frac{\partial \vartheta}{\partial t} + \vec{u}\nabla\vartheta\right] - \chi\Delta\vartheta = \frac{dP}{dt} \tag{3.23}$$

It is important to underline that the term P indicates the thermodinamical pressure, which is not influenced directly from the flow field despite the pressure term arising from the hydrostatic part of internal forces tensor. This definition matches with the incompressibility hypothesis, through the fact that small temperature variations would not induce changes in the static pressure and in the overall flow field.

In conclusion the simplified equations treated for the numerical studies are here summarised:

$$\nabla \cdot \vec{u} = 0 \tag{3.24}$$

$$\frac{\partial \rho\vec{u}}{\partial t} + \nabla \cdot [\rho\vec{u} \cdot \vec{u} + p\vec{\vec{I}} - \mu(\nabla\vec{u} + \nabla\vec{u}^T)] = \rho\vec{g} \tag{3.25}$$

$$\rho c_p \left[\frac{\partial \vartheta}{\partial t} + \vec{u}\nabla\vartheta\right] - \chi\Delta\vartheta = \frac{dP}{dt} \tag{3.26}$$

Even though the simplifications introduced by assuming the above physical hypotheses, from a computational point of view, directly solving Navier-Stokes equations, nowadays still represents a too large effort for most of the industrial configurations of interest, and this approach, also known as Direct Numerical Simulation (*DNS*) is used only for very simple geometries where the turbulent Reynolds number[1]) (Re_t) does not exceed 800. This limit over the last decades has been an incentive for the development of other methods to numerically solve thermal fluid-dynamics-problems. The choice that has shown the most promising results is to manipulate the equations with averaging operators and this is done within the perspective of neglecting some turbulence details and giving the possibility to decrease time and space discretization effort. On the other hand the lost information is required to be reintroduced by modeling terms which arise after the averaging operations. Depending on the average operators and on the assumptions made for turbulence contributions terms, turbulence models can achieve a good description of the overall flow field, limiting the CPU time required for complex geometries and high Reynolds configurations.

Moreover, the perspective to avoid considerable refinments in the meshing near the boundary walls has been taken as one of the "must" to achieve results in reasonable time. To refine the wall boundaries layers as the Sub-Grid-Stress (*SGS*) of LES would require (see below), while using an explicit time scheme, would represent an overall lowering of the diffusion timestep to keep the Courant Friedrichs Lewy stability conditions. In fact, according with the cell Fourier number, the stability timestep decreases with a square power of the mean lenght of the smaller volume. In our cases, to provide an order of magnitude, a mesh element with a main lenght under the scale of the millimiter would mean an advancement timestep limited to be less than 10^{-8} s.

Therefore, wall law has been used in order to achieve reasonable details of the flow behaviour near the boundary walls, keeping the calculation time required under limitations imposed by the work.

---

[1] The turbulent Reynolds number is defined as a power of the ratio between the largest (L) and the Kolmogorov (η) vortex lenght scale. $Re_t = (\frac{L}{\eta})^{4/3}$

In particular, for the near wall modeling, the Reichardt law was chosen, since it includes with good approximations all the subzones required to describe the velocity profile near the wall in a continuous and derivable function.

$$u^+ = \frac{1}{\kappa}\ln\left(1+\kappa y^+\right) + 7.8\left[1 - exp\left(-\frac{y^+}{11}\right) - \frac{y^+}{11}exp\left(-\frac{1}{3}y^+\right)\right] \tag{3.27}$$

where κ stands for the Von Karman constant set to a value of 0.41

3.1.2 Turbulence modeling (statistical (k-ε) and LES)

In the RANS approach the instantaneous scalar ϕ is written as summation of a time averaged value and a fluctuation contribute:

$$\phi(t) = \overline{\phi}(t) + \phi'(t) \tag{3.28}$$

The time average operato is assumed as:

$$\overline{\phi}(t) = \frac{1}{\delta t}\int_t^{t+\delta t} \phi(t)(\tau)d\tau \tag{3.29}$$

$$\int_t^{t+\delta t} \phi'(t)(\tau)d\tau = 0 \tag{3.30}$$

With these definitions the choice of the time interval δt adopted must be made in order to ignore turbulent fluctuations and at the same time capturing the mean term variation of average quantities. By applying the time average operators to the N-S equations, the internal energy and mass balance equations keep formally the same structure while it is interesting to take a look to the momentum balance equation, in which the non linearity of the convective term leads to the presence of the known Reynolds stress tensor $\vec{\vec{\tau}}_{Re}$:

$$\frac{\partial \rho\overline{\vec{u}}}{\partial t} + \nabla\cdot\left(\rho\overline{\overline{\vec{u}}\,\overline{\vec{u}}}\right) = \nabla\cdot\left(\vec{\vec{\tau}} - p\vec{\vec{I}}\right) + \rho\vec{g} - \nabla\cdot\left(\rho\overline{\vec{u}'\vec{u}'}\right) \tag{3.31}$$

$$\vec{\vec{\tau}}_{Re} = -\rho\overline{\vec{u}'\vec{u}'} \tag{3.32}$$

For evaluating this term, the Boussinesq hyphothesis is then introduced in TrioCFD:

$$\vec{\vec{\tau}}_{Reij} = \rho\nu_t\left(\frac{\partial\overline{u}_i}{\partial x_j} + \frac{\partial\overline{u}_j}{\partial x_i}\right) \tag{3.33}$$

This formulation involves the use of the quantity ν_t known as the turbulent viscosity, which must be calculated introducing specific models and additional equations.

The model adopted in the statistical approach uses the transport equations for the kinetic turbulent energy k and its dissipation rate ε

$$\frac{\partial k}{\partial t} + \vec{u}\cdot\nabla k = \nabla\cdot\left(\frac{\nu_t}{\sigma_k}\nabla k\right) - \varepsilon + P \tag{3.34}$$

$$\frac{\partial \varepsilon}{\partial t} + \vec{u}\cdot\nabla\varepsilon = \nabla\cdot\left(\frac{\nu_t}{\sigma_\varepsilon}\nabla\varepsilon\right) - C_{\varepsilon 2}\frac{\varepsilon^2}{k} + C_{\varepsilon 1}P\frac{\varepsilon}{k} \tag{3.35}$$

where the production of turbulent kinetic energy (P) is written as:

$$P = -\overline{u_i'u_j'}\frac{\partial\overline{u}_i}{\partial x_j}; \tag{3.36}$$

After the resolution of these equations the turbulent viscosity is then evaluated using the relationship:

$$\nu_t = C_\mu \frac{k^2}{\varepsilon} \tag{3.37}$$

An analogous term to the Reynolds stress tensor arises when applying the average operator for the internal energy balance, giving then a turbulent contribution on the heat transfer, this terms is treated using the same approach by adopting the turbulent thermal diffusivity (α_t):

$$\rho c_p \overline{\vartheta' \vec{u}'} = \rho c_p \alpha_t \nabla \overline{\vartheta} \tag{3.38}$$

By using this definition, since the structural vortices that transport momentum are the same as those transporting the internal energy, it is possible to evaluate the turbulent thermal diffusivity considering the turbulent Prandtl number (Pr_t):

$$\alpha_t = \frac{\nu_t}{Pr_t} \tag{3.39}$$

Details about the standard values of constants applied in *TrioCFD* are reported in the following Table **??**

C_μ	σ_k	σ_ε	$C_{\varepsilon 1}$	$C_{\varepsilon 2}$	Pr_t
0.09	1.0	1.3	1.44	1.92	0.9

Table 3.1: Transport equation constants

As already underlined at the beginning of the section, the use of the Reynolds averaged equations, through the time filtering operations, cannot describe the detailed behaviouur of the turbulent component of each scalar. This is mainly caused by the need to close the problem by evaluating the Reynolds stress tensor, which implies a direct influence on the turbulence behaviour coming from the time averaged scalars. Therefore the RANS approach represents just a first attempt technique in order to correctly evaluate temperature fluctuations driven by the turbulent conditions of jets in cross flow.

A more accurate study must then be conducted using a model that is able to describe the turbulence by directly evaluating turbulent fluctuations using a model that does not subordinate the actual unsteady behaviour of the flow to its time average.

The LES approach provides this possibility, since it allows to directly solve the large turbulence scales accepting a larger effort from a computational point of view, by simulating the smaller scales using subgrid models.

The LES spatial filtering operation on a volume V is defined as:

$$\overline{\phi(\vec{x}, t)} = \int_V G(\vec{x} - \vec{x}', \Delta) \phi(\vec{x}', t) dV' \tag{3.40}$$

where G, also known as filter function is associated to the cut-off lenght Δ that establish the limit between scales that are solved or modeled.

This operation gives in in apparent formal similarity with the Reynolds time average to a decomposition of the scalar ϕ

$$\phi(\vec{x}, t) = \overline{\phi}(\vec{x}, t) + \phi'(\vec{x}, t) \tag{3.41}$$

However now, the meaning of the average is purely spatial, allowing the construction of the scalar ϕ as a filtered component and subgrid one that must be evaluated their corresponding models.

When such kind of operation is made on the Navier-Stokes equations, once again, the non linear advective term $\overline{\vec{u}\vec{u}}$ of the momentum balance represents the difficult term requires models to re-integrate those informations that have been lost during filtering operations.

On developing the averaged term $\overline{u_i u_j}$ we obtain:

$$\overline{u_i u_j} = \overline{u}_i \overline{u}_j + \underbrace{(\overline{\overline{u}_i \overline{u}_j} - \overline{u_i u_j})}_{L_{ij}} + \underbrace{(\overline{\overline{u}_i u'_j} + \overline{\overline{u}_j u'_i})}_{C_{ij}} + \underbrace{\overline{u'_i u'_j}}_{R_{ij}} \tag{3.42}$$

Each tensor described in the latest equation represent how the turbulence scales interacts, respectively L_{ij} describes interactions among large scales, C_{ij} gives informations on how large and small scales are related and the R_{ij} which is named Reynolds Sub-Grid-Scale tensor directly commands the interaction behaviour between the smaller scales.

Therefore the chosen modelization of the last term must be done to achieve the closure of the problem. Another time, the concept of turbulent viscosity is claimed to play a role on achieving a description on the fluctuations cutted out by the filtering operations. In analogy with the Boussinesq hypothesis R_{ij} is defined as:

$$R_{ij} = \nu_t \left(\frac{\partial \overline{u}_i}{\partial x_j} + \frac{\partial \overline{u}_j}{\partial x_i} \right) \tag{3.43}$$

With the aim to better reproduce the transition from laminar to turbulent flow and then obtain a correct wall-asymptotic variation of the SGS viscosity, the Wall Adaptive Local Eddy-viscosity (WALE) model has been used. This model offers all the advantages of the Dynamic Smagorinsky model without requiring explicit filtering operations. The WALE model turbulent viscosity implemented in *TrioCFD* obeys the following equations:

$$\nu_t = \Delta_s^2 \frac{(S_{ij}^d S_{ij}^d)^{\frac{3}{2}}}{(\overline{S}_{ij} \overline{S}_{ij})^{\frac{5}{2}} + (S_{ij}^d S_{ij}^d)^{\frac{5}{4}} + 10^{-6}}; \tag{3.44}$$

$$\overline{g}_{ij} = \frac{\partial \overline{u}_i}{\partial x_j} \tag{3.45}$$

$$\Delta_s = C_w V^{\frac{1}{3}} \tag{3.46}$$

$$\overline{S}_{ij} = \frac{1}{2}(\overline{g}_{ij} + \overline{g}_{ji}); \tag{3.47}$$

$$S_{ij}^d = \frac{1}{2}(\overline{g}_{ij}^2 + \overline{g}_{ji}^2) - \frac{1}{3}\delta_{ij}\overline{g}_{kk}^2 \tag{3.48}$$

The C_w coefficient is set to be 0.5

It is important to underline the fact that, since the filtering operator is based on the volume of each element, results obtained from LES calculations cannot be fully independent on the spatial discretization adopted. Therefore, mesh convergency has to been interpreted as a qualitative concept.

3.2 Discretization of the N-S equations

The numerical model is based on a finite volume method. The conservation equations are used in conservative form and are integrated over a control volume Ω, which is bounded by the surface Σ_ω. Applying Gauss theorem leads to the following equations set for turbulent flow (notice that the over bar is referred to the applied turbulence model averaging operator):

$$\int_{\Sigma_\omega} \overline{\vec{u}} \cdot \vec{n} d\sigma = 0 \tag{3.49}$$

$$\int_\Omega \frac{\partial \overline{\vec{u}}}{\partial t} d\omega + \int_{\Sigma_\omega} \overline{\vec{u}}(\overline{\vec{u}} \cdot \vec{n}) d\sigma = \int_{\Sigma_\omega} (\nu + \nu_t)(\nabla \overline{\vec{u}} + \nabla \overline{\vec{u}}^T) \cdot \vec{n} d\sigma + \int_{\Sigma_\omega} P \vec{n} d\sigma + \int_\Omega \rho \vec{g} d\omega \qquad (3.50)$$

3.2.1 Space discretization

The calculation domains have been discretized using tetrahedral elements. These have been arranged in both structured and unstructured forms. The structured mesh has been created by generating a previous hexahedral grid, with lenghts defined from geometrical lines disposed on the overall calculation domain, in order to locally control the overall size of the elements. Once this grid is computed, all the elements have been then split in tetrahedrons. By following these operations, the generated mesh ensures the presence of at least one of the element faces to be oriented perpendicularly to the main flow direction, hence numerical diffusion effects are reduced. The criteria for generating the unstructured mesh have been applied through out the whole domain, still follow the local dimensions dictated from the geometrical lines, but since it miss the primitive hexahedrons structure, the elements does not follow a uniform pattern, therefore diffusive effects are less contained whenever the mean size of the elements is larger.

TrioCFD uses a finite volume based element (VEF) approach, which is an hybrid between a pure finite element method and a finite volume method. This tecnique, named VEFPreP1B, integrates in conservative form all the balance equations over the control volumes belonging to the domain. Both vector and scalar quantities are calculated in the center of the faces, the pressure is also discretized along vertices and volume center of gravity as shown in Fig **??**.

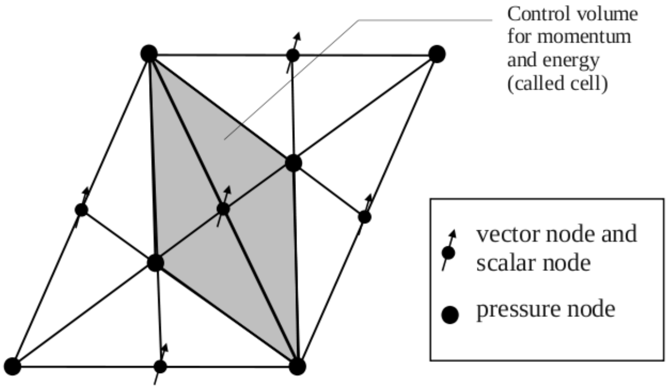

Figure 3.2: Location of pressure, scalar and vector nodes

Along this staggered mesh structure, the unknown values are expressed using the analogue function of a first order polynomials for 3D cases ($\psi : \mathbb{R}^3 \rightarrow \mathbb{R}$) as shape-functions [2]. The VEFPreP1B assumes constant field gradient for both face- and node-centered elements (P1NC-P1Bulle).

To discuss details of how the equations have been discretized a brief review on the convective schemes adopted will be given.

In a finite volume formulation, each node N_i may be located at the center of one face, in one of the vertices or on the center of gravity of an element (following Fig. **??** we will name them respectively F_i, S_i and C_i); all of them belongs to a control volume Ω (indicated in grey in Fig. **??** and bounded by the dotted line in Fig. **??**). This volume is bounded by the faces of area f_{ij} and the velocity computed at its related node F_i will be named u_{F_i}, while the scalar

---

[2] In literature the ψ function is often named "bubble function"

associated with the node F_i will be ϕ_{F_i}.
Using this definitions the convective fluxes are discretized as:

$$\int_{\Sigma_\Omega} \phi \vec{u} \cdot \vec{n} d\sigma = \sum_{j=1}^{4} \phi_{F_i} u_{F_i} f_{ij} \tag{3.51}$$

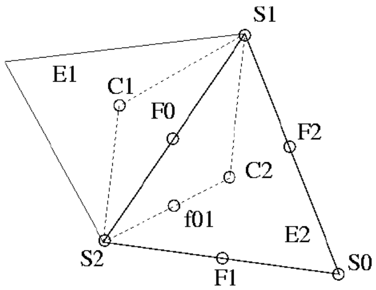

Figure 3.3: Nomenclature and location of nodes and faces of a 2D element

Depending on the convective scheme, the quantity under summation is expressed in different ways:

- For the Upwind scheme the quantity ϕ is evaluated as:

$$\phi_{f_{0_1}} = \phi_{F_0} \qquad if \qquad u_{f_{0_1}} f_{0_1} > 0 \tag{3.52}$$

$$\phi_{f_{0_1}} = \phi_{F_1} \qquad if \qquad u_{f_{0_1}} f_{0_1} < 0 \tag{3.53}$$

- For the Monotone Upstream-Centred Scheme for Convective flows ($MUSCL$) the expression is built to ensure a second order accuracy, following fig. **??** the expression for the flux over the face f_{0_1} is given by an interpolation of the adjacent values:

$$u_{f_{0_1}} \phi_{f_{0_1}} f_{0_1} = \frac{[(u_{S_2} + u_{C_2})(\phi_{S_2} + \phi_{C_2}) + (u_{S_2} + u_{S_1})(\phi_{S_2} + \phi_{S_1}) + (u_{C_2} + u_{S_1})(\phi_{C_2} + \phi_{S_1})]}{12} f_{0_1} \tag{3.54}$$

  ϕ in this case is evaluated from a reconstructed upwind quantity which depends on the flow direction and its gradient, analogously as for the upwind scheme. The formulations given for the gradient term follow different slope limiter formulations which can be chosen via script from the TrioCFD code.

Whenever it is used a finite element formulation, the convection scheme adopted in our cases is an hybrid between second order centered and upwind total variation diminishing method. In this method, a limiter is integrated togheter with the convective scheme, bounding physically the transported quantities. Each scheme is applied and then overlapped with a weight factor named α chosen by the user. A detailed dissertation about of this method is described by Kuzmin and Turek [**?**].

For diffusion terms, the relate scheme adopted is a second order centered scheme based on the finite volume approach [**?**].

3.2.2 Time discretization

Euler implicit and second order Adam Bashfort schemes are adopted for the time discretization, respectevely for RANS and LES calculations. The first one ensure good stability of the solution, and the higher computational costs required are compensated by a lower number of elements generally needed in the calculation domain by RANS equations The time discretization should adaot its accuracy dependently on the spatial discretization, which leads to evaluate explicit multi-step methods as more suitable for LES calculations. Differently from the spatial discretization, within each equation can be treaten with its own scheme, the time discretization is unic for the whole equation set chosen by the user.

Hereafter a short description of the two schemes is provided.

For the implicit Euler scheme, at each time-step the unknown $\phi^{t+\Delta t}$ is calculated:

$$\phi^{t+\Delta t} = \phi^t + \Delta t \frac{\partial \phi}{\partial t}\bigg|_{t+\Delta_t} \tag{3.55}$$

Where $\frac{\partial \phi}{\partial t}\Big|_{t+\Delta_t}$ is evaluated by calculating an approximation of $\phi^{t+\Delta t}$ using the explicit euler scheme:

$$\phi^{t+\Delta t} = \phi^t + \Delta t \frac{\partial \phi}{\partial t}\bigg|_{t} \tag{3.56}$$

The second order Adam-Bashfort scheme is an explicit multi-step method which computes the values $\phi^{t+\Delta t}$ exploiting the knowledge of two older values ϕ^t and $\phi^{t-\Delta t}$. In this case the formulation is the following:

$$\phi^{t+\Delta t} = \phi^t + \frac{3}{2}\Delta t \frac{\partial \phi}{\partial t}\bigg|_{t} - \frac{1}{2}\Delta t \frac{\partial \phi}{\partial t}\bigg|_{t-\Delta t} \tag{3.57}$$

The first step needed to find an extimation of $\frac{\partial \phi}{\partial t}\Big|_{t}$ is resolved using an Euler explicit step.

3.3 Solution method

Nearly all numerical methods for solving Navier Stokes equations in terms of the primitive variables velocity and pressure use a fractional step approach. Some approximation to the momentum equation is advanced to determine the velocity u or a provisional velocity, and then an elliptic equation is solved that enforces the divergence constraint given by the mass balance for incompressible flow to determines the pressure field. Some methods solve directly for the pressure in the elliptic step others solve for an auxiliary variable related to the pressure. Methods are often categorized as "pressure-Poisson" or "projection" methods based on which form of the elliptic constraint equation is being used. A distinguishing feature of projection methods is that the velocity field is forced to satisfy a discrete divergence constraint at the end of each time step.

3.3.1 Projection method

The projection method used in Trio CFD by default is the SOLA[3] alghoritm, published by ref hirt in 1988 at Los Alamos.

At the first step the alghoritm provides a velocity field wich strictly satisfies the continuity equations, then, it guesses a pressure field which obeys to a zero divergence of the velocity field time derivative

---

[3] SOLA stands for SOLution Alghoritm

By writing the matricial form of the discretized Navier stokes we obtain:

$$M \cdot \frac{\partial \vec{u}^t}{\partial t} = A \cdot \vec{u}^t + L(\vec{u}^t) + B^T p^{t+1} + \rho \vec{g} \tag{3.58}$$

$$B \cdot \vec{u}^{t+1} = 0 \tag{3.59}$$

where:

- A is the diffusion matricial operator
- L(u) is the convective matricial operator
- B is the divergence operator
- M is the diagonal mass operator

Multiplying the left hand side of the momentum equation by BM^{-1} and assuming that $B\frac{\partial \vec{u}^t}{\partial t} = 0$ leads to :

$$BM^{-1}(A \cdot \vec{u}^t + L(\vec{u}^t) \cdot \vec{u}^t + B^T p^{t+1}) = BM^{-1}\rho \vec{g} \tag{3.60}$$

Thus, it is possible to obtain the momentum equation in the form

$$BM^{-1}B^T p^{t+1} = BM^{-1}[\rho \vec{g} - (A \cdot \vec{u}^t + L(\vec{u}^t) \cdot \vec{u}^t)] \tag{3.61}$$

which is the one used for obtaining the pressure field guessed by the alghorithm

3.3.2 Algorithm of the semi-implicit scheme

If one adopt the described algorithm using fractional time step using an explicit method, a semi-implicit scheme for the Navier Stokes equation would be:

$$\nabla \vec{u}^{t+1} = 0 \tag{3.62}$$

$$\frac{\vec{u}^{t+1} - \vec{u}^t}{\Delta t} + \nabla \cdot (\vec{u}^t \vec{u}^t) = -\nabla p^{t+1} + \nabla \vec{\tau}^{t+1} + \rho \vec{g} \tag{3.63}$$

$$\frac{\vartheta^{t+1} - \vartheta^t}{\Delta t} + \nabla \cdot (\vec{u}^t \vartheta) = -\nabla \vec{q}^{t+1} \tag{3.64}$$

The main unknowns are updated as soon as they are available for beeing used in the other equations, while the equations related to the turbulence model (e.g. wall functions, transport of k and ε, SGS) are extimated using values of variable at the beginning of the time-step.

Whenever a fully implicit scheme is used the evaluations of the convective and diffusion terms are shifted to time t+1, while multistep methods exploit the use of fractional time-step to compute values as t+1 as a weighted extrapolation of the contributions given for each sub-step.

Chapter4

Computational analysis of the experiments

In this section the practical aspects of the calculations carried out will be discussed. Both the experimental test sections have been studied with statistical and LES approaches. The first it is used as an evaluation instrument to correctly predict, with low computational costs, the settings required for the spatial discretization of the LES approach. This step is made in order to evaluate the Taylor lenght scale required for each test case. The numerical methods described in the latter section are applied in this context; a description of the spatial discretization of the domain and all the settings regarding the numerical schemes adopted are described . Finally the meaningful numerical solutions are evaluated and a comparison between the experimental data and the CFD results is shown.

4.1 Vattenfall experiment

The geometrical domain of the Vattenfall tee junction test section has been modeled using the Geometry tool of the software SALOME 7.7.1 respecting the dimensions given by the experimenters [**?**]; since the turbulence characteristics vary through the whole domain, the geometry has been furthermore divided into four sections (Fig. **??**) in order to apply a proper spatial distribution of the mesh elements. These are listed as:

1. the upstream part of the main pipe (in blue); this zone represent an important element for the whole calculation. Since the flow behaviour on the jet exit sections plays a determinant role in the overall vorticity field; it is extremely important to ensure that the code represents accurately the reference boundaries.

2. the upstream part of the branch pipe (in red); this part has similar purposes as the previous one; it must be reminded that on these test conditions, the jet flow is not in turbulent regime.

3. the core of the mixing zone, where cold and hot fluid meet each (in green); this region bounds the potential region and conserves the scalars transported as long as the smalller mixing layer vortices keep small dimensions.

4. the first downstream part of the main pipe (in orange); this zone provides the turbulent structure evolution, both in the inner and in the outer surfaces of the jet; this part of the domain affect the tracking vortices growth as well as the larger mixing layer structures; at the r ratio given by the experiment, the deflection zone is expected to be found in this sub part of the domain (in orange)

5. the second downstream part of the main pipe, where the flows is fully developed and mixed (in yellow); this region should respect the lenght of the large scale turbulence.

Since the nature of advection and diffusion phenomena vary in each of these parts, local refinements of the domain mesh allow to vary locally the solution accuracy, which is increased in those zones where the jet turbulent structures are involved in thermal fatigue. It must be underlined that this choice still represents a compromise between CPU time required, RAM available and solution accuracy.

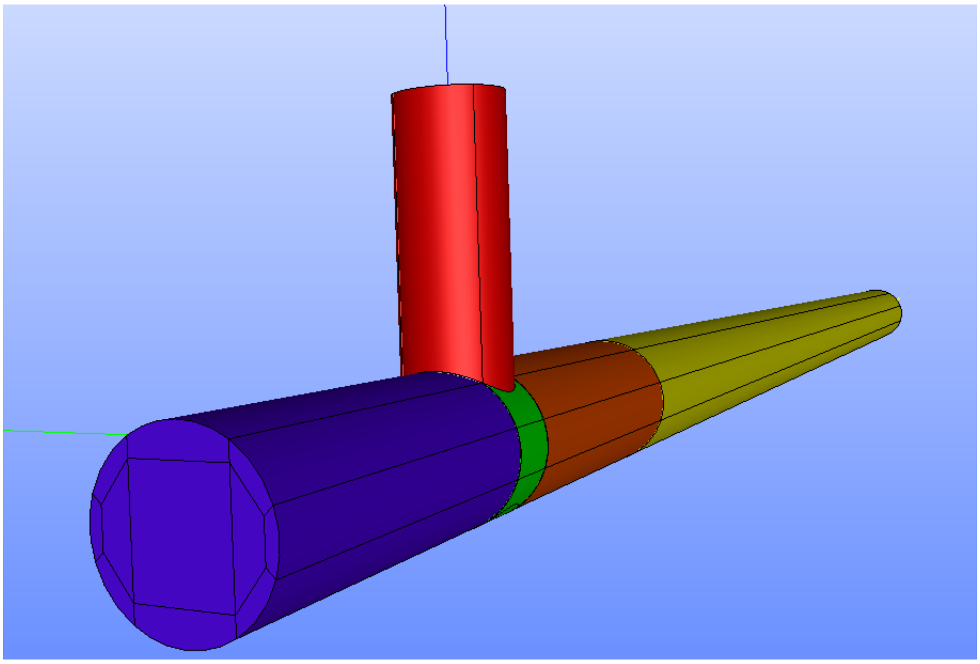

Figure 4.1: Vattenfall Tee Junction domain sub-parts

4.1.1 RANS approach

In the statistical model, the RANS equation are used. These are coupled with the Temperature convection-diffusion equation, the trasport equation of the kinetic turbulent energy (k) and its dissipation rate (ε). In tables **??** and **??**, details on the $k-\varepsilon$ calculations are given.

Spatial discretization scheme	VEFPreP1B on Tetrahedral meshes
Time discretization scheme	Euler Implicit
Fluid physical properties	
$\mu\ \left[\frac{Ns}{m^2}\right]$	$9.34 \cdot 10^{-4}$
$\rho\ \left[\frac{kg}{m^3}\right]$	996.86
$\lambda\ \left[\frac{W}{m^2K}\right]$	0.61
$C_p\ \left[\frac{J}{KgK}\right]$	4186.62
$\beta\ \left[\frac{1}{K}\right]$	$2.55 \cdot 10^{-4}$

Table 4.1: Fluid properties used in the model

Navier Stokes equations	
Pressure Solver	PCG with SSOR
Convective scheme	2^{nd} order MUSCL
Diffusive scheme	Second Order Centered
Turbulence model	RANS $k-\varepsilon$
Transport $k-\varepsilon$ equations	
Convective scheme	Upwind
Diffusion scheme	Second Order Centered
Wall Turbulence Modelization	Reichardt Law
Convection Diffusion Temperature equation	
Convective scheme	Upwind
Diffusion scheme	Second Order Centered
Turbulence	Turbulent Prandtl number

Table 4.2: Numerical schemes adopted in the statistical model

4.1.1.1 Meshing

Two mesh arrangements have been tested in order to observe if there is a considerable impact of the mesh orientation on the final solutions; an example of these structures is given in Fig. **??**

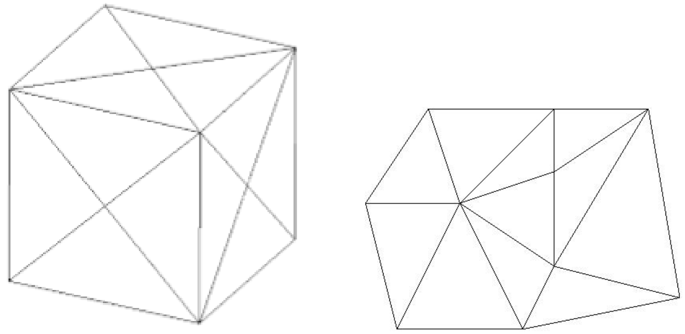

(a) Example of structured mesh (b) Example of unstructured mesh

Figure 4.2: Examples of 3D structured and unstructured arrangments

Both the structured and unstructured arrangements presents weakness and positive aspects.

In the structured arrangement (Fig. **??**), numerical diffusion effects are expected to be lowered, expecially in the upstream parts of the pipes, thanks to the fact that each element has one of the faces normally oriented with respect to the mean flow velocity vector. On the other hand, this alignement can intensify the advection terms of the equations through the main lenght directions. This would give solutions which can be directionally conditioned along the major elements dimensions. This fact is not negative wherever the flow is developed and mostly onedirectional, but it can have an undesired influence on those parts where this condition is not verified (i.e. the mixing zone). Thereby, to minimize such kind of effect, the aspect ratio of these elements must be kept as close as possible to 1. The element orthogonal quality and skeweness distributions has been taken into account; the mesh have been iteratively modified until the 80 % of the overall population of nodes verifies a skeweness lower than 0.25 and an orthogonal quality larger than 0.7.

The unstructured arrangement (Fig. **??** totally avoids these conditioning effects on the solution, but a price is paid requiring a higher refinement in order to bound numerical diffusion effects.

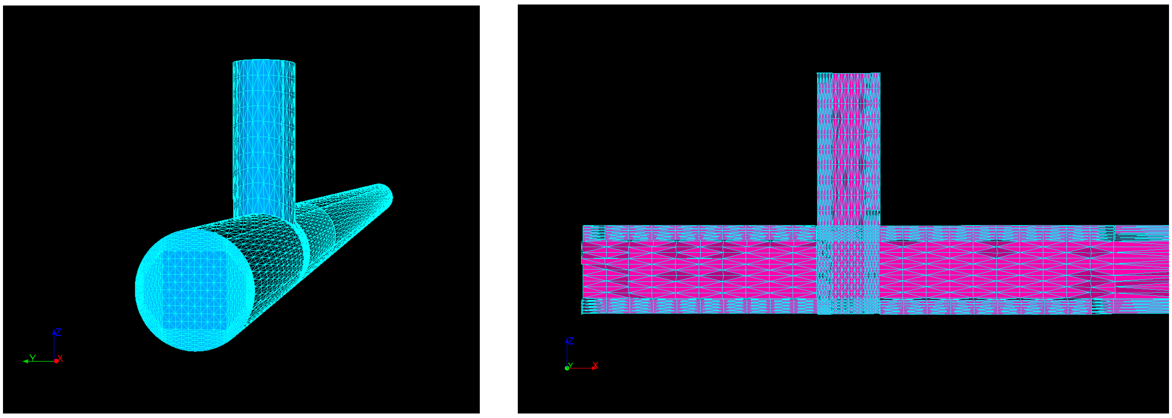
(a) External view

(b) Longitudinal Cut

Figure 4.3: Vattenfall tee junction structured mesh example

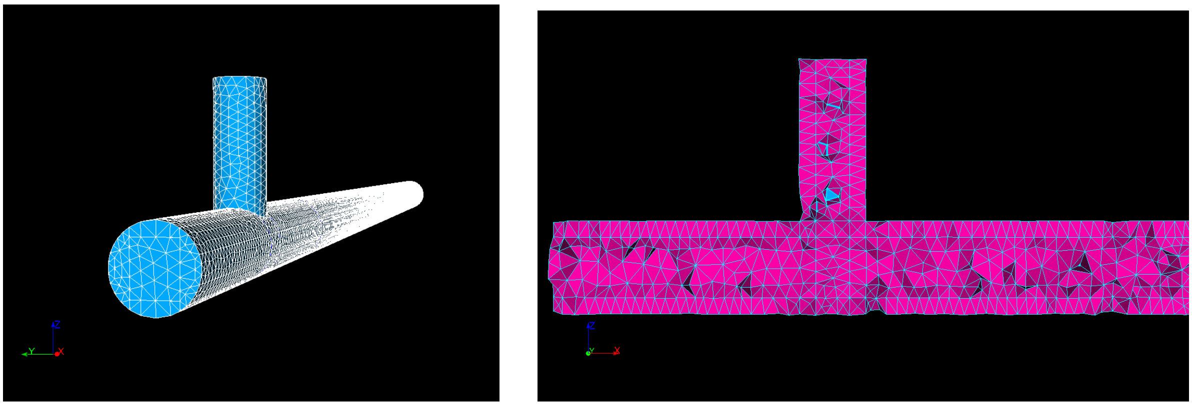
(a) External view

(b) Longitudinal Cut

Figure 4.4: Vattenfall tee junction unstructured mesh example

Further explanations on the mesh impact related to this test case will be examined in the comments to the obtained results.

Keeping the same ratio between the number of elements generated on each geometrical line, different mesh refinments have been tested in order to achieve mesh convergency. In table **??** the tested mesh characteristics used with RANS/$k-\varepsilon$ model are listed.

Mesh No.	**Mesh Structure**	**Number of elements**
1	Structured	765000
2	Unstructured	806988
3	Unstructured	5284484
4	Structured	6019161

Table 4.3: RANS/$k-\varepsilon$ meshes

Elements largest angles are between 60° and 100°.

4.1.1.2 Boundary conditions

The inlet velocities profiles have been set coherently with the data collected during the experimental campaign (Fig. **??**) To set directly the raw data in the boundary inlet would not be a

suitable choice. In TrioCFD the user specifies boundary conditions by defining a field. There are several options than can be adopted in the code to obtain the desired result (e.g. matrixes, input files, analytic laws etc.), but in all cases the alghoritm discretizes the boundary instructions and create a first order interpolation based on the nodes disposition taken from the mesh file. This process can lead to a spatial mismatch of the boundary conditions; however, a good spatial discretization would reduce the errors introduced by this effect.
To increase the approximation quality and avoid the raw linear interpolation given by the code algorithm, the data provided have been fitted with polynomial functions in order to lower as far as possible discrepancies in terms of mass flowrate between the calculations and the experimental conditions.

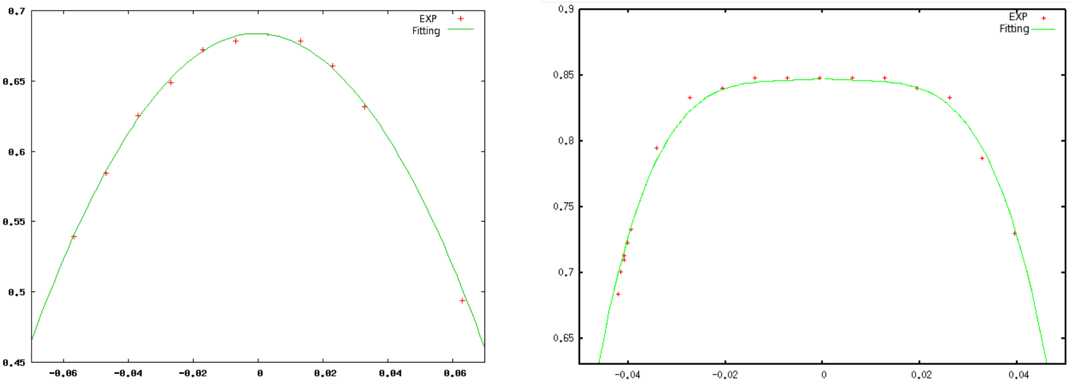

(a) Cold Inlet Velocity Fitting

(b) Hot Inlet Velocity Fitting

Figure 4.5: Channels inlet velocity fitting

The polynomial functions adopted for the fitting shown in Fig. **??** are respectively of second and fourth order. Due to the assumption of radial symmetry, these 1D profiles have been extended in 2D for the whole inlet sections (Fig. **??**).

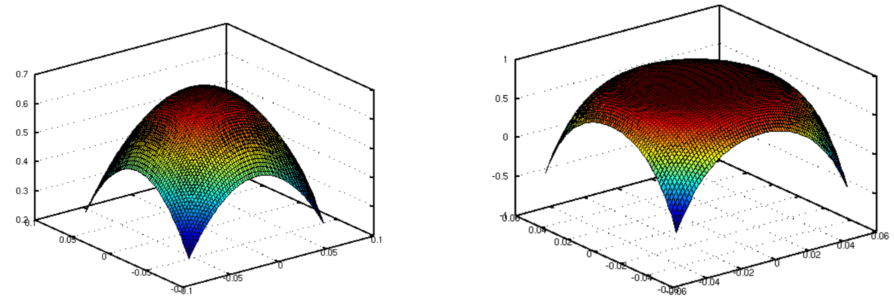

(a) Cold Inlet Velocity Profile

(b) Hot Inlet Velocity Profile

Figure 4.6: 2D boundary velocity profiles distribution

In order to compute the volumetric flow rate obtained from this approximation the fitting functions have been analitically integrated.

$$C \int_0^{2\pi} \int_0^R U_{bulk}(ar^4 + br^3 + cr^2 + dr + e) r dr d\theta \tag{4.1}$$

The coefficient C has been conveniently choosen in order to reduce the differences between the flowrate given by the fitting and the experimental data. In table **??** the parameters used in this operation are given.

	a	b	c	d	e	C	Flowrate (exp) $\left[\frac{l}{s}\right]$	Flowrate (fit) $\left[\frac{l}{s}\right]$
Cold Inlet	0.00	0.00	-45.05	-0.03	0.68	1.023	9	8.998
Hot Inlet	$-5.59 \cdot 10^4$	205.68	13.25	-0.27	0.85	1.021	6	5.999

Table 4.4: Polynomial fitting results

In order to assure marked diagonal dominance of the matrix treated by the pressure solver, a zero pressure has been set on the outlet section.

The turbulence inlet levels, represented by the root mean square of the velocity measurements, have been introduced as boundary conditions by specifying the turbulent kinetic energy on both the inlet sections for the $k - \varepsilon$ calculations performed.
The isotropic and homogeneous turbulence hypothesis is adopted; this assumption is justified by the presence of the stagnation chamber located upstream the section in the experimental test rig. Hence the turbulent kinetic energy k and its dissipation rate ε are obtained via:

$$k = \frac{3}{2} U_{rms}^2; \qquad \varepsilon = C_\mu \frac{100 k^{\frac{3}{2}}}{7 D_h} \tag{4.2}$$

where $C_\mu = 0.09$ is a proportional factor involved in the turbulent viscosity extimation in the $k - \varepsilon$ model implemented in *TrioCFD*. These two parameters are averaged in space in order to adopt a constant value for the whole section (see table **??**.

	$k \left[\frac{m^2}{s^2}\right]$	$\varepsilon \left[\frac{m^2}{s^3}\right]$
Cold Inlet	0.00427851	0.00925108
Hot Inlet	0.00672737	0.0412895

Table 4.5: Inlet turbulence conditions

4.1.1.3 Comparison with experimental data

By comparing the results obtained from the $k - \varepsilon$ calculations it is possible to see, as predicted, that time averaged profiles generally follows coherently the mean behaviour of the experimental values. Fig. **??** shows a view of the temperature field obtained from the analysis.

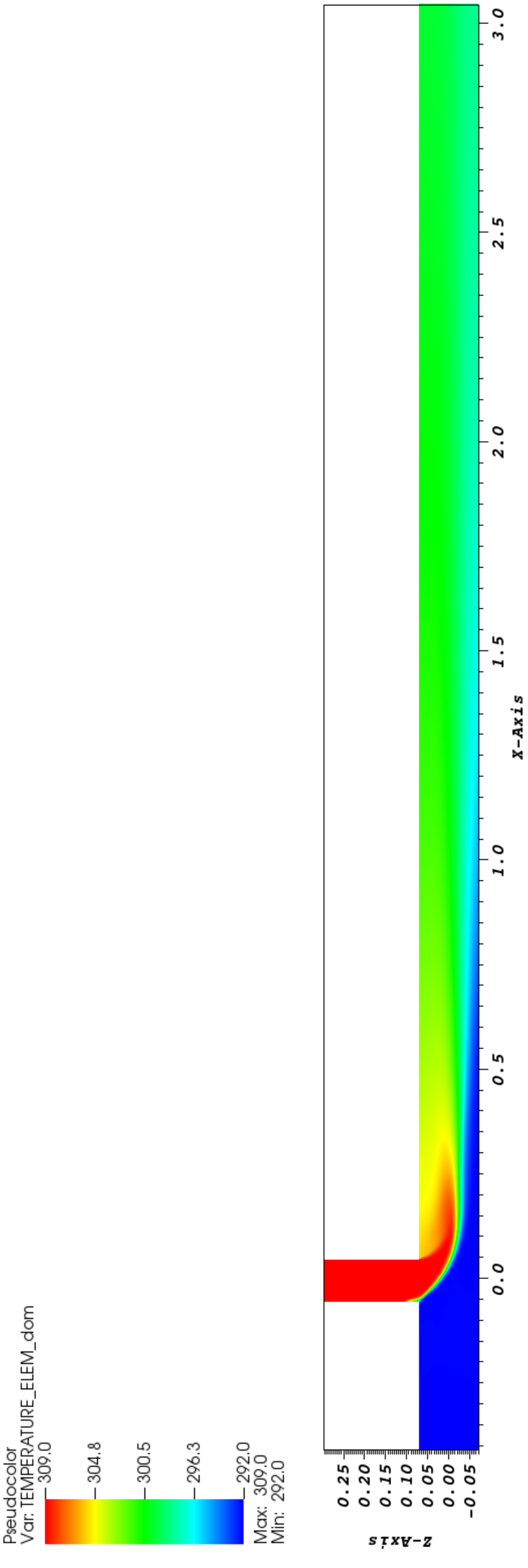

Figure 4.7: Side section of the calculated temperature field with LES WALE model (Mesh No. 4)

This solution identifies all the jet macroscopic structures, from the potential zone up to the far field. As it is possible to notice, the jet penetration lenght reaches approximatively half of the main pipe diameter. The temperature uneven distribution due to the jet along the main channel is pronounced up to 1 m downstream the branch pipe section. A small recirculation zone, located just before the jet exit section, can be found on the outer layer of the jet. The adverse pressure gradient generated by this structure, causes the jet stream to detach and will establish all the outer layer structures, proceeding to the deflection zone, up to the far region. On the inner jet part, it is possible to find other recirculation zones, mostly given by the effect of the tracking vortices presence. Once a general view of the solution is given, comparisons with the experimental data are discussed in the following sections. Velocity fluctuations cannot be extracted from the statistics RMS of the field, but, on the other hand, using the hypothesis of isotropic turbulence gives the possibility to obtain reasonable profiles of this quantity by adopting the definition of turbulent kinetic energy.

$$u' = v' = w' = \sqrt{\frac{2}{3}k} \tag{4.3}$$

Section at 1.6 D from the jet

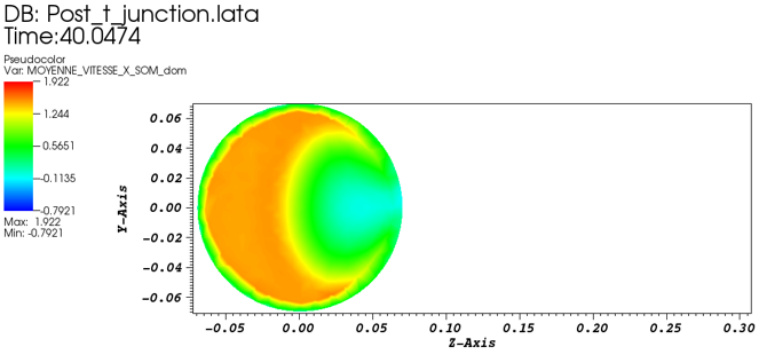

Figure 4.8: Cross section view of the Axial velocity component field, located at 1.6 D diameter downstream the jet. The colorbar scale is in [m/s]

The velocity field reported in Fig. **??** shows the presence of the recirculation zone of the jet in the top part of the channel. The comparison made with the experimental data in this section (Fig. **??** (a)) shows that $k-\varepsilon$ transport equation overrate turbulence levels, this can be noticed in particular by observing the central depression of the horizontal axial-velocity profiles. For the mass conservation law, this depression is balanced by higher peaks nearby the channel walls. On the vertical diameter line (Fig. **??** (b)) the same effects are noticeable, however the mass balance here relies on the overextimation of the recirculation bubble. However, it can be stated that these solutions find a reasonable agreement with the experimental data.

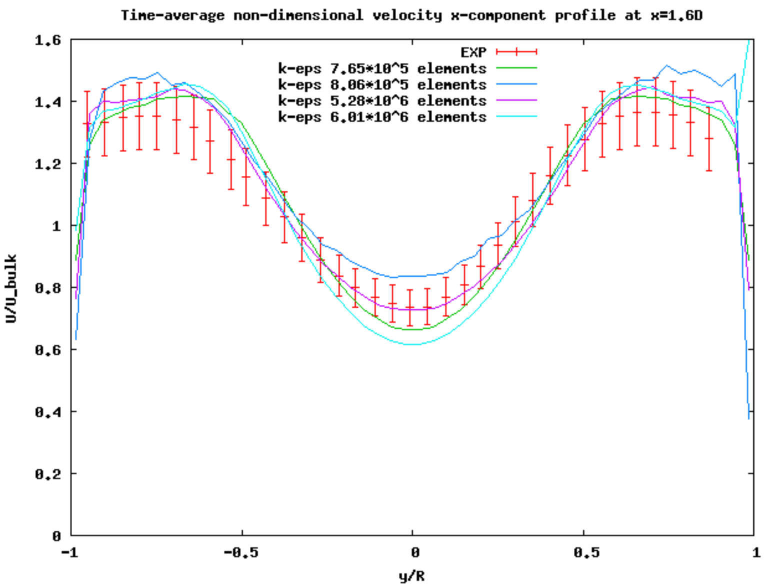

(a) $\overline{U^*}$

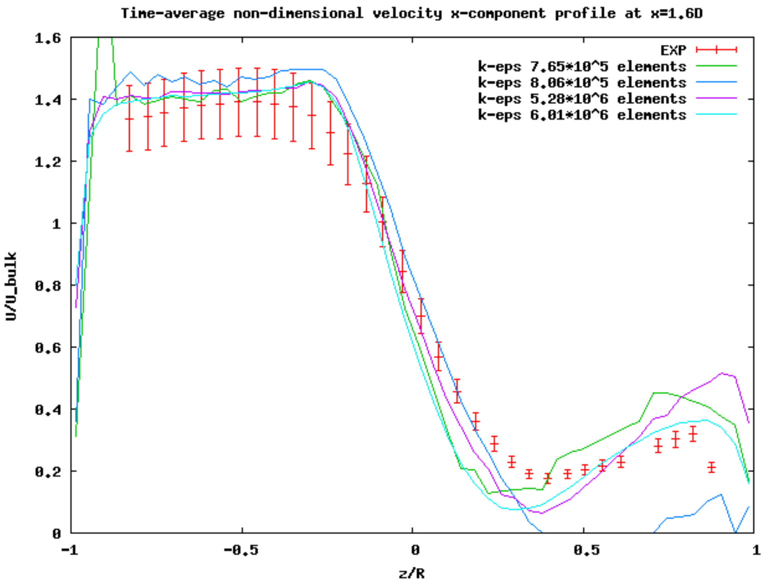

(b) $\overline{U^*}$

Figure 4.9: RANS $k-\varepsilon$ approach, comparison between calculations results and experimental data: axial dimensionless velocity profiles at 1.6 hydraulic diameter downstream the junction. (a) Horizontal profile, (b) vertical profile

Section at 2.6 D from the jet

In section at 2.6 D the z-component of the velocity is investigated. It is possible to observe that the transversal component is negligible if compared to the axial one (Fig. **??**) On the horizontal diameter, the turbulence overestimation can be clearly noticed by the root mean square profiles (Fig. **??** (b)). This has an impact also on the recirculation zone located in the center part of the jet.

In Fig. **??** the effects of the turbulence overestimation increase the recirculation bubble depression by reversing the flow up to the top part of the channel.

This condition shows the weakness of the isotropic turbulence hypothesis. As a consequence it is possible to notice a shift of the transversal velocity root mean square profiles to the central part of the jet.

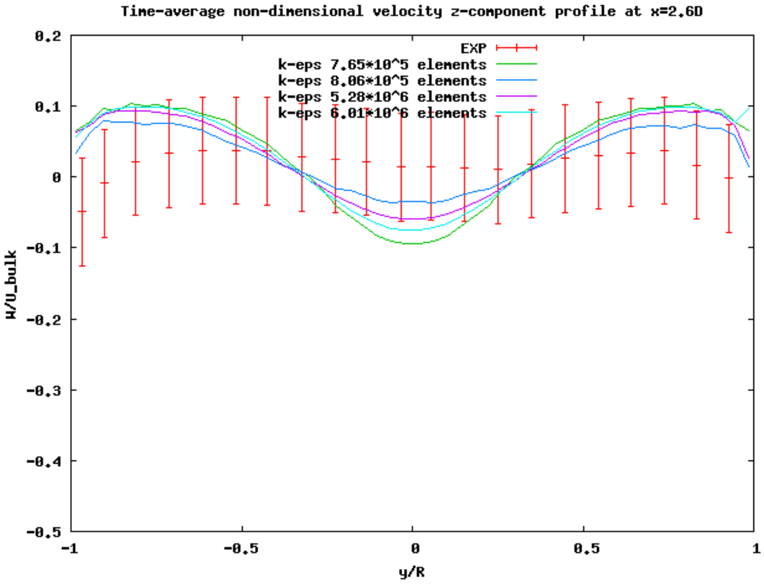

(a) $\overline{W^*}$

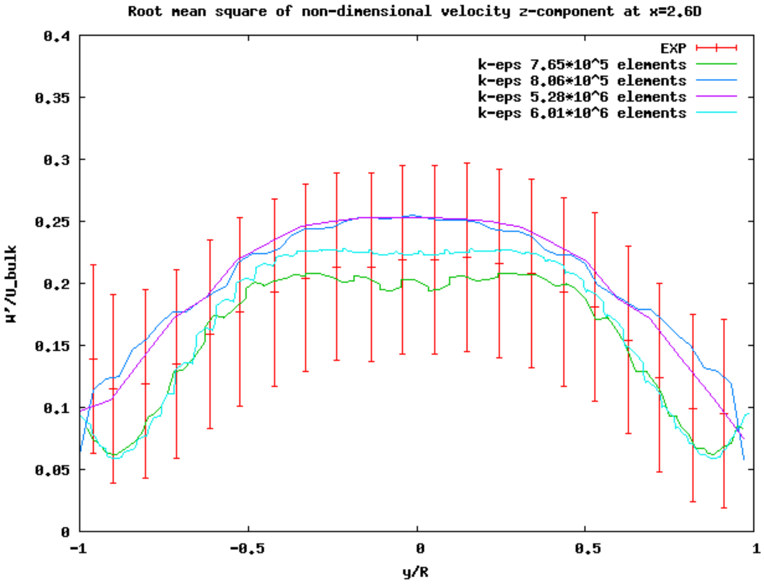

(b) σ_W^*

Figure 4.10: RANS $k - \varepsilon$ approach, comparison between calculation results and experimental data: transversal dimensionless velocity profiles at 2.6 hydraulic diameter downstream the junction. (a) Horizontal time-average distribution, (b) Horizontal Root mean square distribution

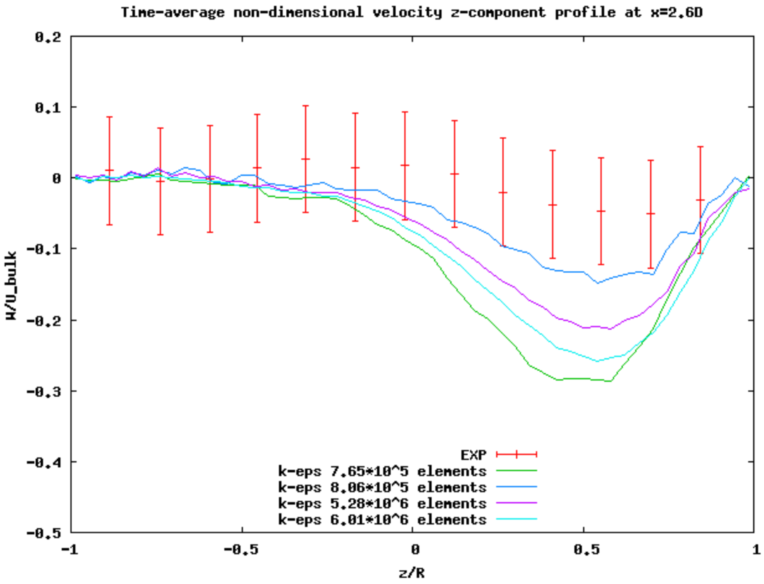

(a) $\overline{W^*}$

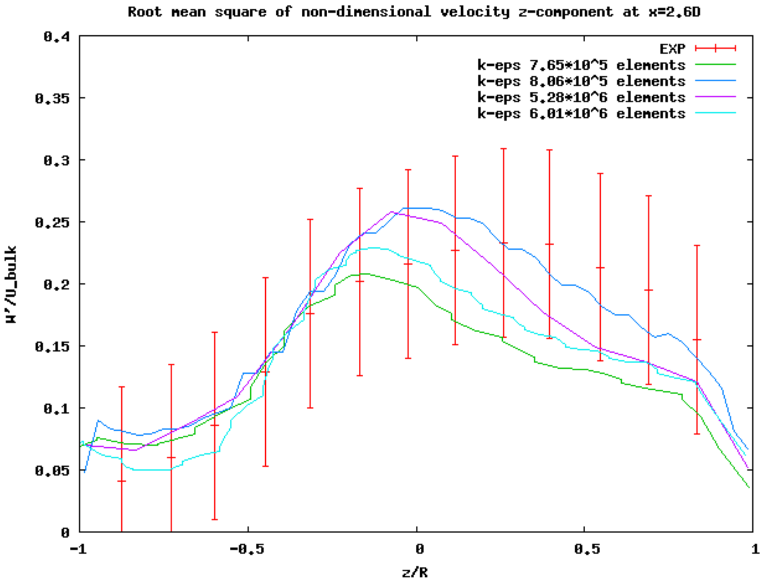

(b) σ_W^*

Figure 4.11: RANS $k-\varepsilon$ approach, comparison between calculations results and experimental data: transversal dimensionless velocity profiles at 2.6 hydraulic diameter downstream the junction. (a) Vertical time-average distribution, (b) Vertical Root mean square distribution

Section at 4.6D from the jet

The axial velocity component profiles are reported hereafter in Fig. **??**. Flatter profiles are obtained from the solutions, but still they mantain the depression in the central part of the jet, which is, however, less evident when compared to the 1.6 D section profile. The horizontal distributions respects the experimental trend, capturing the peaks locations and the flat behaviour in the upper part. This region show a sensible decrease of the pressure gradient generated by the inner part of the jet.

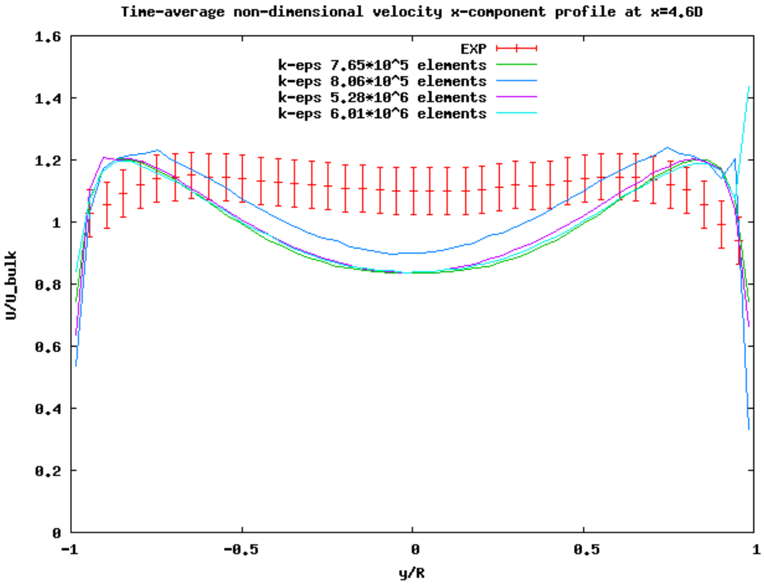

(a) $\overline{U^*}$

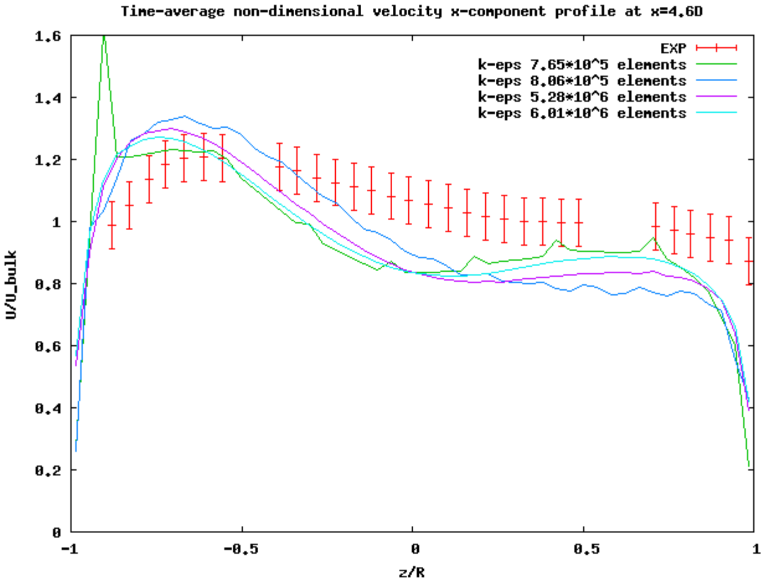

(b) σ_U^*

Figure 4.12: RANS $k - \varepsilon$ approach, comparison between calculations results and experimental data: axial dimensionless velocity profiles at 4.6 hydraulic diameter downstream the junction. (a) Horizontal profile, (b) vertical profile

Temperature fields

Temperature profiles are obtained from the $k-\varepsilon$ models and compared with the experimental data. Calculation results and experimental profiles are reported in lines which are parallel to the axial direction, and disposed on the boundary wall each 90°.
Starting from the top of the channel (0°) (Fig. **??** (a)) the dimensionless temperature decreases until the flow reaches thermally stable conditions (on the far field, temperature gradient are negligible compared to the potencial and deflection zones). RANS equations tends to generate a gradual gradient in contrast to what is shown from the experimental campaign. Experimental data present a steep temperature drop to 60 % of the highest value in less than two hydraulic diameters. The solution behaviour, however, respects the turbulence characteristics represented in the simulations by the flow field, according to the turbulent Prandtl number adopted.

Looking at Fig. **??** (b) the temperature root mean square values given by the numerical calculus are not representative for the same reasons that have been already discussed in chapter 3. The peak shown by the green curve, it is the product of the interpolation alghorithm and does not represents any physical phenomena.

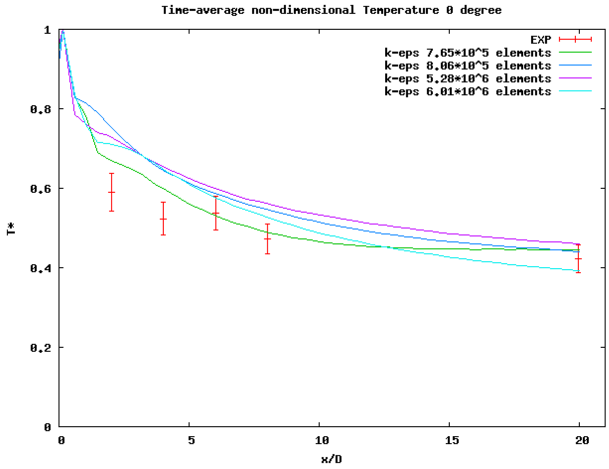

(a) $\overline{T^*}$

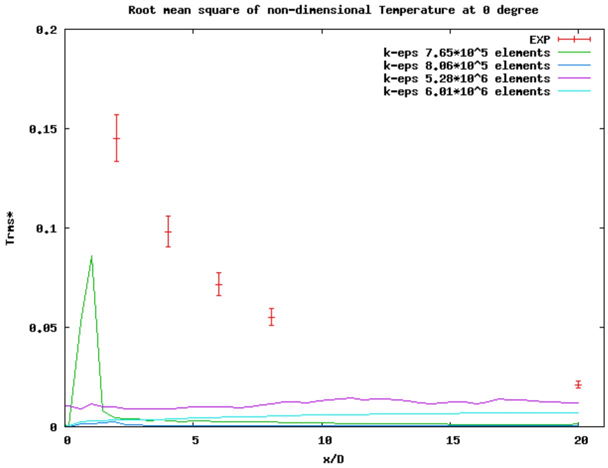

(b) σ_T^*

Figure 4.13: RANS $k-\varepsilon$ approach, comparison between temperature experimental data with $k-\varepsilon$ model along the axial top line of the main channel (0°). Dimensionless temperature average (a), dimensionless root mean square (b)

The domain and boundary symmetry would suggest that significant differences should not be found in both the left and right lines along the wall (respectively 90° and 270°), this condition is verified in the solution and in the experimental data, therefore, these results will be commented sharing almost the same considerations. Firstly, it can be noticed that a full agreement between the results given by the structured (green and cyan curves in Fig. **??** (a) and **??** (a)) and structured meshes (violet and blue curves in Fig. **??** (a) and **??** (a)) is not achieved. It can be noticed that the structured arrangement underestimates the temperature growth along the main channel lenght, expecially in the deflection zone, where the experiment gradient is more steep than the one shown by these solutions. This is a sufficient demonstration of the impact of mesh structure on this kind of configurations. As already outlined in the while discussing of the mesh, in regions where the stream presents steep gradients in the motion field (in both magnitude and direction of the velocity vectors), structured arrangements tends to condition the main flow direction; the thermal energy balance equation reflects this effect and underestimate the exchange phenomena: this leads to lower temperature gradients in the axial lines. The unstructured grid show closer agreement with experimental data since it does not determine this tendency in the same way as the structured arrangments do. As for the previous cases, the root mean square does not lead to any useful information on the temperature fluctuations.

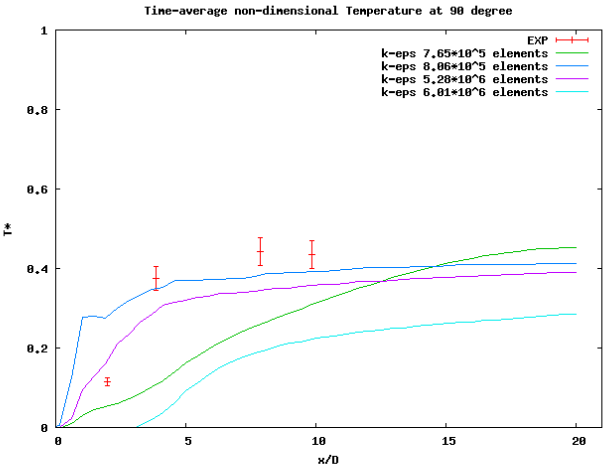

(a) $\overline{T^*}$

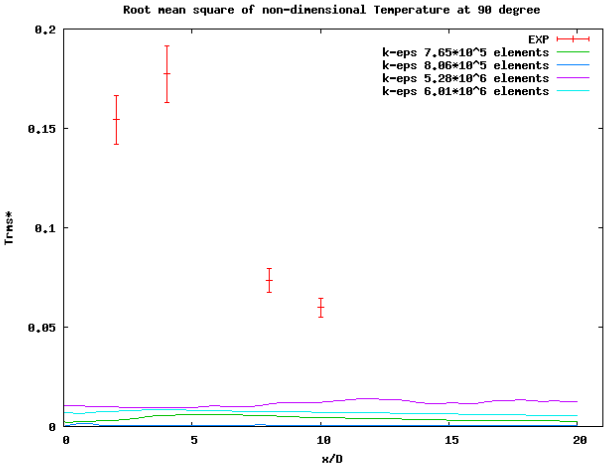

(b) σ_T^*

Figure 4.14: RANS $k - \varepsilon$ approach, comparison between temperature experimental data with $k - \varepsilon$ model along the axial top line of the main channel (90°). dimensionless temperature average (a), dimensionless root mean square (b)

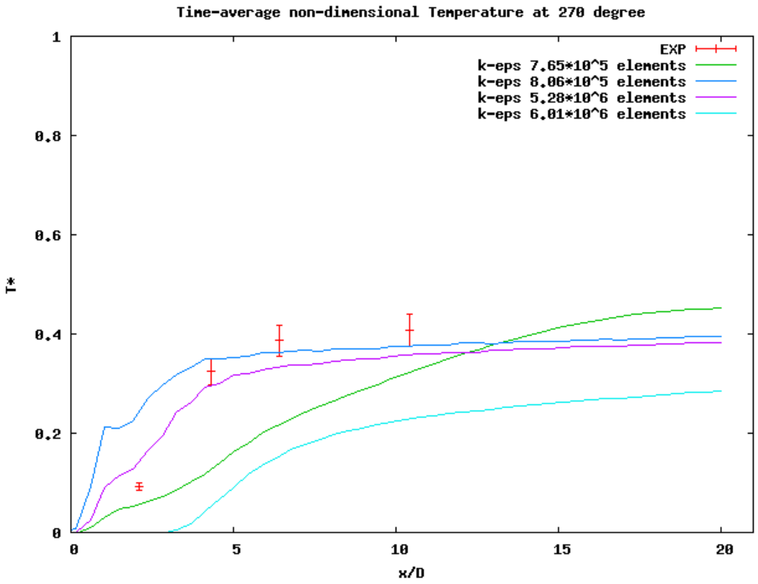

(a) $\overline{T^*}$

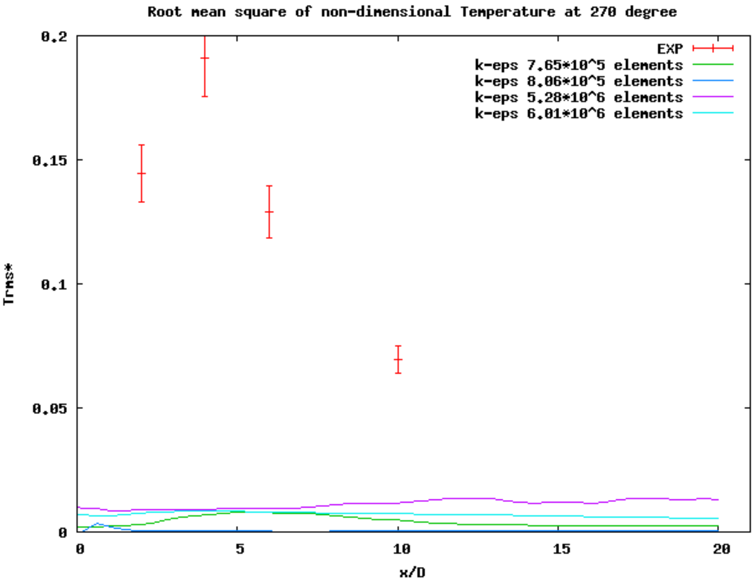

(b) σ_T^*

Figure 4.15: RANS $k-\varepsilon$ approach, comparison between temperature experimental data with $k-\varepsilon$ model along the axial top line of the main channel (270°). dimensionless temperature average (a), dimensionless root mean square (b)

The absence of steep thermal gradients in the axial direction on the bottom part of the main channel lets the solution to easily achieve closer agreement with the experimental profiles, as shown by Fig. **??**. The calculations reach reasonable accuracy gradually from the jet core zone to the far field. The transversal jet penetration lenght does not reach the bottom part of the domain; therefore the flow suddenly follows a more regular path and the solutions converges to satisfactory results.

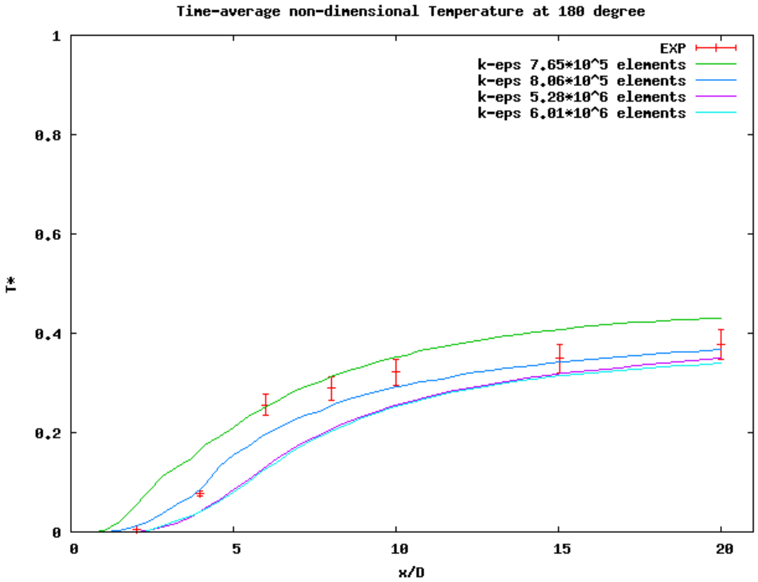

(a) $\overline{T^*}$

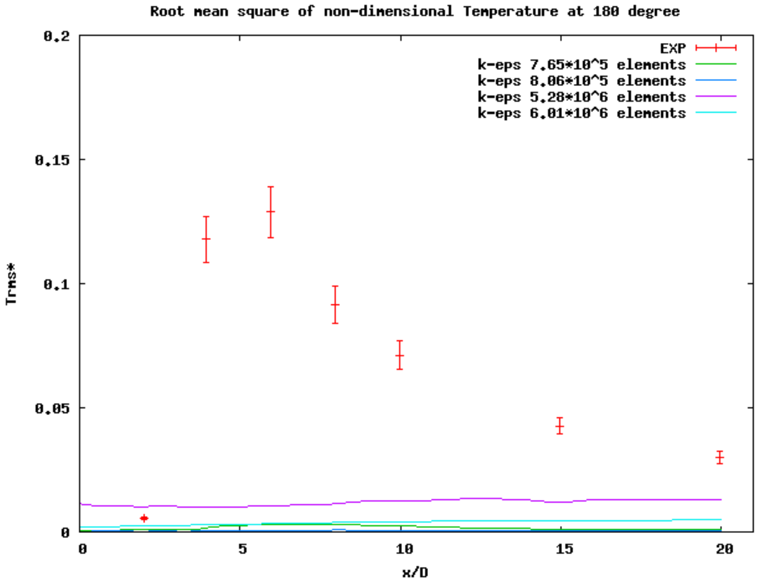

(b) σ_T^*

Figure 4.16: RANS $k-\varepsilon$ approach, comparison between temperature experimental data with $k-\varepsilon$ model along the axial top line of the main channel (180°). dimensionless temperature average (a), dimensionless root mean square (b)

Turbulence characterics have been observed moreover through the calculation domain, in order to evaluate locally Taylor lenght scale.

Figures **??** and **??** zones where both velocity fluctuations amplitudes and their time derivatives are predominant.

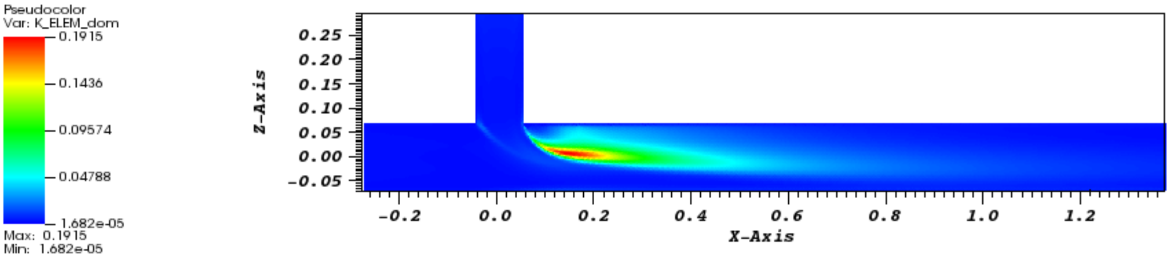

(b) Kinetic turbulent energy

Figure 4.17: Longitudinal cutplane view of the turbulent kinetic energy distribution. The colorbar scale is in m^2/s^2

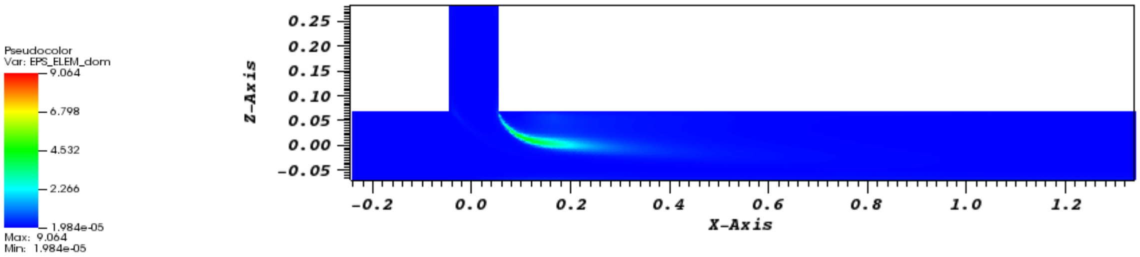

(b) Kinetic turbulent energy dissipation ratio

Figure 4.18: Longitudinal cutplane view of the turbulent kinetic energy dissipation ratio distribution. The colorbar scale is m^2/s^3

Through these plots it is possible to see qualitatively that the main turbulent structures arise and evolves in the downstream part adjacent to the top of the main pipe. From the calculation of the statistical values for k and ε on each subdomain of the test section, the mean Taylor micro scales have been obtained and adopted for the LES modelization (table **??**)

Sub domain	Taylor microscale scale [mm]
Upstream main pipe	2.22
Upstream branch pipe	1.12
Mixing zone and Far field	0.97

Table 4.6: Taylor microscale estimation for each sub zone of the Vattenfall test section

Even if the contributions of turbulence seems to change slighlty its scale, to directly apply in a rigid manneer the Taylor lenght scales to create the LES mesh, would lead to obtain steep gradients on the element size distribution with the consequence of undesired conditioning effects in the solutions. Therefore, the lenghtscales extimated here are just taken as a guideline for the spatial discretization, giving priority to the smaller scale extimated and extrapolating those lenght to the overall domain. The main focus was to keep as much as possible a good aspect ratio of the elements.

4.1.2 LES

For the LES modeling, statistical values are calculated starting from the end of the transient period, up to at least 15 seconds of time flow (Fig. **??**), in order to better resolve amplitude distributions below 0.5 Hz on the spectra. On the average, each time advancement used timesteps of the order of 10^{-5} s keeping the stability conditions required by the Courant Friedrichs Lewy criterion, that would give a required time step one order of magnitude greater. The calculations have been parallelized assigning an average of 36000 elements per processor. Adopting this strategy, the mean CPU time required for computing a timestep was of 1.72 seconds. On the average, the time spent for simulating 15 seconds of flow-time required between 90 and 150 hours. In Fig. **??** a preview of the instantaneous temperature field is shown, while in the table **??** below, the settings adopted to perform each LES calculation are summarised.

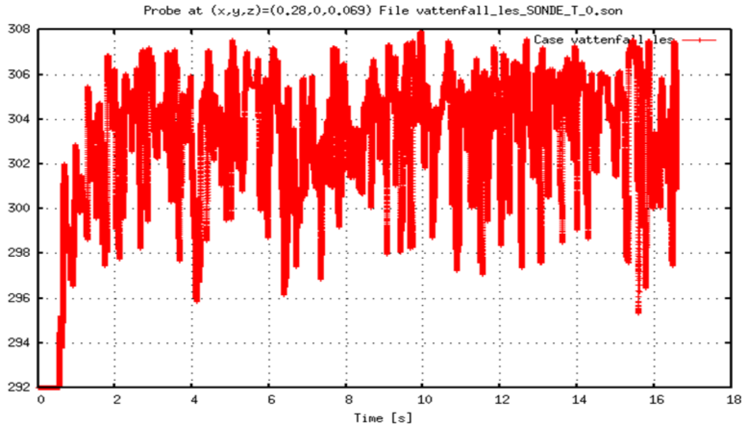

Figure 4.19: Temperature time history example (calculation Mesh no. 3)

Spatial discretization scheme	VEFPreP1B on Tetrahedral meshes
Time discretization scheme	Second Order Adam Bashforth
Fluid physical properties	
$\mu \left[\frac{Ns}{m^2}\right]$	$9.34 \cdot 10^{-4}$
$\rho \left[\frac{kg}{m^3}\right]$	996.86
$\lambda \left[\frac{W}{m^2 K}\right]$	0.61
$C_p \left[\frac{J}{KgK}\right]$	4186.62
$\beta \left[\frac{1}{K}\right]$	$2.55 \cdot 10^{-4}$
Navier Stokes equations	
Pressure Solver	PCG with SSOR
Convective scheme	Ef Stab α 0.2
Diffusive scheme	Second Order Centered
Turbulence model	WALE
Convection Diffusion Temperature equation	
Convective scheme	Ef Stab α 1 (Upwind)
Diffusion scheme	Second Order Centered
Turbulence	Turbulent Prandtl number

Table 4.7: LES Model setup settings

4.1.2.1 Meshing

The mesh adopted for the LES investigations follows the Taylor scale exitmated during the preliminary statistical analysis performed. For these simulations both the structured and unstructured mesh arrangements are tested to analyse the influence of these structures in cases where the transport equation of k and ε are not considered in the problem. In the table **??** the mesh tested are reported.

Mesh No.	**Mesh Structure**	**Number of elements**
1	Unstructured	5284484
2	Structured	6019161
3	Unstructured	9254640

Table 4.8: LES WALE meshes

4.1.2.2 Boundary conditions

Literature works related to this study ([**?**] [**?**] and [**?**]) demonstrated that inlet turbulence levels does not have a strong influence on the final results obtained by the LES approach, since the main turbulence generation relies on the mixing zone and the vortex structures which generate the temperature fluctuations that are required to be captured by the code are reasonably independent on the velocity fluctuations at the inlet section. The statistical approach already showed reasonable predictions of the average evolution of the flow, taking into account this fact the boundary conditions used for LES calculations are kept the same as those described for the RANS calculations.

4.1.2.3 Comparison with experimental data

In Fig. **??** a meaningful view of the instantaneous temperature field obtained from the LES solution is shown and compared to the respective time average plot (Fig. **??**). As it is possible to note, the spatial filter adopted by the choice of the mesh gives a truthful description of the scalar fluctuations given by the vortex structures. This solution shows the presence of the same recirculation zones in the proximity of the jet exit section, in the same way as the RANS approach does.

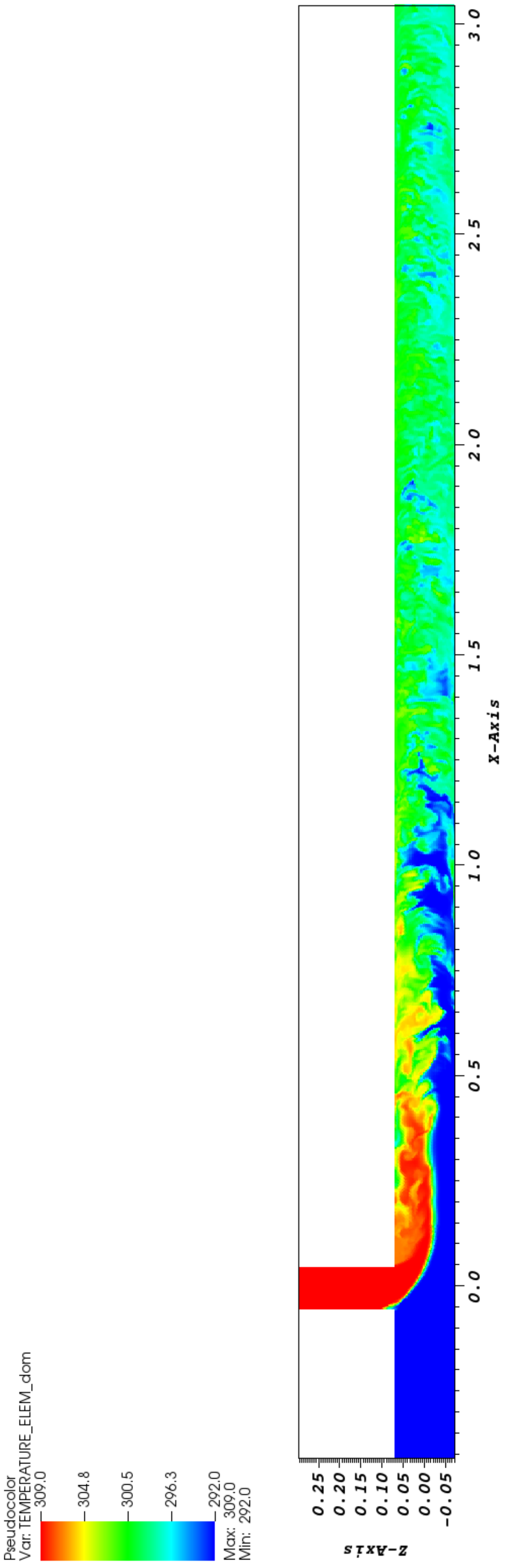

Figure 4.20: Side cut plane of the instantaneous temperature field given by LES WALE model (Mesh no. 3)

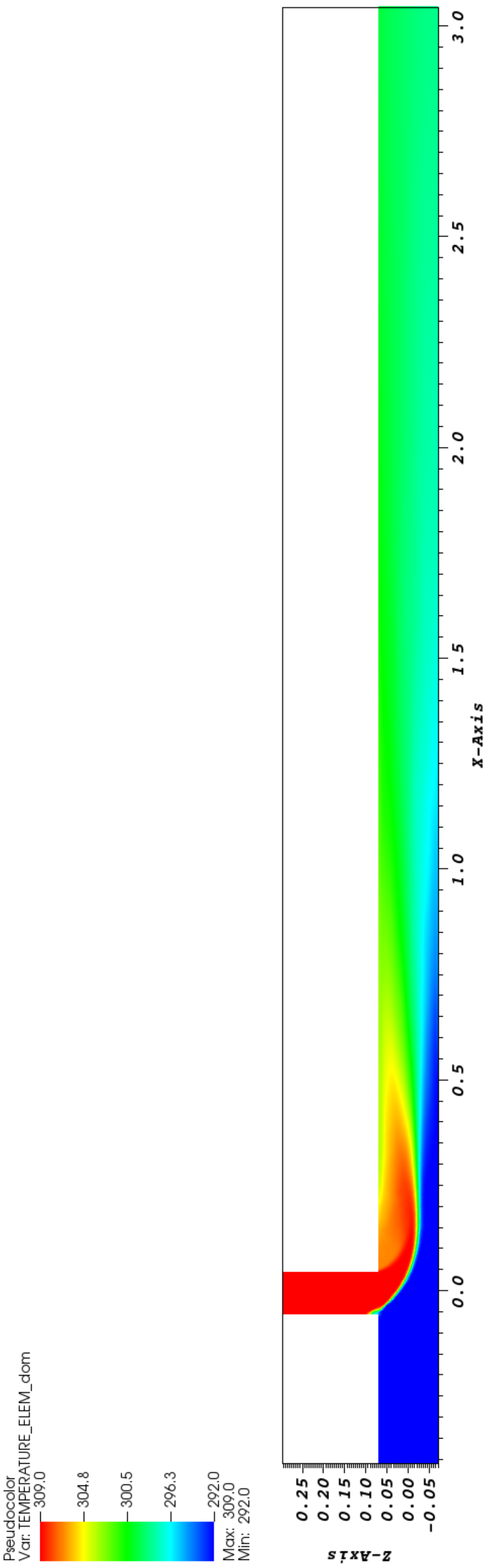

Figure 4.21: Side cut plane of the time average temperature field given by LES WALE model (Mesh no. 3)

Section at 1.6D from the jet

The axial velocity component profiles obtained by the LES WALE model are reported in Fig. **??**. In the horizontal diameter line there is agreement between the three calculations; the general trends match with the experimental data. However, the central depression magnitude has not been fully captured. This can be partially explained with the fact that the jet channel flow is not fully developed when it reaches the exit section. The LES WALE model does not reach the same velocity axial profile at that point. The ratio between the transversal and the axial velocity component magnitude is lower than the one reached during the experimental tests. In Fig. **??** numerical effects can be noticed on the recirculation zone. There is agreement between the unstructured grid arrangments, which produce the same trends, achieving a good prediction when the nodes denstity is increased, on the other hand structured one delays the tracking vortices formation to regions which are located downstream this section; this explain why the velocity peak nearby the wall is not put in evidence.

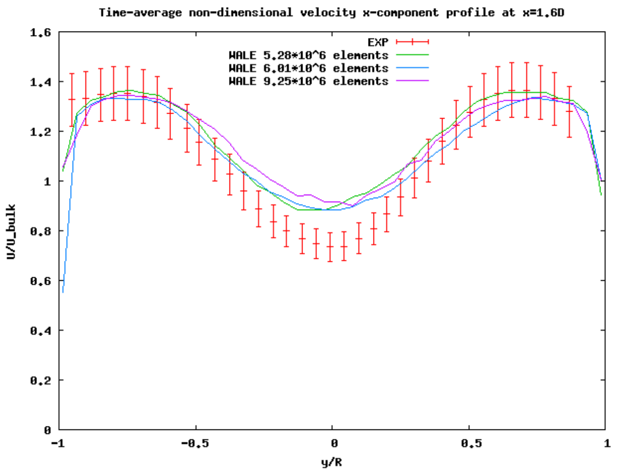

(a) $\overline{U^*}$

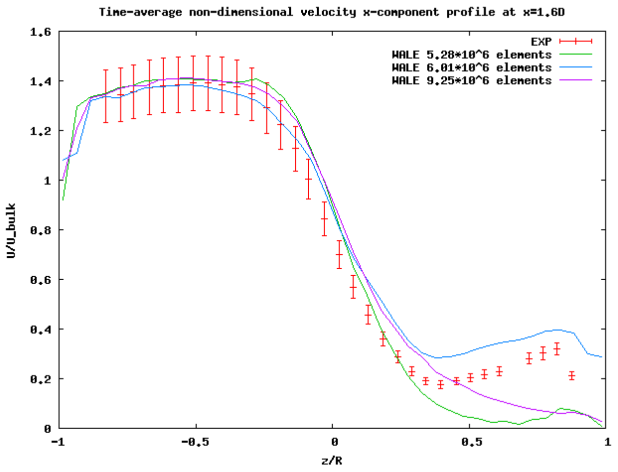

(b) $\overline{U^*}$

Figure 4.22: LES WALE approach, comparison between calculations results and experimental data: axial dimensionless velocity profiles at 1.6 hydraulic diameter downstream the junction. (a) Horizontal profile, (b) vertical profile

Section at 2.6D from the jet

Proceeding downstream the main channel, at 2.6 D, the axial velocity field calculated (Fig. **??** achieves satisfying profiles which represents with good approximation the experimental measures. In LES cases, the root mean square calculated by the numerical schemes represents the same behaviour shown by the experimental campaign, therefore it is ensured that the turbulent fluctuations are well reported by the the WALE model both in the vertical and horizontal diameters.

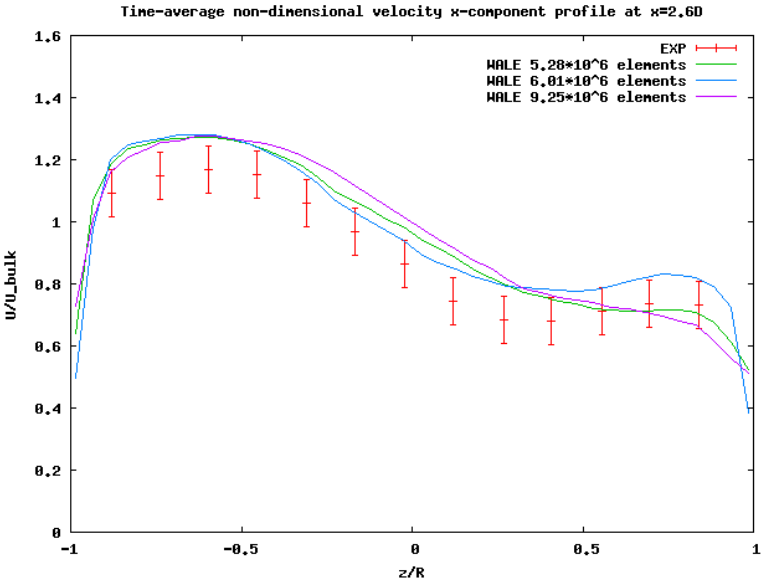

(a) $\overline{U*}$

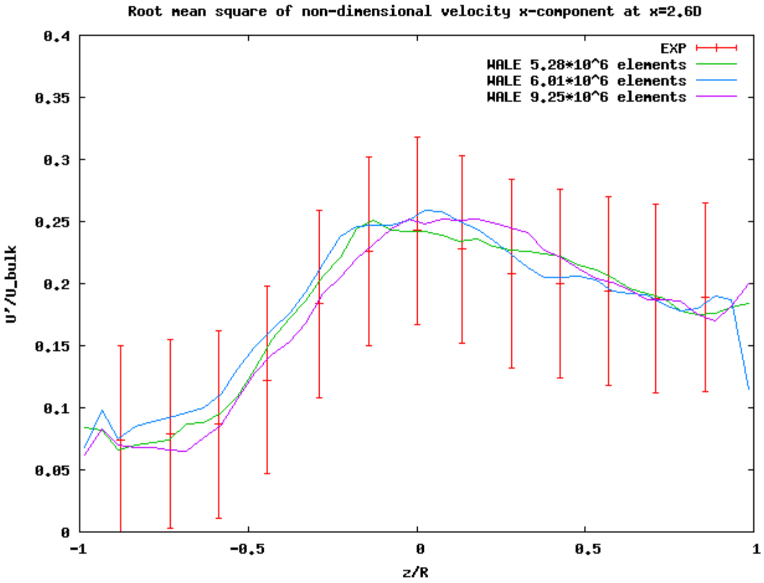

(b) σ_U^*

Figure 4.23: Comparison between LES calculations results and experimental data: axial dimensionless velocity profiles at 2.6 hydraulic diameter downstream the junction. (a) Vertical time average profile, (b) vertical root mean square profile

Section at 4.6 D from the jet

The same considerations made for the 2.6 are valid for this case. In Fig. **??** velocity profiles are well represented by the LES models and reaches satisfactory agreements with the experimental data. In this part, the flow is fully developed as the flat distribution suggests.

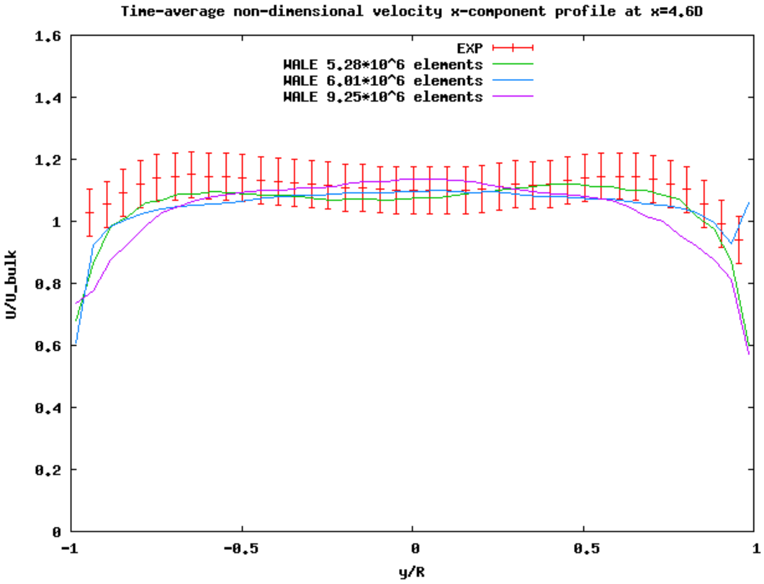

(a) $\overline{U^*}$

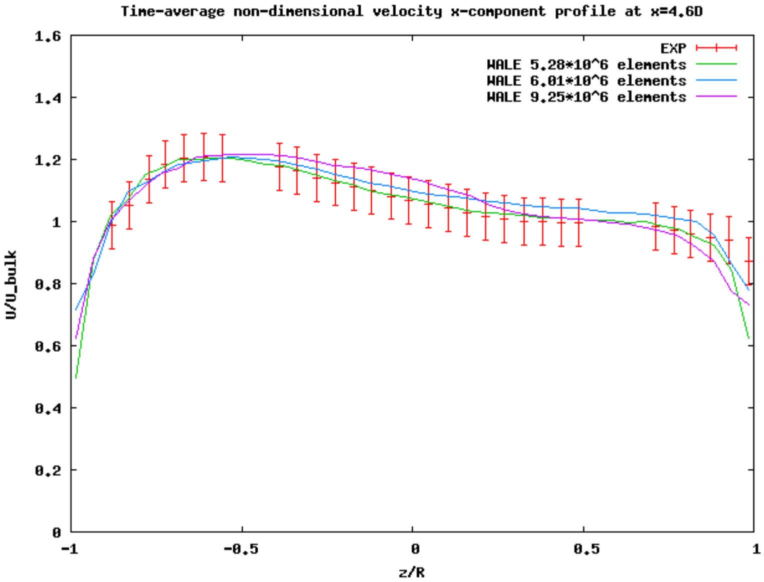

(b) σ_U^*

Figure 4.24: Comparison between LES calculations results and experimental data: axial dimensionless velocity profiles at 4.6 hydraulic diameter downstream the junction. (a) Horizontal profile, (b) vertical profile

Temperature plots

Both average and root mean square profiles reach a good description of the temperature field near wall locations, when the LES WALE model is adopted. On the top part of the channel (Fig. **??** (a)) the numerical solution shows a higher temperature peak located in the jet proximities.

However, since the turbulence behaviour is well represented in this zone (Fig. **??** (b)) this overestimation is not caused by a bad description of the turbulence. The reason of this peak lies into the average description of the flow, as mentioned for the velocity profiles in section 1.6.

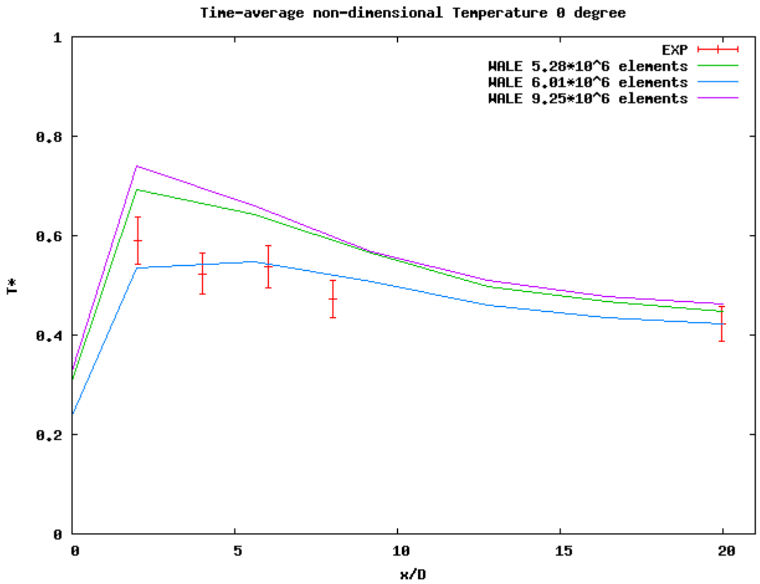

(a) $\overline{T^*}$

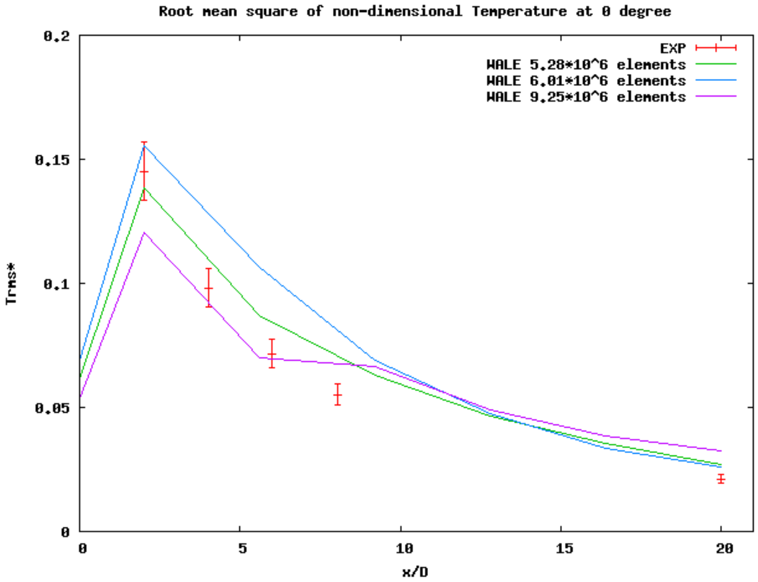

(b) σ_T^*

Figure 4.25: Comparison between temperature experimental data with LES model along the axial top line of the main channel (0°). dimensionless temperature average (a), dimensionless root mean square (b)

The symmetry conditions of the problem finds agreements in LES calculations, which achieve good results for the temperature field along the side lines. In Fig. **??** and **??** results are close enough to the experimental data. It can be noticed that, in contrast with the $k-\varepsilon$ analysis, the different mesh arrangment does not show high discrepancies between solutions, both for the average and root mean square results.

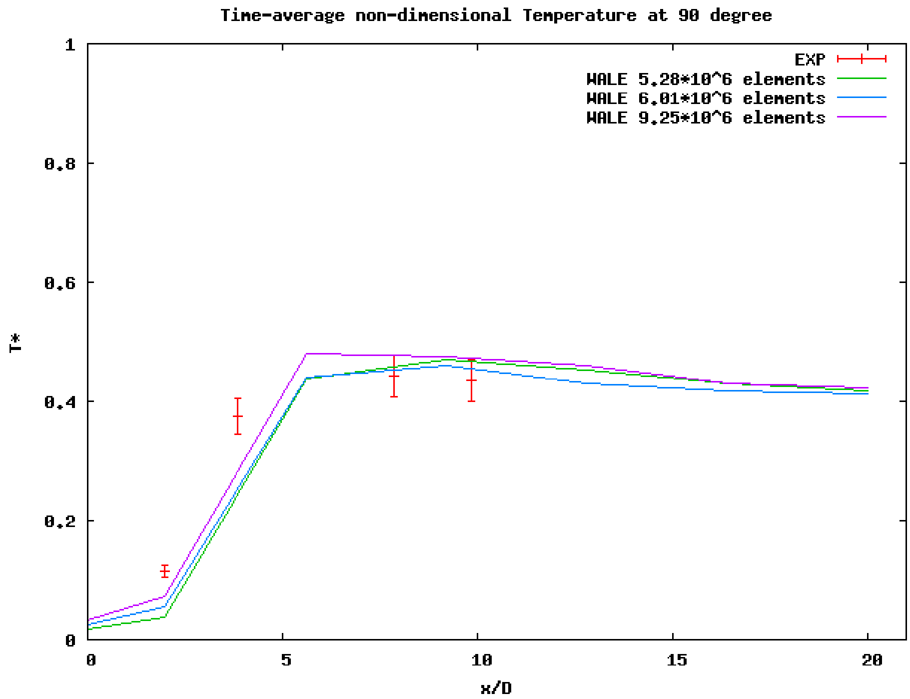

(a) $\overline{T^*}$

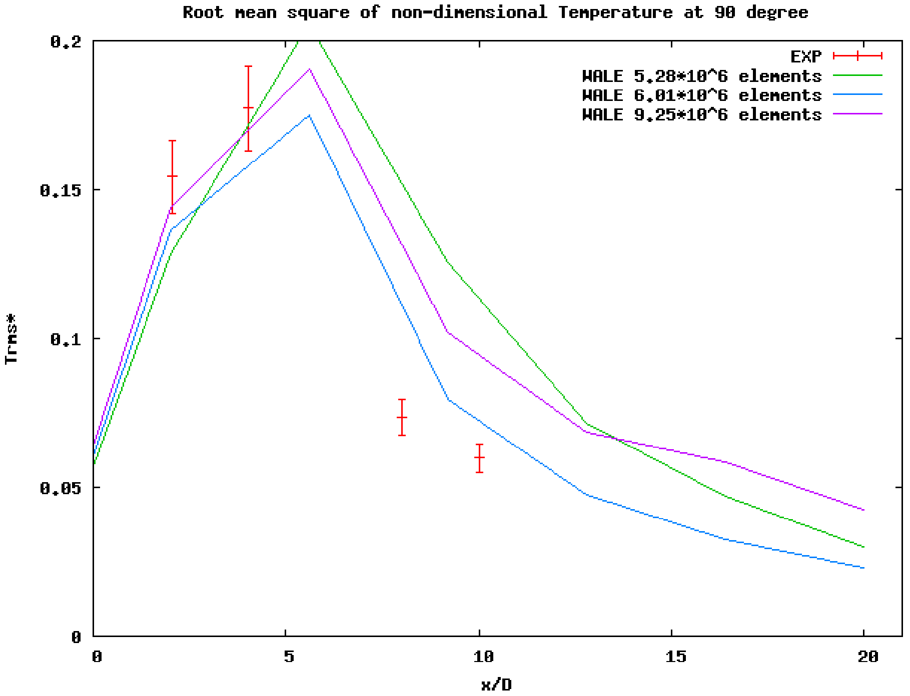

(b) σ_T^*

Figure 4.26: Comparison between temperature experimental data with LES model along the axial left line of the main channel (90°). dimensionless temperature average (a), dimensionless root mean square (b)

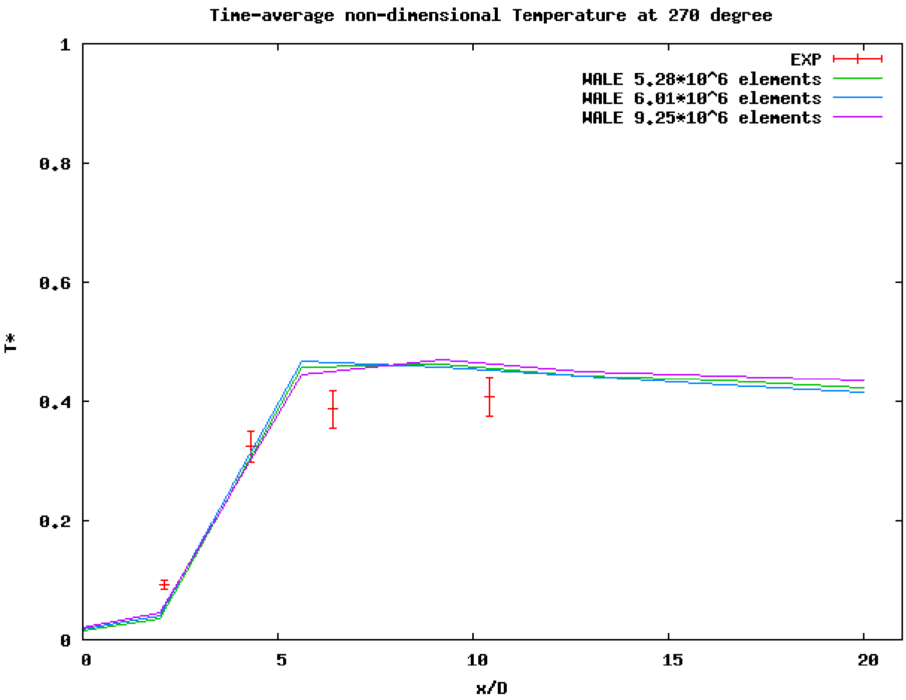

(a) $\overline{T^*}$

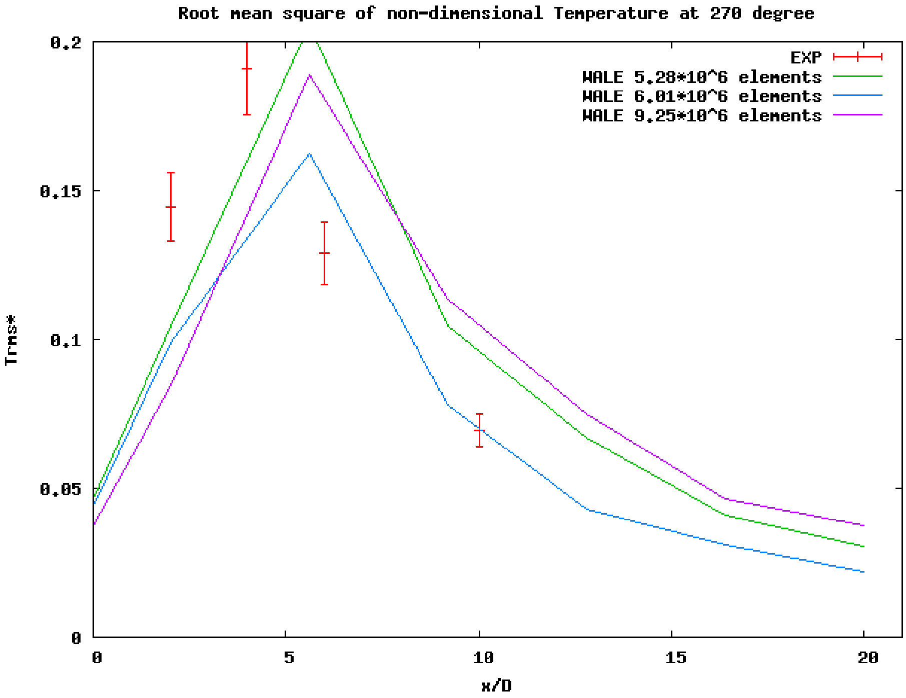

(b) σ_T^*

Figure 4.27: Comparison between temperature experimental data with LES model along the axial right line of the main channel (270°). dimensionless temperature average (a), dimensionless root mean square (b)

In conclusion, the thermal description of the LES WALE model gives fair results on the bottom line of the jet, and good agreement with the experimental data on the outer part of the jet as reported in Fig. **??** (a). However the solution fluctuations (Fig. **??** (b)) seem to be overestimated by the unstructured meshes, as the far field is reached. This behaviour can be explained by numerical diffusion effects, as long as the structured mesh arrangments does not follow the same trends.

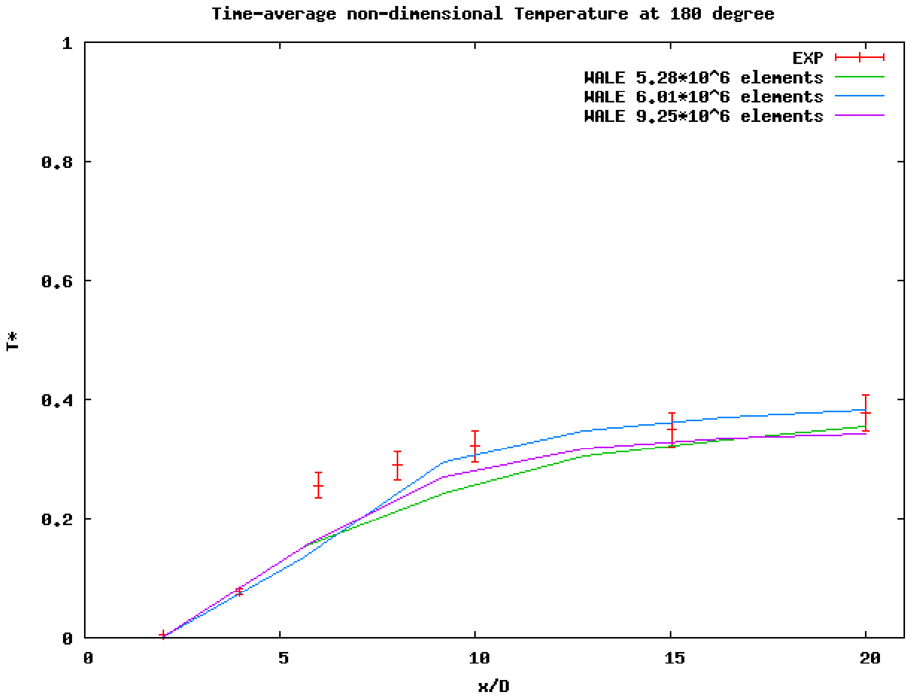

(a) $\overline{T^*}$

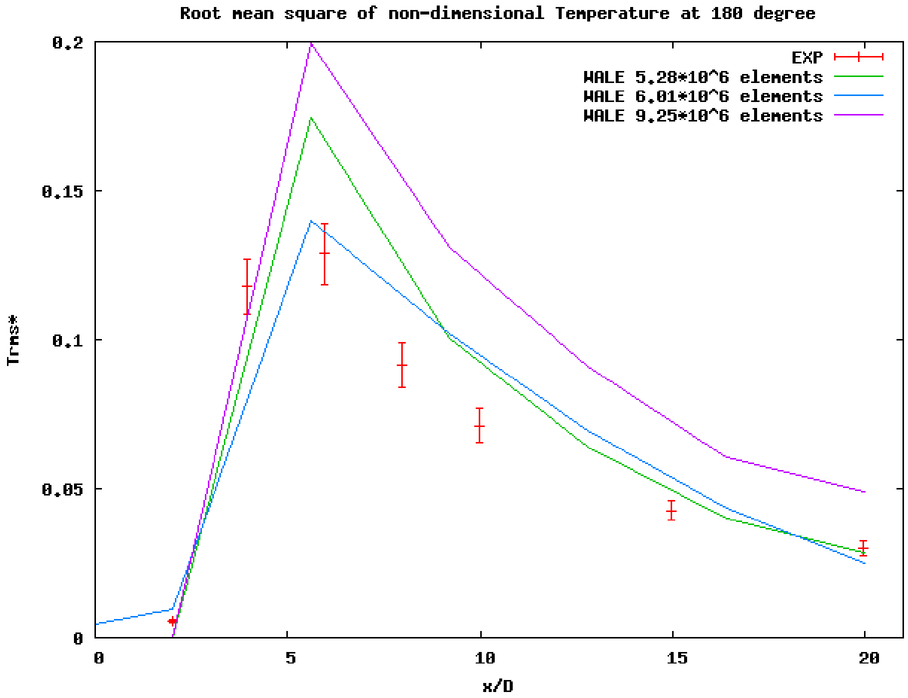

(b) σ_T^*

Figure 4.28: Comparison between temperature experimental data with LES model along the axial bottom line of the main channel (180°). dimensionless temperature average (a), dimensionless root mean square (b)

Spectras

Finally, the spectra of velocity and temperature fluctuations of the experimental campaign are compared with the LES WALE model solutions. Noticeable differences among the various calculations performed were not found for these data, so the unstructured mesh no. 3 was chosen to represents the TrioCFD performances. The magnitude and frequency temperature distributions are reported in Fig.??. The measurement point is located on the right side part of the main channel, 2 hydraulic diameters downstream the jet section. As it is possible to notice, the temperature Fourier transform given by LES WALE model, respects the Kolmogorov -5/3 law. Starting from the lower frequency, the resolution grows up to the smaller time scales, this effect is mostly caused by the total simulated flow-time. Compared to the experimental data, the numerical solution agrees sufficiently with the experimental behaviour, but still misses the clear amplitude peak for frequencies around the range of 4 Hz.

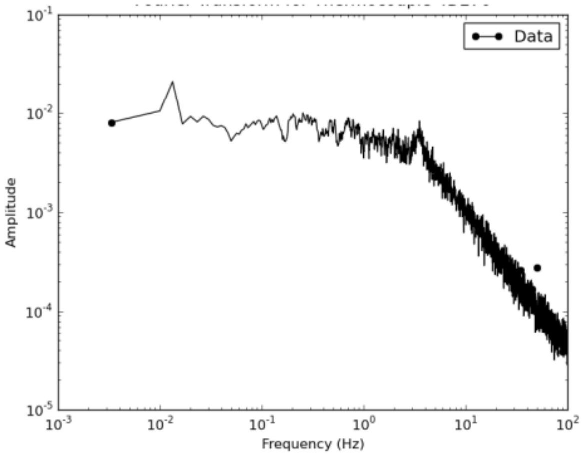

(a) Experiment

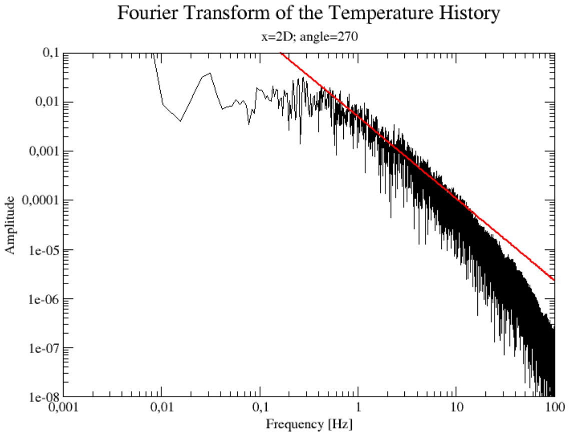

(b) LES WALE (Mesh no. 3)

Figure 4.29: LES WALE approach, comparison between experimental and numerical solution temoerature spectras in a point located at x=2D at 270°. Fourier transform of the temperature time history of (a) experimental data and (b) LES model. The red line represents the -5/3 Kolmogorov law.

In Fig. ?? the transversal velocity transform are shown. The transversal velocity components located in the center point of the 3.6 D section is investigated. The calculation still follows the

-5/3 Kolmogorov trend in the inertial subrange. Even if comparable amplitude peaks can be found around the 10 Hz point, it must be underlined that the stochastic nature of turbulent flows does not allow to ensure that these peaks corresponds to the same physical phenomena. In conclusion it is possible to argue that the general trends given by the solution, fairly represents the vortices lenght scale distributions recorded by the experimenters.

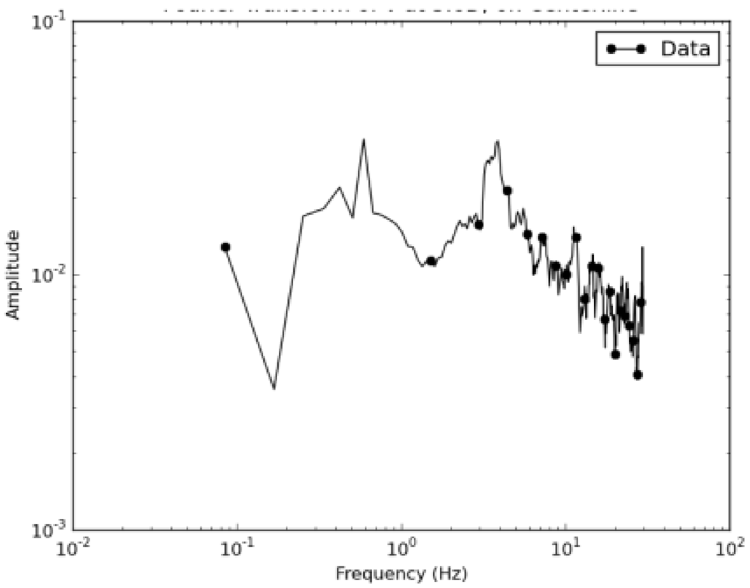

(a) Experiment

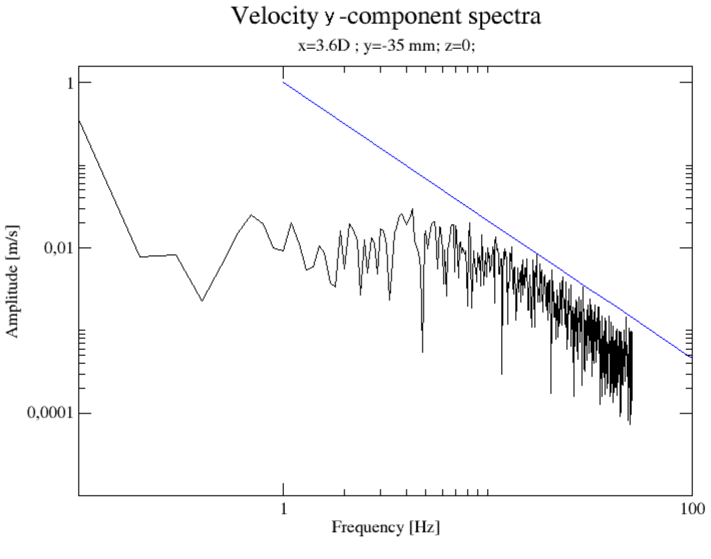

(b) WALE (Mesh no. 3)

Figure 4.30: LES WALE approach, comparison between experimental and numerical solution velocity y-component spectras. Fourier transform of the velocity time history of (a) experimental data and (b) LES model. The blue line represents the -5/3 Kolmogorov law.

4.2 TRANSAT experiment

The geometrical domain of the TRANSAT test section have been modeled using the Geometry tool of the software SALOME 7.7.1. as well. The dimensions of the quotes have been already given in a related section. The original size of the test section would represent a serious problem in terms of computational costs, since the Taylor scale obtained from the statistical analysis within the operating conditions, would require a spatial discretization in the order of the millimeter. With such elements lenght, LES simulations would require grids with more than 130 million of elements. A preliminary RANS study has been conducted to verify the sensitivity of the solutions when the lenght of the domain changes. This process guarantees that good predictions can be achieved using a shorter domain in the axial direction. To locally specify the lenghtscale of the mesh in different parts of the domain, this has been geometrically divided into three sections, similarly to what done for the Vattenfall tee junction case, each part is shown in Fig. **??**.

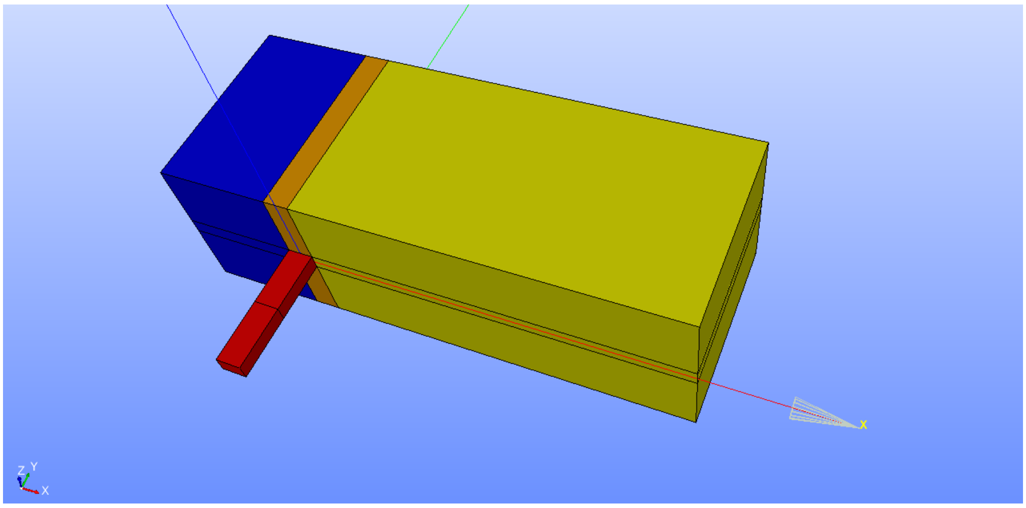

Figure 4.31: TRANSAT domain sub-parts

4.2.1 RANS approach

The model have been created using the most common practices, in order to achieve fastly a reasonable solution that would allow to define properly the subsequent models. The $k-\varepsilon$ (settings reported in table **??**) model used for the TRANSAT case showed some flow instabilities on the numerical solution depending on the mesh refinment adopted. The ratio between the bulk velocities studied is 3.3; in these conditions, the jet channel shape keeps concentrated the fluid streamlines. One can consider that those instabilities are driven by physical phenomena, thinking that the jet behaves almost like a bluff body which generates periodic turbulent structures, that can be assimilated to Von Karman's ones, on the downstream zones (Fig. **??**. On the other hand numerical instabilities must be taken into account in order to split these effects; the fluctuation amplitude and frequencies of these vortices have been observed while changing the mesh refiment and structure. In detail, the refinement process has shown no significant changes in this behaviour up to 2 million cells grids, hereafter an impressive reduction on the fluctuations amplitude (both in time and space) up to five million elements has been observed (Fig. **??**). This example shows how the grid refinment plays an important role on the CFD study of such configurations, so it must be underlined that mesh convergency cannot be neglected during these investigations. Moreover, the use of implicit schemes may have an influence on numerical diffusivity as well.

Spatial discretization scheme	VEFPreP1B on Tetrahedral meshes
Time discretization scheme	Euler Implicit
Fluid physical properties	
$\mu\ \left[\frac{Ns}{m^2}\right]$	$1.76 \cdot 10^{-5}$
$\rho\ \left[\frac{kg}{m^3}\right]$	1.24
$\lambda\ \left[\frac{W}{m^2 K}\right]$	$2.5 \cdot 10^{-2}$
$C_p\ \left[\frac{J}{KgK}\right]$	1005
$\beta\ \left[\frac{1}{K}\right]$	$3.47 \cdot 10^{-3}$
Navier Stokes equations	
Pressure Solver	PCG with SSOR
Convective scheme	Upwind
Diffusive scheme	Second Order Centered
Turbulence model	RANS $k-\varepsilon$
Transport $k-\varepsilon$ equations	
Convective scheme	Upwind
Diffusion scheme	Second Order Centered
Wall Turbulence Modelization	Reichardt Law
Convection Diffusion Temperature equation	
Convective scheme	Upwind
Diffusion scheme	Second Order Centered
Turbulence	Turbulent Prandtl number

Table 4.9: RANS model setup

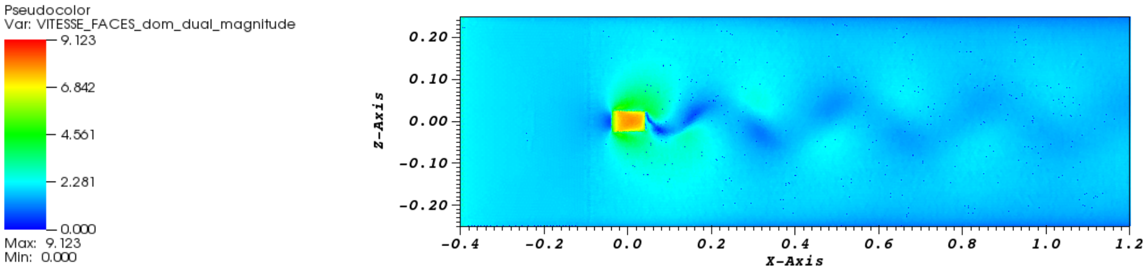

Figure 4.32: Velocity field on a cutplane facing the jet inlet zone, affected from numerical instabilities (mesh no. 1)

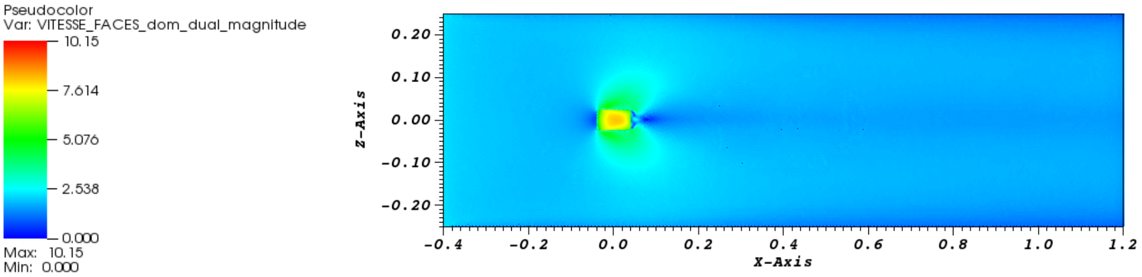

Figure 4.33: Converged Velocity field on a cutplane facing the jet inlet zone (mesh no. 4)

4.2.1.1 Meshing

For the statistical model, the structured and unstructured arrangments are reproposed (Fig. **??** and **??**) once the calculation started to have a stable behavior the mesh refinment has been stopped in order to reduce the calculation time required. y^+ values produced by the refinments process, vary between 15.6 and 27.9 with minimum mesh angles of 35 degrees. Details on the number of elements are given in table **??**.

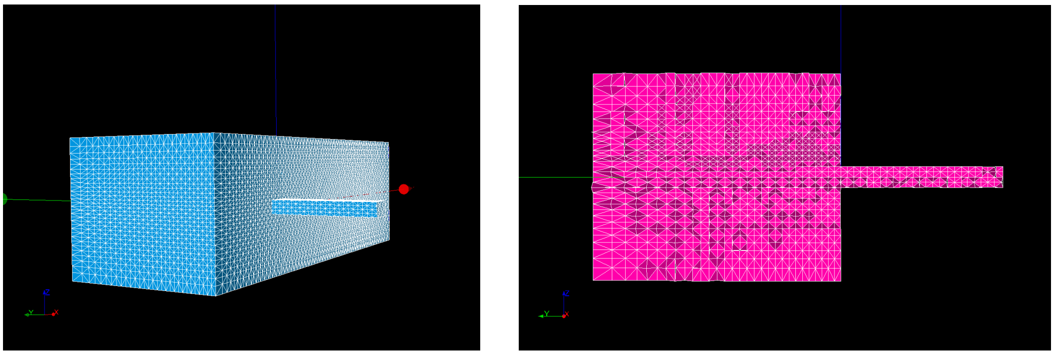

(a) External view

(b) Longitudinal Cut

Figure 4.34: Transat Unstructured mesh example

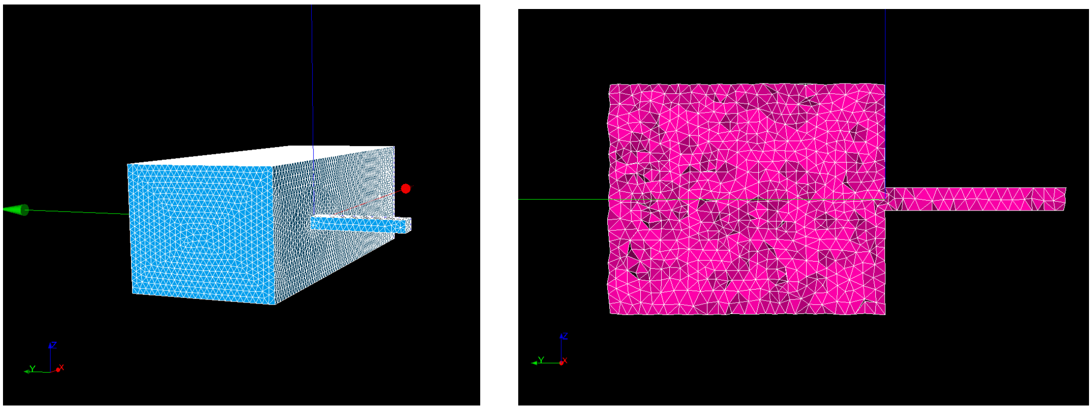

(a) External view

(b) Transversal cut

Figure 4.35: Transat Unstructured mesh example

Mesh No.	**Mesh Structure**	**Number of elements**
1	Unstructured	1253118
2	Unstructured	2027086
3	Unstructured	4550432
4	Structured	4964712

Table 4.10: RANS/$k-\varepsilon$ meshes

4.2.1.2 Boundary conditions

Taking into account the qualitative description given by the experimenters of the TRANSAT campaign, flat velocity profiles have been applied as boundary conditions for the inlet sections, while k and ε respect the turbulence percentage declared, as it has been reported in table **??**

In difference with respect to the Vattenfall tee junction case, the distance between the inlet and outlet sections of the jet channel was not specified by Fougairolle [**?**]. Therefore a study was performed in order to evaluate the minimum lenght required to obtain a velocity profile that would be as close as possible to the measurements recorded on the outlet section. In Fig. **??** and **??** respectively the mesh adopted and the velocity fields are shown.

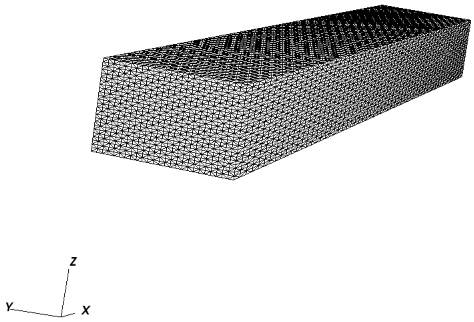

Figure 4.36: Jet channel mesh view

The results show that the closer profile to the experimental data is reached after a lenght of about 30 cm (Fig. **??**)

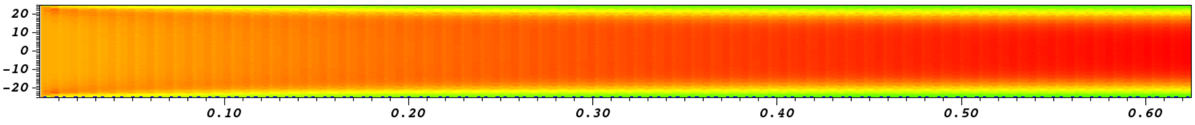

Figure 4.37: Velocity field on a longitudinal cut plane of the jet (RANS $k-\varepsilon$ model

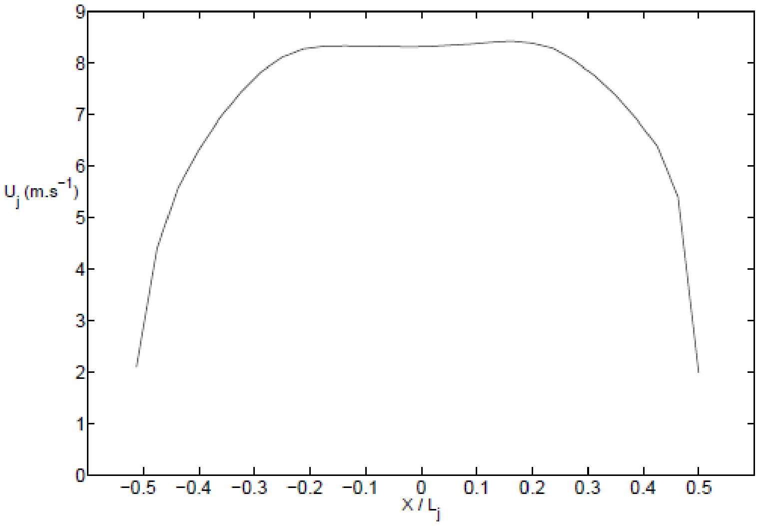

(a) Experimental profile

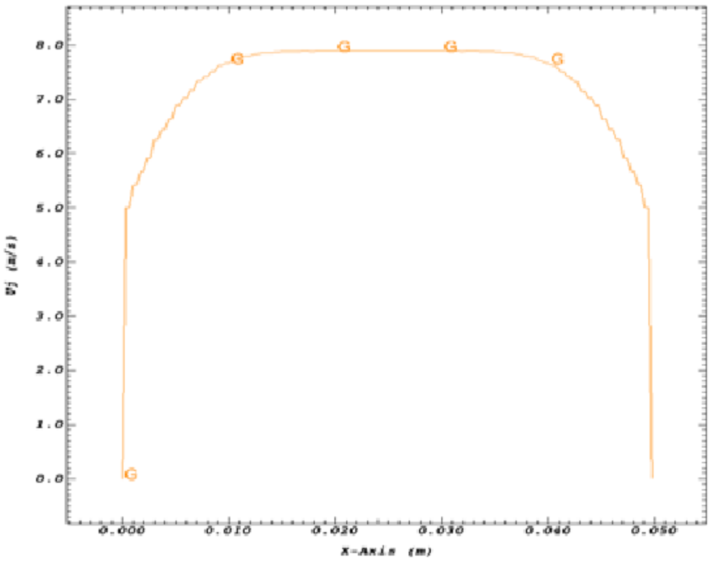

(b) Jet lenght test results

Figure 4.38: Comparison between the $k - \varepsilon$ model and the experimental horizontal velocity profile at the jet outlet section

4.2.1.3 Comparison with experimental data

As it will be possible to see from the figures reported in this section, the mean trends are captured by the $k - \varepsilon$ model, with an average deviation of 0.3 m/s from the experimental values for what concern the velocity fields reported in Fig. **??**, **??** and **??**. However, the mesh adopted in these cases is still not enough refined to achieve a really detailed resolution. The RMS values as expected, are not well predicted, neither in amplitude nor in location; therefore detailed description of this aspect will be postponed to the LES section. By making a comparison between the two mesh arrangements it is possible to notice how the structured one conserve better the total energy, producing a jet penetration that goes further than the lenght estimated by the experimenters if we follow the jet trajectory; however the penetration in the Y direction is still comparable to experimental data. Moreover this effect leads to create a net division between the two sub-vortices along the jet trajectory. On the other hand, the diffusive behaviour of the unstructured arrangement solutions, match better with the experimental data, showing a lower conditioning on all the above-mentioned effects. In Fig. **??** a schematization of the investigation planes is shown.

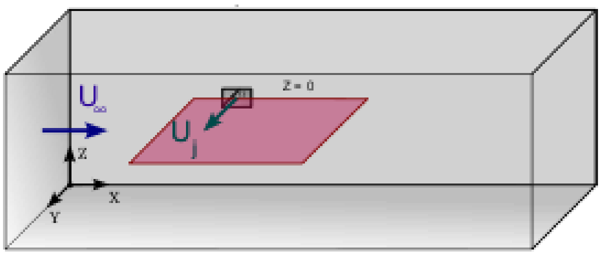

(a) XY plane

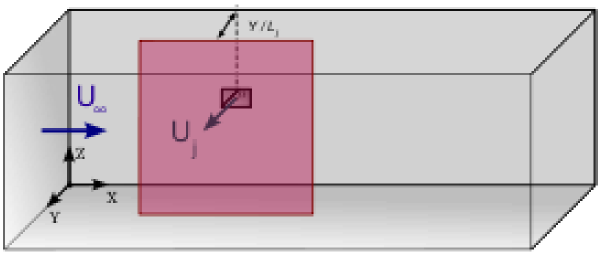

(b) XZ plane

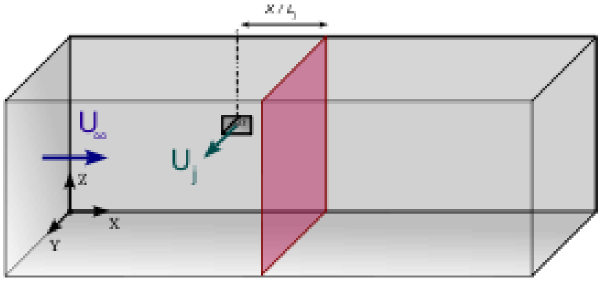

(c) YZ plane

Figure 4.39: Orientation of the measurement planes into the test section domain. [**?**]

Results from the unstructured Mesh no.3

In Fig. **??** (a) it is possible to see that the $k-\varepsilon$ model gives relatively satisfactory solutions both in terms of scalar value and of their spatial collocation in the mean field. However it is possible to notice that the core region of the jet is slighlty enlarged in respect to the experimental one, but the global penetration lenght is still well predicted. Root mean square values (Fig. **??** (b)) does not hold any significative value.

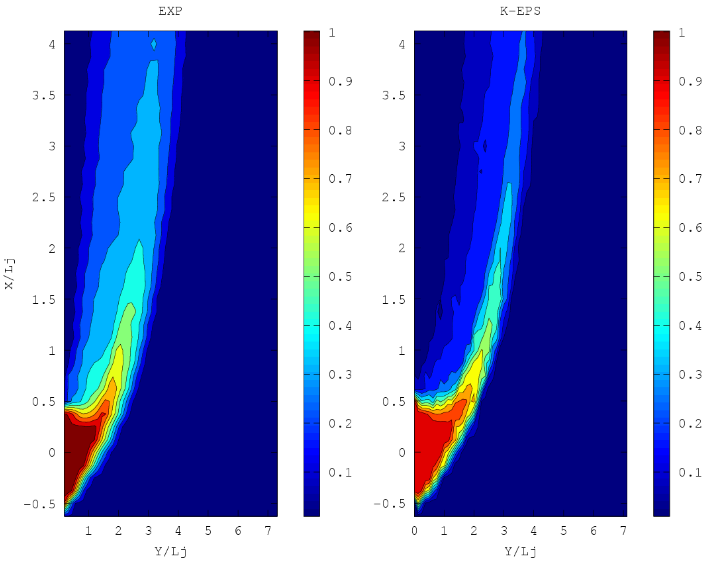

(a) $\overline{T^*}$

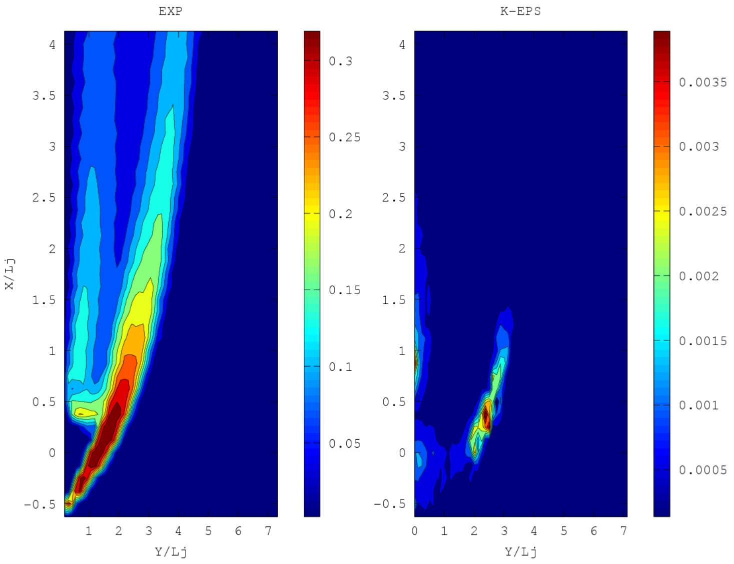

(b) σ_T^*

Figure 4.40: RANS $k-\varepsilon$ approach, dimensionless temperature fields, XY plan at z = 0 mm.: Time average plot (a), root mean square plot (b)

Looking at the region of the jet outlet section (Fig. **??**) the temperature mean field represented by the solution presents fair accuracy, but misses the initial formation of the trailing edge vortices on the outer part of the jet. On the contrary, the lower temperature recorded on the inner parts, suggest that the mixing phenomena already started at this point.

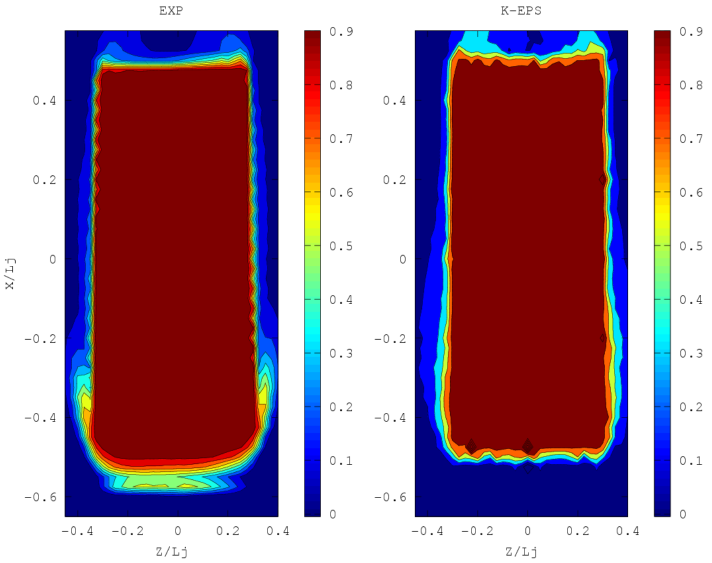

(a) $\overline{T^*}$

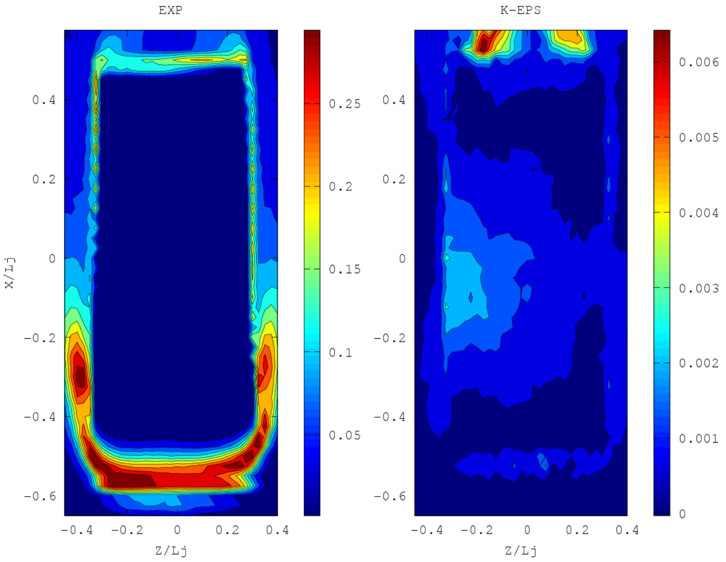

(b) σ^*_T

Figure 4.41: ANS $k-\varepsilon$ approach, dimensionless temperature fields, XZ plan at y = 2 mm. : Time average plot (a), root mean square plot (b)

Proceeding on a parallel plane shifted 20 mm from the jet outlet section, the jet core zone starts to deform. The mesh refinment in this zone does not give an high resolution in the temperature field, however the global shape of the jet is sufficiently accurate for the final aims of the study. The presence of the outer and inner trailing edge vortices in the solution (Fig. **??**) confirm this evaluation.

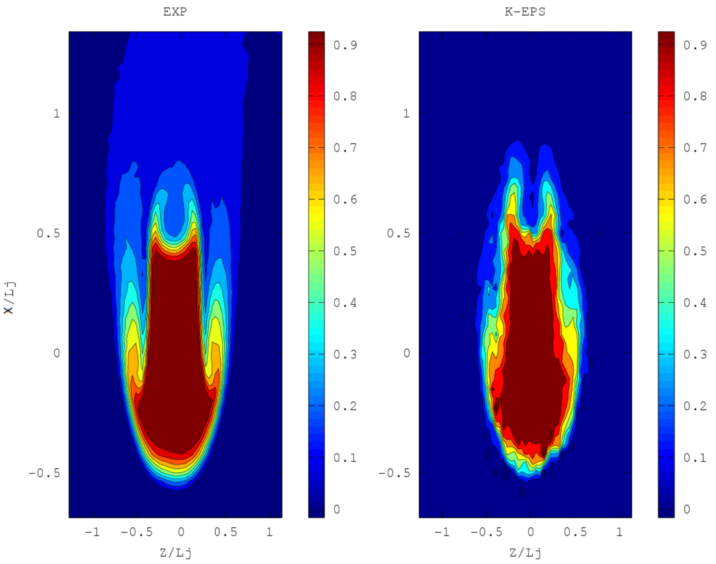

(a) $\overline{T^*}$

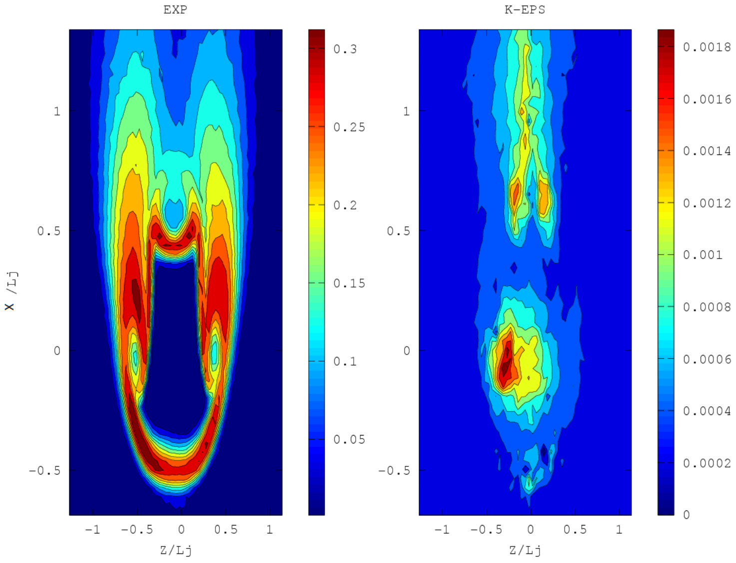

(b) σ_T^*

Figure 4.42: RANS $k - \varepsilon$ approach, dimensionless temperature fields, XZ plan at y = 20 mm. : Time average plot (a), root mean square plot (b)

The section shown in Fig. **??** is placed at a 20 mm distance from the previous one. The shift of the jet core location suggests that the jet is approaching the deflection zone. The solution follow correctly this shift, even if the interpolation quality does not show a good agreement of the thermal layer located on the outer part of the jet. However, the global behaviour of the flow development shown in the solution, suggests that the calculation delays the formation of the inner tracking vortices, as it can be noticed by comparing the thermal gradients downstream the inner zone.

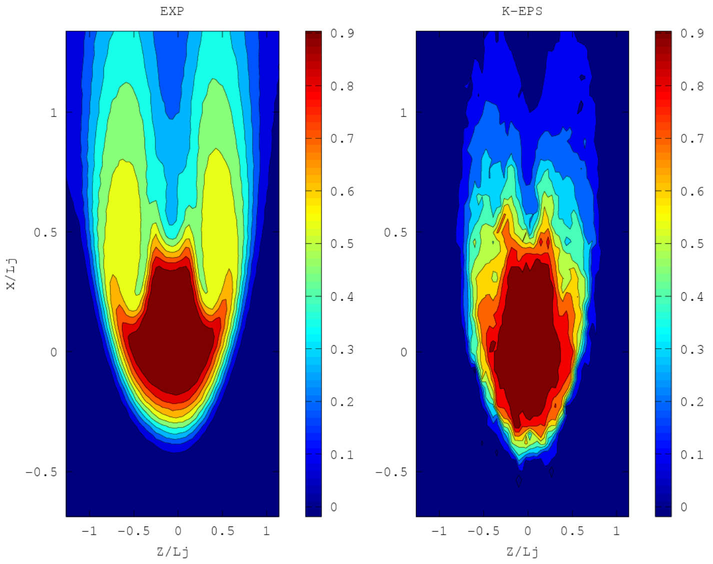

(a) $\overline{T^*}$

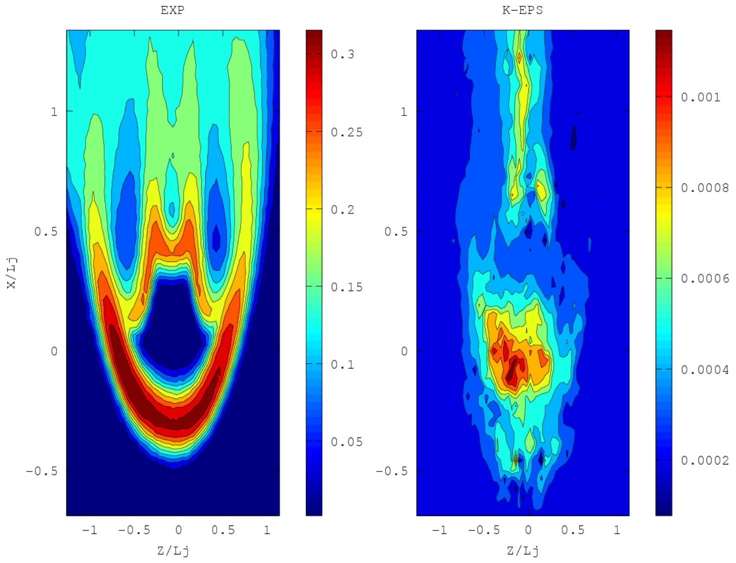

(b) σ_T^*

Figure 4.43: RANS $k - \varepsilon$ approach, dimensionless temperature fields, XZ plan at y = 40 mm. : Time average plot (a), root mean square plot (b)

The last plot of the jet potential zone is shown in Fig.**??**. This plot is located 60 mm far from the jet exit. Experimental data show that the flow coming from the rectangular section almost lose its original shape from this point. The $k - \varepsilon$ solution respects this change in shape, but still underestimate the mixing effects. The temperature distribution on the inner layer has a considerable gradient compared to the one shown by the experimental data. Besides, in the CFD plot it is possible to notice that the advective contributions is prevalent compared to diffusion, and this can be noticed in particular, by observing the presence of small zones at higher temperature than the average on the jet wake. (Fig. **??** (a)).

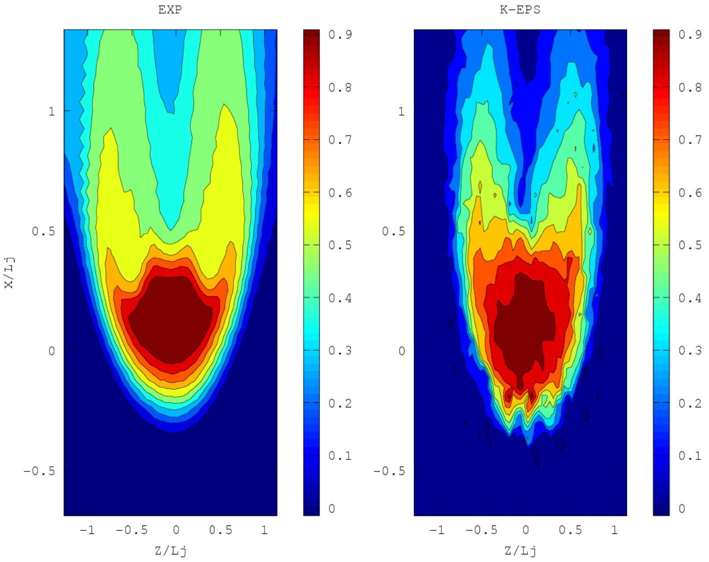

(a) $\overline{T^*}$

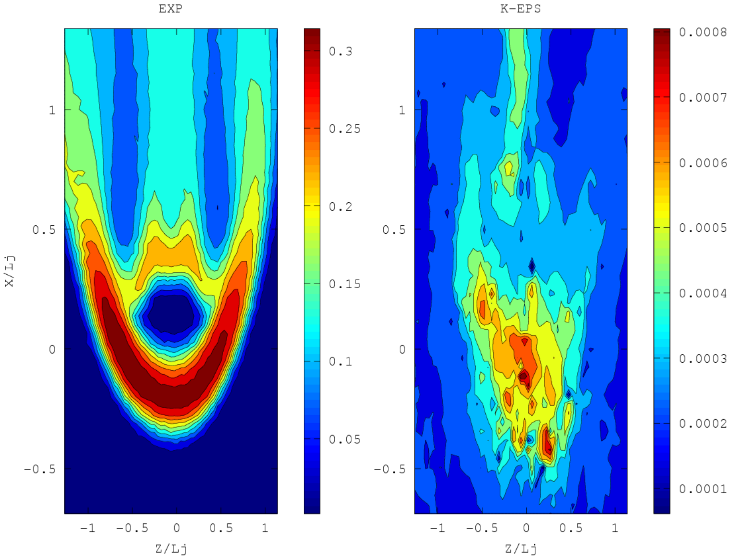

(b) σ^*_T

Figure 4.44: RANS $k - \varepsilon$ approach, dimensionless temperature fields, XZ plan at y = 60 mm. : Time average plot (a), root mean square plot (b)

Starting from this point the comparisons will proceed on YZ planes, parallel to the main channel inlet section. Velocity fields are reported in Fig. **??** and **??** in a plane located 240 mm downstream the jet center. This region belongs to the end part of deflection zone. As it is possible to see the jet outer mixing zone is accelerated by the main flow, so that the flow in this region has stronger transversal components. It should be noted that the axial component u is the same for both the velocity fields, while the v component (named horizontal from this point) represents the jet penetration capabilities (Fig. **??**).

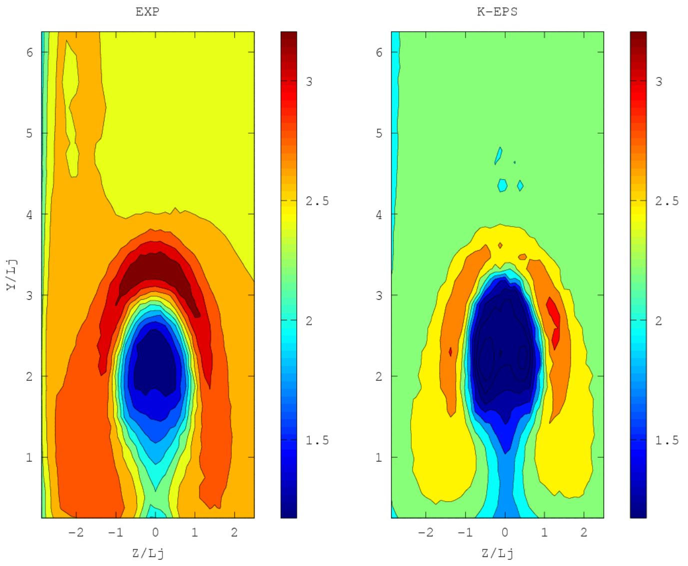

(a) $\sqrt{u^2+w^2}$

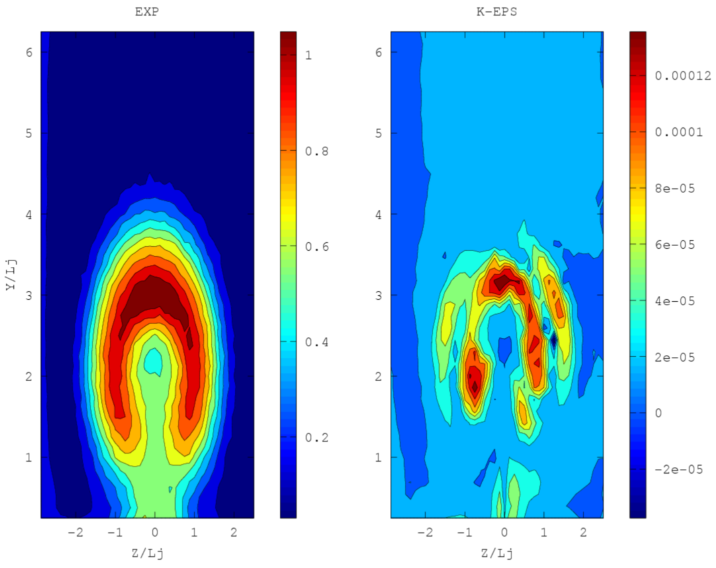

(b) $\sigma_{\sqrt{u^2+w^2}}$

Figure 4.45: RANS $k-\varepsilon$ approach, Comparison between experimental and numerical velocity field. YZ plan at x = 240 mm. : time average values (a), Root mean square. The colorbar scale is in m/s

The w component (named vertical from here on) in Fig. **??** describes better the vertical motions of the fluid, which is more significant fot the description of the CVP structure. At this stage it is possible to observe that the circular shape of the vertical velocity profile suggests a symmetry condition in the XY plane, this can be understood as an absence of rotational movements in the ZX plane. The horizontal v components, still shows symmetry characteristics, but on the central part of the section ($Z/L_j = 0$) this transveral component is predominant compared to the vertical one; leading to the consideration that the flow still has some horizontal deviation in this part of the main channel. For both the velocity fields, the numerical solution seems to respect the global behaviour of the experimental stream. Even if the color contrast appeareance can lead to a mismatch on the average value, the color bar scale shows that the differences between the experimental and numerical velocity field are in the order of few tenth of m/s.

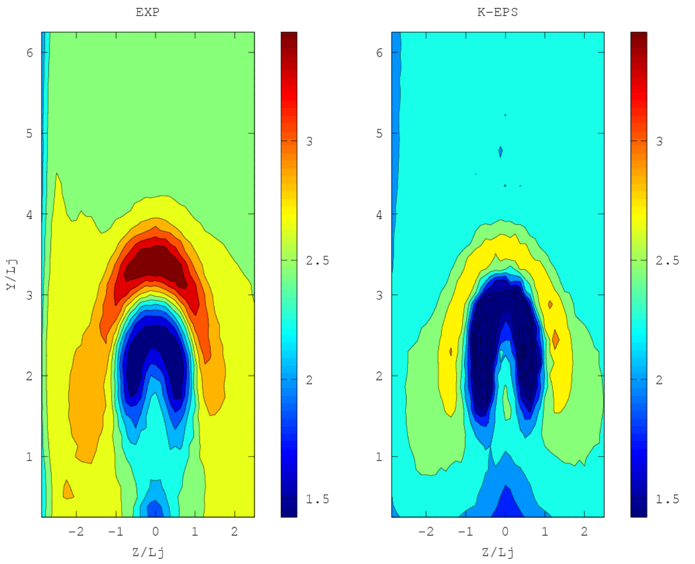

(a) $\sqrt{u^2+v^2}$

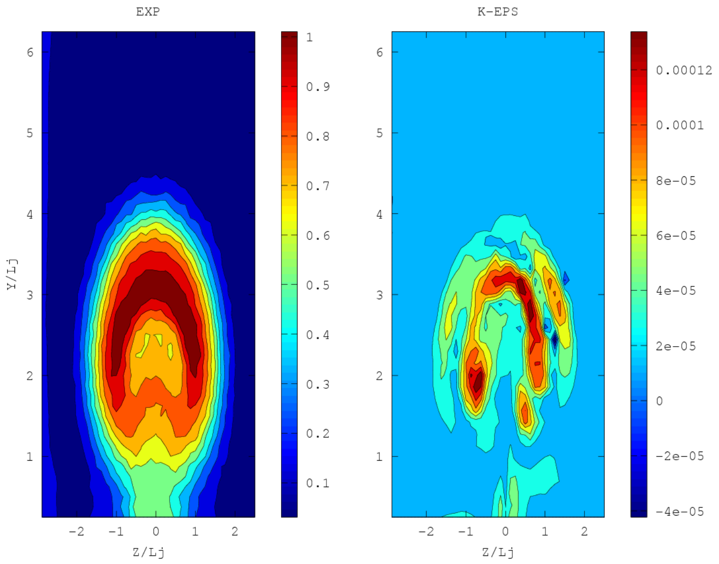

(b) $\sigma_{\sqrt{u^2+v^2}}$

Figure 4.46: RANS $k-\varepsilon$ approach, Comparison between experimental and numerical velocity field. YZ plan at x = 240 mm. : time average values (a), Root mean square (b). The colorbar scale is in m/s

On the same plane, Fig. ?? and ?? shows the dimensionless temperature fields, on the same plane. The measurements in this section of the jet have been repeated twice. The maximum temperature recorded from both the experimental and the numerical solution is in the order of a third of the temperature difference between the inlet main and jet streams. The horseshoe structure here starts to appear, the numerical solution underestimates the diffusion effects on the central symmetry line of the structure, so that the temperature field shown by the calculation is not homogeneous as represented by the experimenters. However the two hot lobes located at $Y/L_j \approx 2$ and $Z/L_j \approx \pm 0.75$ of the experimental data confirm that the same trend is followed by the physical phenomena.

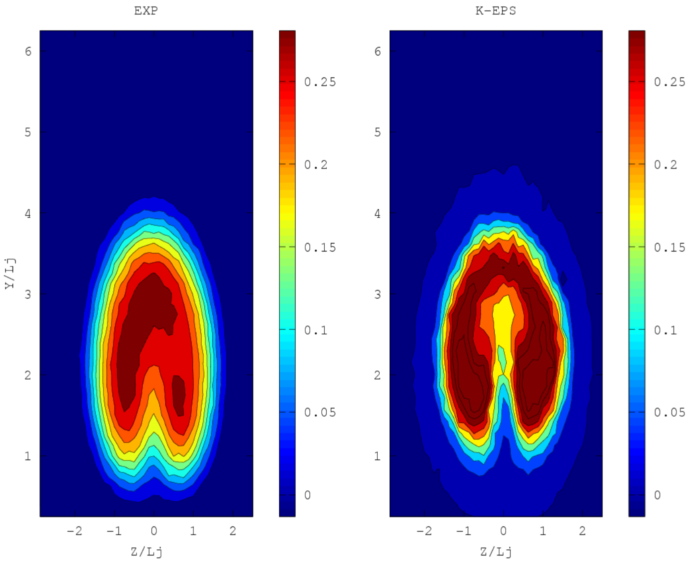

(a) $\overline{T^*}$

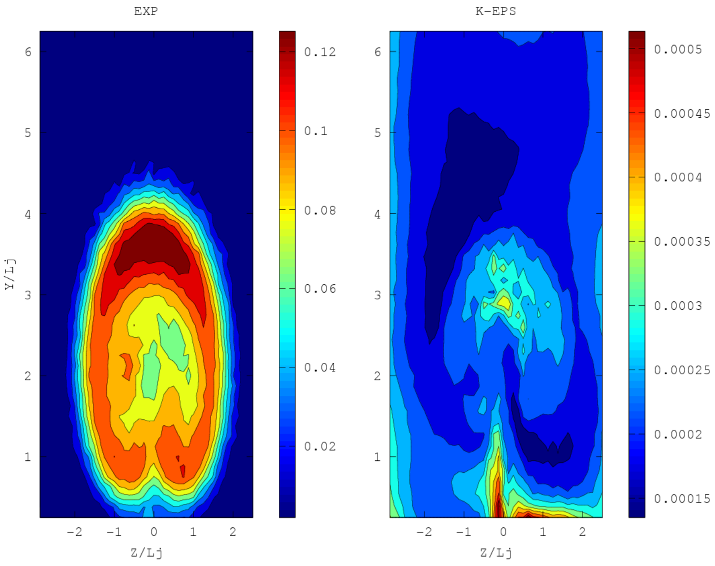

(b) σ_T^*

Figure 4.47: RANS $k - \varepsilon$ approach, comparison between experimental and numerical dimensionless temperature fields. YZ plan at x = 240 mm. : time average values (a), Root mean square (b).

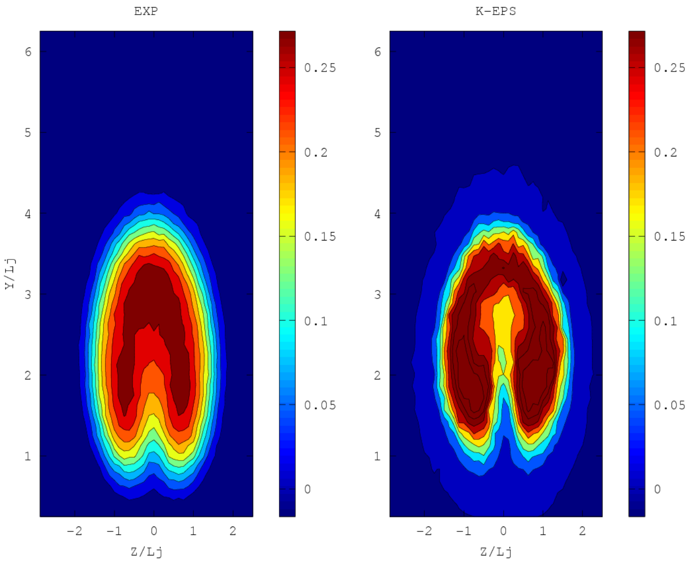

(a) $\overline{T^*}$

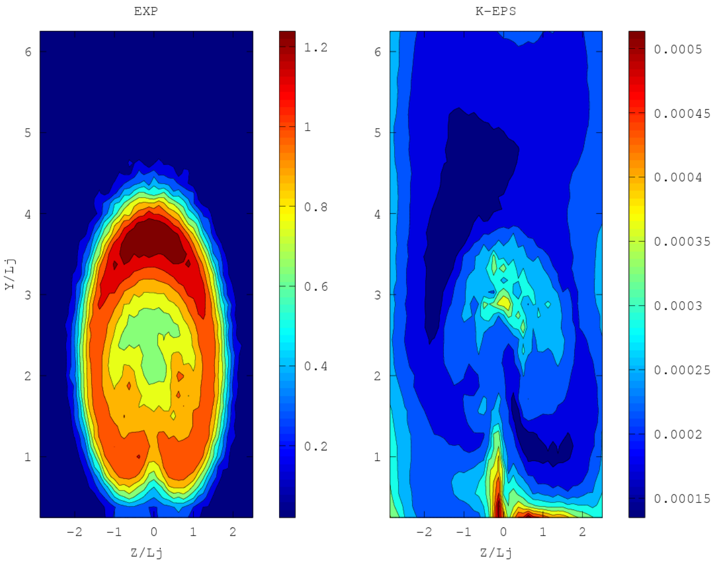

(b) σ_T^*

Figure 4.48: RANS $k-\varepsilon$ approach, comparison between experimental and numerical dimensionless temperature fields. YZ plan at x = 240 mm. : time average values (a), Root mean square (b).

Moving to the next section located in the plane YZ at X/L_j = 6 we approach the far field zone. Fig. **??** shows zones which are similar to those found in the previous plane (Fig. **??**). The maximum velocity zone is still located in the mixing layer region. However it is possible to observe that the velocity gradients are less steep than those recorded in the upstream sections. The solution misses to mark this zone, but still represent the higher velocity contours around the counter rotating vortices.

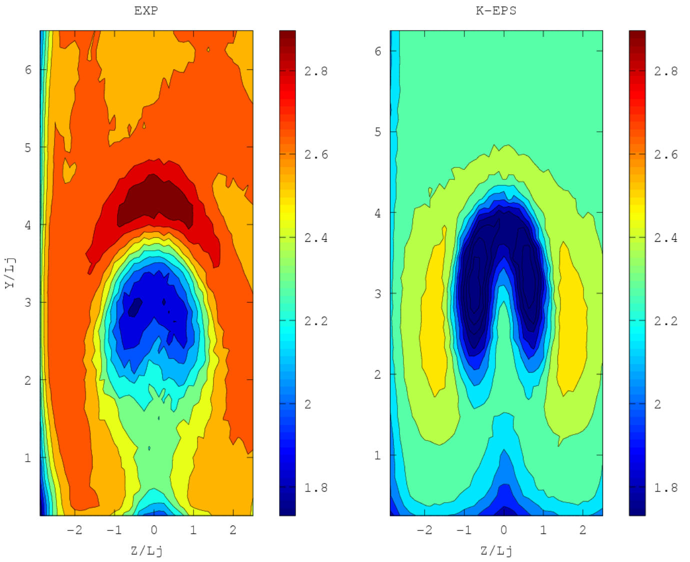

(a) $\sqrt{u^2+v^2}$

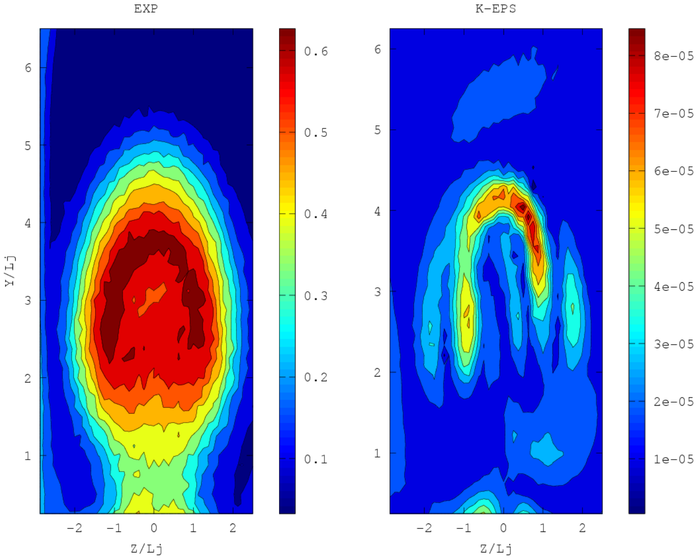

(b) $\sigma_{\sqrt{u^2+v^2}}$

Figure 4.49: RANS $k-\varepsilon$ approach, comparison between experimental and numerical velocity field. YZ plan at x = 480 mm. : time average values (a), Root mean square (b). The colorbar scale is in m/s

The temperature field shown in Fig. **??** describes the CVP structure, the hot core is shifted to the central part of the section, and it is possible to see that the thermal gradient starts to interact with the duct walls. At this point of the main channel, the temperature difference between the jet core and the air coming from the channel, is less than one sixth of its maximum. In the solution the horseshoe shape is emphatized by the advective terms, the diffusion still lack of effectiveness in the central part. However, the core location and the global shape are sufficiently described for the purposes of this study.

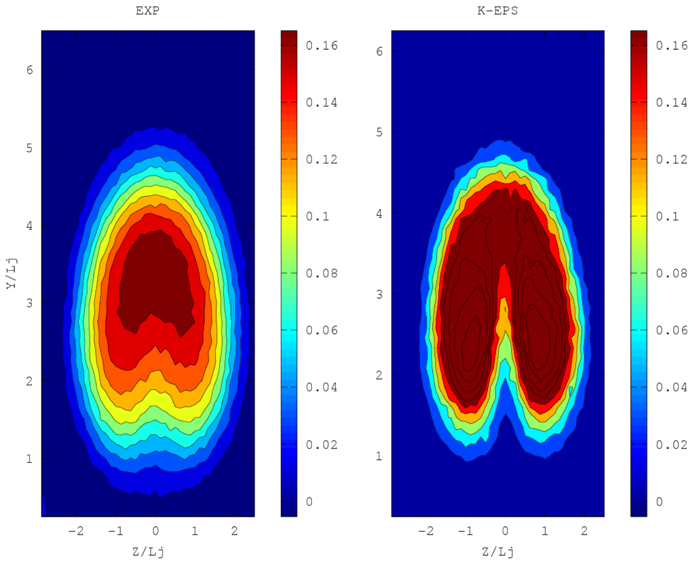

(a) $\overline{T^*}$

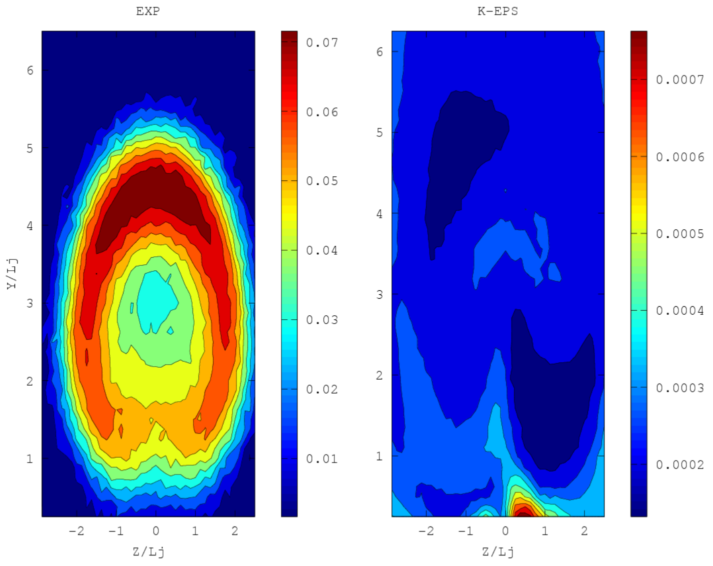

(b) σ_T^*

Figure 4.50: RANS $k-\varepsilon$ approach, comparison between experimental and numerical dimensionless temperature fields. YZ plan at x = 480 mm. : time average values (a), Root mean square (b).

Results of the Structured Mesh no.4

Results from the structured arrangment of the mesh using RANS $k-\varepsilon$ model are shown in this section. Starting from the horizontal cutplane of the domain, the temperature field is investigated in Fig. **??** (a). It is possible to see how the structured arrangment overestimates the prediction the jet core lenght, so that is possible to argue that the advective terms are conditioned by the element face orientation. However, even if there is a mismatch in the core zone dimensions between experiments and CFD results, the jet penetration lenght in the Y direction obtained from the RANS model still respects the experimental observations.

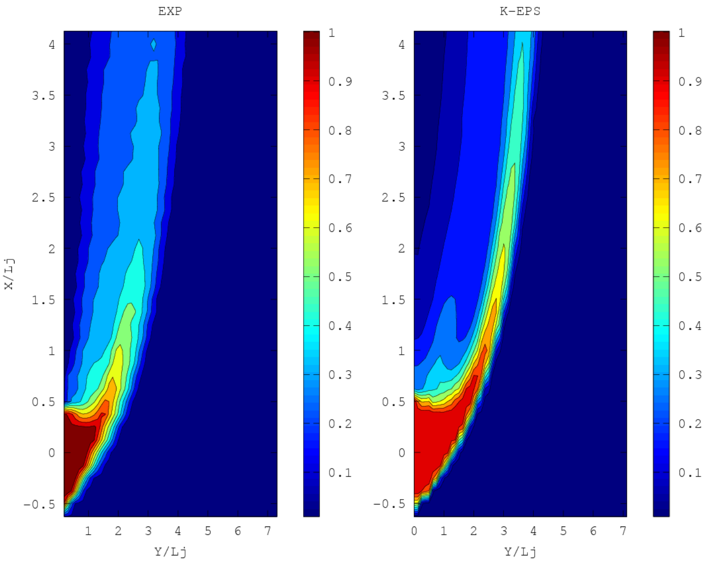

(a) $\overline{T^*}$

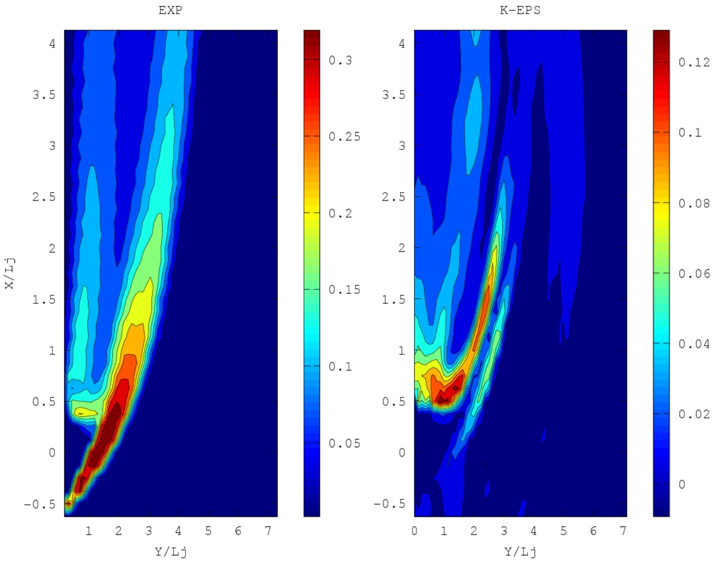

(b) σ_T^*

Figure 4.51: RANS $k - \varepsilon$ approach, comparison between experimental and numerical dimensionless temperature fields. XY plan at z = 0 mm. : time average values (a), Root mean square (b).

Moving to the jet exit cut plane (Fig. **??**) it is possible to observe that the temperature field given by the solution still lacks of generating the initial trailing edge vortices on the outer part of the jet. However the wavy temperature distribution along the top and the bottom lines of the jet is represented but results too marked with respect to the experimental measurements.

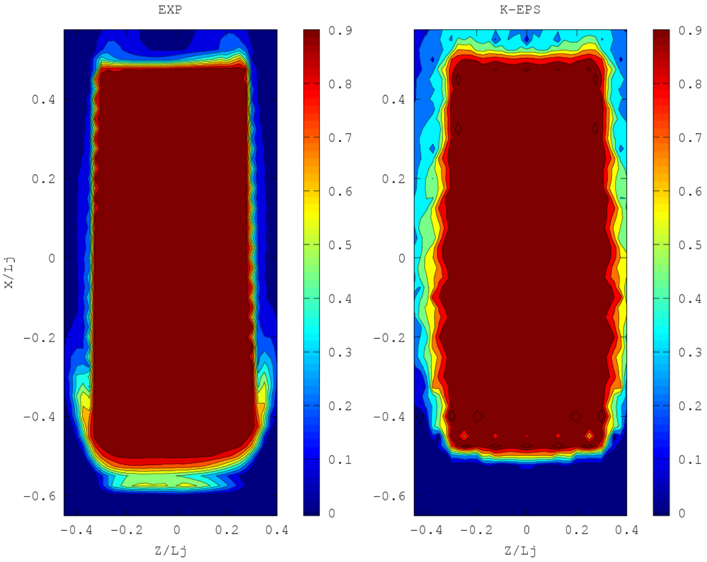

(a) $\overline{T^*}$

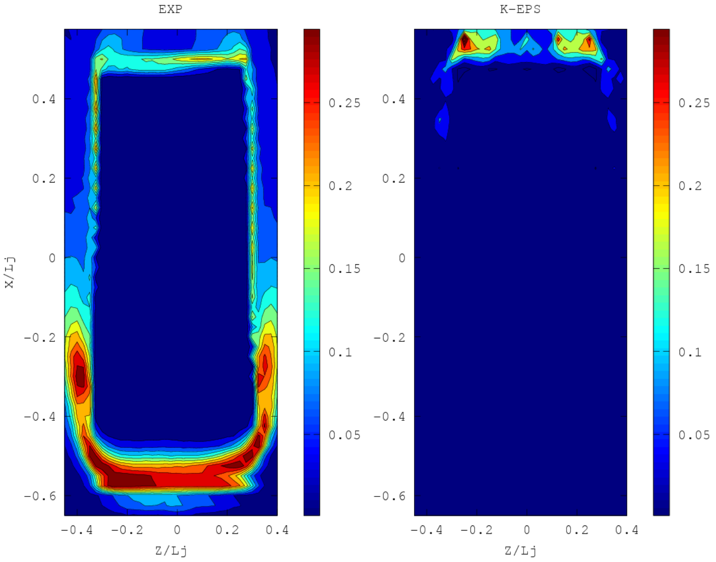

(b) σ_T^*

Figure 4.52: RANS $k - \varepsilon$ approach, comparison between experimental and numerical dimensionless temperature fields. XZ plan at y = 2 mm. : time average values (a), Root mean square (b).

Going forward, through the jet penetration zone (Fig. **??**), the solution still does not generate any trailing edge vortices on the outer part, according to the advective behaviour shown in the horizontal cut plane (Fig. **??**). This explain why the core zone shown in the solution, occupy a greater part of the domain in respect to what the experimental values shows. The lack of these vortices in fact, decreases the mixing phenomena and let causes jet to keep close to the original shape of the exit section.

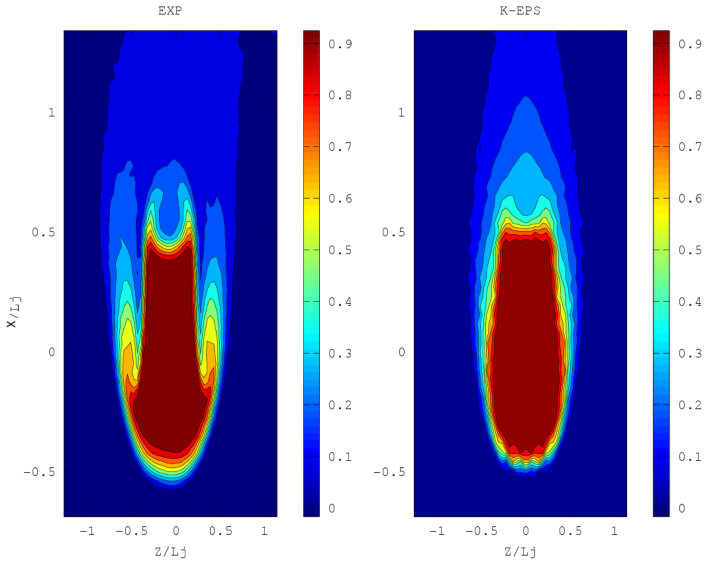

(a) $\overline{T^*}$

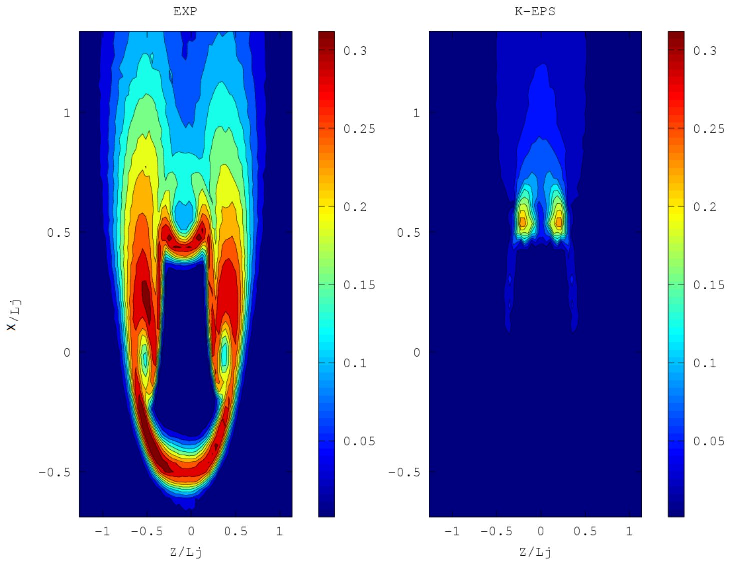

(b) σ_T^*

Figure 4.53: RANS $k-\varepsilon$ approach, comparison between experimental and numerical dimensionless temperature fields. XY plan at z = 20 mm. : time average values (a), Root mean square (b).

This trend is maintained for the whole potential zone as it is possible to see in Fig. **??**; even if the outer parts start to deform, the solution shows that the jet shape trend has a spatial delay on generating the horseshoe structure. This confirms that, to obtain a good resolution in the behaviour of the jet core, the structured arrangment requires a refinment with more elements with respect to those that would be required for the unstructured arrangment. On the other hand, the greater quantity of elements in this mesh still gives a better resolution of the scalar fields if compared to the previous Mesh no. 3 calculation.

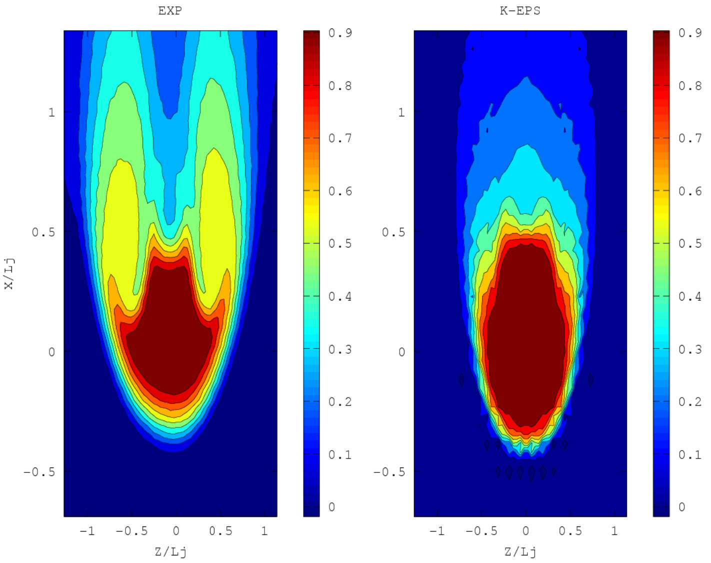

(a) $\overline{T^*}$

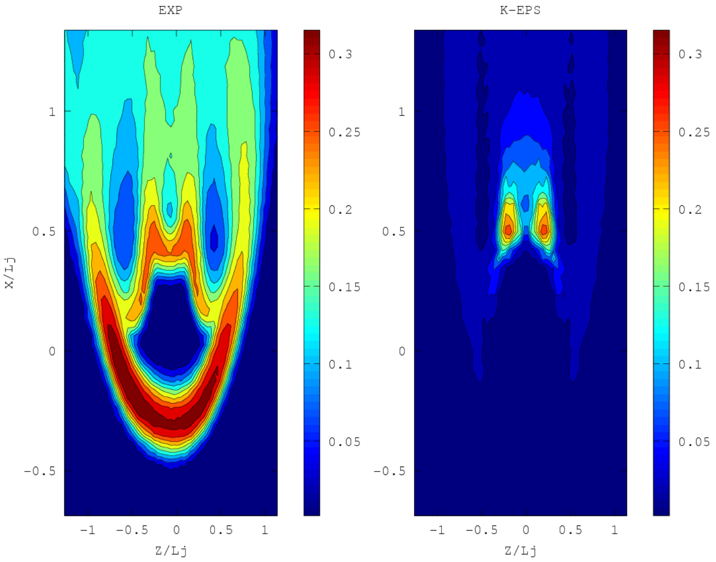

(b) σ_T^*

Figure 4.54: RANS $k - \varepsilon$ approach, comparison between experimental and numerical dimensionless temperature fields. XY plan at z = 40 mm. : time average values (a), Root mean square (b).

Approaching the maximum deflection zone, the temperature field shown in Fig. **??** proves that the solution respects the location of the central part of the jet core, even if the overall extension and shape does not perfectly agree with the experimental data. Moreover both the top and the bottom part of the jet presents a trace of the mixing layer vortices structure which propagate, up to the downstream part of the inner region of the jet, mixing effects. This observation can be confirmed by looking at the thermal gradient in the above-mentioned region.

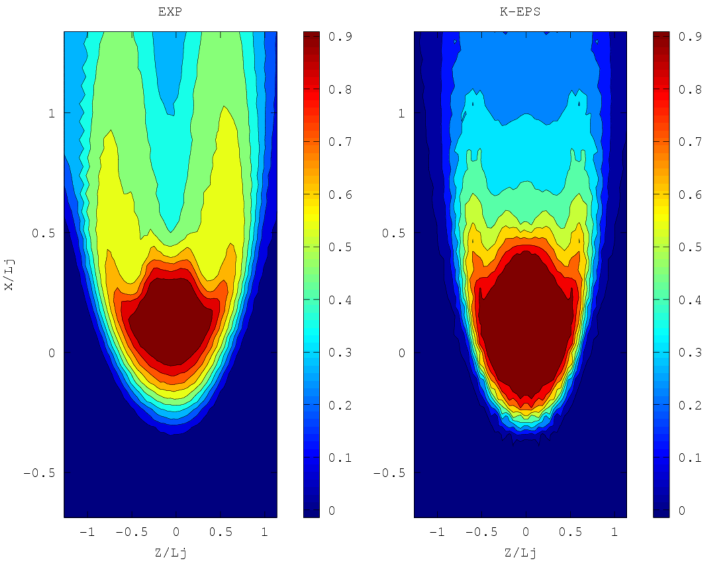

(a) $\overline{T^*}$

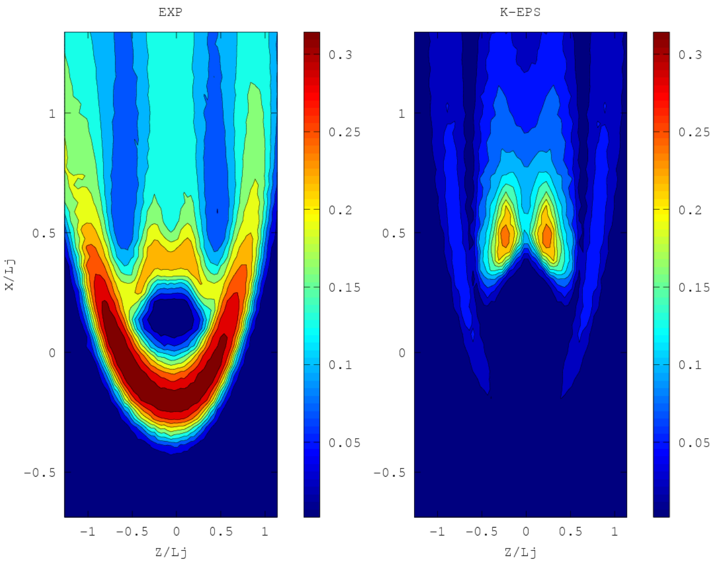

(b) σ_T^*

Figure 4.55: RANS $k - \varepsilon$ approach, comparison between experimental and numerical dimensionless temperature fields. XY plan at z = 60 mm. : time average values (a), Root mean square (b).

Once the maximum deflection zone is reached, the velocity fields reported in Fig. **??** and **??** shows a general good agreement between the solution and the experimental data. In both cases the v and w component predicted agree with the contour shape of the experimental tests. Moreover, the outer part of the jet presents the higher velocity region, which is symmetrical to the XZ plane.

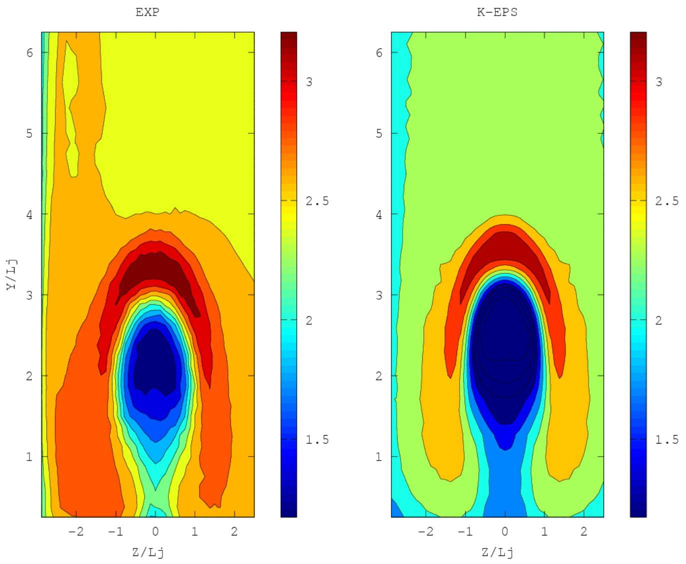

(a) $\sqrt{u^2 + w^2}$

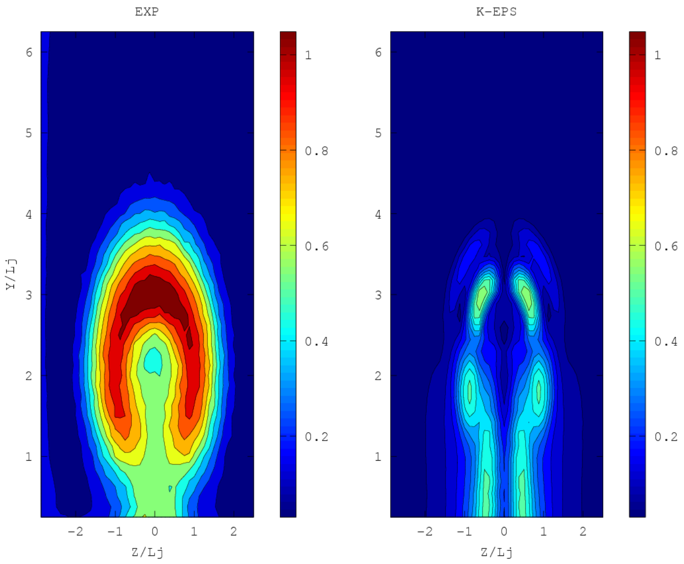

(b) $\sigma_{\sqrt{u^2+w^2}}$

Figure 4.56: RANS $k - \varepsilon$ approach, comparison between experimental and numerical velocity field. YZ plan at x = 240 mm. : time average values (a), Root mean square (b). The colorbar scale is in m/s

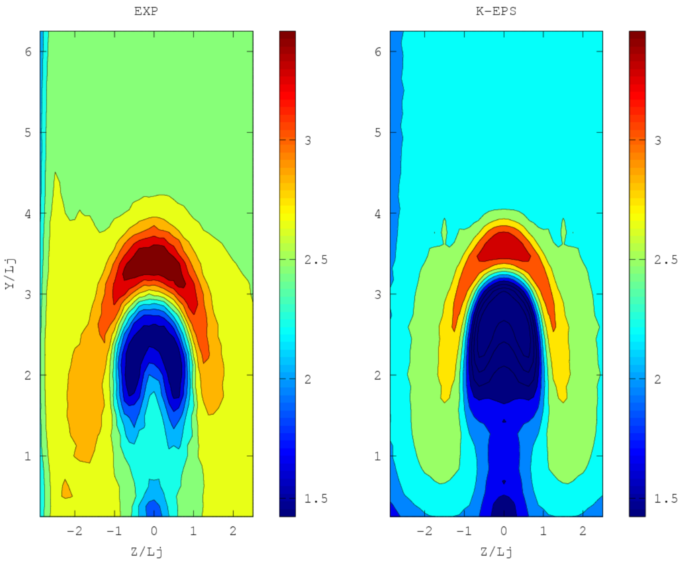

(a) $\sqrt{u^2+v^2}$

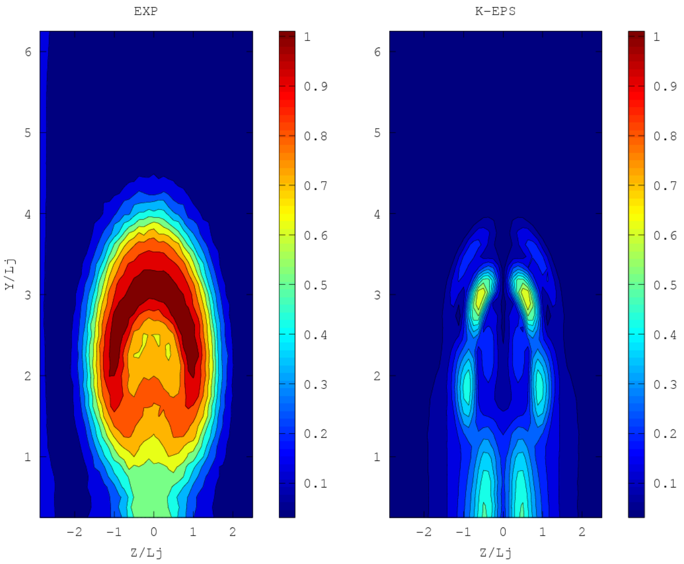

(b) $\sigma_{\sqrt{u^2+v^2}}$

Figure 4.57: RANS $k-\varepsilon$ approach, comparison between experimental and numerical velocity field. YZ plan at x = 480 mm. : time average values (a), Root mean square (b). The colorbar scale is in m/s

At the same location, it is possible to see in Fig. **??** and **??** that the CVP structures are still generated in the $k - \varepsilon$ calculation. However, the strong advection contribution still results in a hotter core with respect to the one obtained by the experimenters. The internal wedged shape of the jet is more pronounced in the numerical solution, according to the considerations about the underestimated diffusion phenomena already made.

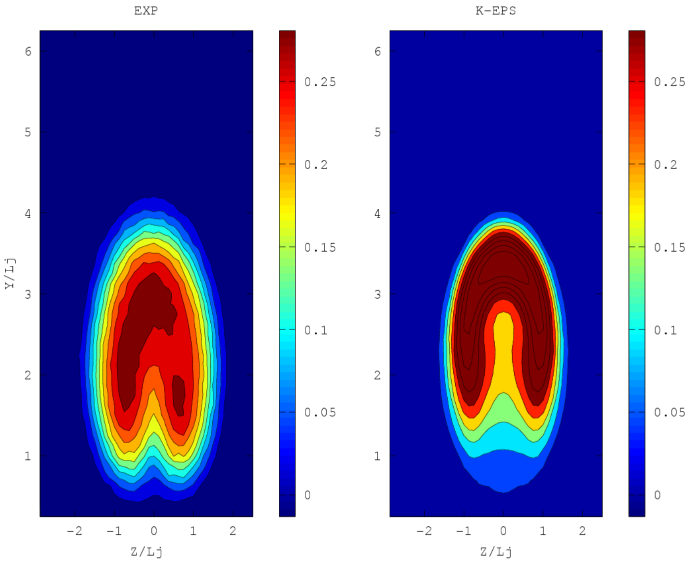

(a) $\overline{T^*}$

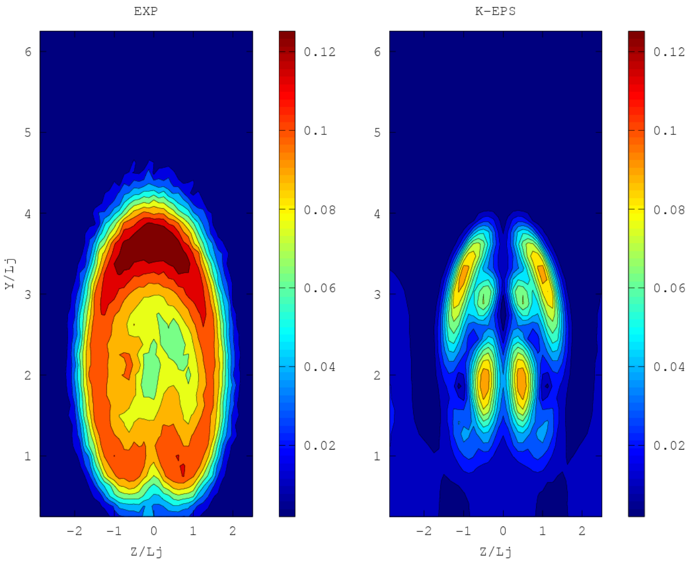

(b) σ_T^*

Figure 4.58: RANS $k - \varepsilon$ approach, comparison between experimental and numerical dimensionless temperature fields. YZ plan at x = 240 mm. : time average values (a), Root mean square

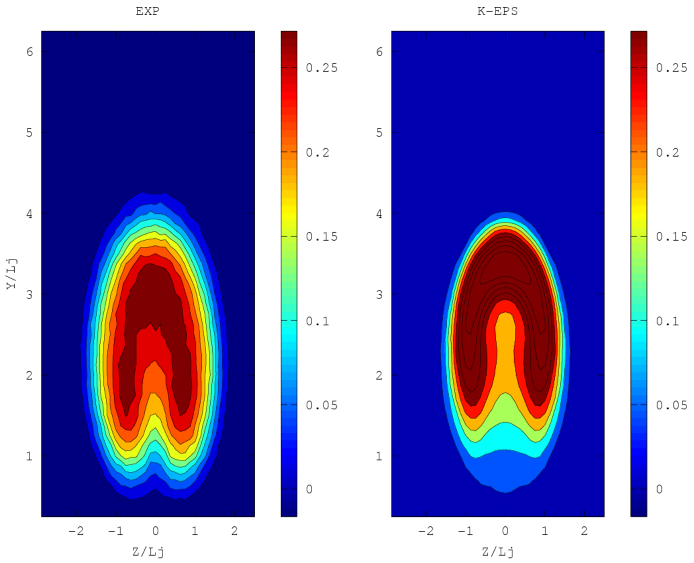

(a) $\overline{T^*}$

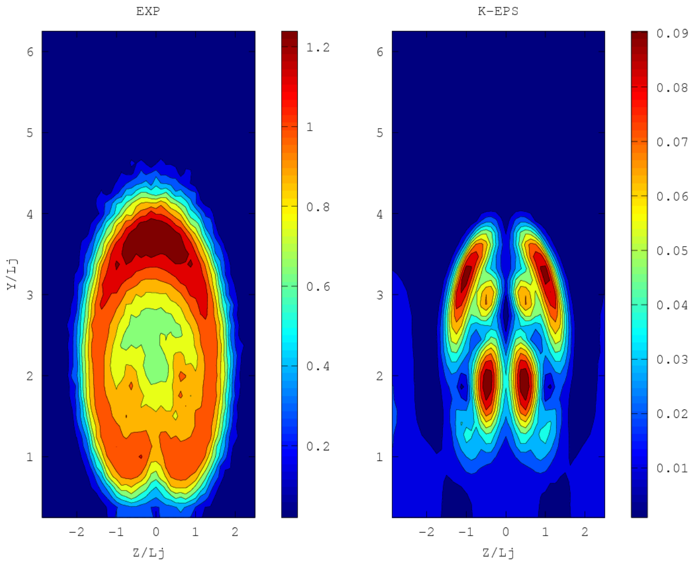

(b) σ_T^*

Figure 4.59: RANS $k - \varepsilon$ approach, comparison between experimental and numerical dimensionless temperature fields. YZ plan at x = 240 mm. : time average values (a), Root mean square (b)

Looking furthermore downstream along the main channel in a parallel plane located at x=480 mm it is possible to notice from Fig. **??** that in this case, the solution shows the largest velocity region in the outer part of the jet. The asymmetry of the experimental plot is due to stochastic effects coming from the inlet section of the main channel, which cannot be accurately predicted and involved into the boundaries definitions.

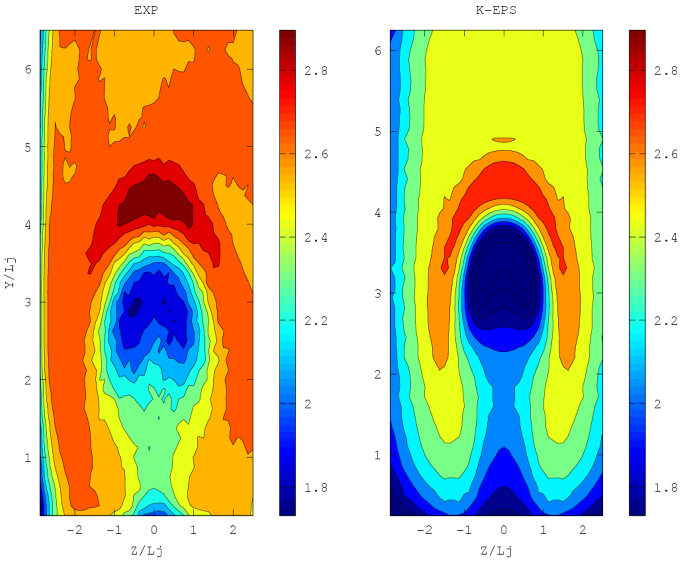

(a) $\sqrt{u^2+v^2}$

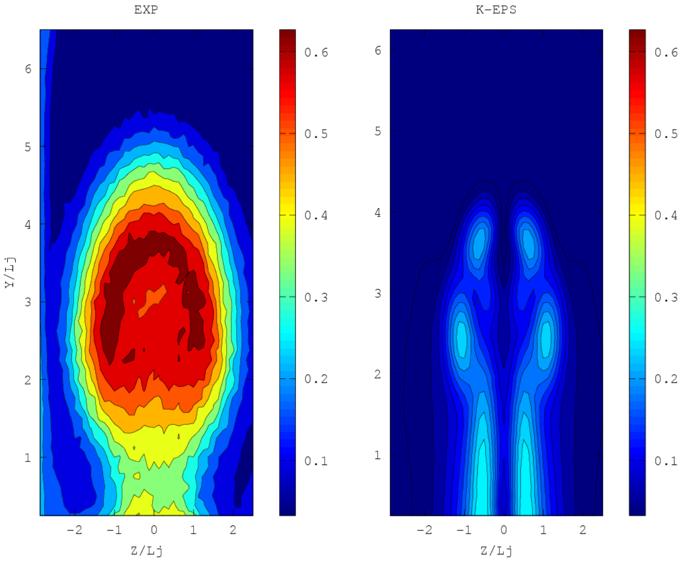

(b) $\sigma_{\sqrt{u^2+v^2}}$

Figure 4.60: RANS $k-\varepsilon$ approach, comparison between experimental and numerical velocity field. YZ plan at x = 480 mm. : time average values (a), Root mean square (b). The colorbar scale is in m/s

At the same location, the temperature field (Fig. **??**) of the solution shows approximatively a good positioning of the jet core and a reasonable prediction of its dimensions. Furthermore, the horseshoe shape is respected and the CVP structures can be distinguished. However, the hot jet core is still too large compared to what is shown by the experiments.

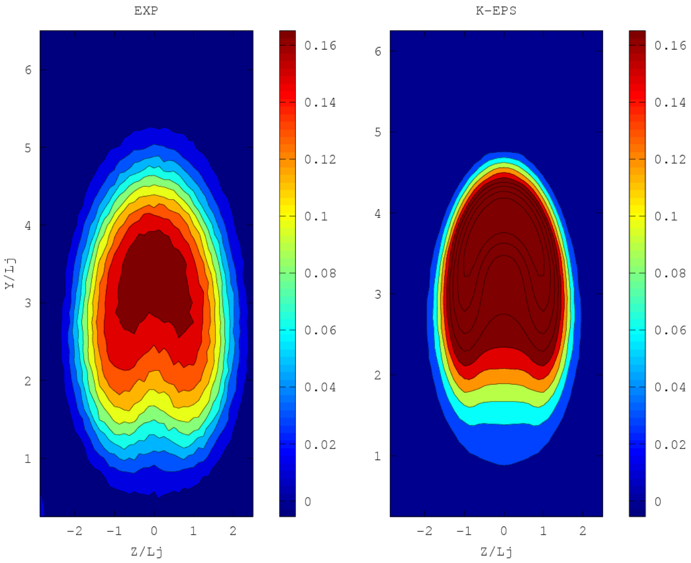

(a) $\overline{T^*}$

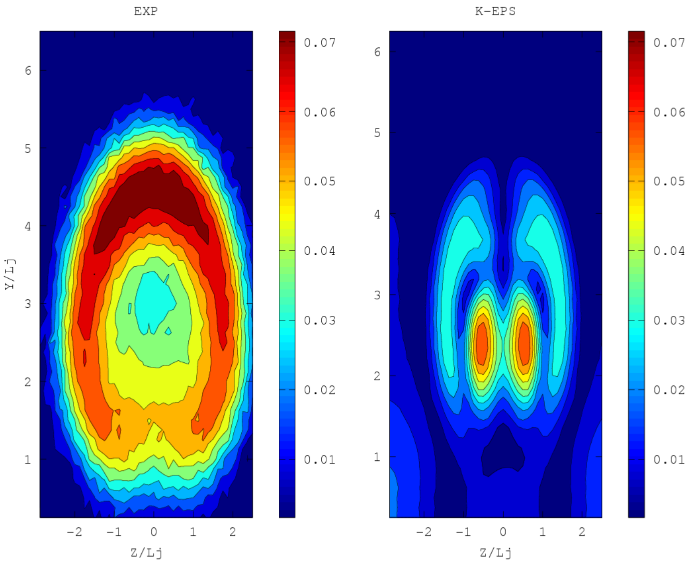

(b) σ^*_T

Figure 4.61: RANS $k - \varepsilon$ approach, comparison between experimental and numerical dimensionless temperature fields. YZ plan at x = 480 mm. : time average values (a), Root mean square (b)

Taylor Lenght Scale

The final objective of the RANS approach was to define a local Taylor Lenght scale for each part of the domain. Following the Turbulent Kinetic Energy (*TKE* in Fig. **??**) and the Turbulent Kinetic Energy Dissipation Ratio (*TKEDR* in Fig. **??**), the calculated values are obtained (Tab. **??**).

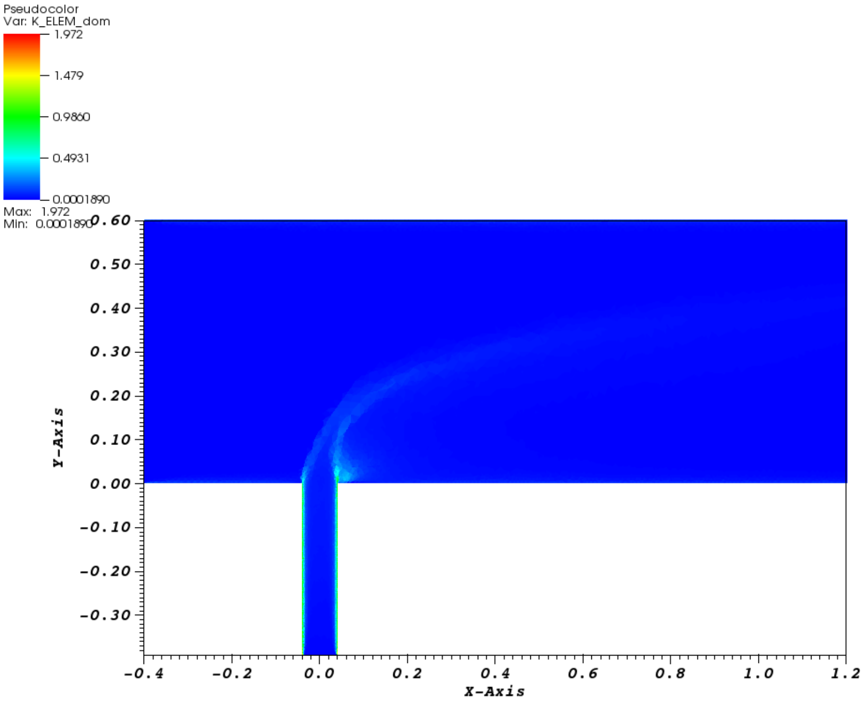

Figure 4.62: Longitudinal cutplane view of the TKE distribution

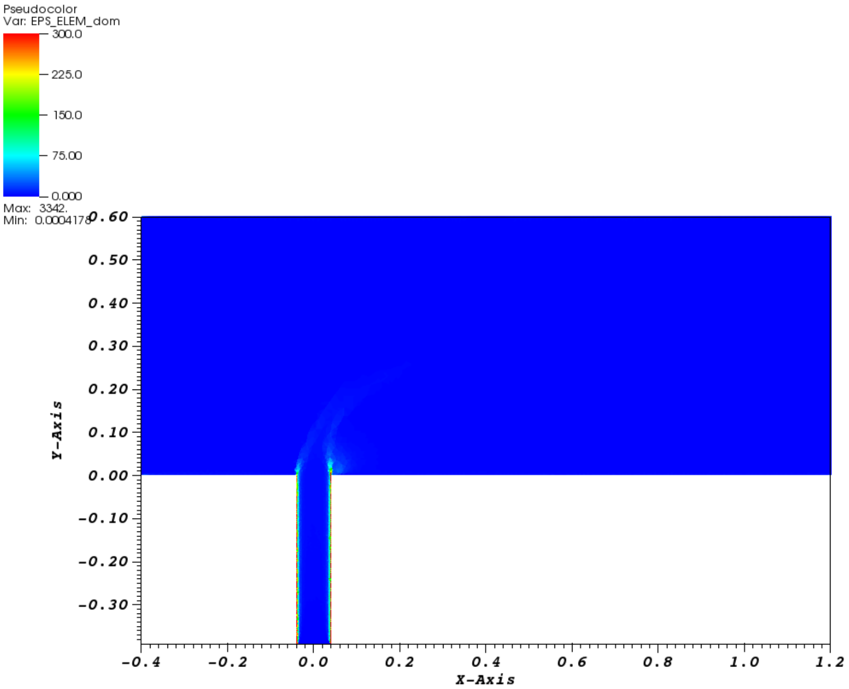

Figure 4.63: Longitudinal cutplane view of the TKEDR distribution

Sub domain	Taylor microscale scale [mm]
Upstream main channel	1.01
Upstream jet channel	1.34
Mixing zone and downstream main channel	1.21

Table 4.11: Taylor microscale extimation for subzones of the TRANSAT test section

Following the discretization scale calculated in table **??**, even though the original domain modification done to reduce the computational efforts made, a mesh of 60 millions of elements would be required for a LES calculation. The choice faced at this point of the work was to run one single calculation using this kind of refinment, or to underestimate the smaller turbulence scales by using a domain with a lower number of element; keeping the possibility to perform more than a single calculation. It must be underlined that the latter choice gives the oppurtunity to see which parameters defined during the modelization process, would have a predominant impact on the solution. Furthermore it gives the chance to evaluate what are the implications of the taylor micro scale on the final results for Jet in Crossflow. This option has been judged as the most reasonable, since it would give the possibilities to compare different model setups. It must be remarked the importance of these aspects. Nevertheless, this CFD study is the first one that has been performend on the TRANSAT facility; there are no other references to consider in literature as it was for the Vattenfall tee Junction test. In order to give a better understanding of the models and to see how much they can be refined still respecting the constraints of the calculation time, larger elements meshes have been tested.

4.2.2 LES

The calculation presents a transient behaviour of a global duration of less than two seconds of timeflow (Fig. **??**), a confidential margin of one second is taken into account to start the evaluation of the statistical values. The scalars transported by the flow, despite the high turbulent regime, reach a steady state in which the mean component is stabilized. In order to capture meaningful statistical informations the flows have been simulated for about twelve seconds. The spatial discretization adopted permits to advance with a timestep having an average magnitude of 10^{-5} s using an explicit scheme. The stability limitation on timestep computed by the code alghoritm is larger but has the same order of magnitude. The most expensive calculations in terms of CPU time involved the use of one thousand processors, keeping a CPU time of 1.56 s per timestep. On each of these CPU, 18000 elements have been assigned. An attempt of distributing 50000 elements per processor has been made[1] but the outcome showed that the CPU time required to reach convergence was in the average of 4.21 s per timestep. This would have caused the whole calculation to be completed in more than 55 days. These considerations should give an idea of how many resources and time are required to approach the Taylor lenght scale for this test case. Hereafter in table **??** the LES model setups used and the fluid properties are reported.

---

[1] The quantity of physical core kept busy for each calculation is one of the parameters used by the cluster owner to determine a priority chart in which each calculation is launched. Whenever the calculation demands is rated to be on the lower part of this chart, it must wait for available CPUs released from the top chart calculations. Until that time the server keeps the lower rated calculation in queue. Depending on how much the server is crowded, the queue time can be a serious limit whenever a time deadline must be defined for such works.

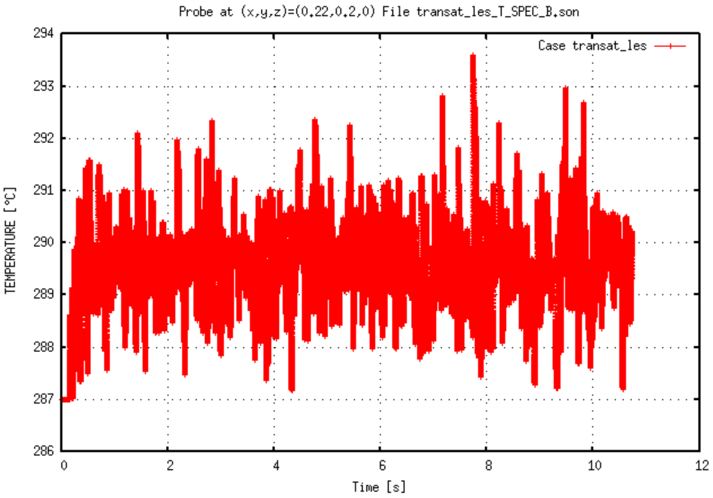

Figure 4.64: Temperature time history of the point A (Mesh no. 3)

Spatial discretization scheme	VEFPreP1B on Tetrahedral meshes
Time discretization scheme	2^{nd} Order Adam Bashforth 3^{rd} Order Runge-Kutta
Fluid physical properties	
$\mu\ \left[\frac{Ns}{m^2}\right]$	$1.76 \cdot 10^{-5}$
$\rho\ \left[\frac{kg}{m^3}\right]$	1.24
$\lambda\ \left[\frac{W}{m^2K}\right]$	$2.5 \cdot 10^{-2}$
$C_p\ \left[\frac{J}{KgK}\right]$	1005
$\beta\ \left[\frac{1}{K}\right]$	$3.47 \cdot 10^{-3}$
Navier Stokes equations	
Pressure Solver	PCG with SSOR
Convective scheme	Ef Stab α 0.2
Diffusive scheme	Second Order Centered
Turbulence model	WALE
Convection Diffusion Temperature equation	
Convective scheme	Ef Stab α 1 (Upwind)
Diffusion scheme	Second Order Centered
Turbulence	Turbulent Prandtl number

Table 4.12: Fluid properties and model setup for the LES calculations

4.2.2.1 Meshing

As already discussed previously, the size of the mesh elements adopted for the LES investigations is larger than the Taylor micro scale obtained from the k-ε analisys. For the finer mesh the mean lenght scale of each element is kept enlarged by a factor 1.5 with respect the Taylor lenght scale estimated from the RANS results, giving an overall integration volume which is 3 times bigger than the one required by adopting the Taylor micro scale. Therefore, the filter used for the SGS model is enlarged, giving less detailed information on the smaller scales. Recalling the transit time obtained from the TRANSAT flow conditions, it should be notice that a great part of the macroscopic turbulence can be still well predicted. Hereafter, the mesh adopted are summarised in table **??**

Mesh No.	**Mesh Structure**	**Number of elements**
1	Unstructured	4964712
2	Structured	14305920
3	Unstructured	18197215

Table 4.13: LES/WALE meshes

4.2.2.2 Boundary conditions

Respecting the hypothesis used for the Vattenfall case, the boundaries adopted are kept the same as those one used for the TRANSAT RANS approach. Low turbulence levels are reached after a path of about 10 cm downstream the inlet section. Nevertheless, the main inlet turbulence does not represent a driving phenomenon for the development of the jet flow. On the other hand, the jet turbulence levels may play a significant role on the overall results.

4.2.2.3 Comparison with experimental data

Results for both Mesh no. 2 and 3 are shown in this section. Average values seems to achieve reasonable velocity and temperature fields. The jet penetration lenght is overestimates by the numerical model: it is possible to see that it extends over $Y/L_j = 2$ in Fig.**??** (a); this effect is caused by different factors. The mesh arrangment affects the results, then it is possible to observe from the RMS images in Fig. **??** (b), that the turbulence is underestimated on the outer layers of the core field; this effect is mostly given by the wall law condition, which overtake the turbulent behaviour in this zone, reminding that the mixing layer vortices properties are higly influenced by the boundary layer of both the streams. As consequence, the generation of these structures is shifted beyond, where the wall law stops to have a predominant role on the turbulence representation. Nonetheless, it should be underlined that the Taylor scale is not fully respected in meshing and, the absence of the smaller turbulent structures is mainly dependant on the SGS model adopted. However, the larger turbulence structures as the CVP and the horseshoe are well captured as well as the overall dimensions of the larger mixing layer structures as it will be shown in the results kinematic and thermal fields from here on. In the following sections, numerical results and experimental data will be compared.

Results of the structured Mesh no.2

Fig. **??** (a) shows the temperature contour plot on the horizontal XY cutplane. The characteristic zones are well represented by the LES WALE model solution, and there is a good agreement between experimental and numerical values. It is possible to notice that the potential zone is still enlarged if compared to the experimental one.

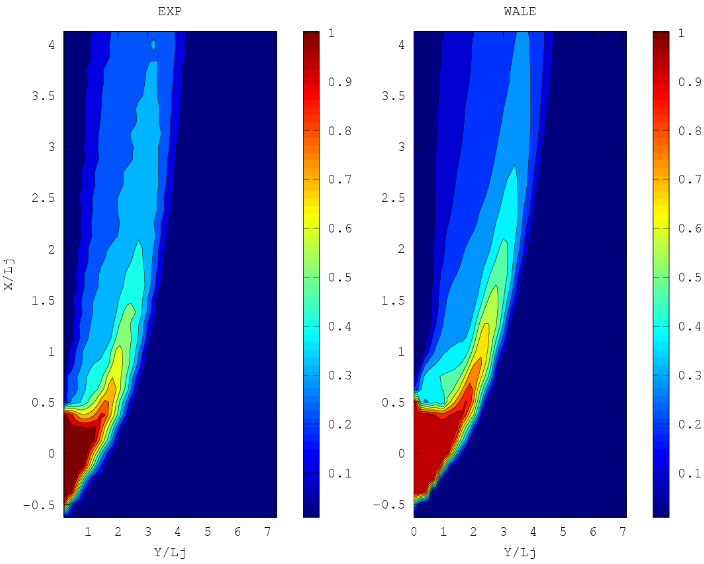

(a) $\overline{T^*}$

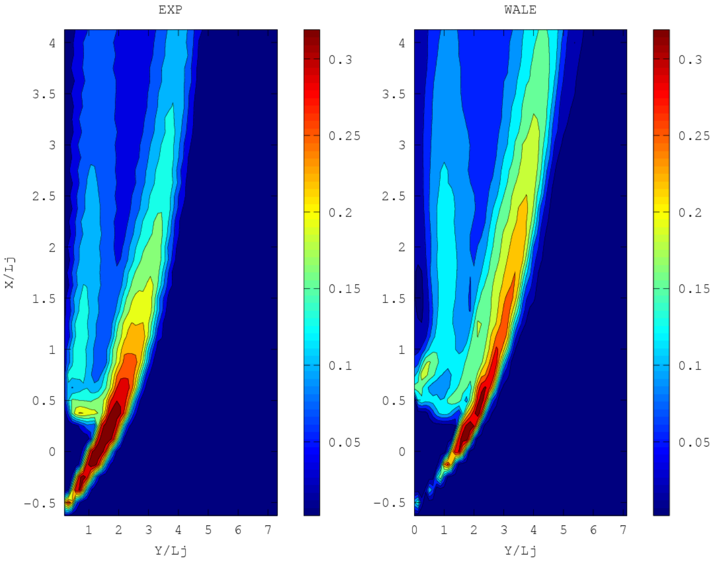

(b) σ_T^*

Figure 4.65: LES WALE approach, comparison between experimental and numerical dimensionless temperature fields. XY plane at z = 0 mm. : time average values (a), Root mean square (b)

From the root mean square plots (Fig. **??** (b)) it is now possible to see that mixing is concentrated on the outer part of the jet, through the whole deflection zone. The calculation respects with high fidelity this behavior with the exception to the near-wall zone located at $Y/L_j \approx 0.5$, $X/L_j \approx -0.5$. This effect can be associated to the wall-law modelization, that seems to underestimate the turbulence levels in this region. On the other hand, this mismatch is not visible on the inner part of the jet, where the turbulence linked with tracking vortices structures, is sufficiently well represented.

On the jet exit section (Fig. **??**) the underestimation of the turbulence level on the outer region of the jet can be noted. As it is possible to see the trailing edges are not completely formed yet. In Fig. **??** (b) it can be found that the turbulence levels are underestimated by a magnitude of 1.7 K.

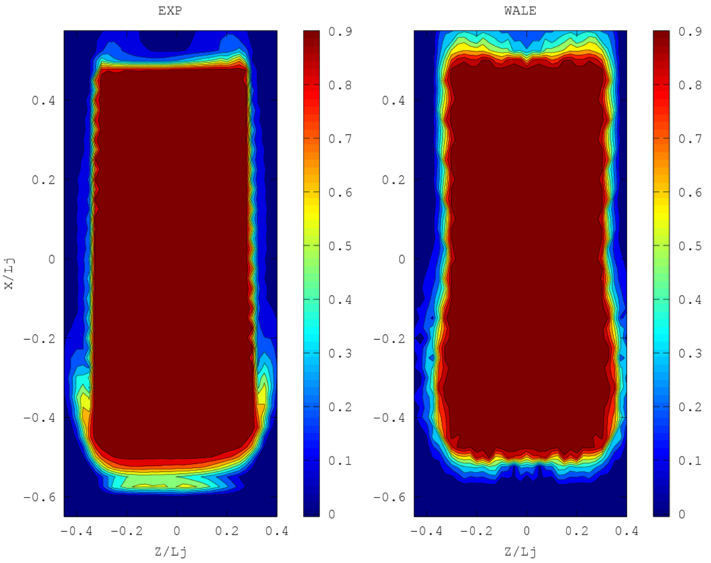

(a) $\overline{T^*}$

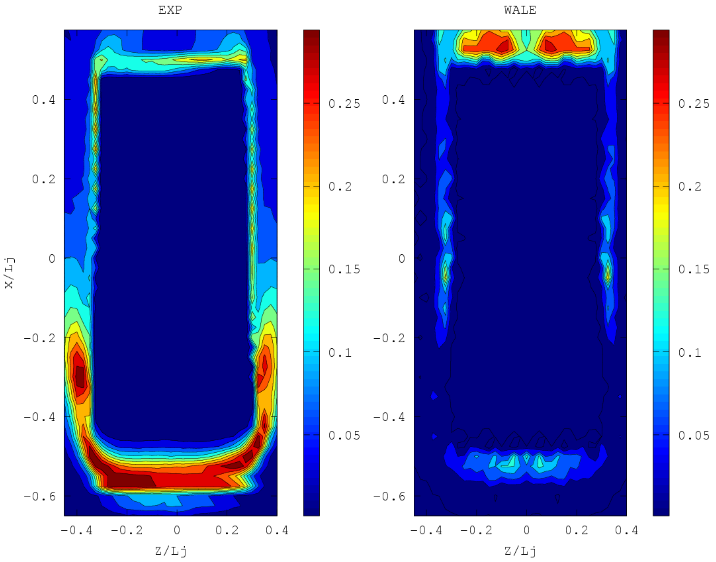

(b) σ_T^*

Figure 4.66: LES WALE approach, comparison between experimental and numerical dimensionless temperature fields. XZ plane at y = 2 mm. : time average values (a), Root mean square (b)

On the next cut plane (Fig. **??** (a)) it is possible to see that the LES WALE model prediction are satisfactory. The comparison between the two temperature fields shows no significant differences, and the accuracy reached by the calculation is impressive. Fig. **??** (b) represents the temperature fluctuations contours. In this case the LES solution unpredict the amplitudes on the outer part of the jet region, however, it still respects closely the position of the turbulent zones.

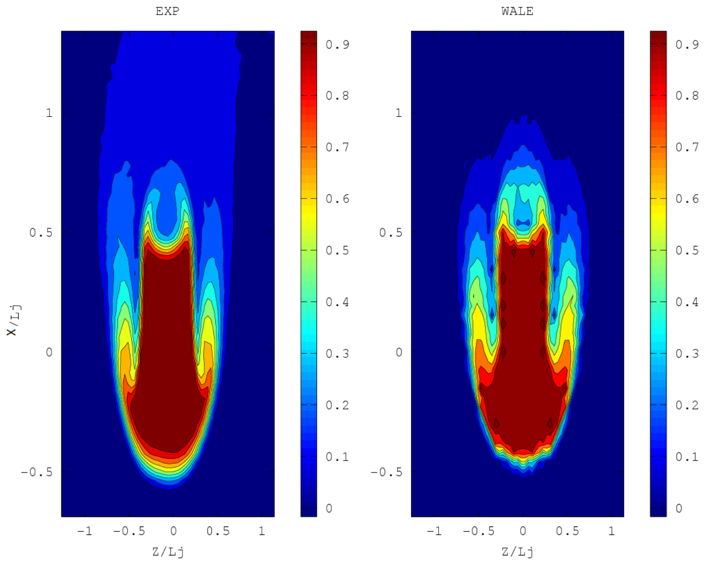

(a) $\overline{T^*}$

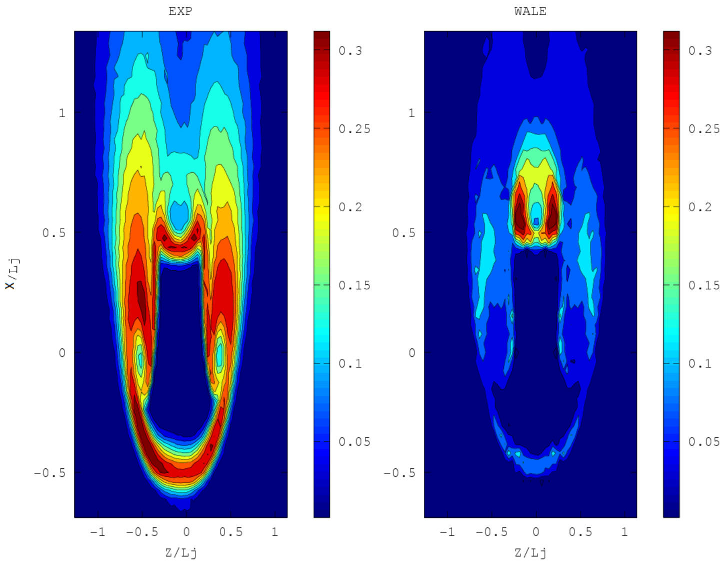

(b) σ_T^*

Figure 4.67: LES WALE approach, comparison between experimental and numerical dimensionless temperature fields. XZ plane at y = 20 mm. : time average values (a), Root mean square (b)

Following the jet penetration lenght, Fig. **??** (a) shows that the solution tends to conserve the original rectangular shape of the jet more than the experimental test shows. Even though, the fluctuations description is improved with respect to the previous zones. In Fig. **??** (b) at $X/L_j \approx 0.5$ and $Y/L_j \approx \pm 0.5$ two recirculation zone can be distinguished in both the experimental and numerical simulation fields.

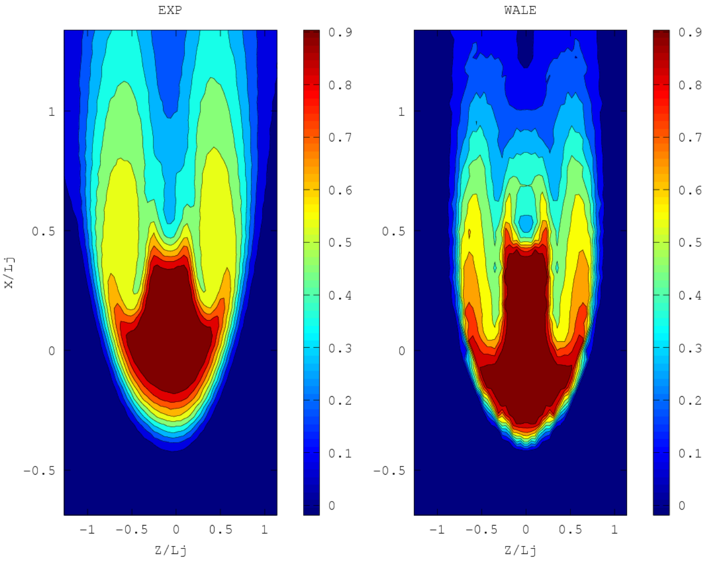

(a) $\overline{T^*}$

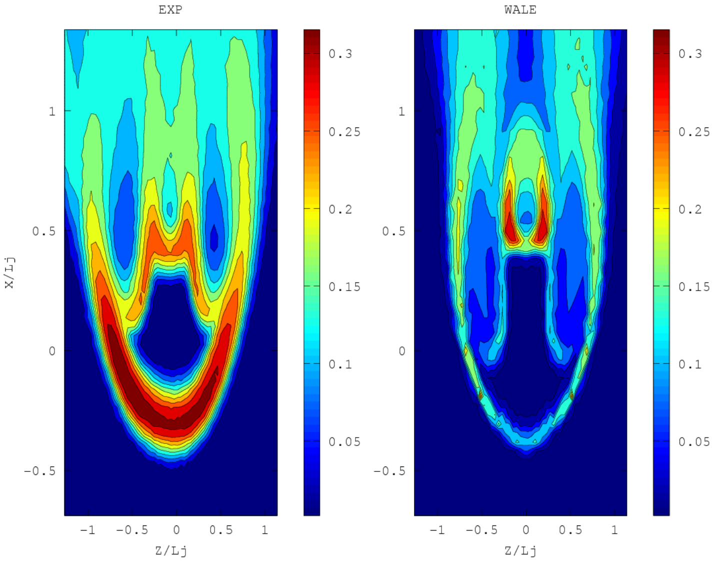

(b) σ_T^*

Figure 4.68: LES WALE approach, comparison between experimental and numerical dimensionless temperature fields. XZ plane at y = 40 mm. : time average values (a), Root mean square (b)

The same considerations can be made moving forward to the next measurement plane (Fig. **??**). A difference that deserves to be considered is that, at the end of the core region, the recirculation structures previously found are disrupted by the main flow momentum beyond this point.

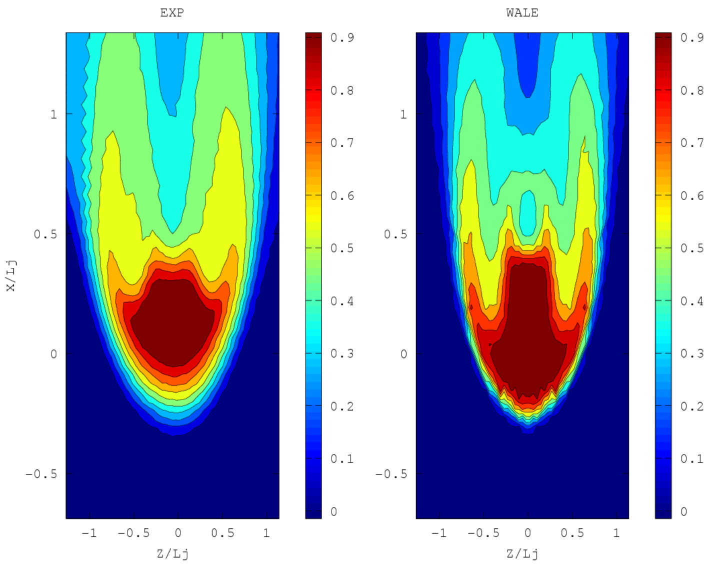

(a) $\overline{T^*}$

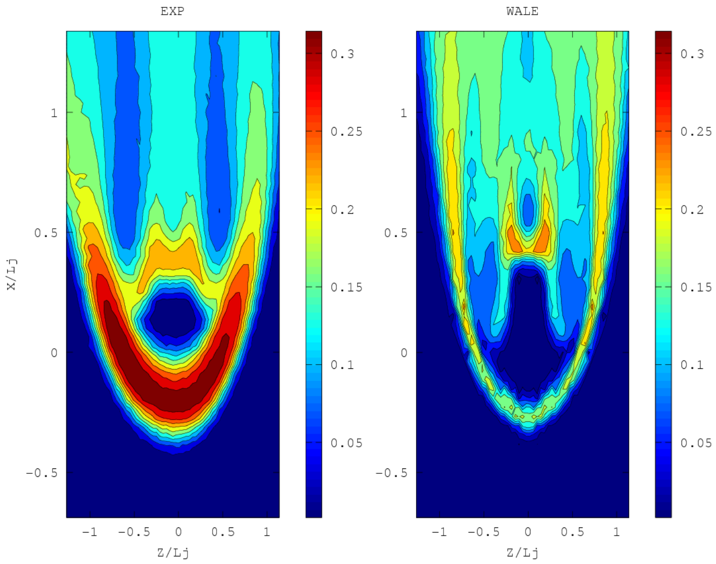

(b) σ_T^*

Figure 4.69: LES WALE approach, comparison between experimental and numerical dimensionless temperature fields. XZ plane at y = 60 mm. : time average values (a), Root mean square (b)

The comparison proceeds to the further planes, which are parallel to the main channel inlet section. From the kinematic point of view, the comparison between the LES WALE solution and the experimental data shows a good agreement. In Fig. **??** and **??** the velocity fields appear to respect the original circular shape of the low velocity core contours. The outer part maximum locus is represented by the solution as well. On the average fields solution it is possible to observe a small velocity gradient in zones where $Y/L_j > 4.3$. It seems that this effect is given by the lower mesh density in this region, anyway this effect is not considered important for the jet description, and does not have relevance on the overall results.

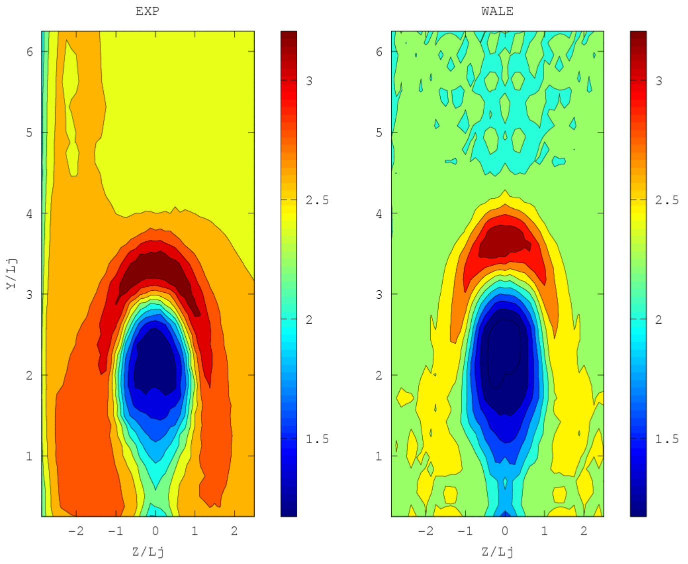

(a) $\sqrt{\overline{u^2 + w^2}}$

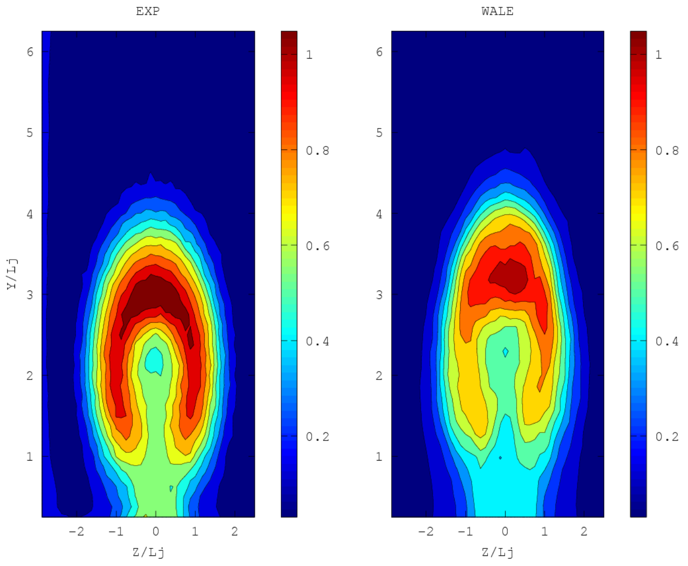

(b) $\sigma_{\sqrt{u^2+w^2}}$

Figure 4.70: LES WALE approach, comparison between experimental and numerical velocity field. YZ plan at x = 240 mm. : time average values (a), Root mean square (b). The colorbar scale is in m/s

Regarding the fluctuations, it is possible to notice that the solution predict well the global field. Nonetheless, the similarities between Fig. **??** (b) and **??** (b) demonstrate that the fluctuations are predominant in the axial direction, so that the u component overtakes v and w fluctuations. However there is still higher turbulent fluctuations of the v into the core jet with respect to the w one. The maximum value is recorded on the outer mixing layer (1.1 m/s).

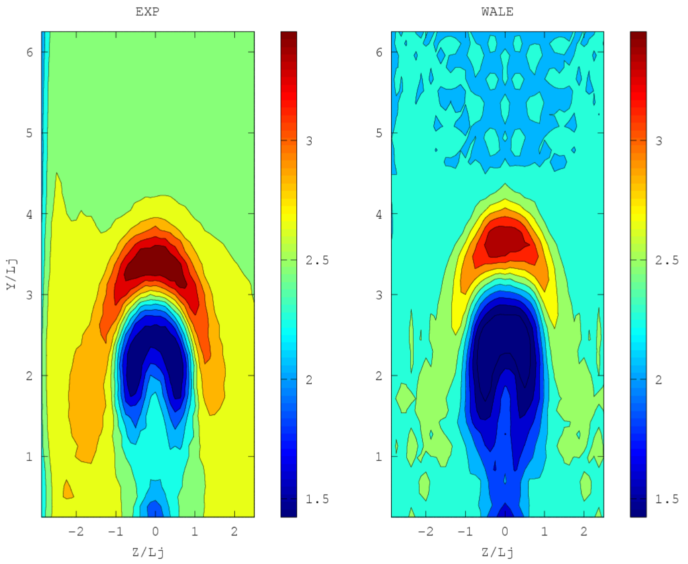

(a) $\overline{\sqrt{u^2+v^2}}$

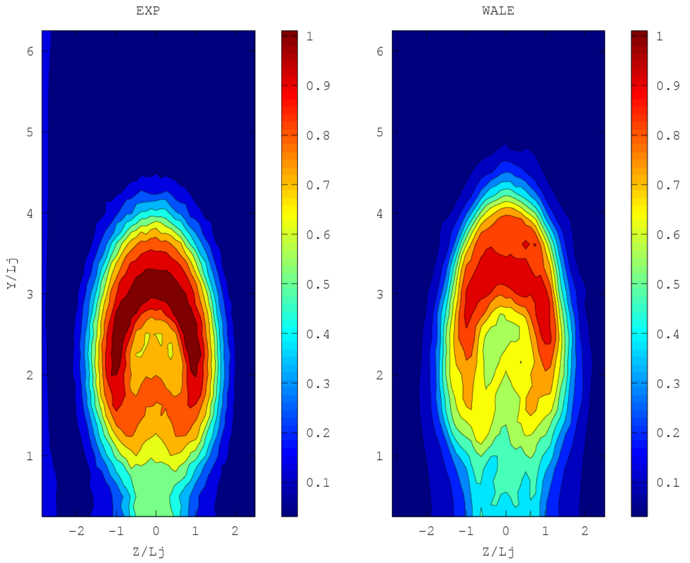

(b) $\sigma_{\sqrt{u^2+v^2}}$

Figure 4.71: LES WALE approach, comparison between experimental and numerical velocity field. YZ plan at x = 240 mm. : time average values (a), Root mean square (b). The colorbar scale is in m/s

The temperature field in the corresponding section is shown in Fig. **??** and Fig. **??**. The horseshoe structure is well predicted both in shape and dimensionless temperature values. From the point of view of the fluctuations, it is possible to observe a considerable turbulent activity which results in a "crown" shape around the outer contours of the jet core. This behaviour seems to be overestimated by the LES WALE model.

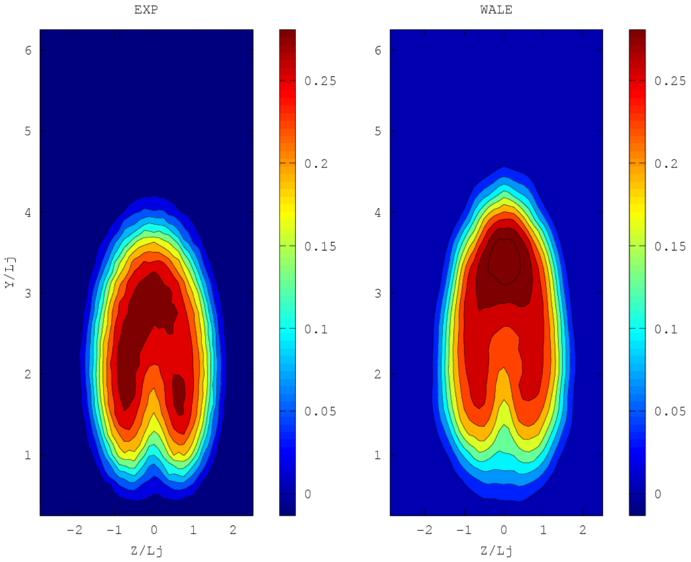

(a) $\overline{T^*}$

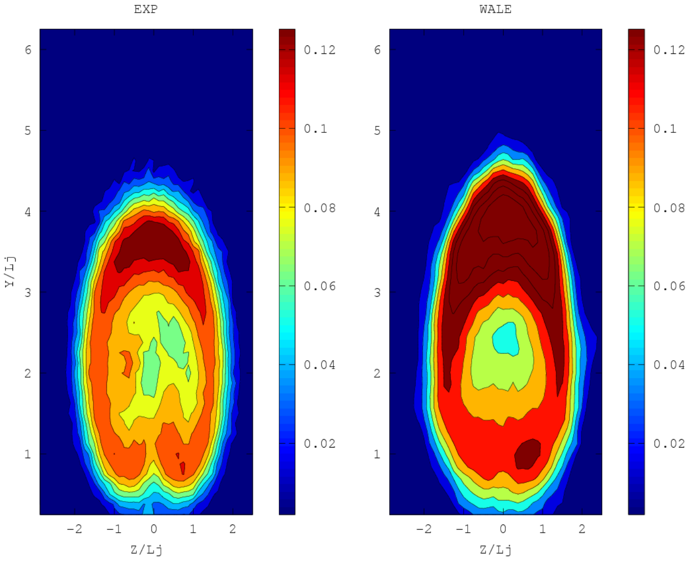

(b) σ_T^*

Figure 4.72: LES WALE approach, comparison between experimental and numerical dimensionless temperature fields. XY plane at x = 240 mm. : time average values (a), Root mean square (b)

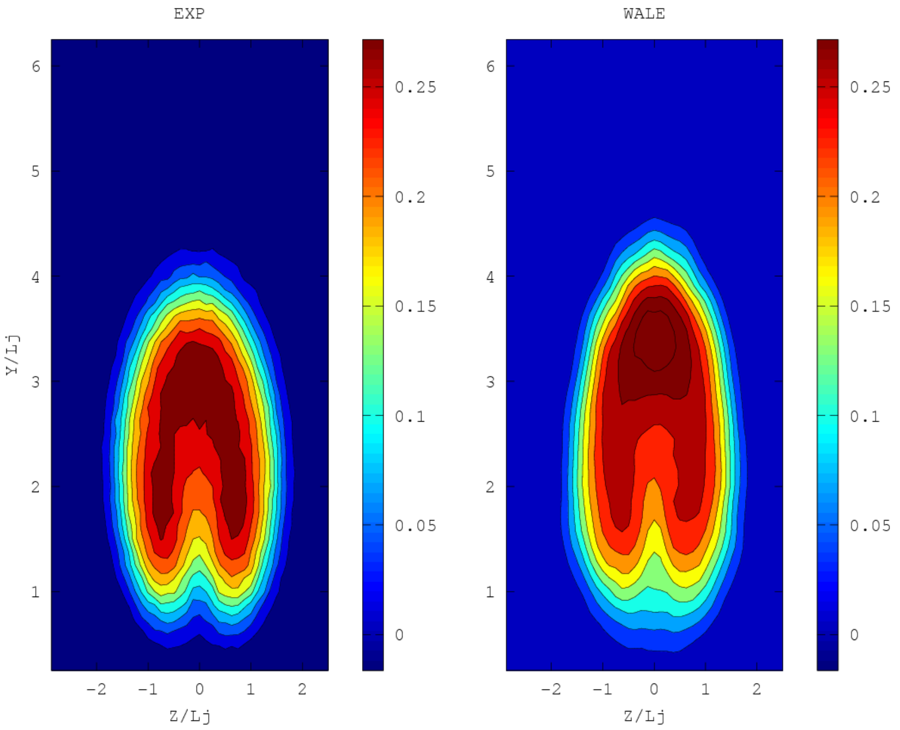

(a) $\overline{T^*}$

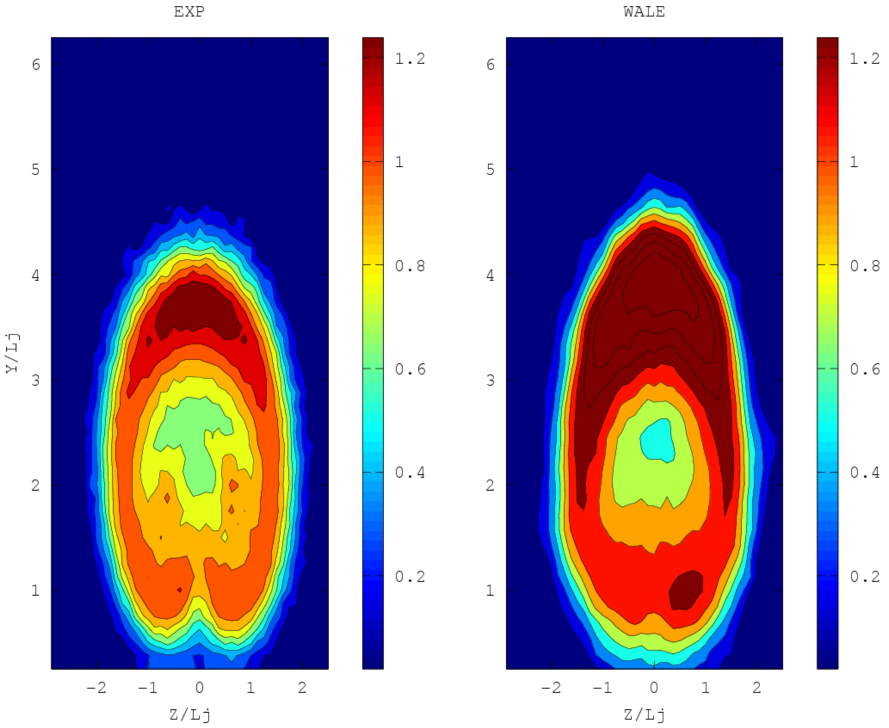

(b) σ_T^*

Figure 4.73: LES WALE approach, comparison between experimental and numerical dimensionless temperature fields. XY plane at x = 240 mm. : time average values (a), Root mean square (b)

In the far field, it is possible to observe from the velocity plots shown in Fig. **??** (a) that the numerical solution starts to degenerate the initial core shape. However there is still a good agreement between CFD and experimental data regarding the highest velocity region located on the outer part of the jet. The discrepancies in terms of velocity magnitude here reach to a maximum of 0.4 m/s.

Considering the related fluctuations it is possible to see from Fig. **??** (b) that the code mantains the same turbulent structures as those one presented by the experiment.

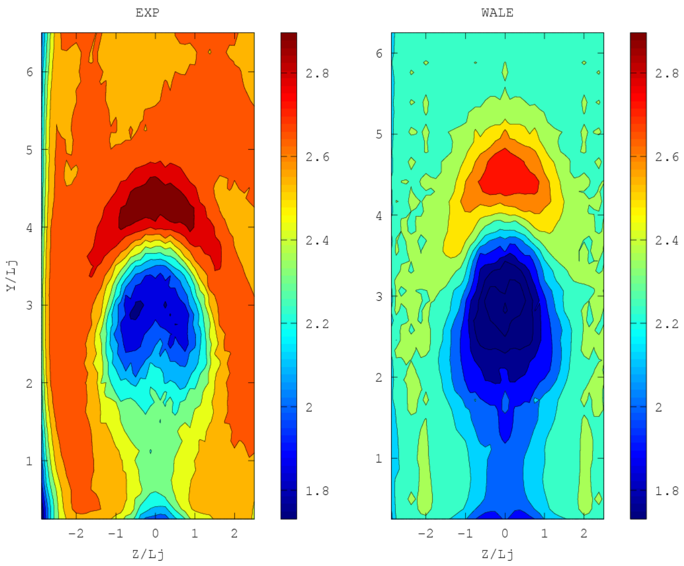

(a) $\sqrt{u^2 + v^2}$

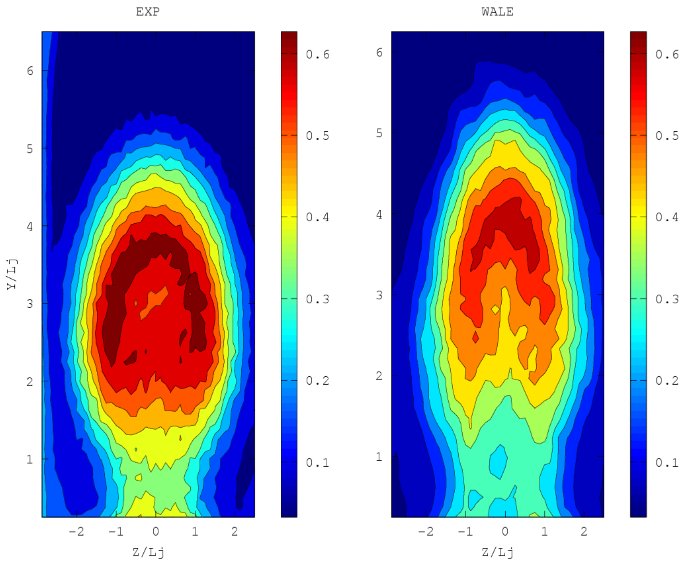

(b) $\sigma_{\sqrt{u^2+v^2}}$

Figure 4.74: LES WALE approach, comparison between experimental and numerical velocity field. YZ plan at x = 480 mm. : time average values (a), Root mean square (b). The colorbar scale is in m/s

On the same plane the temperature distributions (Fig. **??**) shows that the jet core still keeps a rounded horseshoe shape, which is gradually lost proceeding in the Y direction to the inner part. Nevertheless, the root mean square values in Fig. **??** (b) shows that there is still agreement between the experiment and the LES WALE results, and the CVP structure can be distinguished. However it is still possible to notice a weak shift of the outer mixing layer in positive Y direction.

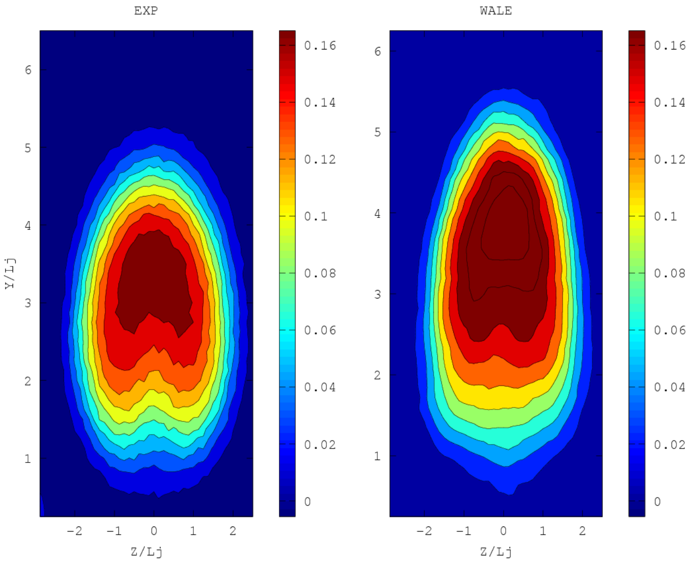

(a) $\overline{T^*}$

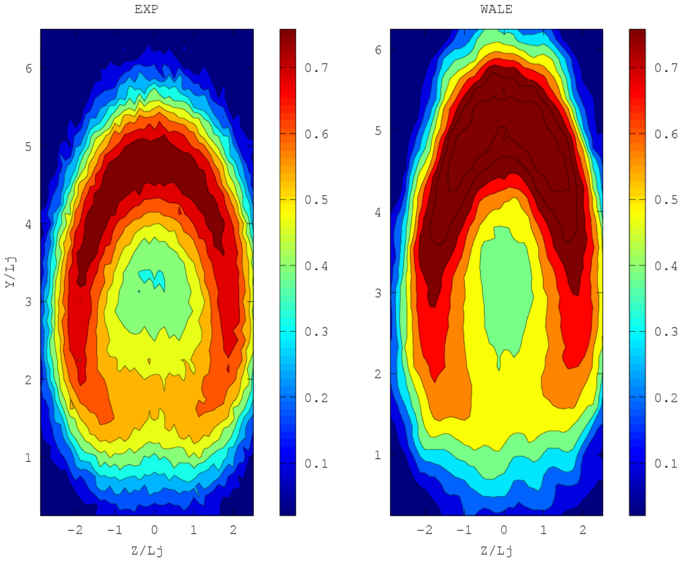

]

(b) σ_T^*

Figure 4.75: LES WALE approach, comparison between experimental and numerical dimensionless temperature fields. YZ plane at x = 480 mm. : time average values (a), Root mean square (b)

Results of the unstructured Mesh no.3

The results given from the LES WALE calculation performed with the structured mesh no. 3 are shown in this sub section.
Starting with the global jet view (Fig. **??** (a)) it is possible to see that the solution in the structured mesh behaviour presents the advections effects already underlined in the RANS $k - \varepsilon$ studies. The solution shows how the jet potential zone is extended beyond the end zone shown by the experimental plots. As a consequence, the jet penetration lenght is slightly extended in the Y direction.

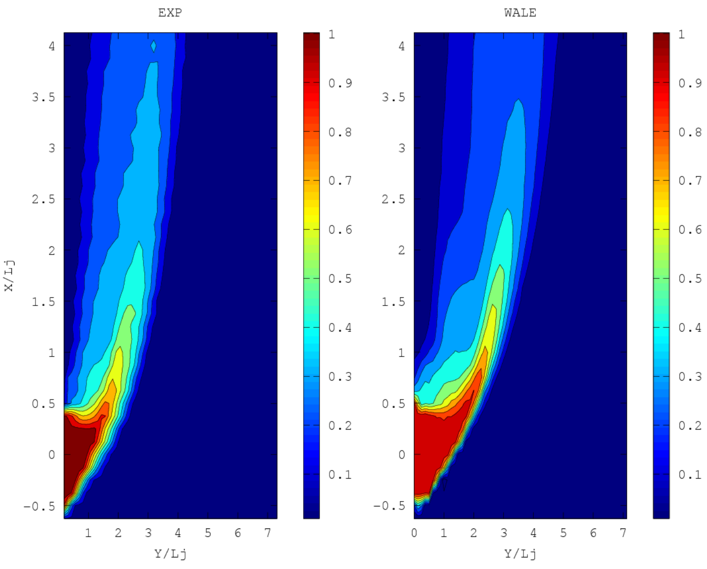

(a) $\overline{T^*}$

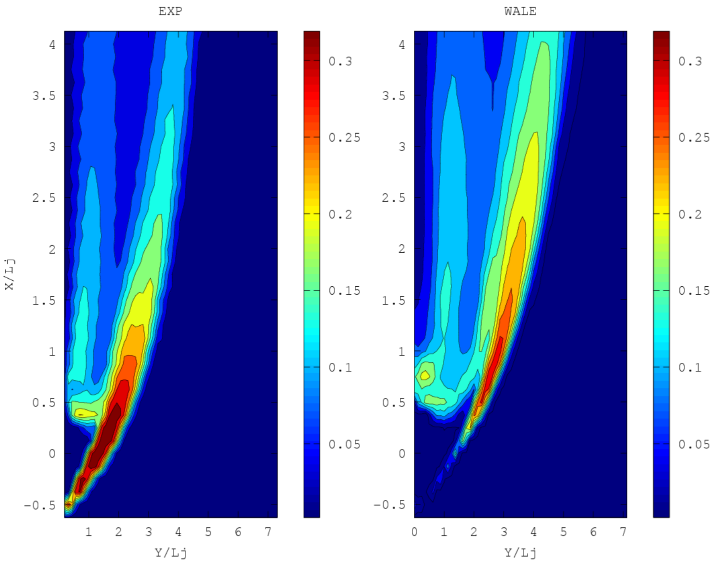

(b) σ_T^*

Figure 4.76: LES WALE approach, comparison between experimental and numerical dimensionless temperature fields. XY plane at z = 0 mm. : time average values (a), Root mean square (b)

In Fig. **??** (b) the fluctuations field of the solutions presents the same characteristics of those one shown in the LES WALE calculation performed with the unstructured mesh. In the outer part of the jet core region, turbulence is underestimated with a difference of 3.4 K in the fluctuations, while the inner region shows a global accordance with the experimental values.

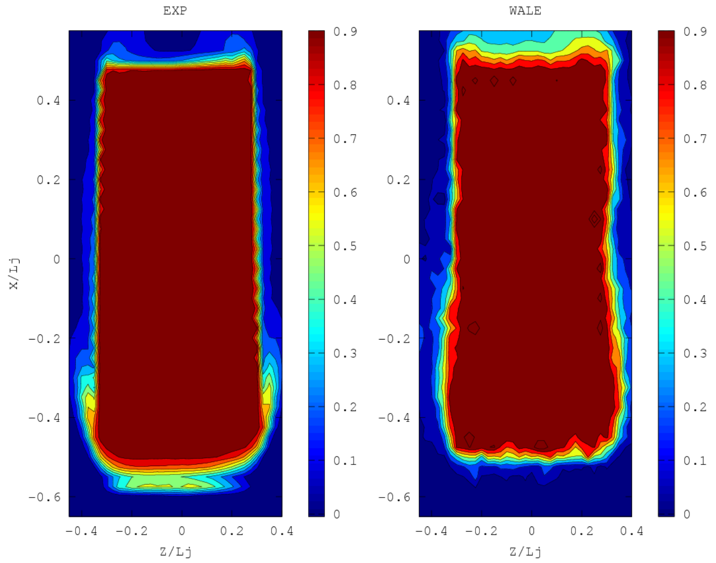

(a) $\overline{T^*}$

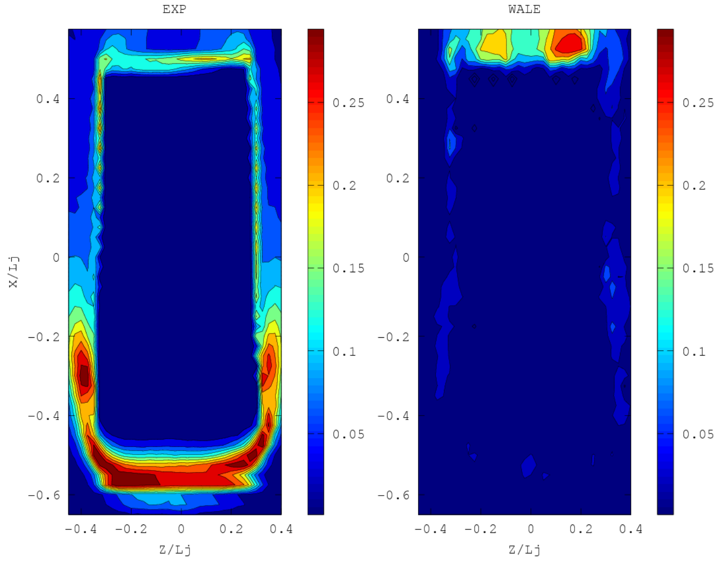

(b) σ_T^*

Figure 4.77: LES WALE approach, comparison between experimental and numerical dimensionless temperature fields. XZ plane at z = 2 mm. : time average values (a), Root mean square (b)

At the exit section of the jet the temperature field shows the fairly the same characteristics of the experimental data (Fig. **??** (a)) . It can be noticed that the trailing edge vortices of the outer part of the jet are not captured by the solution. However, this can be reasonably explained with the fact that in this zone the spatial discretization is larger than the lenght scale of these structures. The turbulence is not directly resolved in this region, therefore the SGS model adopted plays a role on the low resolution obtained at this scale. The same effect can be seen in the fluctuation values, where the outer region shows a discrepance of 4.25 K in the temperature root mean square of the solution (Fig. **??** (b)).

The description of the potential zone proceeds with the thermal fields located in planes XZ positioned 20, 40 and 60 mm far from the jet exit section. In the first one (Fig. **??**) It is possible to notice that the numerical solution respects the core shape conformation. It must be underlined that the indented contours that can be noticed in the solutions can be merely associated to interpolation effects during the post-processing treatment of the data matrix. The linked fluctuations reported in Fig. **??** (b) shows that the calculation is still able to identify the two mixing layer vortices located at $Z/L_j \approx \pm 0.5$, $X/L_j \approx 0$, even though the fluctuations magnitude are moderately different.

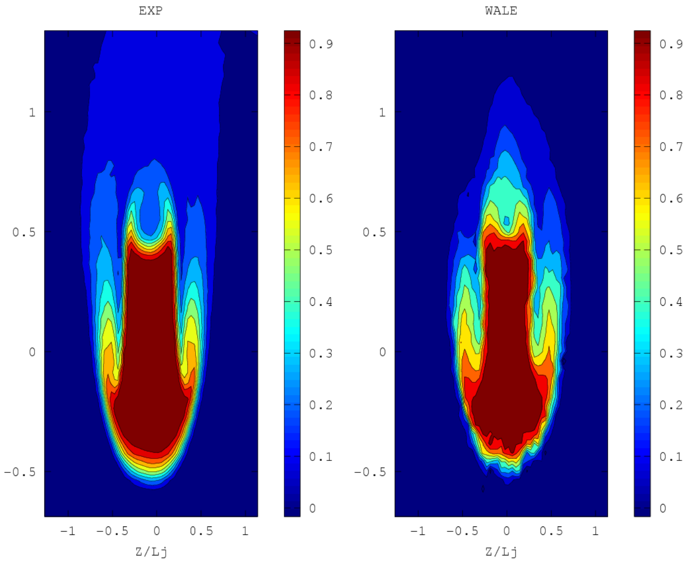

(a) $\overline{T^*}$

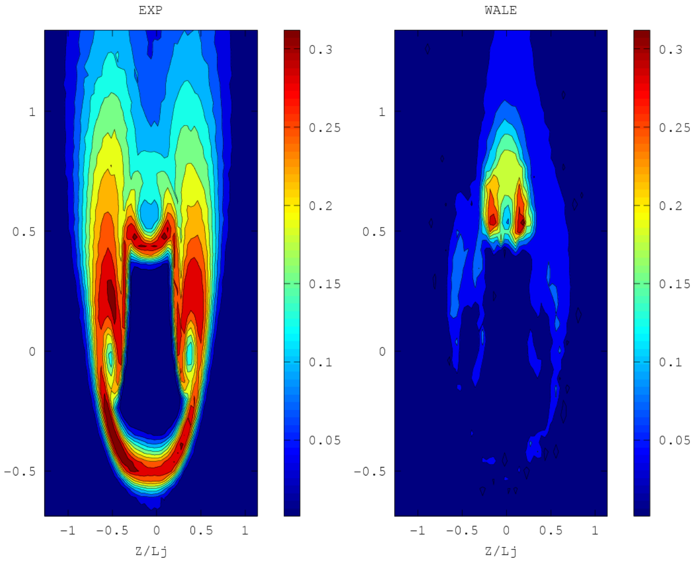

(b) σ_T^*

Figure 4.78: LES WALE approach, comparison between experimental and numerical dimensionless temperature fields. XY plane at z = 20 mm. : time average values (a), Root mean square (b)

In the next plane, the temperature field reported in Fig. **??** (a) shows that the solution tends to conserve the original rectangular shape of the jet more than the test case shows. This behaviour causes a spatial gap between the trailing edge vortices positions in X direction; as it can be noticed by Fig. **??** (b).

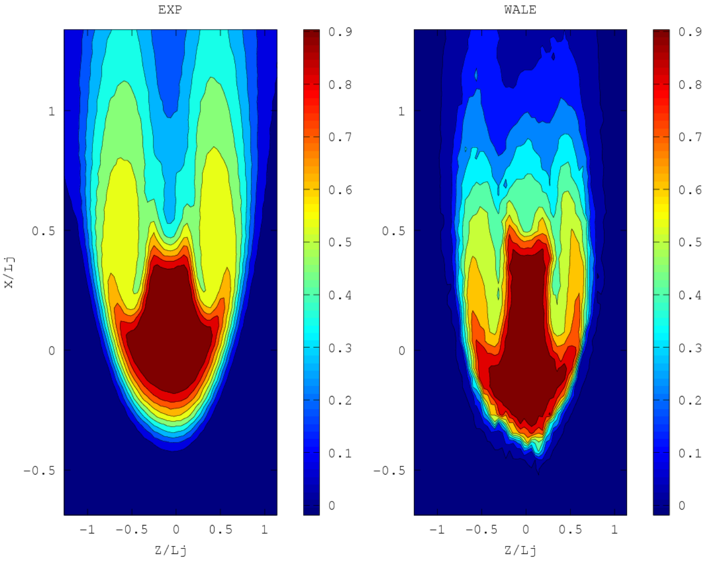

(a) $\overline{T^*}$

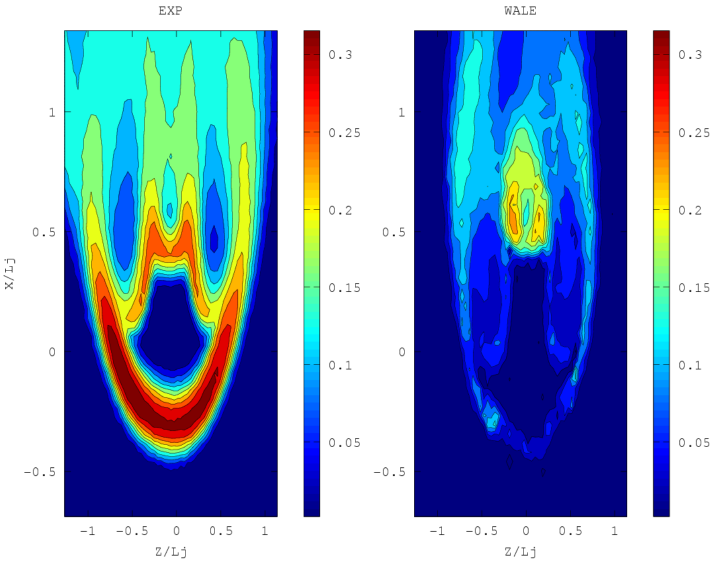

(b) σ_T^*

Figure 4.79: LES WALE approach, comparison between experimental and numerical dimensionless temperature fields. XY plane at z = 20 mm. : time average values (a), Root mean square (b)

When the jet penetration lenght is almost reached, the temperature field shown in Fig. **??** (a) shows that the solution mantains the same trends previously shown in Fig. **??**. However the LES WALE model is still able to depict the shift and the consequent disruption of the mixing layer vortices located on both the top and the bottom parts of the jet main dimensions (Fig. **??** (b) $Z/L_j \approx \pm 0.5$, $X/L_j \approx 0$) and now visible in the downstream region (Fig. **??** at $Z/L_j \approx \pm 0.75$ and $X/L_j \approx 0.5$).

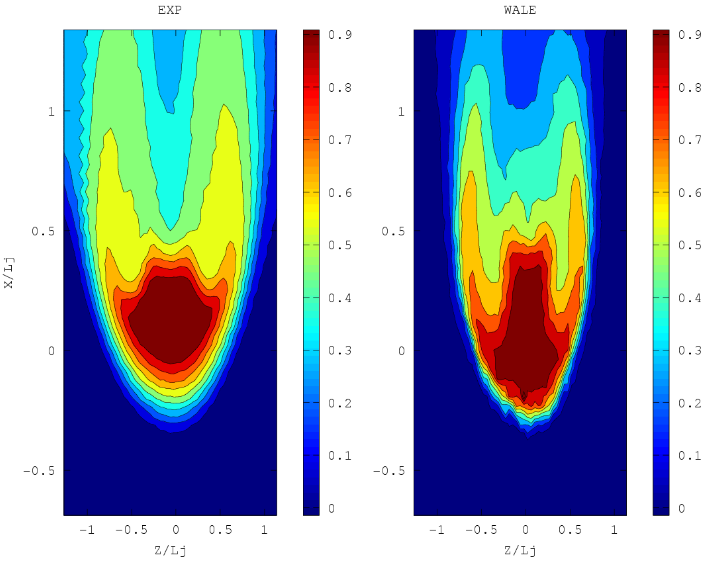

(a) $\overline{T^*}$

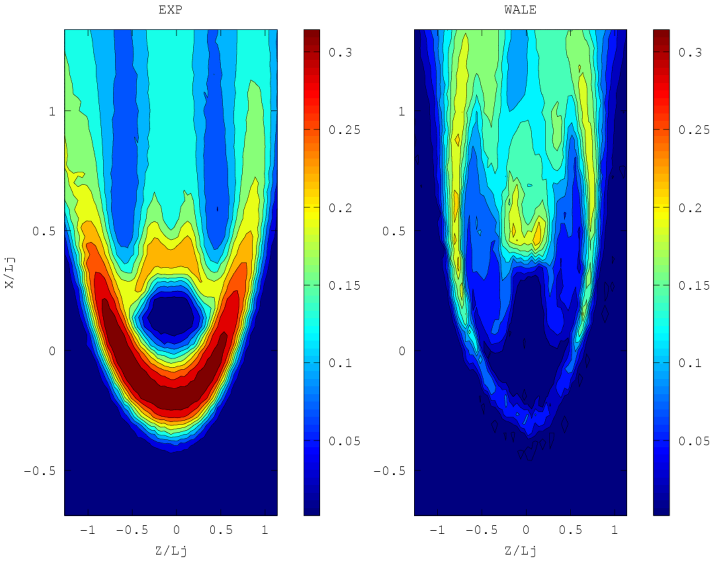

(b) σ_T^*

Figure 4.80: LES WALE approach, comparison between experimental and numerical dimensionless temperature fields. XY plane at z = 20 mm. : time average values (a), Root mean square (b)

Discussing the velocity field obtained by the LES WALE solution, it is possible to notice from the time average plots in Fig. **??** and **??** that the maximum velocity region is well predicted, even if the presence of a slight asymmetry with respect to the central line parallel to the Y axis appears. Fig. **??** (b) and **??** (b) show a full similarity between the velocity root mean square in Z and Y directions, therefore even for this case, the predominant fluctuations of the flow velocity field are aligned with the main channel larger dimension.

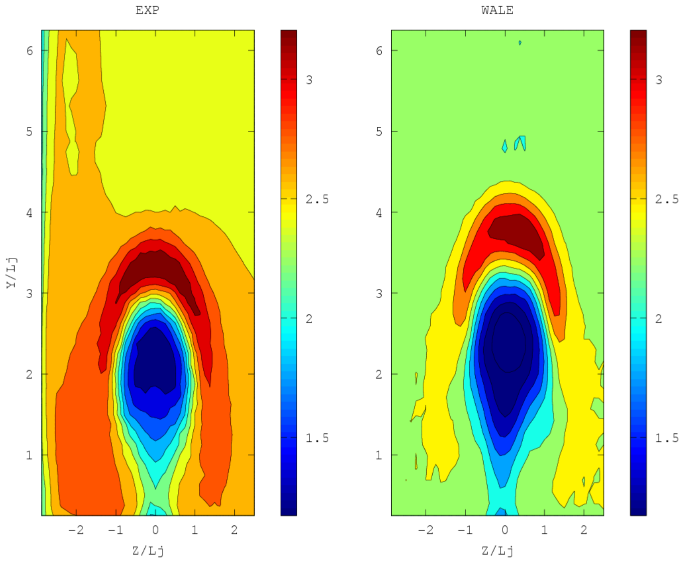

(a) $\sqrt{u^2+w^2}$

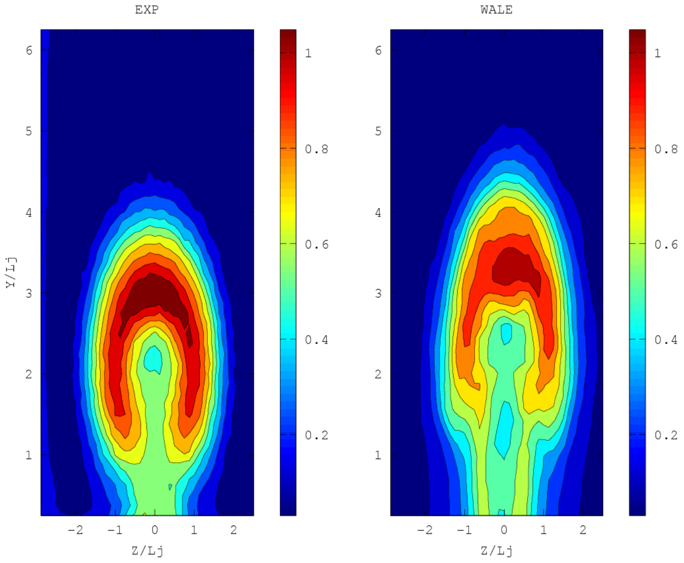

(b) $\sigma_{\sqrt{u^2+w^2}}$

Figure 4.81: LES WALE approach, comparison between experimental and numerical velocity field. YZ plan at x = 240 mm. : time average values (a), Root mean square (b). The colorbar scale is in m/s

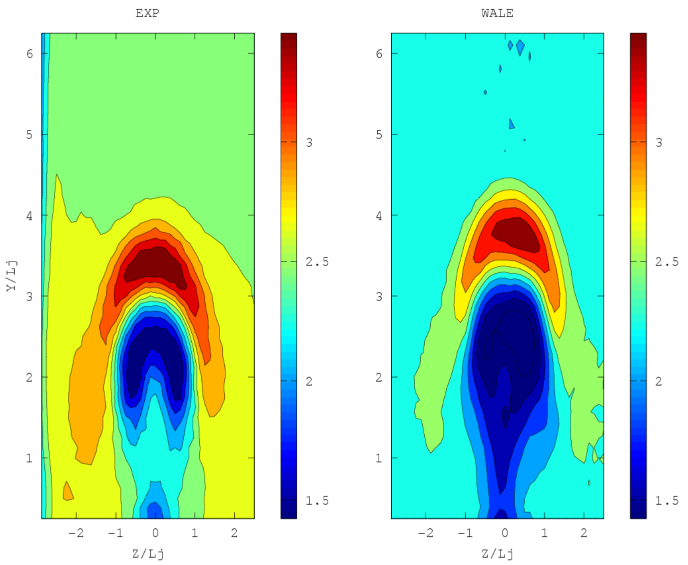

(a) $\sqrt{u^2+v^2}$

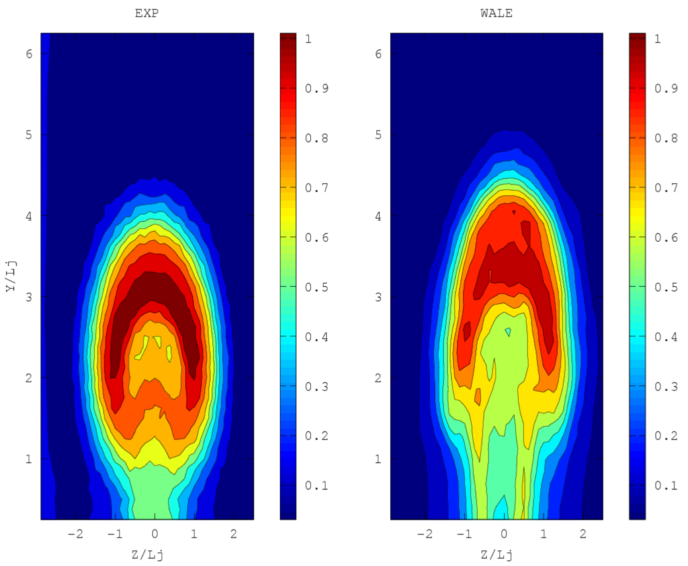

(b) $\sigma_{\sqrt{u^2+v^2}}$

Figure 4.82: LES WALE approach, comparison between experimental and numerical velocity field. YZ plan at x = 240 mm. : time average values (a), Root mean square (b). The colorbar scale is in m/s

The temperature fields in the section located 240 mm downstream the jet exit are shown in Fig. **??** and **??**. In both cases, the mean values obtained from the numerical model match with the experimental profiles. However it can be noticed by looking at the root mean square distributions (Fig. **??** (b) and **??** (b)) that the outer mixing layer turbulence is overestimated in the solution where the maximum magnitude reaches 2.55 K despite the 2.04 K reported by the experiment.

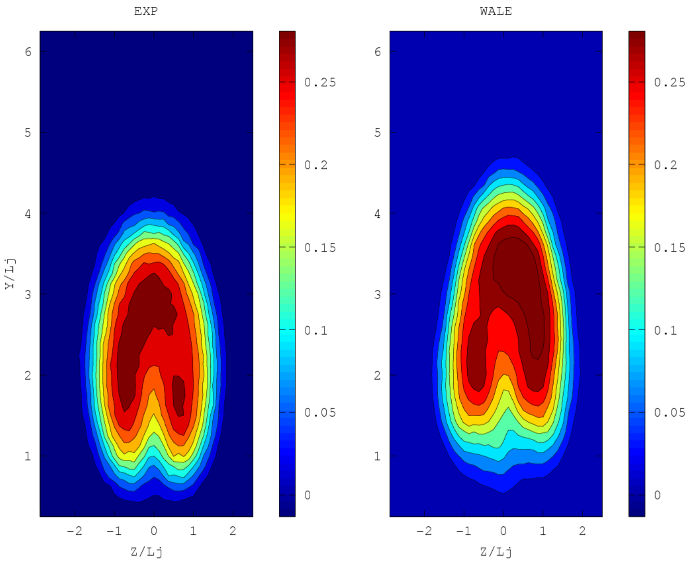

(a) $\overline{T^*}$

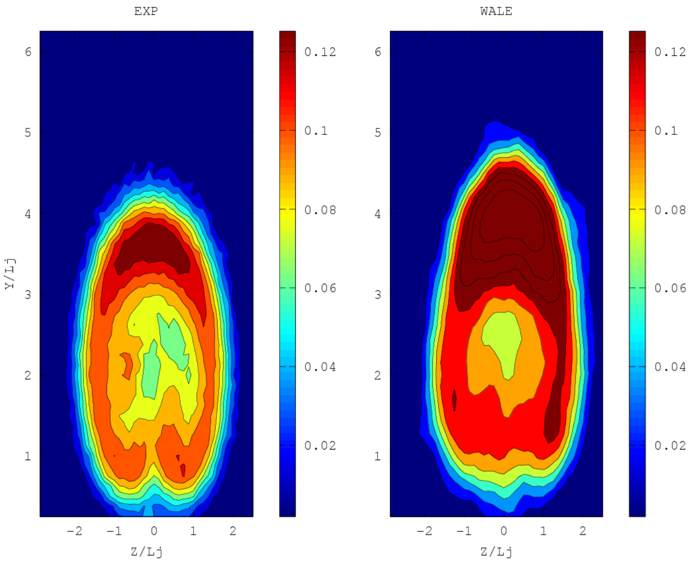

(b) σ_T^*

Figure 4.83: LES WALE approach, comparison between experimental and numerical dimensionless temperature fields. YZ plane at x = 240 mm. : time average values (a), Root mean square (b)

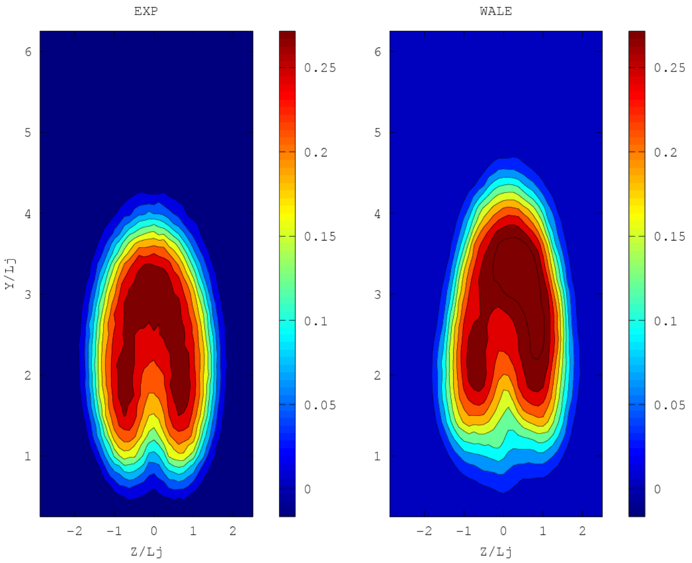

(a) $\overline{T^*}$

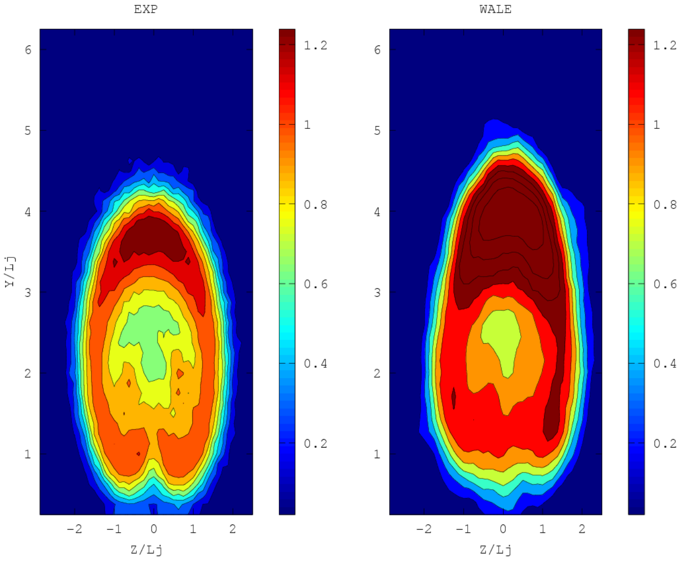

(b) σ_T^*

Figure 4.84: LES WALE approach, comparison between experimental and numerical dimensionless temperature fields. YZ plane at x = 240 mm. : time average values (a), Root mean square (b)

Approaching the far field, the velocity distribution shown in Fig. **??** shows that the solution in this case starts to degenerate, as it can be seen by the shift of the outer jet maximum velocity region with respect to the experimental data. The fluctuation profile (Fig. **??** (b)) preserves a global agreement with the experimental plots, but is rather deformed if compared to the original shape. These effects can be ascribed to a lower mesh refinement achieved starting from this region.

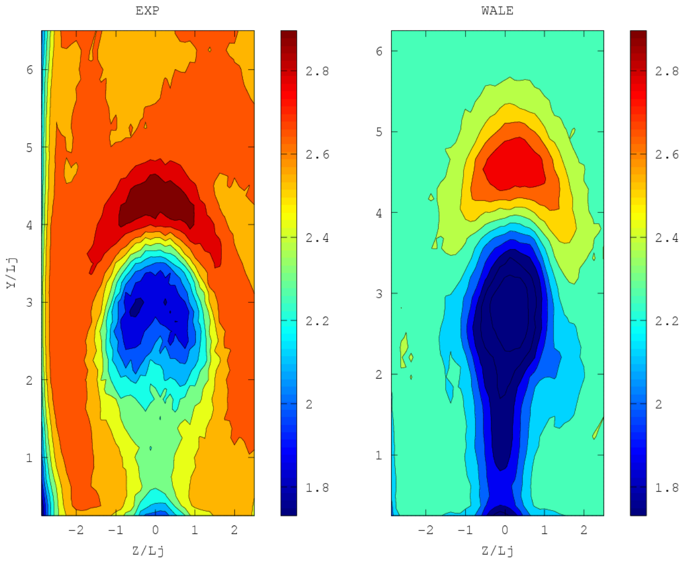

(a) $\sqrt{u^2 + v^2}$

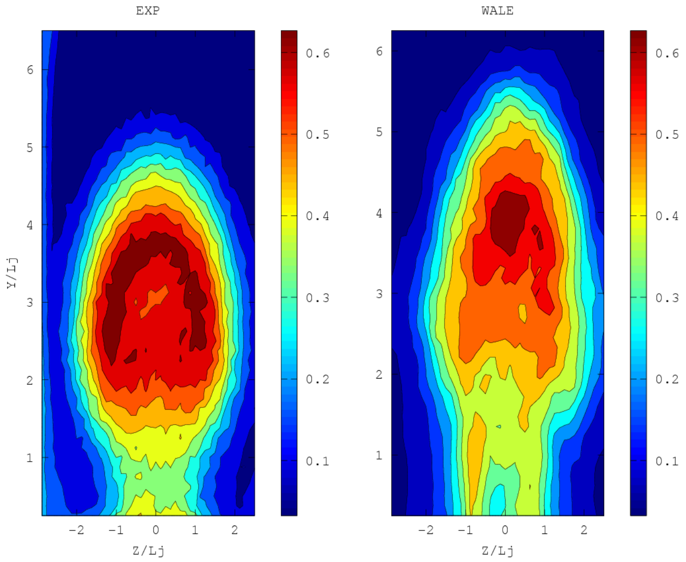

(b) $\sigma_{\sqrt{u^2+v^2}}$

Figure 4.85: LES WALE approach, comparison between experimental and numerical velocity field. YZ plan at x = 480 mm. : time average values (a), Root mean square (b). The colorbar scale is in m/s

In the temperature field (Fig. **??** (a), it can be noticed that the structured mesh arrangement does not represent anymore the main horseshoe shape of the jet, and the impact of SGS model appears in connection with the lower spatial discretization which substantially characterizes this region, even though the main dimension of the core part are respected in both the outer contours and their associated values.

On the other hand, it is shown in Fig. **??** (b) that the turbulent fluctuations are however compatible with the experiment in terms of region positioning and their values.

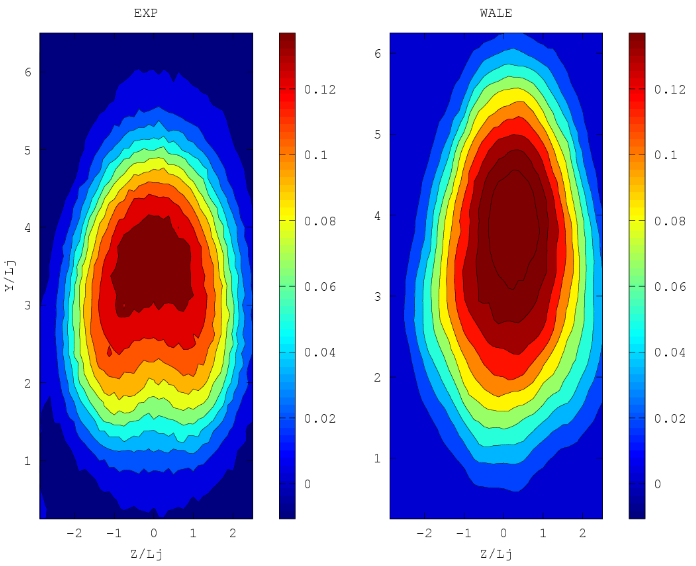

(a) $\overline{T^*}$

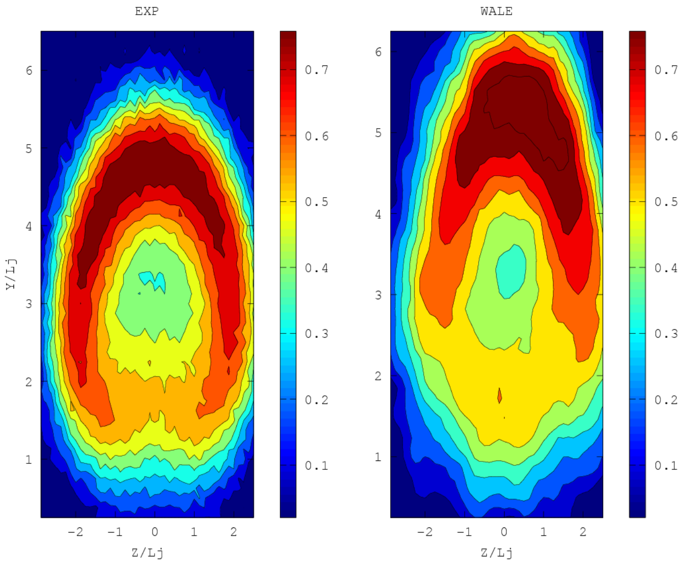

(b) σ_T^*

Figure 4.86: LES WALE approach, comparison between experimental and numerical dimensionless temperature fields. YZ plane at x = 240 mm. : time average values (a), Root mean square (b)

With the purpose to show the physical consistancy of the calculation performed, the Fourier transform of the temperature history recorded on the point A (see section 2.2.3), located nearby the outer jet exit part, is shown in Fig. **??**. It was not possible to directly make a proper comparison between the temperature and velocity spectra, because the experimental boundary conditions for which spectra were measured, were different from those one proposed in this section. It is still possible to observe that CFD spectra respect the fluctuations amplitudes for lower frequencies, thereafter the slope starts to follow a -5/3 law.

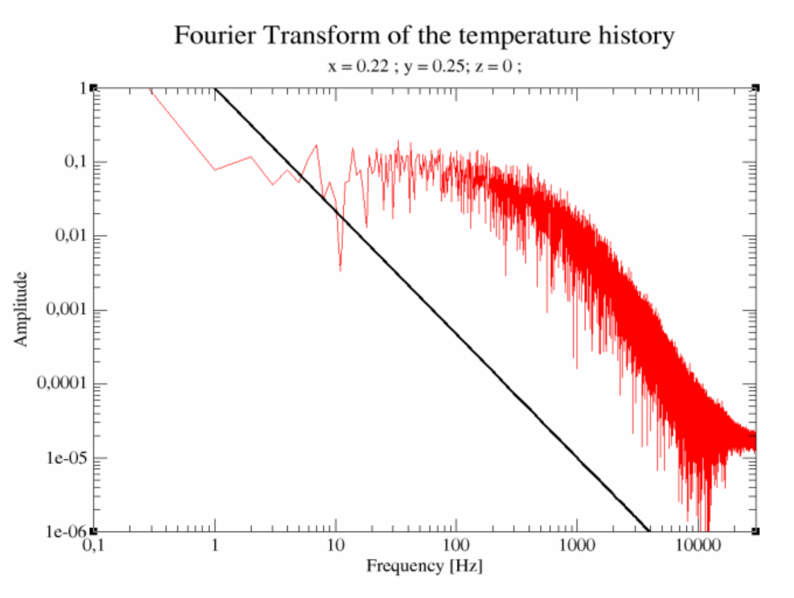

Figure 4.87: LES WALE approach, Temperature Spectra at Point A

Chapter5

Conclusions

Jet in cross flow are important configurations from the insutrial point of view and they play an important role in the validation process of turbulence models. In this work two test case are investigated using the TrioCFD code, which is the reference code of the Nuclear Energy Division of CEA:

- The OECD/NEA Vattenfall tee junction test case, where a heated water jet is discharged into a colder flow

- The TRANSAT closed loop wind tunnel experiment, where a rectangular air jet marked in temperature is mixed with a main stream coming from a larger rectangular channel.

The Tee junction configuration is a diffused layout in the industrial context, and present critical aspects from the thermal fatigue point of view. The OECD/NEA benchmark was chosen to test the TrioCFD LES model to test the code capabilities with the possibility to compare the results with numerical studies already performed by different authors. A LES modeling and calculation strategy has been developed and validated for this case.

The rectangular jet involved in the TRANSAT experiments, that have taken place at the CEA center in Grenoble, is investigated with the main objective to study the mixing phenomena involved for those applications that require a deeper jet penetration lenght. The experiments provided meaningul statistical data that have been used to develop a calculation and modeling strategy for the first time with LES model, taking advantage of the knowledge acquired during the Vattenfall tee junction investigations.

The results suggests that the resolving scales required for a correct modelization of the rectangular jet play an important role in the CFD context. In addition, an improvement on resolving the boundary layers may also have an impact on the global results. However, TrioCFD has shown encouraging responses and the main flow statistical informations, such time averaged, root mean square and spectra have been obtained with a good agreement with the experimental. Further investigations would lead to achieve better prediction in near wall regions.

In both the Vattenfall tee junction and the TRANSAT closed loop wind tunnel, difficulties have been found on achieving high accuracy results in zone located nearby the wall both upstream (TRANSAT) and downstream (Vattenfall tee junction) the jet. This fact suggests that the y^+ distribution must be improved and as well as the related wall law. Moreover, the mixing layer description along the jet penetration zone shows that local grid refinments up to the Taylor lenght scales must be achieved in order to avoid a strenght conditioning from the turbulent viscosity definition of the WALE model.

This work has shown that a correct modeling of the transient behaviour of highly turbulent flows represent one of the most important aspects with respect to the quality of the results

Mixing phenomena involved in jets in crossflow configurations still represent a challenge for CFD applications. The application of transient LES simulations and the validation of the appropriate scale-resolving turbulence model involves some not yer answered questions due to the extreme computational efforts needed to perform a single transient simulation.

During the work structured and unstructured cell arrangments have been tested in order to evaluate advantages and shortcomings of their application. The comparisons showed that the unstructured arrangment achieves a better description of the flow behaviour in zones characterised by strong anysotropies and considerable gradients. However it must be underlined that the algorithms employed in the generation of such kind of grids, due to their complexity, would represent a limit in terms of time required; this aspect cannot be ignored whenever the number of elements required for a calculation exceeds 10^7 cells.

On the other hand, the structured arrangment does not show these limits, since the alghoritm which provides the generation of this kind of structures allows to create the mesh in a fraction of the time normally required by the previous one (at a same number of elements and RAM availability). Thus, it must be underlined that the application of this arrangment represents the optimum choice whenever the user has previous detailed information of what would be the flow development with the appropriate spatial discretization scheme.

Nonetheless, the unstructured arrangment requires higher CPU time to reach convergency of the solution in respect to the structured one. Such difference is in the order of few seconds for each timestep, which is apparently negligeable. In order to perform reasonable statistical studies, a sufficient quantity of data must be obtained from the calculation; the total flow time simulated must allow to collect the meaningful phenomena involved in the system so that they can be shown after the post processing work.

As a consequence a difference of CPU time per timestep in the scale of a second, can not be considered negligeable as the appeareance suggests. This aspect is highlighted in the LES calculation cases, where the simulated time is in the order of ten seconds and the Courant-Friedrichs-Lewy stability condition requires a maximum timestep magnitude of 10^{-5} s. An average difference of just 1 second in CPU time per timestep is amplified with a 10^6 factor, and this would lead to an approximatively global difference of one week of non-stop calculation. The cell sizes adopted in the calculations of this work is the results of a compromise between computational efforts required, time available and solution detail required.

However the CPU time required to reach convergency is also affected by the numerical schemes adopted in the simulation, and their impact is predominat respect to the mesh structure adopted. It must be underlined that the choice of the time explicit schemes for the LES calculation have been made in order to reduce the CPU time required. As a matter of fact a fully implicit approach treats every term throughout the entire computational domain implicitly. However, it requires the solution of a large non-linear system of equations. For realistic applications, the cost of solving the non-linear system may be more than the one required with an explicit time marching scheme. Some methods, such as relaxation-based schemes and multi-grid reduce the cost of a fully implicit approach, but in conclusion none of these techniques ensures improvements that could justify the abandonement of explicit schemes. Furthermore, the memory required to store the Jacobian matrix and preconditioners is considerable and prevent a realistic application of these schemes to the configurations involved in this work. However an attempt has been done by launching a calculation with an implicit time scheme for few timestep, with the purpose to estimate the realistic computational time required. The average CPU time per timestep spent to reach convergency was triple in respect to the explicit schemes.

Bibliography

[1] **Chassaing, P., George, J., Claria, A. and Sananes F.**
Physical characteristics of subsonic jets in a cross-stream.
Journal of Fluid Mechanics. 62, Part.1, 41-64 (1974)

[2] **Patrick, M.A.**
Experimental investigation of the mixing and penetration of a round turbulent jet injected perpendicularly into a transverse stream.
Trans. Institute of Chemical Engineers, 45, 1967.

[3] **Smith, S.H. and Mungal, M.G.**
Mixing, structure and scaling of the jet in crossflow.
Journal of Fluid Mechanics. 357, 83-122 (1998) **357**, 83-122 (1998)

[4] **Pratte, B. D. and Baines, W. D.**
Profiles of the round turbulent jet in a cross flow.
Journal of the Hydraulics Division Proceedings of the *ASCE.* **92**, 53-64 (1967)

[5] **Broadwell, J.E. and Breidenthal, R.E.**
Structure and scaling of a transverse jet in incompressible flow.
Journal of Fluid Mechanics. **148**, , 405-412 (1984)

[6] **Keffer, J. F. and Baines, W. D.**
The round turbulent jet in a cross-wind.
Journal of Fluid Mechanics. **15**, , 481-496 (1963)

[7] **New, T. H., Lim, T. T. and Luo, S. C.**
Effect of jet velocity profiles on a round jet in cross-flow.
Experiments in Fluids. **40**, 859-875 (2006)

[8] **Su, L.K. and Mungal, M.G.**
Simultaneous measurements of scalar and velocity field evolution in turbulent crossflowing jets.
Journal of Fluid Mechanics. **513**, 1-45 (2004)

[9] **Cortelezzi, L. and Karagozian, A.R. .**
On the formation of the counter-rotating vortex pair in transverse jets.
Journal of Fluid Mechanics. Vol.**513**, 347-373 (2001)

[10] **Muppidi, S. and Mahesh, K.**
Direct numerical simulation of passive scalar transport in transverse jets.
Journal of Fluid Mechanics. **598**, 335-360 (2008)

[11] **Kamotani, Y. and Greber, I.**
Experiments on a turbulent jet in a cross flow.
AIAA Journal. **10**, 1425-1429 (1972)

[12] **Margason, R.J.**
The path of a jet directed at large angles to a subsonic free stream. .
TN D-4919 NASA (1968).

[13] **McMahon, H. M. and Mosher, D. K**
Experimental investigation of pressures induced on a flat plate by a jet issuing into a subsonic crosswind.
NASA SP **218**, 49-62 (1969)

[14] **Margason, R.J.**
Fifty years of jet in cross flow research.
In Computational and Experimental Assessment of Jets in Cross Flow AGARD Conference Proceedings. **534** (1993)

[15] **Barre, C.**
Jet en écoulement transversal : observations expérimentales et numériques.
Thèse, Université Henri Poincaré-Nancy 1. (1998)

[16] **Humber, A. J., Grandmaison, E. W. and Pollard, A.**
Mixing between a sharp-edged rectangular jet and a transverse cross flow.
Int. J. Heat Mass Transfer. Vol. **36**. No. 18, 4307-4316 (1993)

[17] **Hasselbrink, E.F. and Mungal, M.G.**
An analysis of the time-averaged properties of the far field of the transverse jet.
AIAA **96-0201**. 34th Aerospace Sciences Meeting and Exhibit, Reno, Nevada, January 15-18 (1996)

[18] **Kelso, R.M. and Smits, A.J.**
Horseshoe vortex system resulting from the interaction between a laminar boundary layer and a transverse jet.
Physics of Fluids. Vol. **7**. No. 1, 153-158 (1995)

[19] **Krothapalli, A., Lourenco, L. and Buchlin, J.**
Separated Flow Upstream of a Jet in a Cross Flow.
AIAA Journal. **28**. 414-420 (1990)

[20] **Fric, T. F. and Roshko, A.**
Vortical structure in the wake of a transverse jet.
Journal of Fluid Mechanics. **279**. 1-47 (1994)

[21] **Kuzo, D. M. and Roshko, A.**
Observations on the wake region of the transverse jet.
Bulletin of the American Physical Society. **29**. 1536 (1984)

[22] **Moussa, Z. M., Trischka, J. W. and Eskinazi, S.**
The near field in the mixing of a round jet with a cross-stream
Journal of Fluid Mechanics. **80**. 40-89 (1977)

[23] **McMahon, H. M., Hester, D. D. and Palfery, J. G.**
Vortex shedding from a turbulent jet in a cross-wind.
Journal of Fluid Mechanics **48**, 73-80 (1971)

[24] **Eiff, O. S., Kawall, J. G. and Keffer, J. F.**
Lock-in of vortices in the wake of an elevated round turbulent jet in a crossflow.
Experiments in Fluids. **19**, 203-213 (1995)

[25] **Andreopoulos, J. and Rodi, W.**
Experimental investigations of jets in a crossflow.
Journal of Fluid Mechanics. **138**, 93-127 (1984)

[26] **Lim, T. T., New, T. H. and Luo, S. C.**
On the development of large-scale structures of a jet normal to a cross flow.
Physics of Fluids. Vol. **13**, No. 3, 770-775 (2001)

[27] **Fraticelli, R., David, L. and Borée, J.**
Jet carré dans un écoulement transverse à faible nombre de Reynolds.
9ème Congrès Francophone de Vélocimétrie Laser. 14-17 septembre 2004.

[28] **Yuan, L.L., Street, R.L. and Ferziger, J.H.**
Large-eddy simulations of a round jet in crossflow.
Journal of Fluid Mechanics. **379**, 71-104 (1999)

[29] **Ma, F., Satish, M. and Islam, M. R.**
Large Eddy Simulation of thermal jets in crossflow.
Engineering Applications Of Computationnal Fluid Dynamics. Vol. **1**, No. 1, pp 25-35 (2007)

[30] **Prière, C.**
Simulation aux grandes échelles : application au jet transverse.
Thèse, Institut National Polytechnique de Toulouse (2005)

[31] **Muppidi, S.**
Direct Numerical Simulations and Modeling of Jets in Crossflow.
PhD Thesis, University of Minnesota (2006)

[32] **S. Chapuliot, C. Gourdina, T. Payen, J.P. Magnaud and A. Monavond**
Hydro-thermal-mechanical analysis of thermal fatigue in a mixing tee.
Nuclear Engineering and Design 235 (2005) 575–596

[33] **BLASIUS, P. R. H.**
Das Aehnlichkeitsgesetz bei Reibungsvorgangen in Flüssigkeiten.
Forschungsheft 131, 1-41. (1913)

[34] **B. L. Smith, J. H. Mahaffy, K. Angele, J. Westin**
OECD/NEA-VATTENFALL T-junction benchmark specifications.
OECD/NEA Report (2009)

[35] **Pierre FOUGAIROLLE**
Caractérisation expérimentale thermo-aéraulique d'un jet transverse impactant ou non, en turbulence de conduite.
PhD Thesis, Université Joseph Fourier (2009)

[36] **Ulka Gaitonde**
Quality Criteria for Large Eddy Simulation
PhD Thesis, University of Manchester (2008)

[37] **D. Kuzmin and S. Turek**
High-resolution FEM-TVD schemes based on a fully multidimensional flux limiter
Journal of Computational Physics, Volume **198**, Issue 1, Pages 131–158, 2009

[38] **Kuczaj, A. K., de Jager, B., Komen, E. M. J.**
An assessment of large eddy simulation for thermal fatigue prediction
International Congress on Advances in Nuclear Power Plants, 2008

[39] **Emonot Ph.**
Methods de volums elements finis: Applications aux equations de navier-stokes et resultats de convergence
Ph.D. Dissertation, University of Lyon, 1992

[40] **Odemark Y., Green T. M., Angele K., Westin J., Alavyoon F., Lundstrom S.**
Highcycle thermal fatigue in mixing tees: new LES validated against new data obtained by piv in the vattenfall experiments
ICONE-17, 2009

[41] **Westin J., Mannetje C., Alavyoon F., Veber P., Andersson L., Andersson U., Eriksson J., Henriksson M., Andersson C.,**
High-cycle thermal fatigue in mixing tees. large eddy simulations compared to a new validation experiment.
ICONE-16, 2008

[42] **M. Merola, M. Biggio**
Valutazione della durata di vita a fatica termica: applicazione alla prima parete di un reattore a fusione di tipo Tokamak.
Scienze e tecniche nucleari, Rapporto EUR 11955 IT